

Airborne Hyperspectral Imaging of Lakes

THÈSE N° 8543 (2018)

PRÉSENTÉE LE 15 JUIN 2018

À LA FACULTÉ DE L'ENVIRONNEMENT NATUREL, ARCHITECTURAL ET CONSTRUIT

LABORATOIRE DE TOPOMÉTRIE

PROGRAMME DOCTORAL EN INFORMATIQUE ET COMMUNICATIONS

ÉCOLE POLYTECHNIQUE FÉDÉRALE DE LAUSANNE

POUR L'OBTENTION DU GRADE DE DOCTEUR ÈS SCIENCES

PAR

Kevin Sylvain BARBIEUX

acceptée sur proposition du jury:

Prof. P. Frossard, président du jury

Prof. B. Merminod, Dr J. Skaloud, directeurs de thèse

Prof. M. Kasser, rapporteur

Dr C. Giardino, rapporteuse

Prof. S. Süssstrunk, rapporteuse



ÉCOLE POLYTECHNIQUE
FÉDÉRALE DE LAUSANNE

Suisse
2018

This work is dedicated to my parents, Véronique and Sylvain, and to my brother Alexandre.

Acknowledgements

I would first like to thank my thesis director, Bertrand Merminod, for giving me the opportunity to work in his laboratory. Apart from the technical challenges that were very exciting to take, I got the chance to work on a project with both theoretical and practical work, meaning, flying above lake Baikal onboard a ultralight plane. I am very grateful to Bertrand for giving me the chance to do things few - if any - other PhD students have done during their thesis. Second, I would like to thank Davide Cucci and Jan Skaloud, for providing technical feedback as well in various occasions, but most importantly during the writing of my last journal article. Bertrand, Jan and Davide have helped me to identify problems and seek solutions several times. This was a very needed support. I also thank Vincent Nouchi, who was my reference when it came to problems with radiometry. Although he was a PhD student like me, Vincent was much more advanced than me in radiometry I could rely on him on various occasions to help me with the understanding of theoretical notions. I thank all the people who I had the opportunity to work with in the lab, beginning with Mehran, who is also a friend and helped me not only professionally but also personally, at a moment when I was really down. I warmly thank Emmanuel, Philipp and Geoffrey for sharing a bit of time with me in the same office, each of them at different times. It was a real pleasure to work with them every day. Thanks to Pierre-Yves for involving in different teaching tasks and in the organisation of the ENC 2017, it was a sincere pleasure for me, and Pierre-Yves has always been very friendly with me. Thanks to Dragos, Martin, Gabriel, Manuel for sharing their professional moments with me, I learnt a lot from interacting with them. I have a very special feeling for each one of the students I had the opportunity to supervise: Lucas, Antigoni, Lukas, Sonia and finally Kalliopi, who is one of the most joyful persons I have met. Special thanks also go to Nikolay, José and Ben, the ULM pilots who made me discover lake Geneva and lake Baikal from high altitudes. I will never forget it. Thanks to Sascha and Oyuna, the administrators of the Baikal Institute for Nature Management, who organised our whole trip at Baikal and made sure we were comfortable there.

On the personal side, I thank my parents and my brother, Alexandre, for unconditionally supporting me throughout the years and having made what I am today. Thanks to my grandparents, who I love and are models for me in my everyday life. And finally, thanks to the one and only Melina, to whom I owe my life.

Abstract

In a time of rising concern about climate change and pollution, the water quality of large lakes acts as an indicator of the health of the environment. To study the water quality at a large scale - up to several hundreds of kilometres - hyperspectral remote sensing is emerging as the main solution. Indeed, different quantities relevant to water quality, like turbidity or concentration in chlorophyll- α , can be measured using the spectral reflectance of the water column. Additionally, airborne and spaceborne sensors can cover large areas, thus allowing to study the water at a much larger scale than when simply taking water samples at specific points. Airborne hyperspectral imaging, in particular, offers an acceptable ground resolution - around a metre - which allows to map relevant quantities precisely. However, few existing projects deliver maps that have both a sufficient ground resolution and a large coverage. Furthermore, most existing sensors do not offer a fine spectral resolution, which is for instance crucial when studying the presence of chlorophyll- α , which can only be detected in a narrow range of the electromagnetic spectrum. This thesis presents our work with a hyperspectral sensor developed and used by the Geodetic Engineering Laboratory of EPFL in the Léman-Baïkal project, a cooperative work which aimed at studying both Lake Geneva (Switzerland) and Lake Baikal (Russia). The project included ultralight plane flights with an onboard pushbroom scanner, which allowed to collect data over large areas with a fine spectral resolution. Alongside the use of this sensor came problematics which are at the centre of this thesis: the georeferencing of the scan lines, their radiometric calibration, their analysis and the software management of this data. In the following, we present a new method to georeference pushbroom scan lines that uses co-acquired frame images to perform co-registration and to achieve a georeferencing, which RMSE is up to 20 times smaller than the direct one. We propose an efficient radiometric self-calibration method to convert the sensor output to water-leaving reflectance; this method makes use of the visible peaks of atmospheric absorption to align the spectral bands with those of a reference acquisition, and uses the near infrared properties of deep water and vegetation to perform absolute calibration. The last part of the processing - the software management, including data compression - was solved by developing a software called HYPerspectral Orthorectification Software (HypOS). This software is the synthesis of our work, including the tools to perform geometric correction, radiometric calibration and data compression of our hyperspectral data. Two examples of applications are given: the first one deals with mapping chlorophyll- α in the Rhone Delta of Lake Geneva; the second, at a larger scale, uses satellite data to monitor ice coverage over large lakes like Onega or Ladoga (Russia).

Abstract

Key words: Hyperspectral, Remote Sensing, Lakes, Radiometry, Georeferencing, Image Processing, Software

Résumé

En cette époque où le changement climatique et la pollution sont au coeur des préoccupations, la qualité de l'eau des lacs est un des indicateurs de la santé de notre environnement. Pour étudier la qualité de l'eau à grande échelle - jusqu'à plusieurs centaines de kilomètres - la télédétection hyperspectrale émerge ces dernières années comme la solution de référence. En effet, différents paramètres liés à la qualité de l'eau, tels que la turbidité ou la concentration en chlorophylle- α , peuvent être estimés à partir des mesures de réflectance spectrale de l'eau. De plus, les capteurs aéroportés et satellitaires couvrent de grandes zones, ce qui permet d'étudier l'eau à des échelles bien plus importantes qu'en prélevant des échantillons d'eau en des points isolés. En particulier, l'imagerie hyperspectrale aéroportée fournit une résolution au sol acceptable - environ un mètre - ce qui permet de cartographier les paramètres d'intérêt avec précision. Cependant, peu de projets existants produisent des images ayant à la fois une grande couverture spatiale et une résolution satisfaisante. De plus, les capteurs utilisés n'ont pas toujours une résolution spectrale élevée, élément pourtant crucial par exemple pour l'étude de la concentration en chlorophylle- α , qui ne peut être détectée que dans des plages très restreintes du spectre électromagnétique. Cette thèse présente notre travail avec une caméra hyperspectrale développée par le Laboratoire de Topométrie de l'EPFL dans le cadre du projet Léman-Baïkal, un projet coopératif visant à étudier à la fois le lac Léman (Suisse) et le lac Baïkal (Russie). Le projet consistait en des vols d'ultralégers motorisés (ULM) avec un capteur dit "pushbroom" (capteur à balayage) embarqué, qui a permis de récolter des données couvrant de larges zones avec une résolution spectral fine. L'utilisation de ce capteur a posé des questions qui constituent l'essence de la présente thèse : le géoréférencement des lignes acquises par le capteur, leur calibration radiométrique, leur analyse et la gestion logicielle de ces données. Nous présentons dans les chapitres suivants une nouvelle méthode pour géoréférencer les lignes scanner qui utilise les images RGB acquises parallèlement pour réaliser un co-référencement et parvenir à un géoréférencement dont la racine de l'erreur carrée moyenne (RMSE) est diminuée par un facteur allant jusqu'à 20, par rapport au géoréférencement direct. Nous proposons une méthode de calibration radiométrique autonome pour convertir les données issues du capteur en réflectance de l'eau ; cette méthode utilise les pics d'absorption atmosphérique pour aligner les bandes spectrales avec celles d'une acquisition de référence, et tire bénéfice des propriétés de l'eau et de la végétation dans le proche infrarouge pour réaliser une calibration absolue. La dernière partie du traitement - la gestion logicielle, comprenant la compression des données - a été résolue par le développement d'un logiciel nommé HYPerspectral Orthorectification Software (HypOS). Ce logiciel est la synthèse

Abstract

de notre travail, incluant les outils de correction géométrique, de calibration radiométrique et de compression des données hyperspectrales. Deux exemples d'applications sont donnés : le premier traite de la cartographie de la chlorophylle- α dans le Delta du Rhône du lac Léman ; le second, à plus grande échelle, utilise des données satellitaires pour observer l'évolution de la couverture de glace de grands lacs tels que Onega ou Ladoga (Russie).

Mots clefs : Hyperspectral, Télédétection, Lacs, Radiométrie, Géoréférencement, Traitement d'Images, Logiciel

Contents

Acknowledgements	i
Abstract (English/Français/Deutsch)	iii
List of Figures	xi
List of Tables	xvii
List of Abbreviations	xix
I Introduction	1
1 Motivation	3
2 Radiometry and Multispectral Cameras	5
2.1 Theory of Radiometry	5
2.2 Operating Principles of Cameras	8
2.2.1 Frame Cameras	8
2.2.2 Pushbroom Cameras	10
2.3 Camera Calibration	10
2.3.1 Quantum Efficiency	10
2.3.2 Spectral Calibration	11
2.3.3 Noise Removal	13
2.3.4 Conversion to Reflectance	15
2.4 Sources of Radiance	16
2.4.1 Sun glint	17
2.4.2 Sky glint	18
2.4.3 Atmospheric Path Radiance	18
3 Georeferencing of Airborne Images	21
3.1 Coordinate Systems	21
3.1.1 Geographic Coordinate Systems	21
3.1.2 Projected Coordinate Systems	22
3.1.3 Coordinate Frames	23
3.2 Standard Approach for Georeferencing Frame Images	23

Contents

3.2.1	Navigation Sensors	23
3.2.2	The Collinearity Equation	25
3.2.3	The Bundle Adjustment Theory	26
3.3	The Challenges of Pushbroom Images Georeferencing	27
3.3.1	Pushbroom Georeferencing: a State of the Art	27
3.3.2	Co-Registration onto a Reference Mosaic with Gradient Descent	28
3.3.3	Co-Registration onto a Reference Mosaic with Mutual Information	30
4	Acquisition System for the Léman-Baïkal Project	33
II	Hyperspectral Data Radiometric and Geometric Processing	35
5	Radiometric Correction	37
5.1	Radiometric Calibration Algorithm	37
5.1.1	Dark Current Noise removal	37
5.1.2	Spectral shifts removal	39
5.1.3	Stripes Effect Correction and Conversion to reflectance	41
5.1.4	BRDF Correction	42
5.1.5	Residual glint removal	45
5.1.6	Rescaling of Reflectance using Expected NIR Reflectance of Vegetation	45
5.2	Results	46
5.2.1	Sample data	46
5.2.2	Comparison between Calibrated Airborne spectrums and Ground Measurements	48
6	Pushbroom Images Georeferencing	51
6.1	Proposed Methodology	52
6.1.1	Pre-processing Step: Radiometric Matching	52
6.1.2	Bundle Adjustment of Frame Images	53
6.1.3	Initial Ortho-Projection of the Scan Lines	58
6.1.4	Systematic Error Correction	59
6.1.5	Geocorrection Using Particle Image Velocimetry	65
6.1.6	Estimation of the Orientation Parameters	68
6.2	Results	69
III	Software Management of Hyperspectral Data	77
7	Orthorectification and Viewing of Hyperspectral Data	79
7.1	Software Architecture	79
7.2	Orthorectification Process	80
7.3	Correction for the Variation of Sky Downwelling Irradiance	81
7.4	Boresight Correction from Manual Tie Points	84

7.5	Mosaic Export	86
7.6	HypOS Scientific Value and Use in Research	86
IV	Data Analysis	91
8	Applications of the Calibrated Léman-Baïkal Data	93
8.1	Estimation of the Concentration in Chlorophyll- α	93
8.1.1	Spectral Properties of Chlorophyll- α	93
8.1.2	Chlorophyll- α Concentration in the Rhône Delta	93
8.2	Study of Baikal Data	95
8.2.1	Filtering of Total Suspended Matter in the Delta	95
8.2.2	Other Related Works	96
9	Large Scale Ice Coverage Monitoring with Satellite Imagery	99
9.1	Landsat 8 Pre-Processing	100
9.2	State of the Art	100
9.2.1	Ice-Water Discrimination using SAR	100
9.2.2	Ice and Water Studies using Multispectral Images	101
9.3	Extraction of the Lake Body	102
9.3.1	Performance of Existing Indexes	102
9.3.2	Icy Lakes Index	105
9.3.3	Results	106
9.3.4	Extraction of Lakes Covered by Snow	110
9.4	Water-Ice Classification	114
9.4.1	Problem Formulation	114
9.4.2	Local Texture and Water-Ice Classification Index	118
9.5	Results	120
9.5.1	Comparison to Reference Data	121
9.5.2	Comparison to Sentinel-1 SAR Data	126
	Conclusion	133
A	Data Compression	135
A.1	Radiometric Calibration Storage: UXM Files	135
A.1.1	Coding Scheme	135
A.1.2	UXM Memory Consumption	137
A.2	Hyperspectral Files Lossless Compression	138
A.2.1	Prediction Phase	139
A.2.2	Entropy Coding	139
A.2.3	Computational Time and Compression Rate	143
	Bibliography	156
	Curriculum Vitae	157

List of Figures

2.1	The electromagnetic spectrum, with a zoom on the visible part.	6
2.2	Illustration of the radiometric quantities. (a) illustrates the concept of power, where all the photons hitting a surface over a period of time are counted. (b) isolates a surface of area dA , putting in evidence the notion of irradiance. (c) focuses on the rays coming from a given solid angle $d\omega$, illustrating the concept of radiance.	7
2.3	Illustration of the reflectance notions. (a) illustrates the concept of spectral irradiance reflectance, which considers all incoming and outgoing rays. (b) isolates a direction (θ_r, φ_r) , representing the concept of remote sensing reflectance. (c) focuses on the irradiance received from a given solid angle $d\omega_i$, illustrating the concept of BRDF	8
2.4	Simplified operating principle of a camera.	8
2.5	Example filters layouts for (a) an RGB camera and (b) a 25 band multispectral camera.	9
2.6	Principle of a pushbroom camera.	10
2.7	Raw output from our sensor, highlighting the different quantum efficiencies, and the dioxygen absorption peak of the atmosphere around 760 nm.	11
2.8	Illustration of the concepts of centre of a band, and Full Width at Half Maximum.	12
2.9	Illustration of the spectral smile: due to the optical system, radiations (in colours) are misprojected on the CCD array (transparent).	13
2.10	At the top, a smile-free column and the representation of its transmittances in two bands; at the bottom, a column affected by smile, with one cell of the CCD now receiving a mix of the two bands, previously separated. The apparent transmittance of this cell has a new centre and a larger FWHM.	14
2.11	Illustration of the striping effect for pushbroom sensors.	15
2.12	The different sources of radiance affecting an airborne sensor over water.	16
2.13	Illustration of the dependence of sun glint on the flight lines angle. In (a) , the aircraft flies parallel to the sun zenith angle. The resulting output is a uniform line. In (b) , the flight line is orthogonal to the sun zenith angle, thus inducing an angle-dependent glint.	17
3.1	Latitude and longitude of a location.	22
3.2	Principle of the UTM projection.	23

List of Figures

3.3	Representation of the local-level frame (in black) and the body frame of the camera (in orange). The two first axis of the local-level frame are aligned with North and East, respectively. The camera frame has its axis aligned with the two dimensions of the CCD array and the viewing direction.	24
3.4	Illustration of the concepts of boresight and lever-arm.	25
3.5	Flowgram of the approach proposed by Rzhanov and Pe'eri.	29
3.6	(Copyright © 2008, IEEE) Sample result from Cariou and Chehdi's work on the geocorrection of CASI data. (a) shows the raw pushbroom image (in red) with the backward projected reference orthoimage from the French Institut National Geographic (IGN) in cyan on top, where the biases ω_0 , ϕ_0 , κ and Z_0 were set to 0. (b) shows the same overlay after optimization of the mutual information. Two roads were highlighted with colours (orange and green) to illustrate the better coherence of the second overlay.	31
4.1	(a) illustrates the setting for our airborne acquisitions. (b) represents the different frame coordinates for the three sensors: the frame camera, the pushbroom (PB) camera, and the IMU.	34
5.1	Flowgram of our approach.	38
5.2	Autocorrelation plot for the 125 th band in the 500 th pixel of our camera.	38
5.3	Signals obtained at the different steps of the smoothing process.	39
5.4	High frequencies of two different pixels. The signals are similar and relevant to establish a band to band match from one signal to another.	40
5.5	Spectrum 1, spectrum 2 and its warped version, around the wavelength corresponding to dioxygen absorption. The warped signal peak is aligned with the corresponding one in spectrum 1.	41
5.6	Illustration of the spatial noise correction in the band 125 (632.5 nm), over the Rhône. Two columns where the stripes effect is particularly visible are indicated by red arrows.	42
5.7	Representation of the angles θ and ϕ for a 2D viewing direction.	43
5.8	Vegetation area and maximum and minimum outputs in this region.	46
5.9	Sample points visualised in Google Earth.	47
5.10	Projection of 1000 hyperspectral lines in our software HypOS. The background imagery is from Bing Maps. The orange line is the flight line.	47
5.11	Plots of Airborne versus in situ data for the points near the Rhône.	49
5.12	Plots of Airborne versus in situ data for the points near Selenga Delta (Lake Baikal).	50
6.1	Flowchart of the proposed geocorrection method.	53
6.2	Processing of the frame images using Agisoft Photoscan: (a) alignment of frames and computation of the orthophoto; (b) computation of the DEM of the area (Selenga Delta Village).	57

6.3	Orthoprojection of the scan lines (cyan) on top of the reference orthomosaic (red) above a village near the Selenga Delta of Lake Baikal. (a) is the orthoprojection of the pushbroom pixels (without interpolation) and (b) is the image as seen after bilinear interpolation of the projected values.	60
6.4	Scatter of the difference vectors for the pairs of points matched by the SURF, for a flight over a village of the Selenga Delta. All the matches are represented by red crosses. Tilted blue crosses correspond to the pairs kept after removing outliers.	64
6.5	Averages of the cross-correlations of corresponding patterns between a reference orthophoto and a co-registered mosaic, for the patterns and their gradients.	66
6.6	Examples of co-registered patterns using PIV on original images ((a),(c),(e)) and on gradient images ((b),(d),(f))	67
6.7	Illustrations of the various steps of our algorithm for a test flight over a village of the Selenga Delta (Russia, 17 August 2014). All images show the superimposed scan lines (in cyan) on top of the reference orthophoto (in red). (a) Initial projection with uncalibrated IOP; (b) Feature matching using SURF; (c) Projection with calibrated IOP and boresight; (d) PIV performed on the gradient images; (e) Deformation of the scan lines, following the PIV; (f) Projection after correction of the EOP.	70
6.8	Superposition of the reference orthophotos and the mosaic produced with the scan lines: (a) , (c) , (e) before geocorrection and (b) , (d) , (f) after geocorrection. (a) , (b) : Selenga Village 2; (c) , (d) : Selenga Rivers; (e) , (f) : Gremyachinsk.	72
6.9	Superposition of the reference orthophoto and the mosaic produced with the scan lines (a) before geocorrection and (b) after geocorrection, for our test region on the shore of Lake Geneva.	73
7.1	Opening screen of HypOS. The green features were included with the SDK. The red features are hyperspectral-specific features that we developed and incorporated in the user interface.	80
7.2	DEM of a part of EPFL, (a) without and (b) with corresponding hyperspectral data superimposed, visualised in HypOS.	82
7.3	Visualisation of a flight from August 2014 over the Selenga Delta. (a) : projection, with the flight lines seen as coloured lines; (b) : selected points for computation of the difference of illumination.	83
7.4	Visualisation of a flight from August 2014 over the Selenga Delta, after illumination correction.	85
7.5	Comparison of the mosaics, before and after illumination correction. Brightness was adjusted in both cases to make the differences clear.	86
7.6	Extracts from flights 1 and 2, corrected using manually input tie points: (a) overview of the flight from an isometric view in HypOS; (b) extract before correction; (c) extract after correction. To put in evidence the effect of the correction, features have been highlighted using red, green and blue colours.	87

List of Figures

7.7	Extract from flight 3, corrected using manually input tie points: (a) overview of the flight from an isometric view in HypOS; (b) extract before correction; (c) extract after correction. To put in evidence the effect of the correction, a feature has been highlighted with a red outline.	88
7.8	Example of (a) export of a mosaic from HypOS and (b) subsequent visualisation in ERDAS Imagine.	89
8.1	Hyperspectral mosaic produced in the Rhône Delta of Lake Geneva, 21 April 2015.	94
8.2	Chlorophyll- α concentration map in the Rhône Delta of Lake Geneva, 21 April 2015. Grey areas are land, excluded from the processing.	95
8.3	(Copyright © Springer 2017) Total suspended matter maps in four areas of the Selenga Delta. The maps were processed from our calibrated hyperspectral data.	96
9.1	Sample points from Lake Onega: (a) April 10th, 2014; (b) March 12th, 2015. Blue points are open water/ice cover, green points are snow, red points are land, and the two magenta points at the top of (a) are ice with crusted snow/with snow cover.	103
9.2	Scores of the three tested indexes for the 120 sample points.	104
9.3	<i>ILI</i> scores for the 120 sample points.	105
9.4	Comparison of the performances of the indexes for lake extraction on the 5 lakes. (a) is the original NIR image with enhanced brightness; (b) is the MNDWI binary classification, (c) is the WRI, (d) is the $NDWI_H$ and (e) is the <i>ILI</i> . The red features are pixels retrieved by the corresponding index and not by the <i>ILI</i> ; the green features are negative for the corresponding index and positive for the <i>ILI</i> . The zones used for quantitative results are tagged in the original images.	107
9.5	Comparison of the performances of the indexes in zones O1, O2 and A. The red features are false positives; the green features are false negatives.	109
9.6	Comparison of the performances of the indexes in zones B1 and B2. The red features are false positives; the green features are false negatives.	110
9.7	Comparison of the performances of the indexes in zones S1, S2 and U. The red features are false positives; the green features are false negatives.	111
9.8	Optimal threshold for each zone and each index; straight lines indicate the average optimal threshold for each index.	115
9.9	Illustration of the difficulty to delineate lake borders in case of important snow cover. (a) is the original Landsat 8 image of Lake Uvs (December 23rd, 2014). It is completely snow-covered and the lake is barely recognisable. (b) is an overlay of the UTM-transferred mask extracted from the image of May 16th, 2015, on top of the red background being the original image. (c) is the comparison of the extracted shoreline in Zone U (blue) with the reference shoreline, drawn manually (green).	116
9.10	The four categories of materials found in lakes: (a) deep water, (b) shallow water/mixed water - land pixels, (c) opaque ice, (d) clear ice.	116

9.11	Box plots of the Landsat 8 TOA reflectances for its first six bands, for the 119 sample points. The horizontal segments represent the 5th, 25th, 50th, 75th, and 95th percentiles; the circles are sample values lying out of the 90% represented by the extreme segments.	117
9.12	(a) 2D plot of the 1000 training samples for training the water-ice discrimination algorithm. The x coordinate is the NIR reflectance, the y coordinate is the average gradient in a 5×5 pixels neighbourhood of the sample point in the ultra blue reflectance. Red points correspond to ice or clear ice, blue points correspond to water or shallow water. The decision tree learnt on this sample is illustrated by the black line ($NIR = 0.021$) and the green line (Average Gradient = 0.008), and shown in (b).	119
9.13	WICI scores for the sample points.	120
9.14	Decision tree used for our water-ice classification algorithm.	120
9.15	Water-ice classification results, part 1: (a) Lake Onega, April 10th, 2014; (b) Lake Amadjuak, August 8th, 2016; (c) Great Bear Lake, June 27th, 2013. Images on the left are the unprocessed Landsat 8 OLI images (NIR band with enhanced brightness), and images on the right are the classifications, with ice in yellow on top on the original image in blue. Zones used to quantify the results are indicated in red.	122
9.16	Water-ice classification results, part 2: (a) Great Slave Lake, May 22th, 2015; (b) Lake Uvs, May 16th, 2015; (c) Lake Onega, March 12th, 2015. Images on the left are the unprocessed Landsat 8 OLI images (NIR band with enhanced brightness), and images on the right are the classifications, with ice in yellow on top on the original image in blue. Zones used to quantify the results are indicated in red.	123
9.17	Classification results for zones C_O14, C_A and C_B. (a) is the original Landsat 8 NIR image with enhanced brightness; (b) is the manually digitised reference data; (c) is our classification, with false positives coloured in red, and false negatives coloured in green.	124
9.18	Classification results for zones C_S and C_U. (a) is the original Landsat 8 NIR image with enhanced brightness; (b) is the manually digitised reference data; (c) is our classification, with false positives coloured in red, and false negatives coloured in green.	125
9.19	SAR HH image of Lake Ladoga (April 11th, 2015), pre-processed with the Sentinel-1 Toolbox.	127
9.20	(a) is the composite of the Landsat blue band image (cyan) and the co-registered Sentinel-1 HH image (red). 30 tie points used for assessing the quality of the co-registration are displayed in yellow to red colours, according to the distance between their locations in the Sentinel-1 image and the Landsat image. An area, highlighted by a rectangular black border, is zoomed on and shown in (b).	128
9.21	Features used for the SVM classification of the Sentinel-1 SAR image of Lake Ladoga (April 11th, 2015). (a): Contrast; (b): Energy; (c): Homogeneity.	129

List of Figures

9.22	Composite image showing the Landsat 8 OLI and the Sentinel-1 SAR binary classification in the northern part of Lake Ladoga, April 11th, 2015. The yellow pixels are the locations classified as ice by both methods; the green pixels are positive for the SAR and not for the OLI; red pixels are positive for the OLI and not for the SAR.	129
9.23	Zoom on four parts of Figure 9.22, from West (a) to East (d)	130
A.1	Example illustrating (a) the matching operated by DTW, and (b) the corresponding path in the DTW matrix.	137
A.2	Finite state machine representing the coding of the DTW path.	137
A.3	Standard system design for compression of hyperspectral images.	138
A.4	Histogram of values for (a) the original hypercube and (b) the residuals hypercubes.	140
A.5	First two iterations of our Huffman tree and dictionary function.	141
A.6	Last two iterations of our Huffman tree and dictionary function.	142

List of Tables

4.1	Characteristics of the navigation system on board the ultralight plane.	33
4.2	Characteristics of the pushbroom scanner on board the ultralight plane.	34
4.3	Characteristics of the frame camera on board the ultralight plane.	34
5.1	list of the points used to assess our results.	46
5.2	Quantitative results of comparison between airborne spectrums and ground spectra.	49
6.1	Maximum correlations of compensated parameters observed in different scenarios at first iteration of the least squares optimisation.	63
6.2	Values and standard deviations of boresight parameters and IOP estimated by the least squares adjustment.	64
6.3	Characteristics of the five test acquisitions.	71
6.4	Planar RMSE for each test area, and percentage evolution from previous step, at each step of the geocorrection.	74
7.1	Comparison of mean residual before and after correction for three flights of different altitudes.	85
8.1	Concentration in chlorophyll- α and image values in the mosaic, for the three points of interest during our experiments in the Rhône Delta of Lake Geneva, 21 April 2015.	95
9.1	Landsat 8 bands specification.	103
9.2	List of Landsat 8 images used in our study.	106
9.3	Errors and κ for the four indexes, in Zones O1, O2 and A.	112
9.4	Errors and κ for the four indexes, in Zones B1 and B2.	113
9.5	Errors and κ for the four indexes, in Zones S1, S2 and U.	114
9.6	Kappa coefficients, commission and omission errors of our water-ice classification in the zones of interest.	121

List of Abbreviations

AISA	Airborne Imaging Spectroradiometer for Applications	SWIR	ShortWave InfraRed
AT	AeroTriangulation	TOA	Top-of-Atmosphere
AWEI	Automated Water Extraction Index	TSM	Total Suspended Matter
BRDF	Bidirectional Reflectance Distribution Function	ULM	Ultraléger Motorisé (Ultralight Plane)
CART	Classification And Regression Trees	UTM	Universal Transverse Mercator
CASI	Compact Airborne Spectrographic Imager	VH	Vertical transmit, Horizontal receive
CCD	Charge Coupled Device	VV	Vertical transmit, Vertical receive
CDOM	Coloured Dissolved Organic Matter	WGS84	World Geodetic System 1984
DEM	Digital Elevation Model	WICI	Water-Ice Classification Index
DTW	Dynamic Time Warping	WRI	Water Ratio Index
ENU	East-North-Up		
EOP	Exterior Orientation Parameters		
ESA	European Space Agency		
FPN	Fixed Pattern Noise		
FWHM	Full Width at Half Maximum		
GCP	Ground Control Point		
GIS	Geographic Information System		
GLCM	Gray Level Co-occurrence Matrix		
GNSS	Global Navigation Satellite System		
GPS	Global Positioning System		
GSD	Ground Sampling Distance		
HH	Horizontal transmit, Horizontal receive		
HV	Horizontal transmit, Vertical receive		
HypOS	Hyperspectral Orthorectification Software		
ILI	Icy Lakes Index		
IMU	Inertial Measurement Unit		
IOP	Interior Orientation Parameters		
IRGS	Iterative Region Growing by Semantics		
LOS	Line Of Sight		
MNDWI	Modified Normalised Differential Water Index		
MNF	Minimal Noise Fraction		
NDWI	Normalised Differential Water Index		
NED	North-East-Down		
NIR	Near InfraRed		
NLAC	Non Local Active Contour		
OLI	Operational Land Imager		
PIV	Particle Image Velocimetry		
PRNU	Photo-Response Non-Uniformity		
QUAC	QUick Atmospheric Correction		
RANSAC	RANdom SAMple Consensus		
RGB	Red Green Blue		
RMSE	Root Mean Square Error		
RTE	Radiative Transfer Equation		
RTK	Real Time Kinematic		
S1TBX	Sentinel-1 ToolBoX		
SAM	Spectral Angle Mapper		
SAR	Synthetic Aperture Radar		
SDK	Software Development Kit		
SURF	Speeded Up Robust Features		
SVM	Support Vector Machine		

Introduction **Part I**

1 Motivation

Monitoring large lakes is an essential task. The quality of their waters needs to be controlled not only to ensure they are drinkable, but also because it is very relevant to the stability of the local ecosystems. Indeed, the micro and macro developments of algae and the overabundance of phytoplankton in lake waters is toxic for the local species, whether plants or animals [129]. The health of lakes has also been proven to be highly correlated with climate change [57, 106]; in particular, global warming increases the temperature of lakes, and alters their carbon cycle and their nutrients productivity [105].

Studying the water quality of large lakes cannot rely only on the collection of water samples and other field studies. For lakes like Baikal, $31\,722\text{ km}^2$, field work allows in the best case to evaluate local concentrations of phytoplankton or turbidity, but no conclusion at larger scales can be extrapolated. The only reliable method to collect information on wide areas is remote sensing. Whether it is with satellite data or airborne data, images from high altitude guarantee a wide ground coverage. The reason why these methods are reliable is because properties like concentration in chlorophyll- α (and therefore phytoplankton) and Coloured Dissolved Organic Matter (CDOM) are strongly correlated with water colour [144]; thus, observing the colour of the water tells us about its quality. However, the notion of colour here is to be clarified. Standard RGB cameras, which collect information in three wide spectral bands, are not sufficient: we need to observe the reflectance of water in very narrow bands of given wavelengths [74, 127]. For this reason, multispectral (especially hyperspectral) remote sensing has become the reference technology for water quality assessment applications.

The work described hereinafter was done in the context of the "Léman - Baïkal" project, a cooperative project involving the geodetic engineering laboratory and the limnology laboratory of EPFL, as well as Russian partners from the Moscow State University and the Baikal Institute of Nature Management. The Russian and Swiss teams pointed out similarities between Lake Geneva (Switzerland), also known as "lac Léman" in French, and Lake Baikal (Republic of Buryatia, Russian Federation). The most important one is their eutrophication: in the recent years, due to human activities (namely, the discharge of products containing phosphate in the lake), the waters accumulated an excessive amount of nutrients, boosting the developments of algae which consume the oxygen of the lakes. The idea behind the project

Chapter 1. Motivation

was to use remote sensing techniques to evaluate these effects: from 2013 to 2015, about 120 ultralight flights, with a pushbroom hyperspectral camera, were performed above both lakes. The objective was to map certain quantities - mainly chlorophyll- α and turbidity - at large scales to evaluate the health of the lakes.

This thesis focuses on the processing needed prior to the analysis of the hyperspectral data. While allowing to collect data with a much better spectral resolution than frame cameras, the pushbroom sensor requires finer processing both on the radiometric and the geometric level. On top of usual radiometric calibration issues, pushbroom sensors suffer from the so-called "smile" effect, shifting the spectrums collected along the wavelength axis. This effect needs to be compensated for, so as to obtain comparable spectrums across the images collected. Geometry-wise, the georeferencing of pushbroom data is challenging: filtered data from navigation sensors allow to perform direct georeferencing, but the inaccuracy of the data delivered (in particular yaw angles) prevent the creation of proper orthomosaics. To achieve better georeferencing, the need of better image processing algorithms arose. Therefore, this thesis shall solve the following problems:

- the georeferencing of the pushbroom hyperspectral data, that is, the accurate location of the data collected by the camera onto the Earth.
- the radiometric calibration of our measurements, from the digital numbers output by the camera, to the surface reflectance.
- the processing of this data to determine water properties (chlorophyll- α and turbidity).

In the rest of this Part, we introduce the scientific notions involved in these problems, together with a review of the literature around these problems.

2 Radiometry and Multispectral Cameras

2.1 Theory of Radiometry

Before entering the core of the subject, it is essential for the reader to understand the basic physical concepts on which aerial imagery relies. We first introduce the notion of radiometry, that is, the measure of light (or electromagnetic radiations) with cameras.

Definition 1. *There exists a physical field, produced by electrically-charged materials, that is called the electromagnetic field. Electromagnetic radiations are distortions of the electromagnetic field in the form of waves or flow of particles.*

Each radiation - visible or not - is characterised by the length of its wave, called wavelength. The light (common name for the visible part of the electromagnetic spectrum) is an electromagnetic radiation, as being both a wave of the electromagnetic field but also a flux of photons; the fact that this light is said to be visible is because it is sensed by the human eye. However, there exist, in our environment, many more radiations that humans cannot see. Figure 2.1 shows the electromagnetic spectrum, as the main categories of electromagnetic radiations as a function of their wavelengths.

Electromagnetic radiations interact with the objects of our environment in four different ways.

- Emission: an object acts like a source for the radiations. Typical examples are the sun, and lamps.
- Reflection: an object reflects the incoming radiations. All the objects of our environment reflect parts of the radiations they receive. Although the concept of "black body" (a body that absorbs all incoming radiations) is used in the theory of radiations, it is more a theoretical view, as no object known reflects exactly 0 % of the radiations.
- Transmission: the object lets radiations through. For example, the surface of water
- Absorption: the object receives radiations, but does not transmit or reflect them.

Chapter 2. Radiometry and Multispectral Cameras

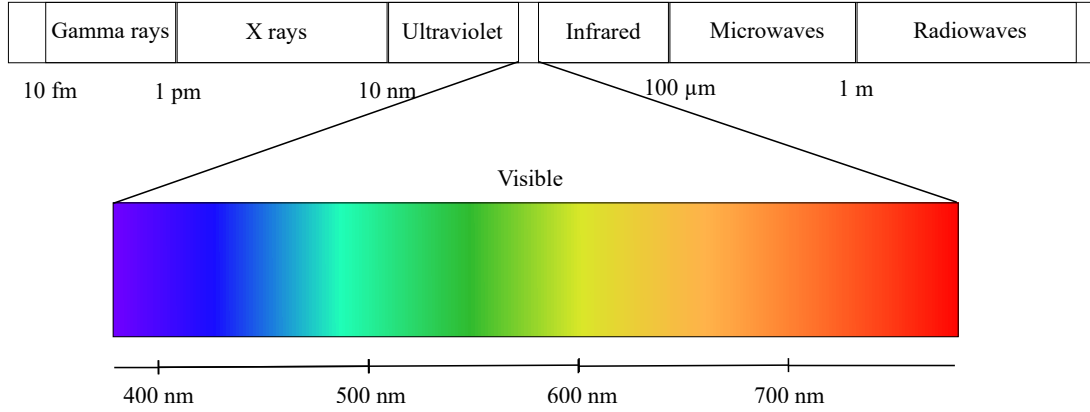


Figure 2.1 The electromagnetic spectrum, with a zoom on the visible part.

In the context for airborne imagery, all the objects on the ground receive radiations from the sun. The radiations they reflect can be characterised using different quantities.

Definition 2. *The radiant energy (Q) is the energy transferred by electromagnetic radiations.*

Definition 3. *The power, or radiant flux (Φ) is the time derivative of the energy. $\Phi = \frac{dQ}{dt}$.*

Definition 4. *The irradiance (E) is the radiant flux emitted or reflected per unit of surface dA : $E = \frac{d\Phi}{dA}$.*

Definition 5. *The radiance (L) is the radiant flux emitted or reflected per unit of surface dA from a direction given by the solid angle $d\omega$: $E = \frac{d\Phi}{dAd\omega}$.*

These definitions are illustrated on Figure 2.2.

None of the quantities presented above is, however, relevant of the properties of the objects. Indeed, the variations of the ambient light directly affect all these quantities. The only intrinsic optical property that can be used in airborne imagery is called the reflectance.

Definition 6. *The reflectance is the ratio between the radiance (or irradiance) received by an object and the radiance (or irradiance) reflected by the object. It is a function of the wavelength of the incoming radiation.*

Definition 6 is purposely not bonded to either irradiance or radiance, because in reality multiple definitions of the reflectance coexist [97, 101].

Definition 7. *The spectral irradiance reflectance (ρ) is the ratio between the upwelling irradiance leaving a surface and the downwelling irradiance received by the same surface.*

$$\rho(\lambda) = \frac{E_u(\lambda)}{E_d(\lambda)} \quad (2.1)$$

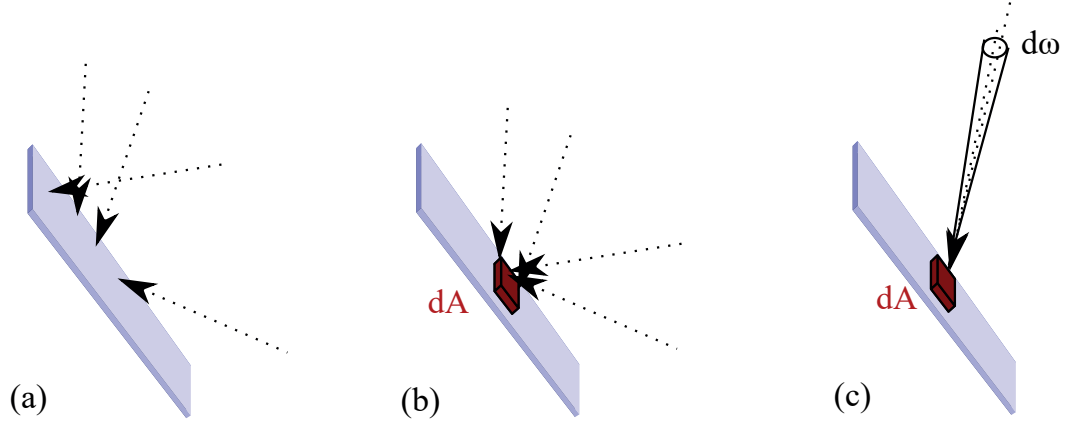


Figure 2.2 Illustration of the radiometric quantities. **(a)** illustrates the concept of power, where all the photons hitting a surface over a period of time are counted. **(b)** isolates a surface of area dA , putting in evidence the notion of irradiance. **(c)** focuses on the rays coming from a given solid angle $d\omega$, illustrating the concept of radiance.

Definition 8. The remote sensing reflectance (ρ_{rs}) is the ratio between the upwelling radiance leaving a surface in a given direction (characterised by two angles) and the downwelling irradiance received by the same surface.

$$\rho_{rs}(\theta, \varphi, \lambda) = \frac{L_u(\theta, \varphi, \lambda)}{E_d(\lambda)} \quad (2.2)$$

Definition 9. The Bidirectional Reflectance Distribution Function (BRDF) is the ratio between the upwelling radiance leaving a surface in a given direction (θ_r, φ_r) and the downwelling irradiance received by the same surface from a given cone of directions (θ_i, φ_i).

$$BRDF(\theta_r, \varphi_r, \theta_i, \varphi_i, \lambda) = \frac{L_u(\theta_r, \varphi_r, \lambda)}{E_i(\theta_i, \varphi_i, \lambda)} \quad (2.3)$$

These definitions and their notations are illustrated on Figure 2.3.

For airborne sensors, we mostly use the remote sensing reflectance, that is, the ratio between what is received by the sensor (the at-sensor radiance) and all the radiations hitting the object (the input irradiance). The remote sensing reflectance is therefore expressed in sr^{-1} . However, the mosaics produced with airborne images usually show a clear dependence of the resulting reflectances on the viewing angles, which is why the BRDF remains the most exhaustive reflectance concept. In order to use the remote sensing reflectance, the effect of the viewing direction, called BRDF effect must be corrected (see Section 5.1.4).

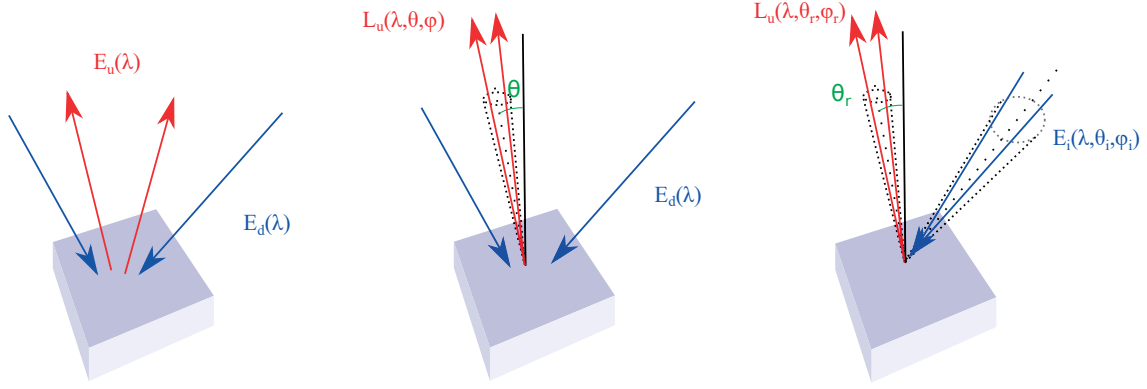


Figure 2.3 Illustration of the reflectance notions. **(a)** illustrates the concept of spectral irradiance reflectance, which considers all incoming and outgoing rays. **(b)** isolates a direction (θ_r, ϕ_r) , representing the concept of remote sensing reflectance. **(c)** focuses on the irradiance received from a given solid angle $d\omega_i$, illustrating the concept of BRDF.

2.2 Operating Principles of Cameras

2.2.1 Frame Cameras

By camera, we refer to any electronic device that transforms light into electronic signals, and allows to store them in images geometrically conforming to the scene. Cameras consist in three main parts: an optical collimation system (usually composed of lenses and mirrors) to collimate incoming light rays into points; an imaging sensor (film, CMOS, CCD array...) that generates electrons from the energy of incoming photons; and a processing system, that filters the electronic signal and digitalises it.

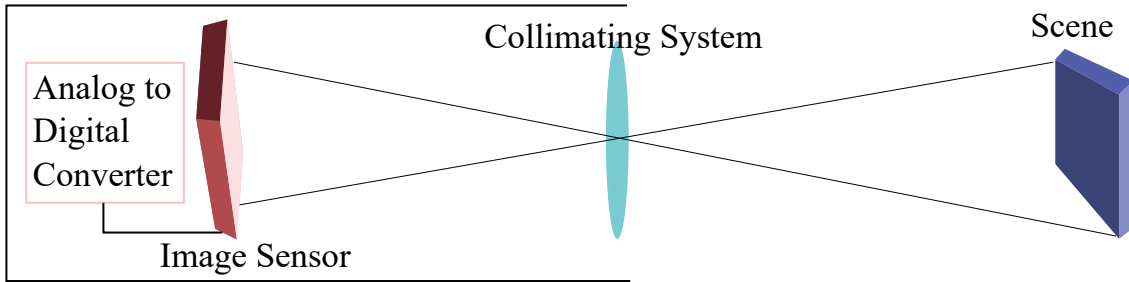


Figure 2.4 Simplified operating principle of a camera.

In the following, we focus on explaining the theory of the imaging systems. Using the photoelectric effect, radiations can be transformed into electricity. Radiations are separated (or gathered) by cameras using spectral filters, that is, surface that transmit or absorb radiations according to their wavelength.

Definition 10. The transmittance T of a surface is the ratio between the irradiance transmitted and the irradiance received by this surface. It is a function of the wavelength of the incoming

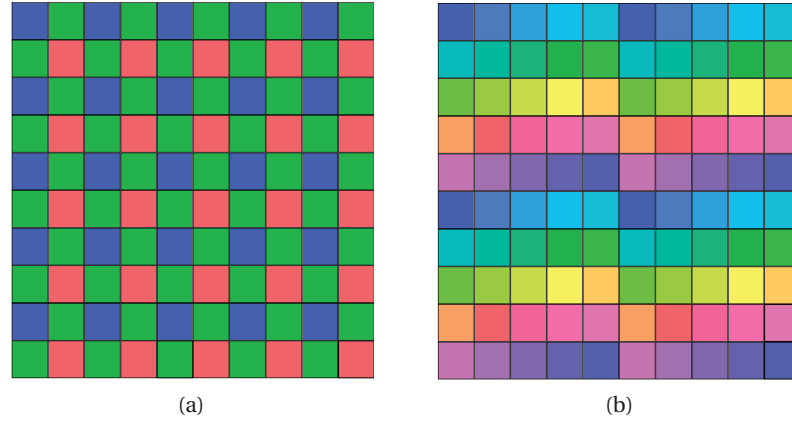


Figure 2.5 Example filters layouts for **(a)** an RGB camera and **(b)** a 25 band multispectral camera.

radiation.

Most commercial cameras are Red - Green - Blue (RGB) cameras: these cameras acquire information in three bands, each of which is characterised by the transmittance spectrum of its filters. On the sensor, filters are placed following a given pattern such as the Bayer filter, to collect red, green and blue information across the whole scene.

However, the information delivered by RGB cameras is far too coarse to allow the study of water. Optical properties of water have to be determined in narrow bands of the spectrum, which in addition are not only in the visible range, but also the infrared range. For this reason, this thesis revolves around multispectral cameras.

Definition 11. *Multispectral cameras are cameras that capture information in many (more than 3) bands.*

Definition 12. *Hyperspectral cameras are multispectral cameras with three additional properties: their bands are disjoint (no wavelength is present in more than one band), thin (this notion is subjective), and all together they describe a continuous range of the electromagnetic spectrum.*

The advantage of multispectral cameras is not only the possibility to collect data in non-visible bands, but also to collect these data in much narrower bands (i.e., with a better spectral resolution). Reflectance in very specific wavelength ranges can be measured, which is crucial in the study of phytoplankton for example. The extra-information delivered by multispectral cameras comes with a price: a bigger number of neighbour cells are needed to collect data in all the bands of a given pixel, as illustrated in Figure 2.5.

2.2.2 Pushbroom Cameras

While 4 cells are needed to collect information in 3 bands for an RGB camera, 25 cells are required for a 25 bands multispectral camera, decreasing the geometrical resolution of the output images in the same proportion. For this reason, the most commonly used type of multispectral camera are pushbroom cameras. A pushbroom camera acquires lines (and not frames) of geometrical pixels: light from each of these geometrical locations is split into radiations of different wavelengths by a prism, and these radiations are all projected onto different lines of the CCD array (see Figure 2.6).

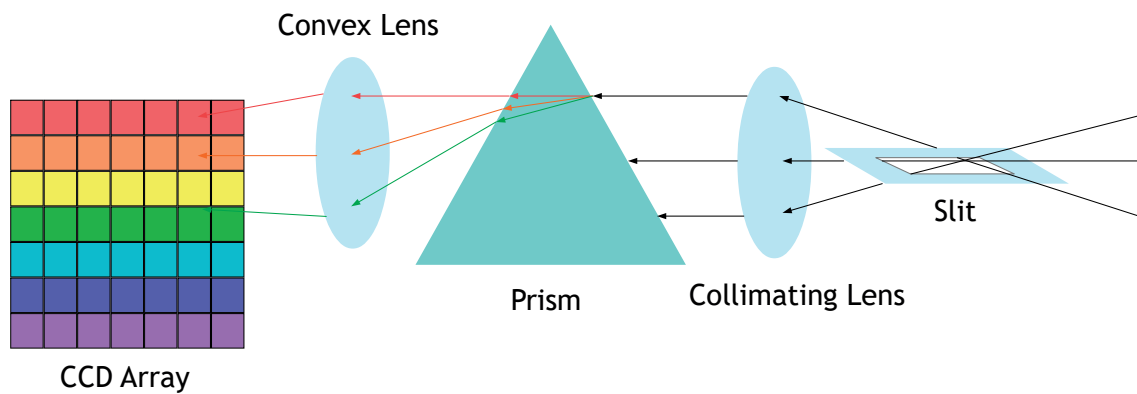


Figure 2.6 Principle of a pushbroom camera.

Pushbroom cameras basically sacrifice one geometrical dimension of their output to provide spectral information with very high resolution. Hence, the pushbroom technology is ideal to collect data with both high geometrical resolution and high spectral resolution. However, reconstructing images, and georeferencing them, is much harder than with standard RGB cameras, as we explain in Section 3.3.

The signal delivered by a hyperspectral camera is composed with digital numbers. There is the need to calibrate the camera to convert these numbers into reflectance, and to apply filters to the output to isolate the contribution of the object of interest.

2.3 Camera Calibration

2.3.1 Quantum Efficiency

Lights of different wavelengths are sensed differently by hyperspectral sensors. While a perfect camera would transform all the energy transmitted by photons into electricity, in practice some wavelengths give lower outputs. This phenomenon is due to the difference in quantum efficiency.

Definition 13. *The quantum efficiency is the ratio of the number of electrons emitted by a photoelectric unit, divided by the number of photons received by this unit. It is a function of the wavelength of the incoming radiations.*

To give energy to electrons in a CCD sensor, photons must be absorbed in the depletion area. Their energy must be enough to pass the electrode gate of the CCD, but small enough not to go through the depletion area without being absorbed. For many CCD sensors in the visible light, blue wavelengths hardly pass the gate, while red wavelengths can pass through the depletion area [134]. As an example, we have recorded the spectral response of our pushbroom sensor (a Headwall Micro Hyperspec VNIR-A) over a Spectralon Panel, which is a unit-reflectance surface. The result is plotted on Figure 2.7.

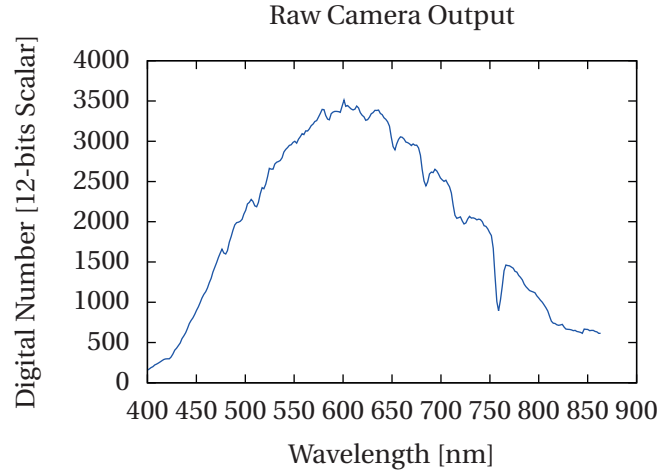


Figure 2.7 Raw output from our sensor, highlighting the different quantum efficiencies, and the dioxygen absorption peak of the atmosphere around 760 nm.

As can be seen on Figure 2.7, while the surface captured had a nearly flat reflectance, the spectral response output by the camera differs greatly according to the wavelengths. In the blue, red and infrared radiations, the system has a very low reponsivity. Low reponsivities need to be compensated for to have uniform measurements across the spectral range of interest.

Usually the gain and offset are determined in each band using a Lambertian (i.e., a surface reflecting radiations similarly, whatever the angle of incidence) unit-reflectance surface and a white lamp. The Lambertian surface, typically a Spectralon, is placed normally to the light source, while the sensor views the surface with an angle of 45° [28, 142].

2.3.2 Spectral Calibration

The use of a hyperspectral camera implies to know the spectral response functions of each of its bands. Using lamps emitting at different known wavelengths [41], it is possible to determine, for each band, its centre and its Full Width at Half Maximum (FWHM). This process is called spectral calibration.

Definition 14. *The Full Width at Half Maximum of a spectral band of a sensor is the width (usually in nm) of the range of wavelengths in which the transmittance is at least half the*

maximum of the transmittance of this band.

The notions of centre and FWHM of a band are illustrated on Figure 2.8.

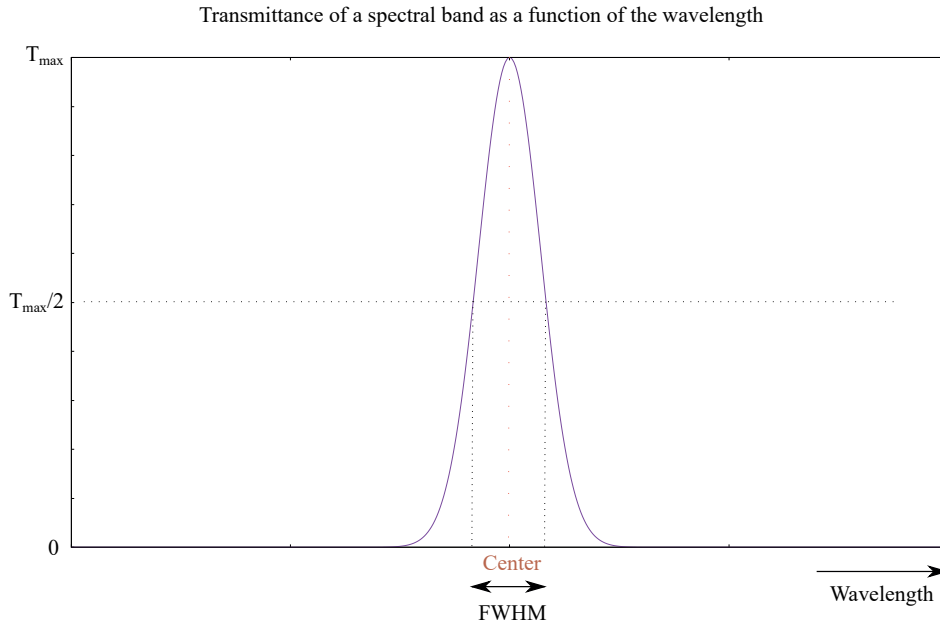


Figure 2.8 Illustration of the concepts of centre of a band, and Full Width at Half Maximum.

It is well known from the literature [100] that small manufacturing defects in pushbroom imaging spectrometers can have two unwanted consequences:

- Smile: spectral smile consists in a misprojection of the radiations on the CCD array, resulting in a convex distortion that has the shape of a smile (see Figure 2.9). As a consequence, the centre and FWHM for a given band vary from one pixel to the other.
- Keystone: keystone is also due to misprojection of the radiations, but results in a shift in the geometrical dimension (unlike the smile which induces shifts in the spectral dimension).

We can compensate for keystone by spatially filtering the hyperspectral images. However, the smile effect is a whole different problem that needs to be treated separately. Together with the mechanical movements of the diffraction grating of the sensor, they affect the signals by shifting them along the spectral dimension. As a consequence, we need to do spectral calibration, in the sense that all the signals shall be properly aligned with respect to the wavelengths.

Although the primary way of dealing with spectral smile is ensuring a good technical design of the sensor [80], [8], there is a strong need of algorithms able to "desmile" camera outputs

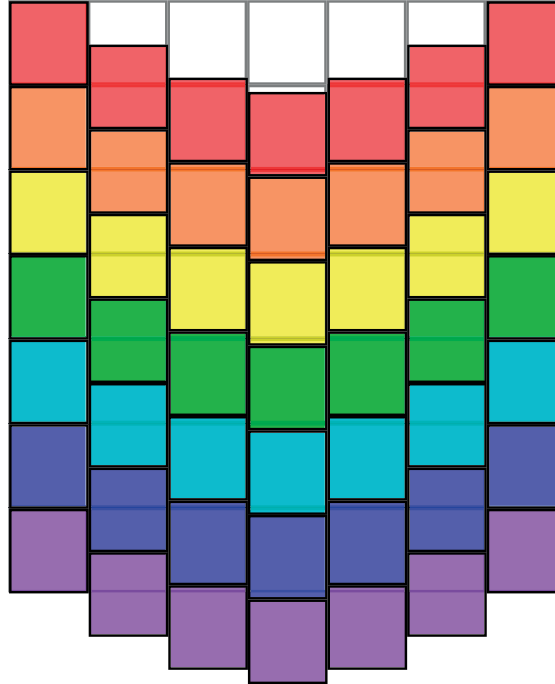


Figure 2.9 Illustration of the spectral smile: due to the optical system, radiations (in colours) are misprojected on the CCD array (transparent).

after acquisition. Many algorithms [32, 46] rely on the observation of artefacts in the images to quantify and correct smile. For example, Dadon & al. [32] quantify the variation of the spectrum around the dioxygen absorption peak in a processed image called the Minimal Noise Fraction - 1 (MNF-1) image. This image is the result of a Minimal Noise Fraction processing (see [51]) that gives the representation of the hypercube with the least possible noise. They process the shifts of the spectrums for each column compared with the column with minimal smile, and transform the MNF back to the radiance image. However, this process was found to create distortions when transforming MNF back to radiance. Ceamanos & Douté [23] proposed another method based on spectral sharpening; since the smile increases the FWHM of the bands (see Figure 2.10), the spectrums are upsampled, assuming spectral regularity for the extrapolated data. Their alignment procedure uses the CO_2 absorption band. Finally, another method is to evaluate spectral shifts inside the same procedure as the atmospheric correction (see Section 2.4.3) parameters by optimisation and with the use of Look-Up Tables (LUT [111]).

2.3.3 Noise Removal

Note: parts of this section were extracted from our article Airborne hyperspectral sensor radiometric self-calibration using near infrared properties of deep water and vegetation [7], in the proceedings of the SPIE Remote Sensing Conference. They are copied according to the SPIE Transfer of

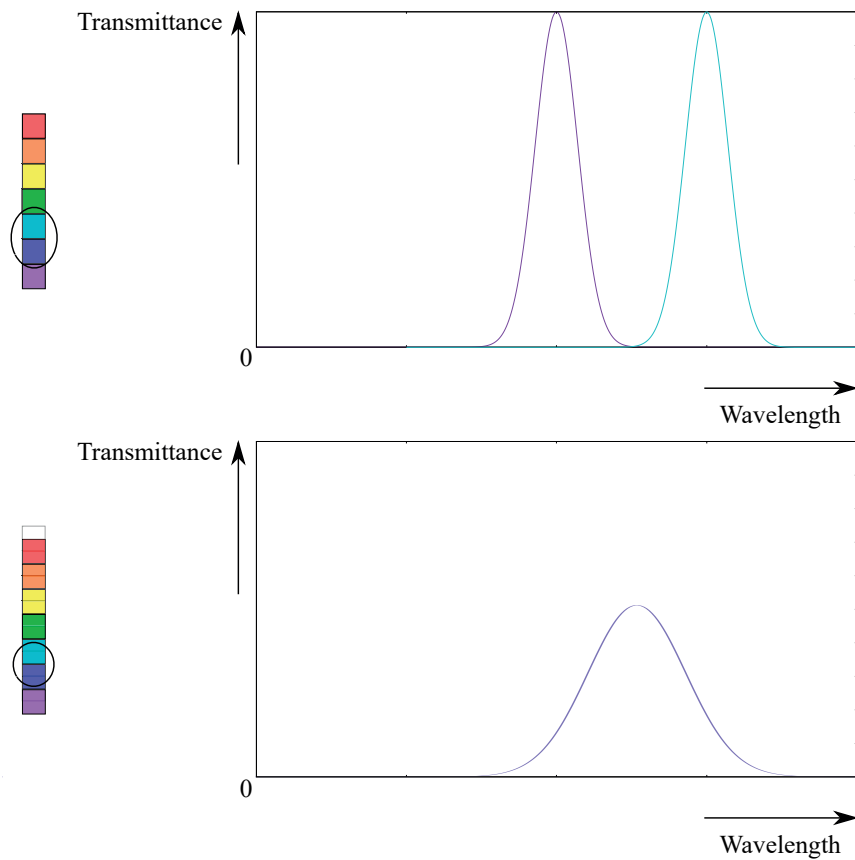


Figure 2.10 At the top, a smile-free column and the representation of its transmittances in two bands; at the bottom, a column affected by smile, with one cell of the CCD now receiving a mix of the two bands, previously separated. The apparent transmittance of this cell has a new centre and a larger FWHM.

Copyright agreement.

Every camera inherently has noise, and this noise itself is a mix of different noises.

- white noise is a zero-expectancy, random variable added to the output at each acquisition.
- quantization noise represents the loss when converting the "analogical" signal (the light) to digital values.
- dark current noise (also called Fixed Pattern Noise, FPN) is the output of the system when it is not exposed to any light. A flow of electrons is created through thermal processes. This noise is a function of temperature and integration time.
- spatial noise (also called Photo-Response Non-Uniformity, PRNU) stands for the difference of values between pixels when they are exposed to homogeneous light. For

pushbroom sensors, this results in a "stripes" effect that can be seen on Figure 2.11.

The white and quantization noises are random contributions to each image shot and are therefore called shot noises. The dark current and spatial noises are deterministic and called pattern noises [89]. Mathematically, the dark current is represented by a bias only depending on the pixel and the band (but timewise constant).

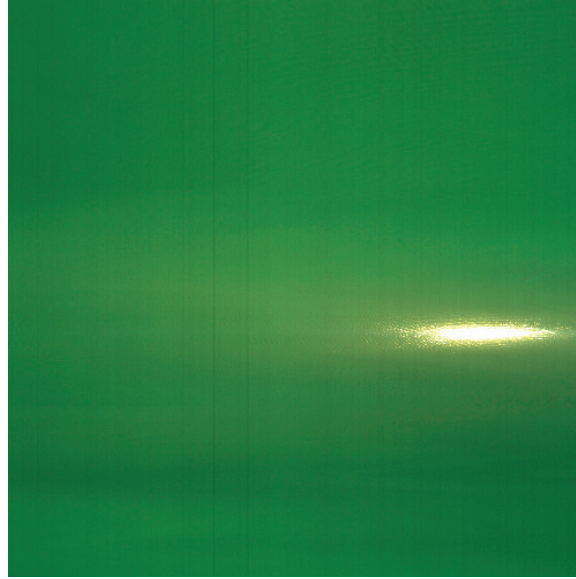


Figure 2.11 Illustration of the striping effect for pushbroom sensors.

2.3.4 Conversion to Reflectance

The camera output needs to be converted to reflectance, which is (unlike radiance) an intrinsic optical property of a surface. Two scenarios can happen: either the sensor output has been calibrated to radiance, or it has not. In the first case, one needs to know the downwelling irradiance on the scene captured, according to Definition 8, to convert the output to reflectance. The downwelling irradiance E_d can be measured with an instrument called a cosine collector [78]. In the second case, one can collect data over a Spectralon panel to directly convert the digital numbers of the camera to reflectance. This second scenario is worse: the calibration can be altered by the quality of the panel, which has theoretically a unit-reflectance. But in practice, defects in the panel can modify its reflectance in certain bands. For airborne applications, calibration with a Spectralon panel alone suffers from practical constraints: the data can be collected only before or after the flight, so the variations of irradiance during the flight are not taken into account.

The APEX project [59] of the European Space Agency designed a complex system with onboard calibration to overcome this limitation [103]. Their system includes a shifting surface to bring a mirror in the pathway of the sensor so that it receives the light from a Quartz-Tungsten Halogen lamp, allowing to monitor the stability of the calibration during the flight. Such a

system is much too complex and costly for our purpose. For the Léman-Baïkal project, some equipment was purchased before any calibration procedure was designed. Hence, our work in this thesis focuses on the creation of an approximate, totally image-based calibration (see Chapter 5).

2.4 Sources of Radiance

Parallel to the calibration of the camera, another important problem must be solved: the goal of the acquisitions is to measure the reflectance (or radiance) leaving the water. However, the radiance received by an airborne sensor does not come exclusively from the water, but is also influenced by the noise of the camera (as mentioned in Section 2.3.3), the reflection of the sun and sky radiations on the surface of the water, and - most of all - the atmosphere.

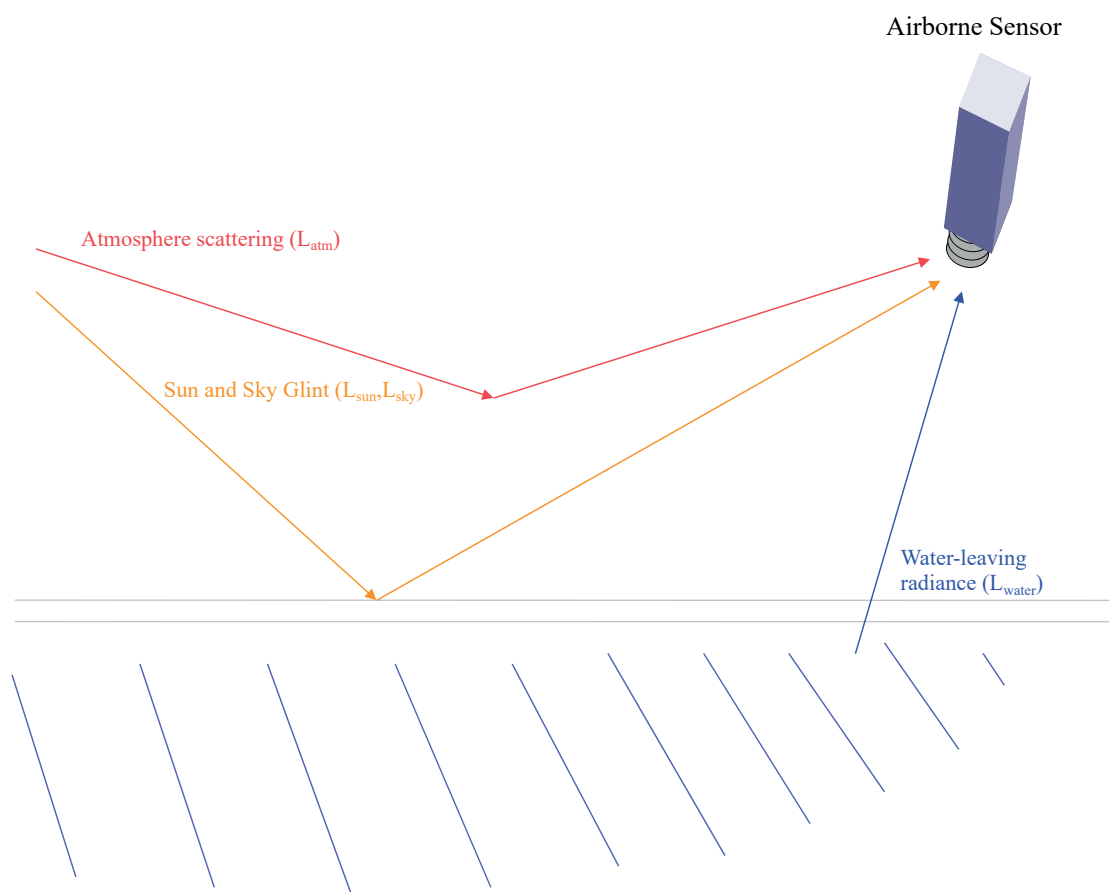


Figure 2.12 The different sources of radiance affecting an airborne sensor over water.

The total at-sensor radiance is the sum of all the corresponding radiances, as specified in

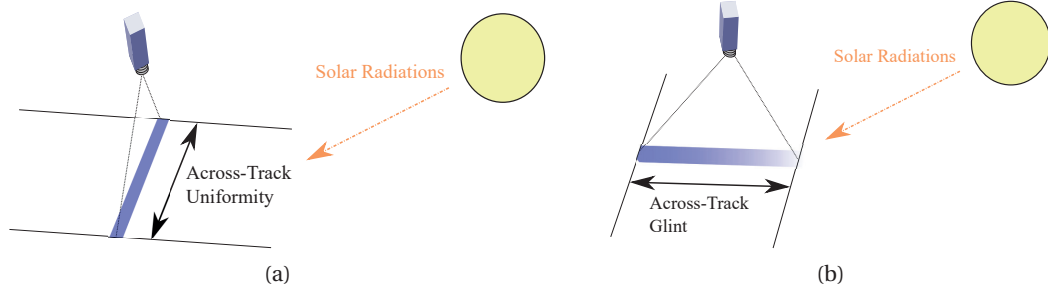


Figure 2.13 Illustration of the dependence of sun glint on the flight lines angle. In (a), the aircraft flies parallel to the sun zenith angle. The resulting output is a uniform line. In (b), the flight line is orthogonal to the sun zenith angle, thus inducing an angle-dependent glint.

Equation 2.4.

$$L_{sensor} = L_{noise} + L_{sun} + L_{sky} + L_{atm} + L_{water} \quad (2.4)$$

In the following, we describe these sources of radiances, and how to deal with them, in details.

2.4.1 Sun glint

Depending on the solar zenith/azimuth angle, and the orientation of the camera, the sun light can be directly reflected in the viewing direction of the sensor. There are two sorts of methods to deal with sun glint [70]:

- the flight time and the flight path can be adapted to limit the influence of the sun on the acquisition. For pushbroom sensors, the flight usually consists in scanning a zone with several parallel, overlapping flight lines. The main criterion to choose the flight lines angle is that it should allow to avoid the glint across the track, as illustrated on Figure 2.13.

To meet this requirement, it is preferable to avoid flying around noon (where the zenith angle variation is the fastest) and fly parallel to the zenith angle.

- various post-acquisition algorithmic methods allow to reduce sun glint in images. Most of them assume the water-leaving radiance in the near infrared should be negligible, subtract the near infrared value of a deep water point in the image and correct other bands by finding mathematical relations between the outputs of each band [47, 90, 56].

2.4.2 Sky glint

The water surface also reflects sky radiance, and its contribution to the total at-sensor radiance is called L_{sky} . Estimating or removing L_{sky} from images is a challenging task, since the sky contribution, unlike the sun, comes from all possible directions of the upward hemisphere. Most of the works on sky glint removal rely on concurrent in situ measurements and are therefore (semi-)supervised methods [34, 79]. Image-based, unsupervised methods (for example, Kim & al. [73]) are less frequent in the literature. In our work, we neglect the sky glint, as its influence usually represents less than 5 % of the total at-sensor radiance [70].

2.4.3 Atmospheric Path Radiance

The atmosphere interacts with the radiations transmitted to the sensor via two processes.

Absorption Due to the presence of certain gases, parts of the radiations are absorbed in the atmosphere. This causes the presence of absorption peaks in the radiance captured by the sensor. In the range of wavelengths captured by our sensor (400 nm to 850 nm), only the dioxygen absorption peak, around 760 nm, is significant. Figure 2.7 shows a typical raw output from our camera, where this absorption peak is clearly visible. The absorption can be dealt with easily using smoothing techniques.

Scattering The atmospheric scattering consists in the deviation of radiations by the particles in the atmosphere. Parts of the light coming from the sun are deviated directly towards the sensor, thus inducing a change in the radiance that we call L_{atm} . Light can be scattered either by atmospheric particles themselves (ozone...), or by aerosols present in the air.

These effects need to be compensated for: this is the atmospheric correction problem. Traditionally, this problem is expressed mathematically by the Radiative Transfer Equation 2.5, see [15].

$$\rho(\lambda) = A(\lambda) + \frac{B(\lambda)}{1 - S(\lambda)\langle\rho(\lambda)\rangle}\rho_0(\lambda) + \frac{C(\lambda)}{1 - S(\lambda)\langle\rho(\lambda)\rangle}\langle\rho(\lambda)\rangle \quad (2.5)$$

In Equation 2.5, $\rho(\lambda)$ is the at-sensor spectral irradiance reflectance, as given by Definition 7; $\rho_0(\lambda)$ is the surface reflectance; $\langle\rho(\lambda)\rangle$ is the average reflectance in a neighbourhood of the pixel of interest; A, B, C and S are all parameters relative to the atmospheric scattering effects. Although $\rho(\lambda)$ is not directly measured, it is related to the measured remote sensing

reflectance $\rho_{rs}(\lambda)$ by Equation 2.6 (see [48]).

$$\rho(\lambda) = \pi \rho_{rs}(\lambda) \quad (2.6)$$

Solutions to Equation 2.5 in the current state of the art are split into two categories: physical models, and image-based algorithms.

Physical Models

The reference for atmospheric correction is Modtran [14]. Modtran (MODerate resolution atmospheric TRANsmittance) computes line-of-sight (LOS) atmospheric spectral transmittances and radiances by solving the radiative transfer equation, assuming a horizontally homogeneous atmosphere. From input parameters (atmosphere type, concentration of certain gases, aerosols, visibility, ground temperature and albedo), Modtran can reconstruct the atmospheric path radiance (thus accounting for scattering) and transmittance (accounting for absorption) of the local atmosphere.

To perform atmospheric correction on images using the atmospheric properties output by Modtran, the most-utilised algorithm is the Fast Line-of-sight Atmospheric Analysis of Hypercubes (FLAASH [1]). This algorithm uses Modtran to solve the RTE for the A, B, C and S parameters as functions of the water vapour column. The water vapour column itself is computed for each pixel by using a spectral range of the hyperimage where the water vapour has particular characteristics; then, a average spectral radiance image is computed by convolving the image with a kernel depending on the altitude of the sensor and the properties of the aerosols. Taking the standard deviation of the RTE then allows to retrieve $\langle \rho(\lambda) \rangle$, which in turn allows to solve the equation for the surface radiance (or reflectance).

FLAASH, using the Modtran data, is the reference algorithm for accurate atmospheric correction. It is frequently updated and improved for speed and accuracy [108].

Image-Based Atmospheric Correction

The reference image-based algorithm for atmospheric correction is the QUick Atmospheric Correction (QUAC) [15]. As its name suggests, its main advantage over algorithms like FLAASH is its processing speed, 5 to 10 times superior. The algorithm relies on various assumptions:

- in various scenarios mentioned in the article [15], the S term of Equation 2.5 can be neglected.
- the spectrums are "different enough" across the image.
- the standard deviation of $\rho_0(\lambda)$ for this diverse spectrums is nearly independent on the wavelength λ .

- there are "dark pixels" ($\rho_0(\lambda) \approx 0$) in the image.

Using the dark pixels, the term $A(\lambda) + C(\lambda)\langle\rho(\lambda)\rangle$ can be computed. Then, taking the standard deviation of Equation 2.5 leads to $\sigma_{\rho(\lambda)} = B(\lambda)\sigma_{\rho_0(\lambda)}$, where σ stands for the standard deviation. $\sigma_{\rho_0(\lambda)}$ has been assumed to be wavelength independent, therefore $B(\lambda) = g_0\sigma_{\rho(\lambda)}$ where g_0 is a constant, that is either determined by calibration or by the knowledge of $B(\lambda)$ in some specific wavelengths [31].

The QUAC is not usable in our work for a simple reason: water pixels are usually the ones used as "dark pixels" as water has a very low reflectance, especially for longer wavelengths. In our work, where the main objective is to retrieve accurate low-reflectance spectrums from water, this assumption cannot be made.

3 Georeferencing of Airborne Images

Airborne images are valuable when the end user can identify its features, that is, match them to a known representation of the scene. This matching can be achieved in two ways: georeferencing and co-registration.

Definition 15. *Georeferencing is the process matching pixel coordinates of an aerial image to geographic coordinates.*

Definition 16. *Co-Registration is the process matching pixel coordinates of an aerial image to pixel coordinates of a reference image.*

One of the purposes of georeferencing is to allow images to be viewed in Geographic Information Systems (GIS) that implement models of the Earth surface, by overlaying them on top of existing maps. Georeferencing methods are split in three categories : direct, indirect and integrated georeferencing.

- Direct georeferencing refers to the use of navigation sensors onboard of the aircraft to measure the position and the attitude during the acquisition of the images.
- Indirect georeferencing is relative to the use of ancillary data like Ground Control Points (GCP) to adjust the positioning of the data on the globe.
- Integrated Georeferencing is the mix of both direct and indirect techniques.

Let us first describe the coordinate systems with which we work.

3.1 Coordinate Systems

3.1.1 Geographic Coordinate Systems

The Earth is traditionally represented by an ellipsoid of revolution (or spheroid), that is characterised by the lengths of its smaller axis and its larger axis. Along the years, different spheroids

have been used in geodesy; our purpose is not to list them here. In the recent years, the World Geodetic System 1984 (WGS84) is widely regarded as the reference geographic system, and we will use it for all our geographic applications.

On such a surface, every point can be located by two angles describing in which direction it is located, relatively to the centre of the Earth. The standard angles used are the latitude and the longitude: the latitude is the angle formed by the location of interest, the centre of the Earth and the Equator, and the longitude is the angle formed by the location of interest, the centre of the Earth and the Greenwich Meridian (see Figure 3.1).

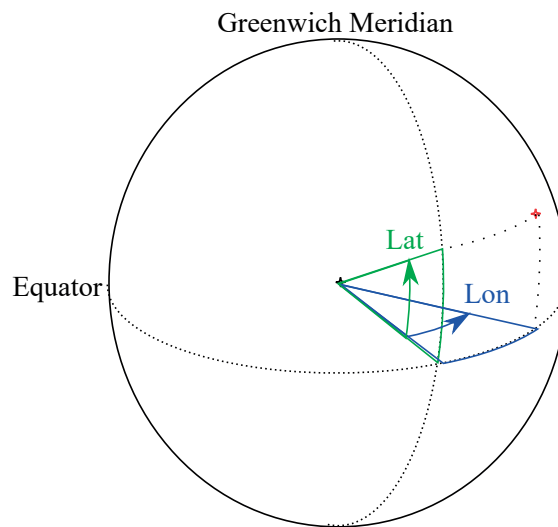


Figure 3.1 Latitude and longitude of a location.

3.1.2 Projected Coordinate Systems

The use of geographic coordinates suffers practical limitations, as positions, velocities and accelerations are always expressed in a metric system in navigation problems. To overcome these limitations, we use local metric systems called projected coordinate systems.

Definition 17. *A projected coordinate system is a metric coordinate system resulting from the local projection of an ellipsoid representing the Earth on a planar surface.*

As we will see, the use of a metric coordinate system facilitates the use of accelerometers, and the computations related to the Collinearity Equation (see 3.2.2). The projected system we use for most of our work is the Universal Transverse Mercator (UTM), which separates the Earth into 120 and projects locally these zones onto a cylinder (see Figure 3.2).

For more details about the UTM projection, the reader can refer to [50, 125].

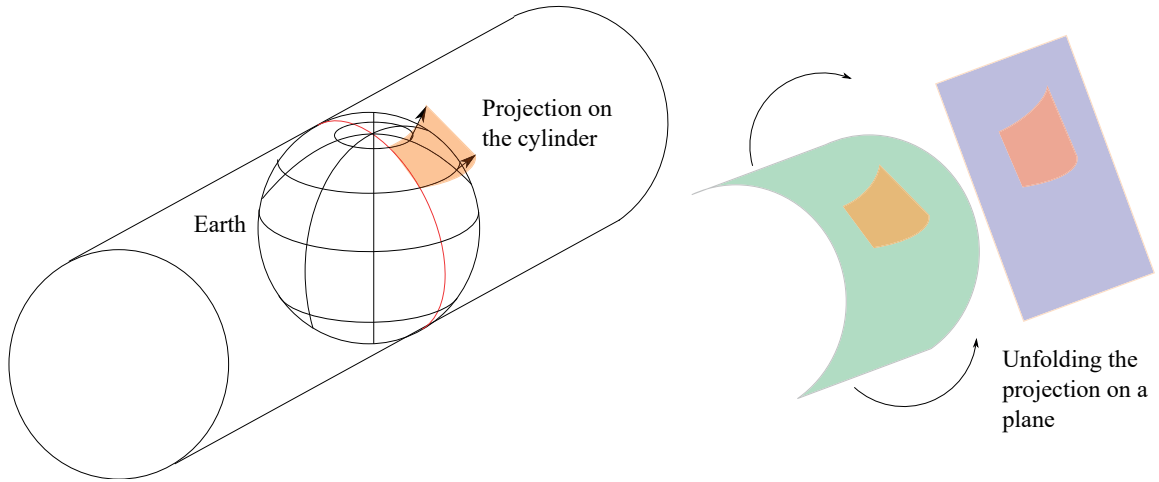


Figure 3.2 Principle of the UTM projection.

3.1.3 Coordinate Frames

In the following, we mainly use two coordinate frames: the local-level frame, and the body frame.

Definition 18. *The local-level frame is a right-handed coordinate frame centred at an arbitrary point on (or above) the surface of the Earth. Its axis can either point to the North, the East, and Down (NED) or to the East, North and Up (ENU).*

Definition 19. *The body frame of a camera is a right-handed coordinate frame centred at the optical centre of the camera, which third axis is the front of the camera.*

While Definition 18 is standard in the literature, Definition 19 is specifically adapted to our case, that is, a camera mounted on an aircraft. Let us call (X_l, Y_l, Z_l) the axis of the local-level frame (also called l-frame) and (X_b, Y_b, Z_b) the axis of the body frame (also called b-frame). Their definitions are illustrated on Figure 3.3.

3.2 Standard Approach for Georeferencing Frame Images

3.2.1 Navigation Sensors

To georeference the airborne data, the trajectory of the vehicle (including its position and its attitude) must be known. For this, the almost universal solution is the use of navigation sensors, and more specifically a global navigation satellite system (GNSS) device, and an Inertial Measurement Unit (IMU) comprising accelerometers and gyroscopes. GNSS devices have their distances to various visible satellite measured and computed to give an estimation of their position; IMUs measure their accelerations and angular velocities, and integrate them to obtain the position and the attitude. These two devices have their advantages and disadvantages: in a specific context (baseline, constellation...) GNSS devices give the position with

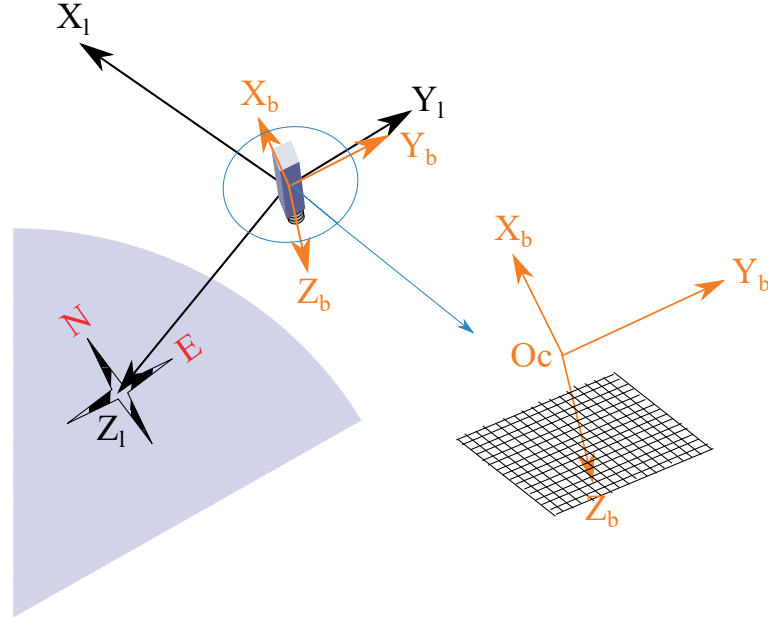


Figure 3.3 Representation of the local-level frame (in black) and the body frame of the camera (in orange). The two first axis of the local-level frame are aligned with North and East, respectively. The camera frame has its axis aligned with the two dimensions of the CCD array and the viewing direction.

a constant uncertainty (in our case, 2 cm with Real Time Kinematic, RTK), while IMUs provide precise measurements, but with growing error when integrating the accelerations/velocities. For this reason, they are almost always combined using Kalman filtering [67, 76].

The purpose of this section is not to provide a complete state of the art about navigations sensors and inertial navigation, which constitute a scientific discipline by themselves; the reader can refer to various works to find more information about these topics [120, 136]. However, we can mention here that several factors can impact the quality of the estimation of the trajectory. Besides the precision of the sensors themselves, both the lever-arm and the boresight between the camera and the navigation sensors alter the measurements.

Definition 20. *The boresight (usually referring to a couple camera/IMU) is the 3D rotation characterising the difference between the body frames of two different devices.*

Definition 21. *The lever-arm (usually referring to a couple camera/GNSS Antenna) is the 3D vector between the optical centre of the camera and the GNSS Antenna.*

The angles measured by the IMU characterise the viewing direction of the camera, up to the boresight correction; the position measured by the GNSS device corresponds to the position of the camera up to a translation along the lever-arm, as illustrated on Figure 3.4.

Additionally, although the absolute position parameters as well as the roll and the pitch are usually well estimated after filtering, the yaw is problematic. Indeed, the absolute positioning

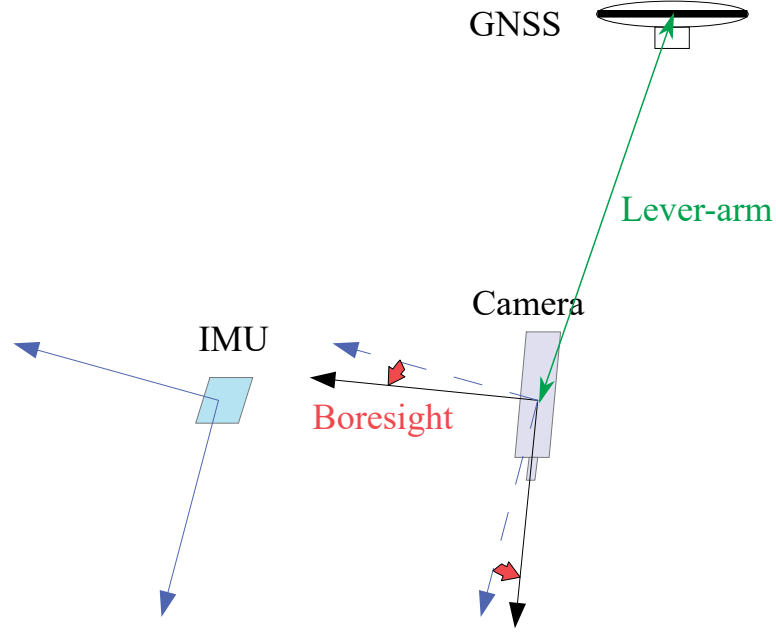


Figure 3.4 Illustration of the concepts of boresight and lever-arm.

is well corrected by the GNSS input; the gravity force, sensed by the accelerometers, is very strong compared with their biases, therefore its direction can be measured accurately and allow for absolute alignment of roll and pitch. However, a yaw misalignment does not alter the acceleration measurements, and thus cannot be detected without the help of another sensor [99, 13]. For our acquisitions during the Léman-Baïkal project, we have used a SBG Systems Ekinox2-N sensor (which includes a GPS, an IMU, a magnetometer and processes the Kalman Filter in real time). The magnetometer senses the Earth's magnetic field to provide an absolute estimate of the heading (yaw). However, magnetometers are subjected to electromagnetic interferences with other electronic devices on board, resulting in a poor estimation of the yaw.

3.2.2 The Collinearity Equation

We consider here the local-level frame centred at the optical centre of the camera, and the body frame of the camera, as illustrated in Figure 3.3.

Consider the following notations.

- (X_{oC}, Y_{oC}, Z_{oC}) are the coordinates of the optical centre (0 in the local-level frame).
- (X_G, Y_G, Z_G) are the coordinates of the corresponding ground point in the same frame.
- (u, v) are the metric coordinates of a pixel of interest in the body frame of the pushbroom camera. Its third coordinate is the focal length of the camera, f .
- (u_{pp}, v_{pp}) are the coordinates of the principal point of the camera in the same frame.

Chapter 3. Georeferencing of Airborne Images

- (r, p, y) are the roll, pitch and yaw angles representing the attitude of the vehicle.

Then, the rotation matrix from the body frame of the camera to the local-level frame is given by equation 3.1.

$$R_b^l(r, p, y) = \begin{bmatrix} \cos y \cos p & \cos y \sin p \sin r - \sin y \cos r & \cos y \sin p \cos r + \sin y \sin r \\ \sin y \cos p & \sin y \sin p \sin r + \cos y \cos r & \sin y \sin p \cos r - \cos y \sin r \\ -\sin p & \cos p \sin r & \cos p \cos r \end{bmatrix} \quad (3.1)$$

Using the collinearity equation (Equation 3.2), the coordinates of the ground point corresponding to a given pixel can be retrieved. This is usually achieved using ray tracing from the optical centre of the camera to the DEM.

$$\mu R_b^l(r, p, y) \begin{bmatrix} u - u_{pp} \\ v - v_{pp} \\ f \end{bmatrix} = \begin{bmatrix} X_{oC} \\ Y_{oC} \\ Z_{oC} \end{bmatrix} - \begin{bmatrix} X_G \\ Y_G \\ Z_G \end{bmatrix} \quad (3.2)$$

μ corresponds to the collinearity coefficient pixel vector and the ground point vector in the local-level frame. Using the collinearity equation, one can compute the geographic coordinates of every pixel of an image. A more rigorous model accounts for the distortion of the image due to the lens of the camera; Brown's distortion model [40, 33] represent the radial distortion with parameters usually noted (K_1, K_2) and the tangent distortion with parameters coined (P_1, P_2) . Considering the radius $r = \sqrt{(u - u_{pp})^2 + (v - v_{pp})^2}$ of a given pixel, the collinearity equation accounting for lens distortion is given by Equation 3.3.

$$\begin{aligned} \lambda R_b^l(r, p, y) \begin{bmatrix} (u - u_{pp})(K_1 r^2 + K_2 r^4) + (P_1(r^2 + 2(u - u_{pp})) + 2P_2(u - u_{pp})(v - v_{pp})) \\ (v - v_{pp})(K_1 r^2 + K_2 r^4) + (2P_1(u - u_{pp})(v - v_{pp}) + P_2(r^2 + 2(u - u_{pp}))) \\ f \end{bmatrix} \\ = \begin{bmatrix} X_{oC} \\ Y_{oC} \\ Z_{oC} \end{bmatrix} - \begin{bmatrix} X_G \\ Y_G \\ Z_G \end{bmatrix} \end{aligned} \quad (3.3)$$

3.2.3 The Bundle Adjustment Theory

To further improve the quality of the georeferencing, ancillary data can be used.

Definition 22. *Ground Control Points (GCP) are points with known coordinates, contained in one (or more) image(s) collected during the flight.*

Definition 23. *Tie Points are points that can be identified in multiple images.*

Tie points allow to correct the relative orientation of some images to others when the points are in an area where they overlap. GCPs rather refine the absolute orientation of some images. To merge the information from the navigation data and the GCPs/Tie Points, the standard method is the Bundle Adjustment [128]. The Bundle Adjustment refines the estimation of the orientation parameters along the trajectory, while also allowing to create an orthomosaic and a DEM of the area flown. It consists in an optimization algorithm: find orientation parameters as close as possible to the ones output by the navigation sensors, under the constraints given by the tie points and the GCPs.

Commercial softwares usually include feature-matching algorithms like SIFT [88] or SURF [10] to generate tie points between images.

3.3 The Challenges of Pushbroom Images Georeferencing

The bundle adjustment theory is, however, of little help in the case of pushbroom imagery: 3 GCPs per scan line would be required to georeference them properly [83]; the automatic tie points matching between scan lines is extremely difficult because, as said in Section 3.2.3, it usually relies on feature-matching algorithms for frame images, and consequently the 2D neighbourhoods of the points, which are not available in a 1D acquisition. To bypass these constraints, extra assumptions can be made about the trajectory of the vehicle. More specifically, assuming smoothness of the orientation parameters, the complexity of the problem can be reduced down to the determination of Gauss-Markov processes for said parameters [52, 82].

We start by giving an overview of the existing contributions in Section 3.3.1. In Section 3.3.2 and 3.3.3, two contributions are analysed in more details.

3.3.1 Pushbroom Georeferencing: a State of the Art

Georeferencing scan lines from a pushbroom sensor can be achieved with various setups and assumptions on the motion of the scanner. The most common approach is Integrated Sensor Orientation (InSO) involving the use of GCPs together with a model of the trajectory of the airborne vehicle/satellite. Such contributions include [52], assuming constant biases of roll, pitch and yaw angles across the scan lines, and estimating these biases using control points and Aerotriangulation (AT); in [109], the EOP of either a satellite or an airborne vehicle are modelled by piecewise polynomials, and optimised together with ephemeris or GPS/IMU data and GCPs using a least squares method; some additional parameters like the lever-arm between the GPS antenna and the pushbroom scanner, the boresight between the IMU and the scanner, or the non-uniform geometry of the CCD array can also be optimised by a least square method [140]. Using the co-registration to pre-existing reference orthoimages, relying on point features or linear features, can replace the measurements of GCPs [53]. Simple

methods, like the identification of a straight line, coupled with GCPs, even allow to obtain a decent mosaic from the scan lines [64], though such method obviously does not provide any information on the vehicle's trajectory. However, if no assumption on the smoothness of the trajectory is made, estimating the EOP for each scan line would imply to measure an unrealistically high number of GCPs [83]. To alleviate reliance on GCPs, a significant amount of contributions make use the co-acquisition of frame images, and develop methods to co-register the frame images and the scan lines. The most sophisticated algorithm seems to be given by [110]: the interior orientation of the pushbroom scanner is calibrated and the sensor is aligned with the frame camera using a target not parallel to the plan of the CCD array, and then the stitching of the frame images allow to build the hyperspectral mosaic. Additionally, this method does not require any navigation data; however, it supposes either the calibration with the triangle target prior to every flight, or the stability of the relative orientation of the two sensors. The ultralight plane flights operated during the Léman-Baïkal project were typically two to three hours long, therefore such stability cannot be assumed. Approaches involving the co-acquisition of frame images, scan lines and navigation data perform well [123]. The existence of frame images allows to get around the problem of weak geometry of the scan lines; the bundle adjustment of frame images outputs better orientation for said images, which in turn can be used as orientation for the pushbroom scanner, by estimating the boresight between the two cameras and defining an interpolation scheme to compensate for the difference of acquisition frequencies [6]. Among other contributions, [22] proposes a co-registration to an existing referencing using a mutual information criterion, and explores different scenarios of missing/inaccurate orientation data.

Considering the existing contributions, the originality of our work, presented in Chapter 6, is that the problem of georeferencing pushbroom scan lines is solved using navigation data and co-acquired frame images, without needing:

- GCPs
- a model for the vehicle's trajectory
- a priori knowledge on the boresight between the IMU and the pushbroom scanner (which is crucial, as there is no guarantee that the in-flight boresight did not change compared with its value before take-off)

and leads to new estimates of EOP for every scan line independently.

3.3.2 Co-Registration onto a Reference Mosaic with Gradient Descent

Y. Rzhanov and S. Pe'eri [112] designed a practical procedure to compute the correlation between the values in the scan lines and the values of a reference image. It relies on three assumptions:

3.3. The Challenges of Pushbroom Images Georeferencing

- Geographically co-localised points from the pushbroom scan lines and the reference have their values connected by a linear function. This assumption justifies the use of the correlation later in the algorithm. It is valid as long as the sensors are calibrated for noise and saturation, and the bands of the hyperspectral camera are combined properly to match the transmittance of the bands of the camera with which the reference was acquired.
- The Earth is locally flat, meaning, the elevation is modelled as a constant height across the area of interest. Although acceptable, this assumption collides with the use of a DEM, and hurts the third assumption.
- The ortho-rectified scan lines should be straight when co-registered onto the reference. This is not true when the terrain is not flat.

The flowgram of their method is given in Figure 3.5.

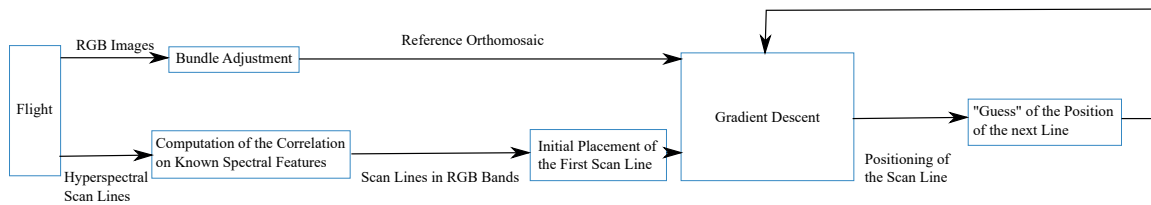


Figure 3.5 Flowgram of the approach proposed by Rzhanov and Pe'eri.

Their flights, like ours in the Léman-Baïkal campaign, were performed with an RGB camera and a pushbroom hyperspectral camera onboard. The RGB images are processed with a Bundle Adjustment, allowing the generation of an orthomosaic of the area flown. For the RGB and the hyperspectral information to be compared and correlated, hyperspectral data must be processed to give values comparable to the visible ones. The most rigorous method would be to multiply the values by the transmittance function of each channel of the RGB camera; since the transmittance functions were not known, the correlations between the bands of the hyperspectral cameras and the three bands of the RGB cameras were computed on spectral features they identified in both sets of images. The three bands with highest correlation to the red, green and blue bands were chosen to compute the RGB version of the hyperspectral data. The three bands chosen all had between 83 % and 86 % correlations to their equivalent in the other set.

The RGB reference, with much higher spatial resolution, was downsampled to the resolution of the pushbroom data. Starting from an initial position given by the user, the first scan line is iteratively repositioned by a gradient descent implemented using the Levenberg-Marquardt algorithm, which criterion is the correlation of pixel values between the line and the co-localised test line from the reference. When the line is matched, the following line is guessed to be at a position given by the previous line, plus a translation depending on the velocity of the vehicle. The optimization is then run again, and so on until all the scan lines are localised.

This simple approach suffers multiple problems. First of all, in spite of good visual results, the algorithm had to be computed several times with different initial positions for the first scan lines, as the gradient descent easily falls down into local minimums for the correlation. Second, as already mentioned, this method is not suitable for use with a digital elevation model, especially for large altitude variations inside the area. Third, the algorithms seems to not be suitable for flights with important changes in the aircraft altitude. In particular, U-turns, where the heading of the vehicle changes very rapidly, would probably prevent the algorithm from converging to an acceptable location, as the scan lines are supposed to be close to aligned. Finally, as the whole procedure is designed to work without the help of navigation data, no information about the aircraft trajectory can be retrieved from the geometrical correction.

3.3.3 Co-Registration onto a Reference Mosaic with Mutual Information

C. Cariou and K. Chehdi [22] also designed a procedure to co-register scan lines onto a reference image. Unlike Rzhannov and Pe'eri, their method takes into consideration - and corrects - the navigation parameters for the flight.

The mathematical model of the trajectory is similar to the one presented in Section 3.2, with two exceptions. The first one is that there is a set of exterior orientation parameters $(X, Y, Z), (\omega, \phi, \kappa)$ (last three being respectively roll, pitch and yaw) for each scan line. The second one is the assumed smoothness of the trajectory: all the scan lines have a similar attitude $(\omega_0, \phi_0, \kappa_0)$ with little variations for each scan line called instantaneous relative angles $(\omega_j, \phi_j, \kappa_j)$, where j is the index of the scan line. The authors assume that only ω_0, ϕ_0, Z_0 (the average altitude above ground) and all the κ are to be optimised. This is a reasonable assumption, since the small variations of the angles between lines is usually well captured by the inertial sensors; the κ angles are not measured by the system used in this paper. Regarding Z_0 , while other coordinates are well measured by a GNSS system, the altitude above ground can be biased by the error of the Geoid used compared with the true altitude.

The reference image is backward-projected onto the sensor: unlike the work of Rzhannov and Pe'eri, the ground coordinates of the reference image pixels are known, and transformed into sensor pixel coordinates using the collinearity equation (Equation 3.2). The geocorrection is performed iteratively: the algorithm searches for the maximum of the mutual information between the raw pushbroom image and the backward-projected reference image. Considering the deformed image from the pushbroom sensor I_d , the reference image I_r , the deformation operator D_Θ (Θ being the set of orientation parameters to optimise), f_g the (1D or 2D) probability density function of function g , u_1 the linear coordinate of a pixel of I_d and u_2 the linear coordinate of a pixel of I_r , then the criterion to optimise is the mutual information between I_d and $I_r \circ D_\Theta$, as given by Equation 3.4.

$$MI(I_d, I_r \circ D_\Theta) = \sum_{u_1, u_2} f_{I_d, I_r \circ D_\Theta}(u_1, u_2) \times \log \frac{f_{I_d, I_r \circ D_\Theta}(u_1, u_2)}{f_{I_d}(u_1) f_{I_r \circ D_\Theta}(u_2)} \quad (3.4)$$

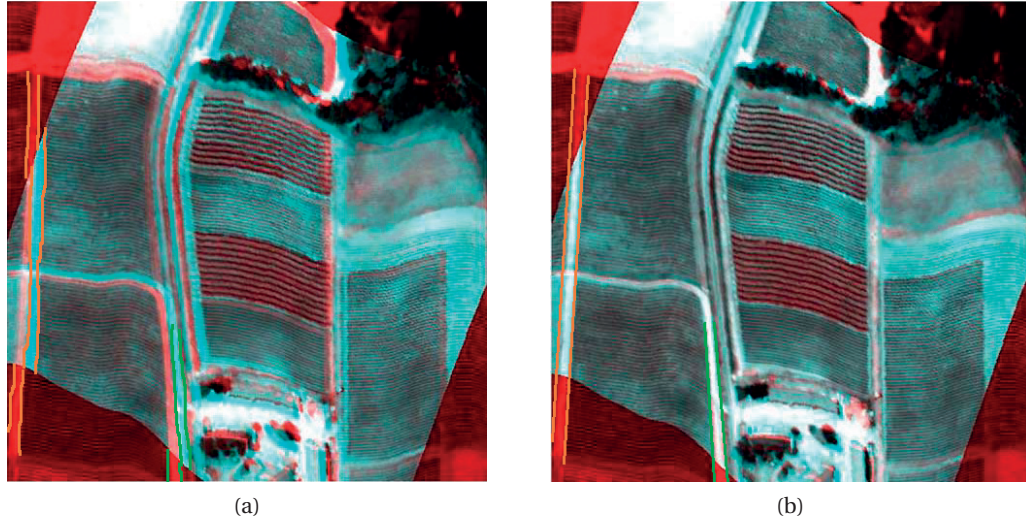


Figure 3.6 (Copyright © 2008, IEEE) Sample result from Cariou and Chehdi's work on the geocorrection of CASI data. **(a)** shows the raw pushbroom image (in red) with the backward projected reference orthoimage from the French Institut National Geographic (IGN) in cyan on top, where the biases ω_0 , ϕ_0 , κ and Z_0 were set to 0. **(b)** shows the same overlay after optimization of the mutual information. Two roads were highlighted with colours (orange and green) to illustrate the better coherence of the second overlay.

The advantage of the mutual information over the correlation is that it does not require any assumption about the relation between the two sets of data [26, 71]. More precisely, mutual information is more reliable than correlation when the images come from two sensors with a priori distinct characteristics [132].

Cariou and Chehdi have tested and validated their algorithm over different data from the Compact Airborne Spectrographic Imager (CASI) and the Airborne Imaging Spectroradiometer for Applications (AISA). Their experiments include different scenarios: constant height area, area with a DEM, presence or not of yaw data. A sample visual result can be seen on Figure 3.6b. The main output of their work is that, even in the absence of initial estimation of the yaw angles, the quality of the georeferencing in terms of Root Mean Square Error (RMSE) on sets of GCPs, in all their experiments, is comparable to the one obtained with direct georeferencing. Although Cariou and Chehdi's work is - to our knowledge - the best example of a pushbroom geocorrection method, it does not contain the necessary tools to deal with highly irregular trajectories, nor to estimate other orientation parameters (IOP included).

4 Acquisition System for the Léman-Baïkal Project

Before we enter in the technical details of the calibration methods proposed, we present in this chapter the system used for the Léman-Baïkal campaigns. The system, called "Hyperbox", was designed and assembled in the context of another PhD thesis by Dragos Constantin. All the details can be found in his thesis [30]. For the self-readability of the present thesis, we present the system briefly.

The hyperbox is composed with a navigation system, a pushbroom scanner, a frame camera and a NUC processor for interfacing the different devices. The hyperbox is mounted together with a Wi-Fi router and an Android tablet on board the ultralight plane; a user interface is available on the tablet for the user to pilot and monitor the system during the flight. Figure 4.1 shows the system and the different coordinate frames involved.

Tables 4.1, 4.2 and 4.3 summarise the characteristics of the different sensors.

Name	Ekinox2-N
Manufacturer	SBG Systems
Type	Integrated GPS+IMU system
Position Accuracy	2 cm with RTK
Roll and Pitch Accuracy	0.02°
Yaw Accuracy	0.05°
Maximum Frequency	200 Hz

Table 4.1 Characteristics of the navigation system on board the ultralight plane.

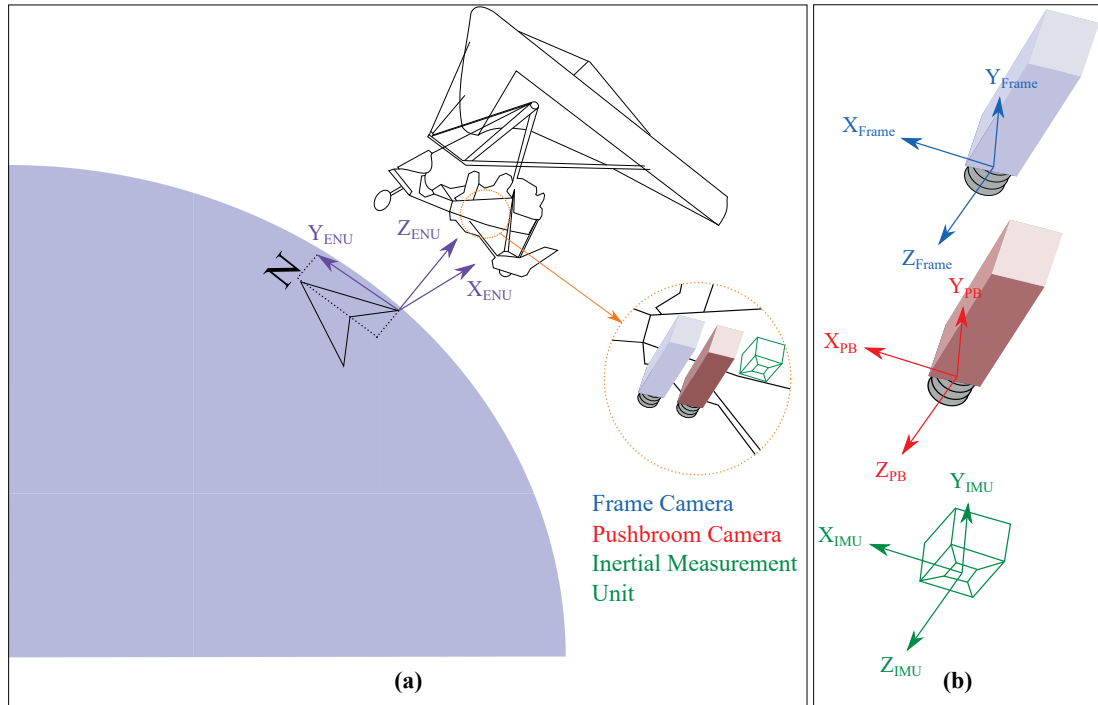


Figure 4.1 (a) illustrates the setting for our airborne acquisitions. (b) represents the different frame coordinates for the three sensors: the frame camera, the pushbroom (PB) camera, and the IMU.

Name	Micro Hyperspec VNIR-A
Manufacturer	Headwall Photonics
Type	Pushbroom hyperspectral scanner
Sensor Technology	Silicon CCD
FWHM Slit Image	5.8 nm
Spectral Bands	250
Spectral Coverage	400 to 900 nm
Number of Pixels	1000
Maximum Frequency	90 Hz

Table 4.2 Characteristics of the pushbroom scanner on board the ultralight plane.

Name	Micro UI-2280SE-C-HQ
Manufacturer	IDS Imaging
Type	Frame camera
Sensor Technology	CCD
Spectral Bands	3
Spectral Coverage	RGB
Number of Pixels	2448 × 2048
Maximum Frequency	6.5 Hz

Table 4.3 Characteristics of the frame camera on board the ultralight plane.

Hyperspectral Data Radiometric and Geometric Processing

Part II

5 Radiometric Correction

Note: parts of this section were extracted from our article Airborne hyperspectral sensor radiometric self-calibration using near-infrared properties of deep water and vegetation [7], in the proceedings of the SPIE Remote Sensing Conference. They are copied in accordance with the SPIE Transfer of Copyright agreement.

This part describes the methods and algorithms we have developed to perform radiometric and spectral correction of the pushbroom images acquired with our Headwall Micro Hyperspec VNIR-A camera. It is important to understand that the calibration methods detailed in the following were designed to be entirely image-based. The reason is that images of interest had been collected prior to the beginning of our work at the Geodetic Engineering Laboratory of EPFL, and no camera calibration had been performed prior to these acquisitions.

5.1 Radiometric Calibration Algorithm

Our algorithm is split into six steps: dark current noise removal, spectral calibration, stripes effect correction, BRDF effect correction, residual glint removal and rescaling of reflectance. Figure 5.1 summarises this process.

5.1.1 Dark Current Noise removal

Dark current can be represented by a constant bias. There is one bias per pixel and per band, and its value is a digital number. To compute it, we acquire a large number of lines in the dark. Then we consider the time series from a single pixel and a single band. The values of its autocorrelation at non-zero lags should practically only be influenced by the bias as shown on Figure 5.2.

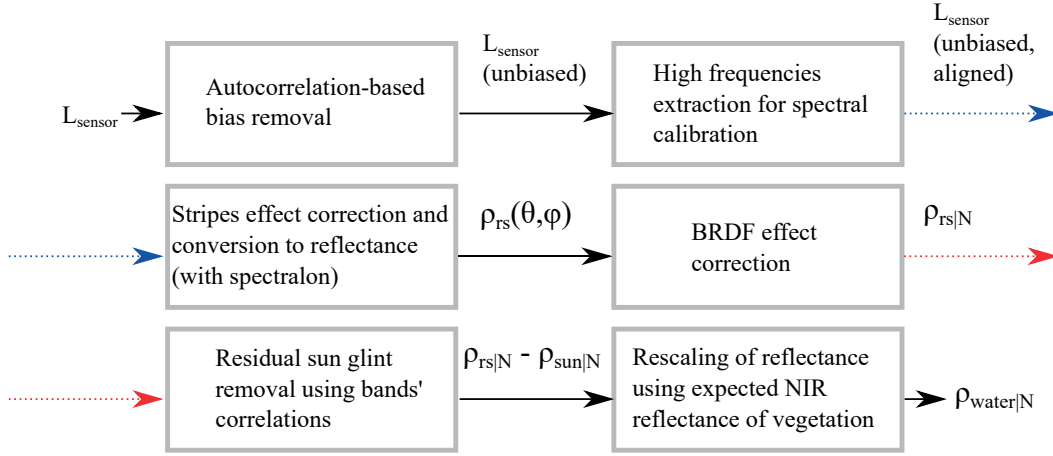


Figure 5.1 Flowgram of our approach.

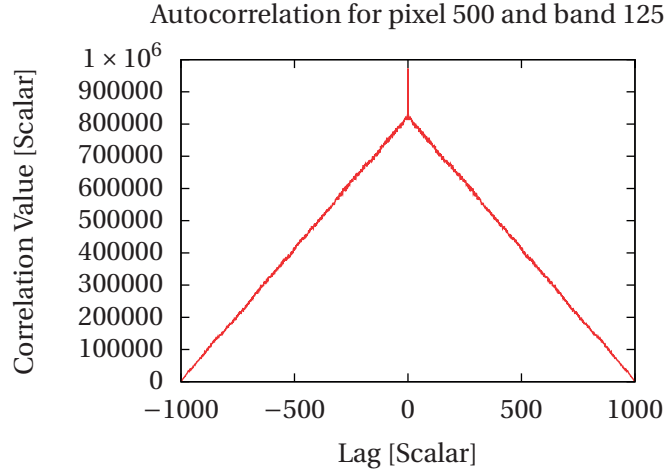


Figure 5.2 Autocorrelation plot for the 125th band in the 500th pixel of our camera.

It thus leads us to retrieve all the biases using Equation 5.1:

$$bias(i, b) = \sqrt{\frac{autocorr(dark(i, b))}{n - 1}} \quad (5.1)$$

where "i" is the index of the pixel in the pushbroom line, "b" is the index of the band, "dark" is the concatenation of the 1000 dark lines acquired, and n is the length of the time series ($n = 1000$ here). In each band and each pixel, we subtract the bias from L_{sensor} . It should be noted that this process is not error-free, since the dark current signal depends on the integration time of the camera, and its temperature. The variations of the temperature during the airborne acquisition might alter slightly the values of the biases.

5.1.2 Spectral shifts removal

High Frequencies Extraction

To compensate for the spectral shifts, a method has been developed, relying on the apparent dioxygen absorption peak, and the computation of the "high frequencies" of the signal. The idea is to represent the fast variations within the spectrums, and to match these variations in order to realign all the signals.

The first step consists in processing these high frequencies as follows: smooth the spectrum, and divide the original spectrum by the smoothed version. The resulting signal (referred to as "high frequencies signal" in the following) has values much superior to 1 when the original signal has upward peaks, and values much inferior to 1 when the original signal has downward peaks.

Our smoothing method is iterative: at each iteration, an upper and a lower envelope of the signal are computed using Algorithm 1. Figure 5.3 illustrates the processing of one iteration.

Data: Original signal, as an array of size 1 by n

Result: Upper envelope of the signal

```
/* Number of iterations is typically 5. Gaussian Smoothing is
   performed with a kernel of size 3. */
currentSignal = originalSignal;
for i from 1 to # iterations do
    smoothedSignal = GaussianSmooth(currentSignal);
    currentSignal = max(smoothedSignal, originalSignal);
    /* Min for a lower envelope. */
end
output currentSignal;
```

Algorithm 1: computation of the upper envelope of a signal.

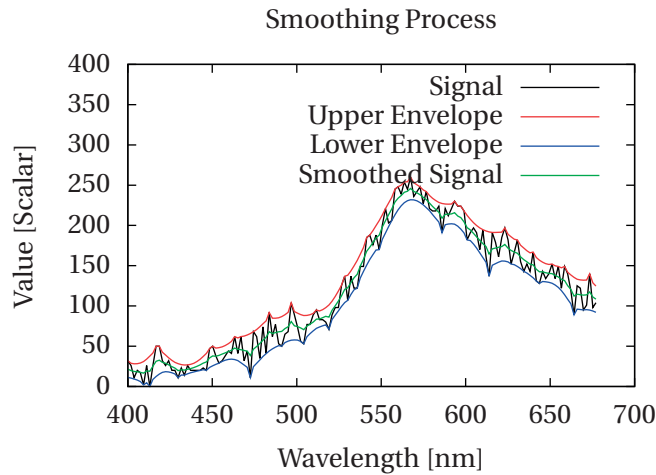


Figure 5.3 Signals obtained at the different steps of the smoothing process.

After a few iterations, we get a smooth version of the original signal. The high frequencies are then computed. Figure 5.4 shows plots of high frequencies for two random spectrums of an image.

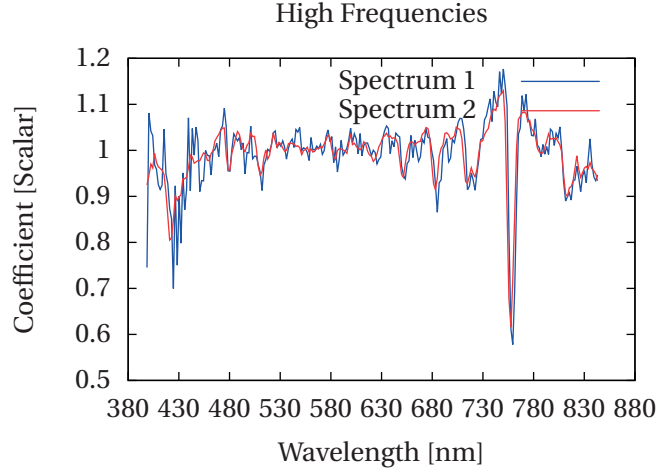


Figure 5.4 High frequencies of two different pixels. The signals are similar and relevant to establish a band to band match from one signal to another.

It is clear that the two plots shown on Figure 5.4 are alike, but misaligned.

Matching with Dynamic Time Warping

When these high frequencies have been extracted, peaks can be matched using Dynamic Time Warping (DTW), a process designed to match values of two similar signals one to one. We determine the best elastic transformation (including shifts, or stretchings) with respect to the timelines of both signals (see [118] for reference).

DTW tries to make two signal match: its output is a function (usually called path) p . The criterion to choose p is the minimisation of

$$\sum_{i=1}^N [s_1(i) - s_2(p(i))]^2 \quad (5.2)$$

where s_1 and s_2 are the two signals to match, and i is the time index of the signal (in our case, i is the band index). In other words, DTW finds the best path p which minimises the distance between signal 1 and the elastic transformation of signal 2. We call $i \mapsto s_2(p(i))$ the warped version of signal 2.

DTW is applied on the high frequencies signals, and its output path p is then used to warp the original signal 2. We can recreate the signal that we would have got without any mechanical move inside the system or spectral smile. Figure 5.5 shows locally the obtained (warped)

spectrum 2 from Figure 5.4 and compares it to the uncalibrated version.

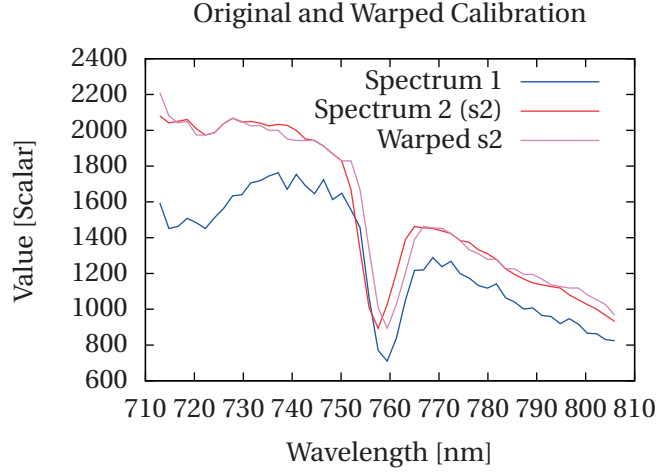


Figure 5.5 Spectrum 1, spectrum 2 and its warped version, around the wavelength corresponding to dioxygen absorption. The warped signal peak is aligned with the corresponding one in spectrum 1.

It has to be noted that, though all the signals can be aligned using this process, this is a relative correction: no absolute positioning of the absorption peak is performed. Therefore, we arbitrarily align all the spectrums so that the peak is centred at 760 nm.

Finally, when all the spectrums are aligned, they are smoothed in the spectral dimension to further reduce potential noise, using the smoothing process described in 5.1.2.

5.1.3 Stripes Effect Correction and Conversion to reflectance

Before each flight, an acquisition over a Spectralon (Lambertian, unit-reflectance panel) is made. After aligning the bands using the method described in Section 5.1.2, it is now safe to divide the signals of each of the scan lines by the signals collected over the Spectralon, so as to remove the stripes effect, but also perform a first conversion to reflectance. Figure 5.6 shows an example of such spatial noise correction and reflectance output over the mouth of the Rhône river in Lake Geneva.

The output is a first approximation of the reflectance $\rho_{rs}(\theta, \phi)$, still depending on the viewing direction (θ, ϕ) . However, such output cannot be considered yet as the final output. Not only some effects (glints, BRDF effect) have not been corrected yet, but the data of interest and the Spectralon data were collected at different times, meaning, with a different sun elevation angle. The radiance received from the Spectralon cannot be considered to be a proper measure of the downwelling irradiance E_d at the moment of the airborne acquisition. The rescaling of the reflectance obtained at this stage is discussed in Section 5.1.6.

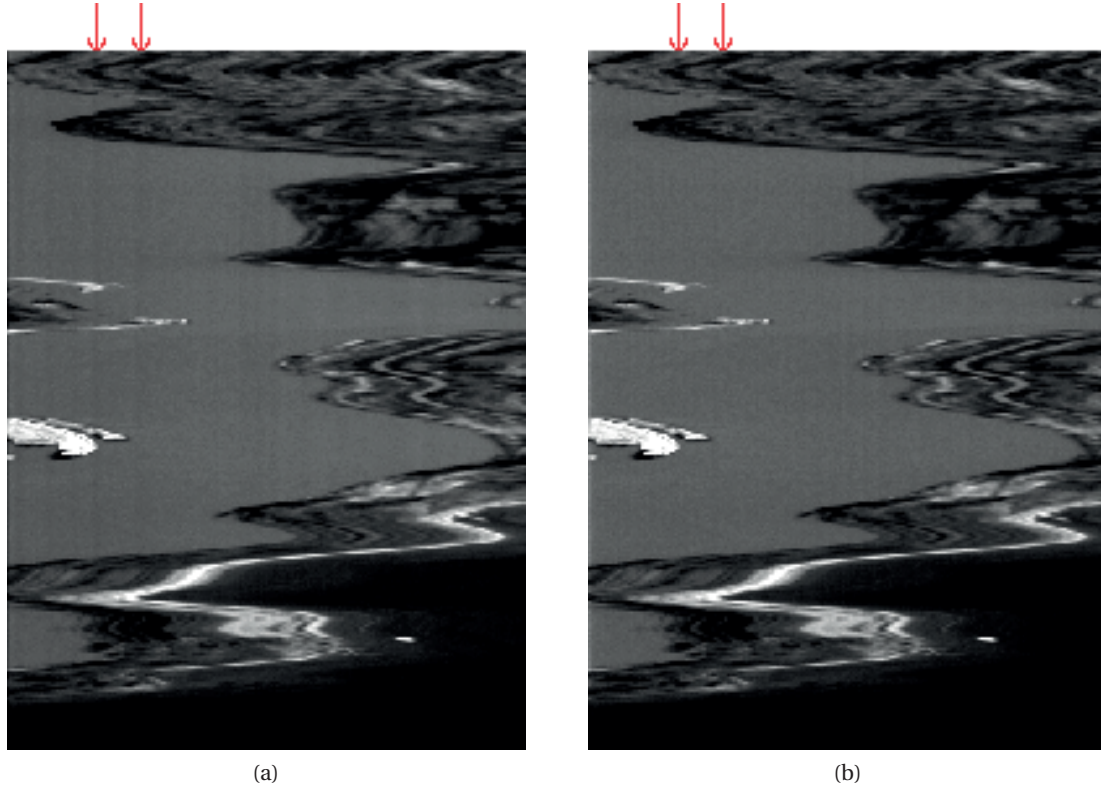


Figure 5.6 Illustration of the spatial noise correction in the band 125 (632.5 nm), over the Rhône. Two columns where the stripes effect is particularly visible are indicated by red arrows.

5.1.4 BRDF Correction

At this stage, the reflectance is still impacted by various external factors: the sun elevation angle (which acts as a scaling factor on the downwelling irradiance), the atmospheric scattering, and the BRDF effect. The elevation of the sun is accounted for in the rescaling of the reflectance (see Section 5.1.6). The data presented in this chapter were acquired at low to medium altitudes, between 500 m and 800 m, where the scattering effects can be neglected. However, the last factor, the BRDF effect, is significant and needs to be corrected.

Background: BRDF Correction Kernels

The remote sensing reflectance ρ_{rs} is a function of the viewing direction (θ, ϕ) . Let us call $\rho_{rs|N}$ the remote sensing reflectance, corrected for the BRDF effect, that is, where the data was normalised so as to appear as taken from nadir point of view. This normalisation can be modelled as a function of the Earth-Sun distance, the upwelling radiance, the upwelling irradiance and the downwelling irradiance just below the surface of the water observed, and estimated by numerical methods, when ground measurements are available [98, 96]. Such measurements are available in a very limited number of points in the context of the Léman-

Baïkal project, which is why extra assumptions must be made so as to model the BRDF effect and correct it based on airborne images only. The BRDF effect is usually modelled with so-called kernels: the observed reflectance $\rho_{rs}(\theta, \phi)$ is expressed as the sum of the normalised reflectance, $\rho_{rs|N}$, and a linear combination of functions of the viewing direction of known expressions, called kernels. The expressions of the kernels are either derived from physical models [133] or expressed as a Taylor expansion of the different parameters, with no further assumption [29].

BRDF Correction with a Quadratic Kernel

Our strategy, much like Collings et al. [29], considers all the reflectances obtained in the previous section as observations. Provided that the viewing direction presents enough variations across the observations, they could allow to estimate the coefficients of a Taylor expansion function representing the BRDF effect. Consider the angles θ and ϕ as represented on Figure 5.7.

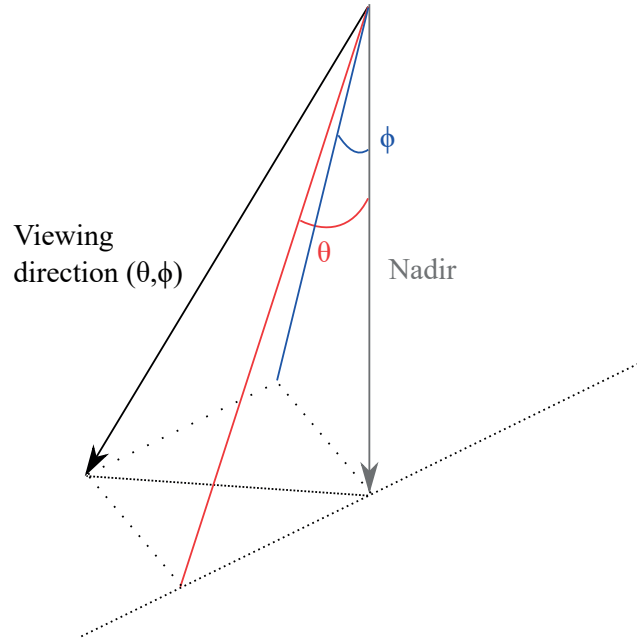


Figure 5.7 Representation of the angles θ and ϕ for a 2D viewing direction.

Then the relation between the remote sensing reflectance and the viewing direction is given by Equation 5.3.

$$\rho_{rs}(\theta, \phi) = \alpha_0 + \alpha_1\theta + \alpha_2\phi + \alpha_3\theta^2 + \alpha_4\theta\phi + \alpha_5\phi^2 \quad (5.3)$$

In order to compute the best parameters α_i , $i \in [0, 5]$, a large area of water, acquired in a turn of

the ultralight plane, is used to provide numerous observations of $\rho_{rs}(\theta, \phi)$ for different angles. The turning motion of the aircraft allows to span a variety of viewing directions, so that the estimation of the parameters is accurate. The area of water covered shall be uniform enough so that the main variations observed are a consequence of the different viewing directions. Both flights of interest include acquisitions over homogeneous water areas in turns, that can be used to estimate the parameters of the model.

Before processing the optimal parameters, the viewing direction of each observation must be computed. It should be noted at this point that we made the deliberate choice to perform radiometric calibration before sensor orientation. Although the correction of the orientation of the pushbroom camera would have allowed to compute better estimates of the viewing angles, the difference with using the estimates directly from the navigation sensors is negligible. On the other hand, radiometric calibration is needed to compare and correlate data from the hyperspectral sensor and the RGB sensor in our orientation method (Section 6.1.1).

Consequently, ignoring inherent camera calibration parameters, the rotation between the local-level frame and the body frame of the pushbroom camera, R_b^l is given by Equation 3.1, and the viewing direction of a pixel of metric, signed coordinate v in the scan line is given by Equation 5.4.

$$v = R_b^l \begin{bmatrix} 0 \\ v \\ f \end{bmatrix} \quad (5.4)$$

In Equation 5.4, f stands for the focal length of the pushbroom camera. Considering $v = (v_x, v_y, v_z)$, the angles θ and ϕ are given by Equations 5.5 and 5.6.

$$\theta = \arctan\left(\frac{v_x}{v_z}\right) \quad (5.5)$$

$$\phi = \arctan\left(\frac{v_y}{v_z}\right) \quad (5.6)$$

Using the observations from a homogeneous water image covered during a turn, the parameters $\alpha_i, i \in [0, 5]$ are retrieved from a least squares adjustment. The subsequent correction is processed as follows: each reflectance, if acquired from a viewing direction of (θ, ϕ) , is multiplied by a factor of

$$\frac{\alpha_0}{\alpha_0 + \alpha_1\theta + \alpha_2\phi + \alpha_3\theta^2 + \alpha_4\theta\phi + \alpha_5\phi^2}.$$

5.1.5 Residual glint removal

In some images, direct reflection from the sun still appear and needs to be corrected. To do so, we use Lyzenga & al.'s method [90]. The process is as follows: we compute the correlations of the different bands with a chosen Near InfraRed (NIR) band in a deep water area that we choose arbitrarily. Assuming negligible water-leaving radiance in the near infrared (in our case, for the largest wavelength, 850 nm), we correct the spectrums using Equation 5.7.

$$\rho_{b,corrected} = \rho_b - r_{b,NIR}(\rho_{NIR} - \langle \rho_{NIR} \rangle). \quad (5.7)$$

In Equation 5.7, ρ_b stands for the reflectance in band b, $r_{b,NIR}$ for the correlation in the deep water region between band b and the NIR band, and $\langle \rho_{NIR} \rangle$ for the mean reflectance value in the NIR band in the same region. The logic behind this equation is that the NIR reflectance of water should be negligible. We can then apply appropriate corrections in the other bands by scaling the NIR correction according to the correlation between the NIR and the bands to correct.

5.1.6 Rescaling of Reflectance using Expected NIR Reflectance of Vegetation

A first approximation for downwelling irradiance E_d would be given by the data collected over the Spectralon, but this suffers two issues: first, acquiring data over the Spectralon obviously cannot be done during the flight. Therefore, the changes of weather conditions, especially the solar azimuth, are such that a single acquisition of the Spectralon before the flight cannot reliably help to scale the signal to reflectance. Second, the reflectance of the Spectralon may not be exactly 100% in the visible and the near infrared. To be able to scale our data to reflectance without adopting a supervised approach (i.e., to be independent of the ground data), we rely on the acquisition of vegetation data during the flight. For coastal areas like lake shores, this is a reasonable assumption. The idea is to use the spectral properties of vegetation in the near infrared. Typically, the reflectance spectrum of a plant is very stable between 800 nm and 850 nm, and its value - depending on its health and its species - can vary from 20 % to 90 %. We use this information by choosing (arbitrarily) a large vegetation area on the shore, acquired close (timewise) to the point of interest. We compute the maximum and the minimum spectrums in this area; we assume that the mean between the highest value and the lowest value in the near infrared band (850 nm in our case) corresponds to a 50 % reflectance. Using the Spectralon, we compute the ratios between the transmittance of each band and the NIR transmittance. These transmittance ratios are then scaled knowing the value found in the NIR should be scaled to 50 %. The result is a signal representing the theoretical output of the sensor for 100 % reflectance, that we can use to scale our spectrums to reflectance.

Figure 5.8a shows, for the studied region near the Rhône, the vegetation area chosen, and Figure 5.8b represents the plots (in digital numbers) of the minimum and maximum reflectances

found in this area.

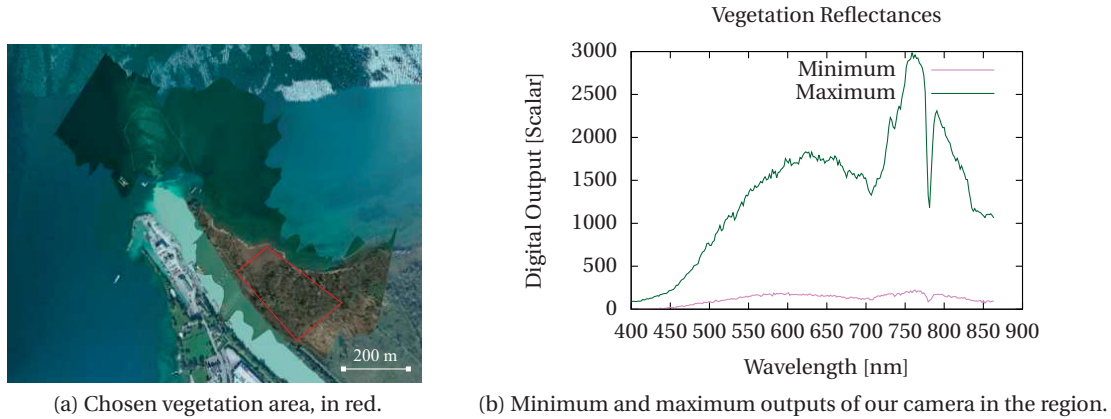


Figure 5.8 Vegetation area and maximum and minimum outputs in this region.

For instance here, all the signals would be scaled so that 578 (the mean of the NIR digital number of minimum and maximum reflectances of Figure 5.8b) would correspond to 50 % reflectance. Depending on the heterogeneity, the species and the health of the vegetation in the chosen area, this scaling may be inaccurate. In this case, the proper scaling factor can be learnt on one of the ground samples, and used for the others. The method then becomes supervised, in the sense that it needs information from the in situ measurements.

5.2 Results

5.2.1 Sample data

The acquisition campaigns took place from March 2013 to August 2015. In order to cover large areas, flights were often performed at an altitude of 1 km or higher. Nevertheless, several points on both lakes, Geneva and Baikal, have been acquired at medium altitudes (less than 800 m). They are summarised in Table 5.1 and shown on Figure 5.9. All the points were acquired in good weather conditions, with negligible wind.

Designation	Date	Time (CEST)	Latitude (°)	Longitude (°)	Altitude (m)	Spectrometer
Av4	09.04.2015	10:50	46.45157	6.81665	410	WISP-3
Av7	21.04.2015	10:35	46.40443	6.86055	570	Ramses
Av8	21.04.2015	10:30	46.39745	6.85414	570	Ramses
Av9	21.04.2015	10:32	46.40860	6.84326	570	Ramses
Ba50	11.08.2014	05:14	52.31581	106.23075	280	WISP-3
Ba51	11.08.2014	05:10	52.31462	106.24342	760	WISP-3
Ba52	11.08.2014	05:10	52.31015	106.24089	710	WISP-3
Ba53	11.08.2014	05:11	52.30845	106.25411	530	WISP-3

Table 5.1 list of the points used to assess our results.

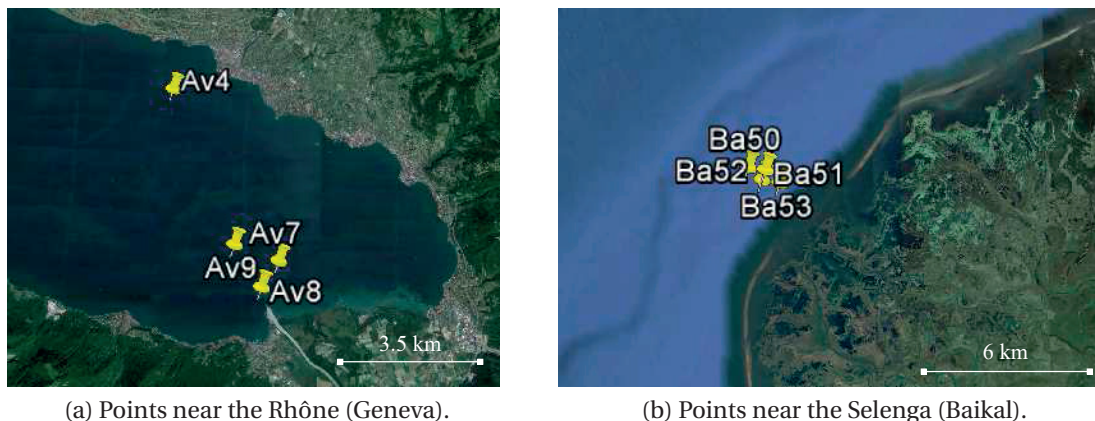


Figure 5.9 Sample points visualised in Google Earth.

Our georeferencing method [6] is an integrated sensor orientation approach using tie points in concurrent frame images to correct the hyperspectral lines orthorectification. This method relies on salient points in the images and cannot be applied directly to water areas, which are too homogeneous. But the correction of orientation on the ground before and after acquisition over water allows, by interpolation and use of the navigation data, to get decent georeferencing of the water elements captured by the airborne hyperspectral sensor. Figure 5.10 shows the orthorectification of lines above the mouth of the Rhône river, as seen in our software HypOS, based on NASA SDK Worldwind.



Figure 5.10 Projection of 1000 hyperspectral lines in our software HypOS. The background imagery is from Bing Maps. The orange line is the flight line.

5.2.2 Comparison between Calibrated Airborne spectrums and Ground Measurements

To assess the quality of our results, we compare the output spectrums to their equivalent ground measurements from a TriOS Ramses and a water-insight WISP-3. They measure the upwelling radiance L_u , the sky radiance L_s and the downwelling irradiance E_d . In absence of wind, we can then compute the spectral remote sensing reflectance using Equation 5.8.

$$R_{rs} = \frac{L_u - 0.028L_s}{E_d} \text{ (in } sr^{-1}\text{)}. \quad (5.8)$$

The similarity of ground and airborne data is assessed using three indicators: the correlation (Equation 5.9), the Spectral Angle Mapper (SAM, Equation 5.10) and the Root Mean Square Error (RMSE, Equation 5.11). In all these equations, λ stands for the band index, N is the total number of bands (250 in our case), and x and y are the airborne and ground spectrums, respectively.

$$\rho_{X,Y} = \frac{\sum_{\lambda=1}^N (x_{\lambda} - \bar{x})(y_{\lambda} - \bar{y})}{\sqrt{\sum_{\lambda=1}^N (x_{\lambda} - \bar{x})^2 \sum_{\lambda=1}^N (y_{\lambda} - \bar{y})^2}}. \quad (5.9)$$

$$SAM_{X,Y} = \cos^{-1} \left(\frac{\sum_{\lambda=1}^N x_{\lambda} y_{\lambda}}{\sqrt{\sum_{\lambda=1}^N x_{\lambda}^2 \sum_{\lambda=1}^N y_{\lambda}^2}} \right). \quad (5.10)$$

$$RMSE_{X,Y} = \sqrt{\frac{1}{N} \sum_{\lambda=1}^N (x_{\lambda} - y_{\lambda})^2}. \quad (5.11)$$

Results are summarised in Table 5.2. Figure 5.11 shows plots of airborne and in situ measurements near the mouth of the Rhône in Lake Geneva, and Figure 5.12 shows plots for points in the Selenga Delta of Lake Baikal.

The main source of error is due to the sensitivity of our sensor at short wavelengths. As can be seen on Figure 2.7, our camera has a very low quantum efficiency for wavelengths below 450

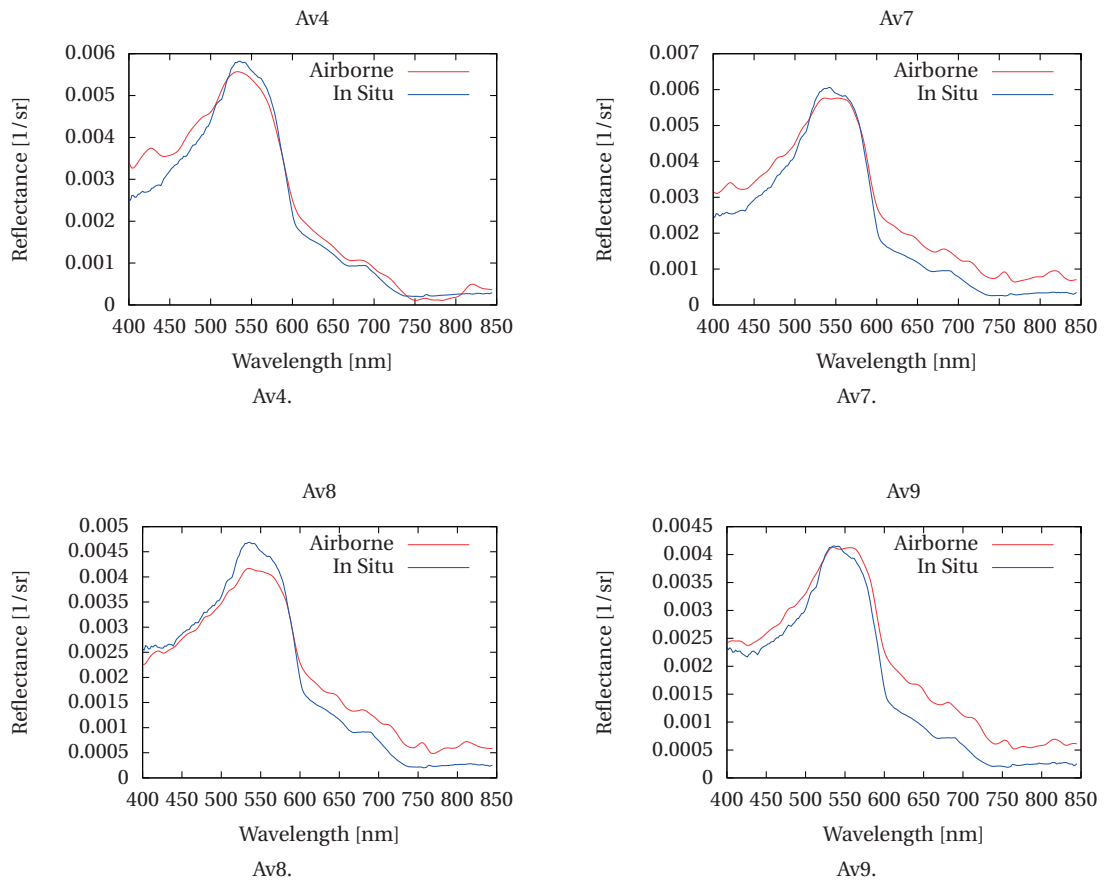


Figure 5.11 Plots of Airborne versus in situ data for the points near the Rhône.

Point	Correlation	SAM (°)	RMSE
Av4	0.988	5.97	3.35×10^{-4}
Av7	0.995	8.50	5.05×10^{-4}
Av8	0.996	8.09	3.50×10^{-4}
Av9	0.992	9.03	4.22×10^{-4}
Ba50	0.979	7.54	1.86×10^{-4}
Ba51	0.969	10.94	3.71×10^{-4}
Ba52	0.968	8.04	3.33×10^{-4}
Ba53	0.937	11.38	3.97×10^{-4}

Table 5.2 Quantitative results of comparison between airborne spectrums and ground spectra.

nm. The signal-to-noise ratio in this area of the spectrum is therefore lower than in the rest of the spectrum, which leads to discrepancies. The second main issue is the altitude. It is clear that, for the point measured at the highest altitude (Ba51, see Figure 5.12b), the similarity of

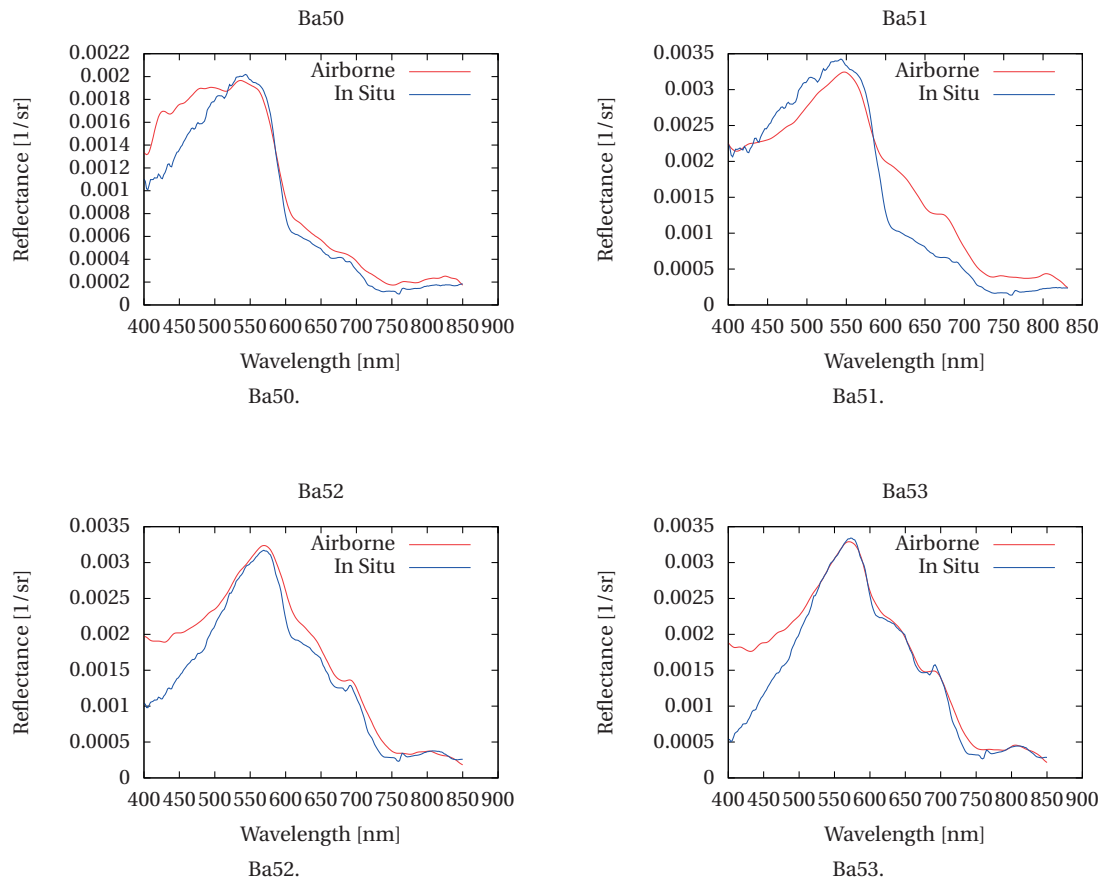


Figure 5.12 Plots of Airborne versus in situ data for the points near Selenga Delta (Lake Baikal).

the two spectrums is lower. This is most probably due to additional atmospheric scattering at this altitude. Though the scattering should remain weak, it is stronger than for other points and diminishes the performance of our algorithm. Apart from these two issues, the rest of the error sources (remaining noise, glint) are dealt with efficiently and the spectrums from airborne data and in situ data correspond very well. However, overall, reflectance spectrums are very similar to the ones concurrently acquired using ground spectrometers like the WISP-3 and the TriOS Ramses, for points acquired at low altitudes. The reflectance data can be used to retrieve information about water quality.

6 Pushbroom Images Georeferencing

Note: parts of this section were extracted from our articles Correction of Airborne Pushbroom Images Using Bundle Adjustment of Frame Images [6], in the International Archives of the Photogrammetry, Remote Sensing & Spatial Information Sciences, and Pushbroom Hyperspectral Data Orientation by Combining Feature-Based and Area-Based Co-Registration Techniques [4], in Preprints, and accepted for publication in Remote Sensing. They are copied under the Creative Commons Attribution 3.0 License.

In this chapter, we explain the methods we developed to georeference pushbroom scan lines. We wish to:

- compute a georeferenced orthomosaic composed with the scan lines collected by the hyperspectral pushbroom sensor.
- retrieve the corrected orientation parameters. They include Interior Orientation Parameters (IOP: principal distance, principal point of the pushbroom camera, and potentially the distortion parameters of the lens) and Exterior Orientation Parameters (EOP: roll, pitch, yaw, and 3 position parameters) for all the scan lines.
- estimate the boresight between the IMU and the pushbroom sensor.

The system used for the acquisition consisted in an SBG Ekinox2-N Integrated GPS+IMU system, a Headwall Micro Hyperspec VNIR-A hyperspectral camera, an IDS-Imaging USB 2 uEye SE UI-2280 SE RGB camera, and an Intel NUC to handle the communication between devices. The latitude, longitude and altitude, relatively to the WGS84 Geoid, and attitude as roll, pitch and yaw output by the GPS+IMU system are considered as initial estimates, which our geocorrection algorithm should refine. Additionally, we want the algorithm to not depend on the measure of GCPs: measuring GCPs is a time consuming task, and using the information they provide for pushbroom scan lines would imply to make assumptions on the trajectory of the aircraft to reduce the complexity of the problem.

6.1 Proposed Methodology

The geocorrection method proposed consists in five steps. First, we process a bundle adjustment of the frame images to retrieve corrected EOP for the frame camera and the navigation sensors; the adjustment allows the creation, in parallel, of a DEM of the area. Second, using these EOP for the pushbroom camera, a first mosaic is created by projecting the scan lines on the DEM. Third, points are matched between the orthophoto from the frame images and the pushbroom mosaic; these matches allow to estimate the systematic error in the pushbroom georeferencing, in the form of the boresight between the IMU and the pushbroom scanner, and the IOP of the scanner. The projection of the scan lines is updated using the estimated boresight parameters. Fourth, the residual errors are compensated for by computing the local normalised cross correlations between the reference orthophoto and the mosaic. The mosaic is elastically deformed into a new mosaic which fits the orthophoto better. Fifth, these deformations allow to estimate better EOP for each scan line and compute a final mosaic that is well co-registered onto the reference orthophoto. The flowchart of this method is given in Figure 6.1.

6.1.1 Pre-processing Step: Radiometric Matching

Knowing the later steps of our algorithm (Sections 6.1.4 and 6.1.5) rely on matching features or areas of the RGB images to the pushbroom hyperspectral images, the radiometric properties of both sources need to match accordingly. The hyperspectral camera is calibrated (spectrally and radiometrically) using a Spectralon panel, which is Lambertian and has a nearly unit-reflectance across the spectral range of our camera (400-850 nm). The band-wise quantum efficiency for each band of the RGB camera is provided by the manufacturer; to produce comparable RGB data from our hyperspectral camera, we integrate the quantum efficiency of one band of the frame camera, times the spectral signal delivered by the hyperspectral camera. Concretely, let λ be the wavelength variable, and $QE_b(\lambda)$ the quantum efficiency of the frame camera in the band b (red, green or blue). Let λ_n be the central wavelength of the n^{th} band of the hyperspectral camera. Then, h_b , the data in band b synthesised from the hyperspectral image h , is given by Equation 6.1.

$$h_b = \frac{\sum_n QE(\lambda_n) h(\lambda_n)}{\sum_n QE(\lambda_n)} \quad (6.1)$$

A 3-bands image is then created by applying Equation 6.1 to the three bands of the frame camera. Images of both cameras are then converted to greyscale for the following steps of the algorithm.

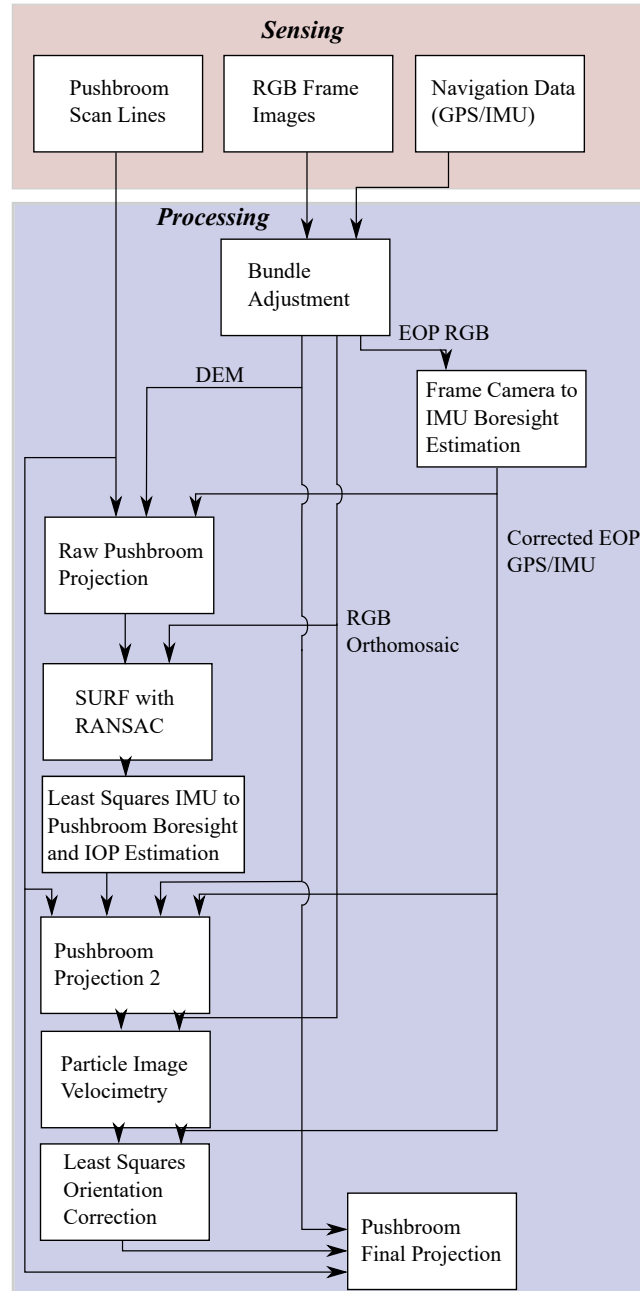


Figure 6.1 Flowchart of the proposed geocorrection method.

6.1.2 Bundle Adjustment of Frame Images

In the first stage of the geocorrection, the information available in frame imagery is used to refine the estimates of the EOP given by the navigation sensors. Using the commercial software Agisoft Photoscan, we perform a bundle adjustment of frame images (Figure 6.2). Each image is associated with a set of EOP, initialised with the values output by the GPS+IMU system. Photoscan handles the stitching of the RGB images by finding tie points; EOP are optimised in

the process and can be exported from the software. However, these parameters correspond to the frame camera. To retrieve corrected parameters for the IMU, two additional steps must be completed: the interpolation of the corrected parameters, since the acquisition frequency of the frame camera is much lower than the one of the navigation system; the computation of the boresight between the frame camera and the IMU. Our solutions to both of these problems are described in [6].

The orientation parameters output by the previous step are for the frame camera. The correct parameters for navigation sensors are not the same, since there is a lever-arm as well as a boresight between them and the camera. Since our hyperspectral camera has a frequency 50 times higher than the one of our RGB camera, only one pushbroom line out of 50 can be directly corrected; we need to use the data acquired by navigation sensors to interpolate between the corrections.

Position Correction

The position of the IMU will not be computed. Indeed, in our system, the norm of the lever-arm between the pushbroom camera and the frame camera is less than 10 cm. Therefore, we use the position parameters retrieved from the bundle adjustment step for the pushbroom camera. As a consequence, navigation sensors data can be used as such to interpolate between the corrections of the camera position.

Consider a position parameter q among latitude, longitude and altitude. Let q_r and q_c be respectively the raw value of this parameter (output of the Kalman Filter) and the corrected value. Let t_0 be the timestamp of a line corrected thanks to the bundle adjustment. So is the line which timestamp is $t_0 + 50\Delta t$, where Δt is the sampling time of the hyperspectral camera. Since the IMU is a drifting sensor (accurate for short periods of time, but getting less and less accurate as time goes by), the variations it gives around t_0 are highly reliable close to t_0 , and less when getting closer to $t_0 + 50\Delta t$. Same goes for the variations around $t_0 + 50\Delta t$. We therefore interpolate q_c , for $t \in [t_0, t_0 + 50\Delta t]$, using Equation 6.2.

$$\begin{aligned} q_c(t) = & \alpha(t) \left(q_c(t_0) + (q_r(t) - q_r(t_0)) \right) \\ & + (1 - \alpha(t)) \left(q_c(t_0 + 50\Delta t) + (q_r(t) - q_r(t_0 + 50\Delta t)) \right) \end{aligned} \quad (6.2)$$

$\alpha(t)$ is the weight given to the navigation data close to t_0 . Its value is given by Equation 6.3.

$$\alpha(t) = \frac{t_0 + 50\Delta t - t}{50\Delta t} \quad (6.3)$$

Attitude Correction

The attitude of the navigation sensors has to be computed. Indeed, to interpolate the attitude data, it is not possible to use the data from the navigation sensors as such, since it refers to its own frame, while the attitude given by the bundle adjustment refers to the RGB camera frame. At a given location, let R_{ned}^{Camera} be the rotation matrix from the North-East-Down local-level frame to the camera frame, R_{NED}^{IMU} the one from the local-level frame to the IMU and R_{IMU}^{Camera} the rotation representing the boresight from the IMU to the camera. The relation between these matrices is given by Equation 6.4.

$$R_{IMU}^{Camera} R_{ned}^{IMU} = R_{ned}^{Camera} \quad (6.4)$$

Each of these rotation operators can be characterised by its roll, its pitch and its yaw, applied in this order: roll rotation around the x-axis, pitch rotation around the y-axis, and yaw rotation around the z-axis. Let r, p, y be these 3 parameters; the corresponding rotation operator is given by Equation 6.5.

$$R(r, p, y) = \begin{bmatrix} \cos y \cos p & \cos y \sin p \sin r - \sin y \cos r & \cos y \sin p \cos r + \sin y \sin r \\ \sin y \cos p & \sin y \sin p \sin r + \cos y \cos r & \sin y \sin p \cos r - \cos y \sin r \\ -\sin p & \cos p \sin r & \cos p \cos r \end{bmatrix} \quad (6.5)$$

This boresight is constant during the flight as the sensors are rigidly attached to the vehicle. We call (r_b, p_b, y_b) its roll, pitch and yaw. Similarly, at time t , let $(r_n(t), p_n(t), y_n(t))$ be the orientation parameters output by the navigation sensors, and $(r_c(t), p_c(t), y_c(t))$ the one for the RGB camera (given by the bundle adjustment). Let k be the number of RGB images available, and $(t_i), i \in [1, k]$ the times of acquisition of each image. The drifts (errors) in the orientation parameters added to the current drifts at time t_i are called (dr_i, dp_i, dy_i) . For each time $t_i, i \in [1, k]$, we can rewrite Equation 6.4 using the orientation parameters of each

rotation matrix. The set of equations obtained is given by 6.6.

$$\begin{aligned}
 & h(dr_1, dp_1, dy_1, dr_2, \dots, dr_k, dp_k, dy_k, r_b, p_b, y_b) \\
 &= \begin{bmatrix} R(r_b, p_b, y_b)R(r_n(t_1) + dr_1, p_n(t_1) + dp_1, y_n(t_1) + dy_1) - R(r_c(t_1), p_c(t_1), y_c(t_1)) \\ R(r_b, p_b, y_b)R(r_n(t_2) + dr_1 + dr_2, p_n(t_2) + dp_1 + dp_2, y_n(t_2) + dy_1 + dy_2) - R(r_c(t_2), p_c(t_2), y_c(t_2)) \\ \vdots \\ R(r_b, p_b, y_b)R(r_n(t_k) + \sum_{j=1}^k dr_j, p_n(t_k) + \sum_{j=1}^k dp_j, y_n(t_k) + \sum_{j=1}^k dy_j) - R(r_c(t_k), p_c(t_k), y_c(t_k)) \end{bmatrix} \\
 &= 0
 \end{aligned} \tag{6.6}$$

At time t_i , (dr_i, dp_i, dy_i) are small, unlike the total drifts $(\sum_{j=1}^i dr_j, \sum_{j=1}^i dp_j, \sum_{j=1}^i dy_j)$, where all the drifting errors and the subsequent noise from gyrometers have been added. Therefore, this model allows to keep the time-dependency of the drifts while having parameters that shall be small. Boresight parameters shall also have low values, as the sensors are rigidly attached, pointing in the same direction, in our system. By retrieving the orientation parameters from the left-hand side and the right-hand side of each equation in 6.6, we get a set of $3k$ equations with $3k + 3$ unknown parameters (all the drifts plus the 3 parameters of the boresight). This can be seen as an optimisation problem: consider the vector of all the parameters to be determined, as given by Equation 6.7.

$$v = \begin{bmatrix} dr_1 \\ dp_1 \\ dy_1 \\ dr_2 \\ \vdots \\ dr_k \\ dp_k \\ dy_k \\ r_b \\ p_b \\ y_b \end{bmatrix} \tag{6.7}$$

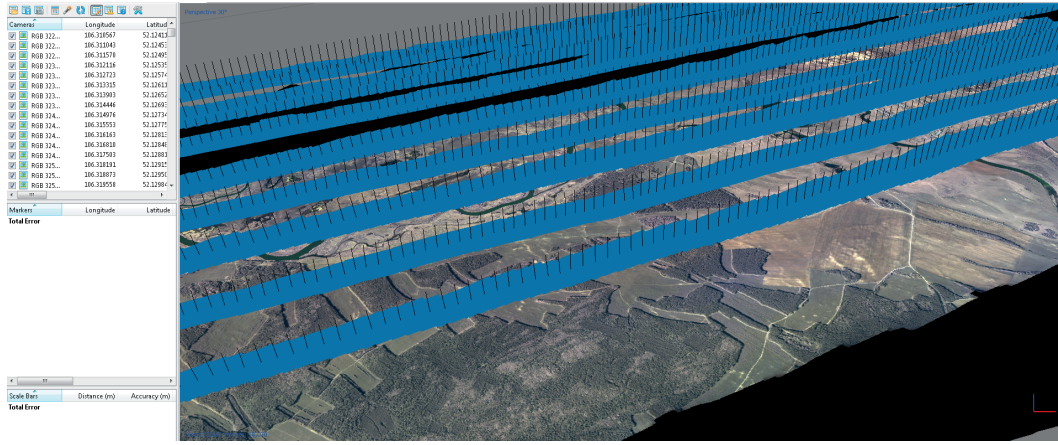
Our goal is to minimise $v^T v$ under the constraints given by the set of equations 6.6. With all parameters equal to 0, the equations are not verified, and for each equation there is a gap between the left-hand side and the right-hand side. If we call $w = h(0, \dots, 0)$ and B the Jacobian matrix of h relatively to all the parameters, then it is known, using Lagrange multipliers theory,

that v can be approximated by Equation 6.8.

$$v = B^T(BB^T)^{-1}w \quad (6.8)$$

As a result, we get all corrected parameters for the navigation sensors for the times of RGB acquisitions, as well as a side-product (the boresight). The rest of the corrected navigation sensors data is interpolated using the exact same interpolation method as described in 6.1.2.

Alongside the optimisation, the bundle adjustment allows to build and export an orthophoto and a DEM (Figure 6.2).



(a)



(b)

Figure 6.2 Processing of the frame images using Agisoft Photoscan: **(a)** alignment of frames and computation of the orthophoto; **(b)** computation of the DEM of the area (Selenga Delta Village).

6.1.3 Initial Ortho-Projection of the Scan Lines

With the set of optimised orientation parameters for the navigation system derived in Section 6.1.2, we create an orthomosaic composed with the scan lines collected by the pushbroom sensor. From the bundle adjustment, we already have a georeferenced orthophoto and the corresponding DEM; the orthomosaic is obtained by projecting the scan lines on the DEM using the collinearity equation. Let us call R_{ned}^{enu} the rotation matrix from the North-East-Down (NED) local-level frame (l-frame) to the East-North-Up (ENU) l-frame, both centred at the optical centre of the pushbroom camera. Let R_{IMU}^{ned} be the rotation matrix from the IMU frame to the NED l-frame, and R_{pb}^{IMU} the rotation matrix corresponding to the boresight from the pushbroom camera to the IMU. At this stage, R_{IMU}^{ned} is given by the estimates of the roll, pitch and yaw obtained in Section 6.1.2, and noted \hat{R}_{IMU}^{ned} . Initially, the boresight is unknown and supposed to be negligible, hence \hat{R}_{pb}^{IMU} is the identity matrix. The total rotation from the pushbroom camera to the ENU l-frame is given by Equation 6.9.

$$\hat{R}_{pb}^{enu} = R_{ned}^{enu} \times \hat{R}_{IMU}^{ned} \times \hat{R}_{pb}^{IMU} \quad (6.9)$$

We can georeference the pushbroom data according to the collinearity equation (Equation 6.10).

$$\mu R_{pb}^{enu} \begin{bmatrix} 0 - u_{pp} + \delta u \\ v - v_{pp} + \delta v \\ f \end{bmatrix} = \begin{bmatrix} X_G \\ Y_G \\ Z_G \end{bmatrix} - \begin{bmatrix} X_{oC} \\ Y_{oC} \\ Z_{oC} \end{bmatrix} \quad (6.10)$$

In Equation 6.10, μ corresponds to the collinearity coefficient, v is the metric coordinate of the pixel of interest in the body frame of the pushbroom camera. (u_{pp}, v_{pp}) are the coordinates of the principal point of the camera in the same frame, f is the focal length of the camera, (X_G, Y_G, Z_G) are the coordinates of the corresponding ground point in the ENU l-frame and (X_{oC}, Y_{oC}, Z_{oC}) are the coordinates of the optical centre in the same frame. Considering the radial distortion parameters K_1, K_2, K_3, \dots , the decentring coefficients P_1 and P_2 , $u' = 0 - u_{pp}$ and $v' = v - v_{pp}$, Brown's model for lens distortion [36] gives the expressions of δu and δv (Equations 6.11 and 6.12).

$$\delta u = u' (K_1 r^2 + K_2 r^4 + K_3 r^6 + \dots) + P_1 (r^2 + 2u'^2) + 2P_2 u' v' \quad (6.11)$$

$$\delta v = v'(K_1 r^2 + K_2 r^4 + K_3 r^6 + \dots) + P_2(r^2 + 2v'^2) + 2P_1 u' v' \quad (6.12)$$

Equation 6.10 gives the most generic form of the collinearity equation for our problem. However, at this stage, $R_{pb}^{enu} = \hat{R}_{pb}^{enu}$, the position of the optical centre is the one output by the bundle adjustment, the optical centre's coordinates and the distortion parameters are unknown and the focal length is known with limited precision. Therefore, $X_{oC} = \hat{X}_{oC}$, $Y_{oC} = \hat{Y}_{oC}$, $Z_{oC} = \hat{Z}_{oC}$, $\hat{u}_{pp} = \hat{v}_{pp} = 0$, the distortion parameters are all set to zero, $f = \hat{f}$ ($\hat{f} = 0.012$ m in our case) and the collinearity equation turns into Equation 6.13.

$$\mu \hat{R}_{pb}^{enu} \begin{bmatrix} 0 \\ v \\ \hat{f} \end{bmatrix} = \begin{bmatrix} X_G \\ Y_G \\ Z_G \end{bmatrix} - \begin{bmatrix} \hat{X}_{oC} \\ \hat{Y}_{oC} \\ \hat{Z}_{oC} \end{bmatrix} \quad (6.13)$$

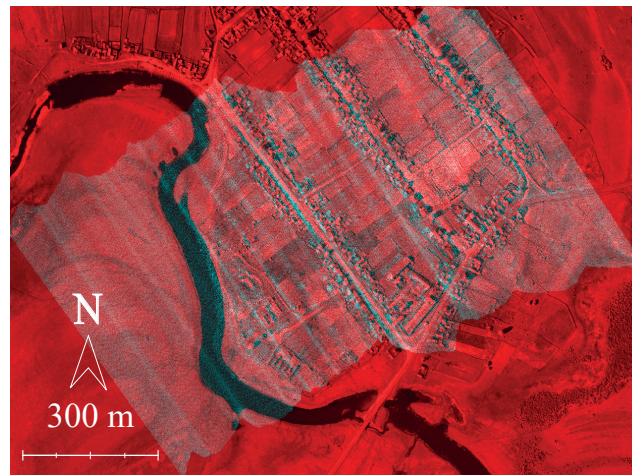
We use ray casting to find the ground coordinates (X_G, Y_G, Z_G) . The intersection of the rays with the DEM is computed using the following algorithm [16]: from the optical centre of coordinates $(\hat{X}_{oC}, \hat{Y}_{oC}, \hat{Z}_{oC})$, trace the ray driven by the vector $\hat{R}_{total} \times (0, v, \hat{f})^T$. The candidate 2D pixels are the pixels that are crossed by the ray, and where the ray is between the lowest and the highest altitude of the DEM. The projection pixel is the first pixel below which the ray passes.

This process is applied to all the pixels of all the scan lines collected, and the resulting ground pixels form an image that is superimposed on the reference mosaic. Since the resolution of our reference mosaic is much higher than the one of our pushbroom camera, the image produced is sparse, with important gaps between the projected points. Around each of these pixels, we leave a marker of size $n \times n$ (where n is the number of pixels; we choose $n = 5$ here) to compute a dilated footprint of the pushbroom projection. Inside this footprint, the isolated pixel values projected using the collinearity equation are interpolated with a 2D bilinear interpolation to produce the final projected image. An example of such image can be seen on Figure 6.3.

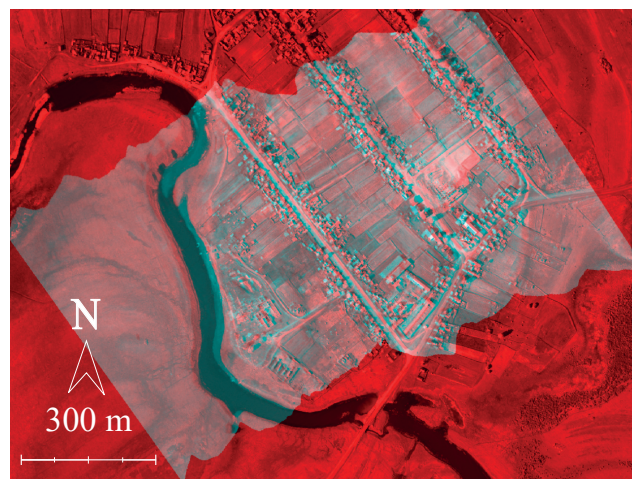
6.1.4 Systematic Error Correction

As can be seen on Figure 6.3b, the georeferencing is far from perfect, as the co-registration between the reference orthophoto and the scan lines exhibit significant discrepancies. However, the error made seems quite coherent across the image, suggesting that it mainly comes from systematic errors:

- bad intrinsic camera calibration (inaccurate focal length, principal point coordinates, or lens distortion parameters).



(a)



(b)

Figure 6.3 Orthoprojection of the scan lines (cyan) on top of the reference orthomosaic (red) above a village near the Selenga Delta of Lake Baikal. **(a)** is the orthoprojection of the pushbroom pixels (without interpolation) and **(b)** is the image as seen after bilinear interpolation of the projected values.

- non-negligible boresight between the IMU and the pushbroom camera.

To compensate for these errors, we proceed in two steps: we first identify tie points between the reference and the pushbroom mosaic, and then use these tie points as observations to adjust the IOP and the boresight parameters using a least squares method.

Matching Points with SURF

We use the Speeded Up Robust Features (SURF) [9] to find corresponding points between the RGB reference and the pushbroom mosaic. SURF is a powerful tool for point matching that determines points of interest from multiple Gaussian-filtered version of the image, and match them according to local-orientation descriptors computed with Haar wavelets. Provided that our images are radiometrically similar (which was discussed in Section 6.1.1), SURF is very suitable to find matching points between our reference orthophoto and the scan lines mosaic. The only obstacle is the use of bilinear interpolation when creating the mosaic: SURF relies on properties of the neighbourhoods of the points of interest, which are synthetic data in the case of an interpolation. However, as discussed further in the results section (Section 6.2), this was a problem only when the aircraft's motion was significant, in which case the interpolation had to fill important gaps between scan lines.

The SURF algorithm is applied to our reference orthophoto and the current pushbroom mosaic. The pairs of points chosen are filtered in two ways: first, the points too close to the border of the footprint of the mosaic are removed. Indeed, no-data (dark) points outside of the footprint might influence their neighbourhoods. Second, absurd matches found by SURF must be discarded. Although methods could be considered at this stage to discard these outliers, they will be dealt with at the least squares adjustment step.

The matches for the same flight are shown on Figure 6.7b.

Interior Orientation and Boresight Estimation

The matched points act as measures that can be used to perform a least squares adjustment and estimate the IOP and the boresight. Since the mosaic of scan lines derives from an interpolation, not every point matched corresponds to an actual pixel from the pushbroom scanner; for each point matched, we simply compute the closest point which did not derive from the interpolation, and get the index of its scan line l as well as the index k of its pixel in the scan line. We wish to find the best parameters so that Equation 6.10 is verified. Ideally, the

functions $g_{k,l,1}$, $g_{k,l,2}$ and $g_{k,l,3}$ given by Equation 6.14 should equal zero for all matches.

$$\begin{aligned}
 & \begin{bmatrix} g_{k,l,1}(r_b, p_b, y_b, f, K_1, K_2, P_1, P_2) \\ g_{k,l,2}(r_b, p_b, y_b, f, K_1, K_2, P_1, P_2) \\ g_{k,l,3}(r_b, p_b, y_b, f, K_1, K_2, P_1, P_2) \end{bmatrix} \\
 &= \mu_{k,l} R_{pb_{k,l}}^{enu}(r_b, p_b, y_b) \begin{bmatrix} 0 + \delta u_{k,l}(K_1, K_2, P_1, P_2) \\ v_k + \delta v_{k,l}(K_1, K_2, P_1, P_2) \\ f \end{bmatrix} \\
 &- \begin{bmatrix} X_{G_{k,l}} \\ Y_{G_{k,l}} \\ Z_{G_{k,l}} \end{bmatrix} + \begin{bmatrix} X_{oC_l} \\ Y_{oC_l} \\ Z_{oC_l} \end{bmatrix} \\
 &= 0
 \end{aligned} \tag{6.14}$$

The boresight roll, pitch and yaw are noted respectively r_b , p_b and y_b in Equation 6.14. The planar coordinates of each corrected ground point, $(X_{G_{k,l}}, Y_{G_{k,l}})$ are the ones output by the SURF; $Z_{G_{k,l}}$ is the value of the DEM at coordinates $(X_{G_{k,l}}, Y_{G_{k,l}})$. From the third line of Equation 6.14, $\mu_{k,l}$ can be computed, leaving the first two lines as two constraints that ideal parameters should satisfy. The input system of our least squares optimisation is given by Equation 6.15.

$$\begin{aligned}
 & g(r_b, p_b, y_b, f, K_1, K_2, P_1, P_2) \\
 &= \begin{bmatrix} g_{k_1,l_1,1}(r_b, p_b, y_b, f, K_1, K_2, P_1, P_2) \\ g_{k_1,l_1,2}(r_b, p_b, y_b, f, K_1, K_2, P_1, P_2) \\ g_{k_2,l_2,1}(r_b, p_b, y_b, f, K_1, K_2, P_1, P_2) \\ g_{k_2,l_2,2}(r_b, p_b, y_b, f, K_1, K_2, P_1, P_2) \\ \vdots \\ g_{k_{N_M},l_{N_M},1}(r_b, p_b, y_b, f, K_1, K_2, P_1, P_2) \\ g_{k_{N_M},l_{N_M},2}(r_b, p_b, y_b, f, K_1, K_2, P_1, P_2) \end{bmatrix}
 \end{aligned} \tag{6.15}$$

In Equation 6.15, N_M is the number of matches kept by the RANSAC; the indexes k are not necessarily distinct, neither are the indexes j , as matches can occur in the same scan line, or for the same pixel in different scan lines. Consider A to be the Jacobian matrix of g relatively to the eight parameters to optimise, and $\dot{v} = -\dot{g}$ where $\dot{g} = g(\dot{r}_b, \dot{p}_b, \dot{y}_b, \dot{f}, \dot{K}_1, \dot{K}_2, \dot{P}_1, \dot{P}_2)$ is the

vector obtained with set initial parameters (Equation 6.16).

$$\begin{aligned}
r_b^\circ &= 0 \\
p_b^\circ &= 0 \\
y_b^\circ &= 0 \\
f^\circ &= 12 \text{ mm} \\
K_1^\circ &= 0 \\
K_2^\circ &= 0 \\
P_1^\circ &= 0 \\
P_2^\circ &= 0
\end{aligned} \tag{6.16}$$

Then the increment of the parameters is given by $(A^T A)^{-1} A^T \hat{v}$, according to the theory of least squares optimisation. It should be noted that we do not estimate the coordinates of the optical centre. Ideally, using as parameters all the IOP (focal length, principal point, distortion parameters) and the three boresight parameters, computing the least squares adjustment would bring corrected values for all these parameters. However, this is not possible, as the position of the optical centre and the couple (boresight roll, boresight pitch) are strongly correlated and prevent the algorithm from converging. Indeed, in a linearised model, a discrepancy in roll results in a shift of the ground points orthogonally to the direction of the vehicle, and so does an error on the v_{pp} . A similar correlation exists between the boresight pitch and the second coordinate of the optical centre. Consequently, we have studied all the existing correlations between compensated parameters, for the images and tie points given in Figure 6.7b, in three different optimisation scenarios. Significant correlations were reported in Table 6.1.

Parameters	Maximum Correlation	Correlated Parameters
Boresight, u_{pp} , v_{pp} , f , K_1 , K_2 , P_1 , P_2	1; -1	Roll and v_{pp} ; Pitch and u_{pp}
Boresight, f , K_1 , K_2 , P_1 , P_2	0.71; 0.69	Roll and P_2 ; Pitch and P_1
Boresight, f , K_1 , K_2	0.68	K_1 and K_2

Table 6.1 Maximum correlations of compensated parameters observed in different scenarios at first iteration of the least squares optimisation.

From the correlations given in Table 6.1, we have decided to optimise the boresight, f , K_1 , K_2 , P_1 and P_2 . It is to be noted that, due to the one-dimensional nature of pushbroom sensors ($u = 0$), P_1 and P_2 are significantly correlated with respectively the boresight pitch and the boresight roll. We have not observed convergence problem when optimising P_1 , P_2 and the rest of the parameters; however, such problems might occur when the tie points found all have

similar ν coordinates.

In order to discard outliers output by SURE, we compute the standard deviation $\sigma(\check{g})$ of the residuals after compensation, $\check{g} = g(\check{r}_b, \check{p}_b, \check{y}_b, \check{f}, \check{K}_1, \check{K}_2, \check{P}_1, \check{P}_2)$. We discard any matched pixel k, l for which $\check{g}_{k,l} > 3\sigma(\check{g})$, and compute the least squares adjustment with the remaining matches. Figure 6.4 shows an example of outliers removal for the flight of Selenga village.

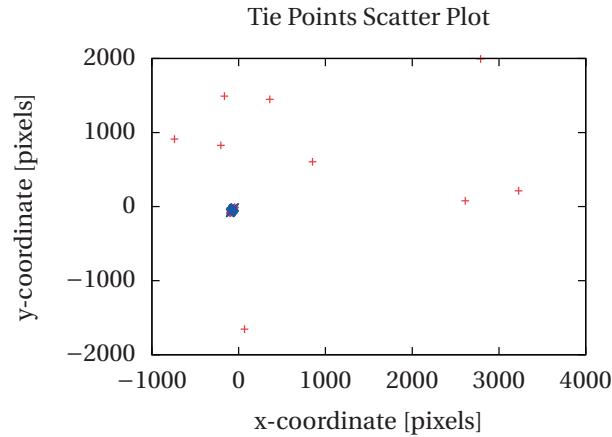


Figure 6.4 Scatter of the difference vectors for the pairs of points matched by the SURE for a flight over a village of the Selenga Delta. All the matches are represented by red crosses. Tilted blue crosses correspond to the pairs kept after removing outliers.

The uncertainty on the estimated values of the boresight and IOP need to be known for a second least squares adjustment used later in our algorithm (Section 6.1.6). They are given as the square root of the diagonal elements of $(A^T A)^{-1}$. In Table 6.2, we have reported the values and standard deviations obtained for our Selenga village flight.

Parameters	Value	σ
Roll	1.1 °	9.3×10^{-3} °
Pitch	-0.54 °	8.8×10^{-3} °
Yaw	-0.17 °	5.2×10^{-2} °
Focal length	11.4 mm	1.5×10^{-2} mm
K_1	294.2 m ⁻²	44.8 m ⁻²
K_2	-1.6×10^8 m ⁻⁴	350.7 m ⁻⁴
P_1	0.54 m ⁻¹	0.57 m ⁻¹
P_2	0.74 m ⁻¹	0.22 m ⁻¹

Table 6.2 Values and standard deviations of boresight parameters and IOP estimated by the least squares adjustment.

The optimised boresight and IOP are used in the projection process described in Section 6.1.3, resulting in a new mosaic that fits the reference orthophoto better (see Figure 6.7c).

6.1.5 Geocorrection Using Particle Image Velocimetry

In this section, we introduce the concept of Particle Image Velocimetry (PIV) and explain how we use it to perform geocorrection and retrieve better estimates of the orientation parameters.

PIV Theory

Particle Image Velocimetry is a technique primarily designed to quantify the movements of fluids [2]. During the Ph.D we had the opportunity to work on the processing of images for biomedical purposes, in which PIV plays an important role [115]. It is an image processing algorithm that computes local instantaneous velocities between two images. The algorithm proceeds in two steps:

- split the two images into a grid of cells, which sizes are given by the user.
- find the new location of each cell of the first image into the second image, by finding the maximum of the cross-correlation of the cell (normalised in mean and standard deviation) and its neighbourhood in the second image (also normalised).

Two sizes have to be input: the size of the cells in the first image, and the size of the interrogation areas in the second image. Interrogation areas are subimages of bigger size than the cells of the first image, in which the algorithm will try to match the cell. Considering a cell as a 2D function $c(x, y)$ from one image, and the corresponding interrogation area $i(x, y)$ in the second image, the estimated position of c in i is the 2D vector (a, b) that maximises the cross-correlation between c and the subimage found following the vector (a, b) from the origin of i (see Equation 6.17).

$$(a, b) = \max_{j,k} \left\{ \frac{1}{n} \sum_{x,y} \frac{1}{\sigma_c \sigma_{i_{jk}}} (c(x, y) - \bar{c}) (i(x - j, y - k) - \bar{i}_{jk}) \right\} \quad (6.17)$$

In Equation 6.17, n refers to the number of pixels in the cell c , \bar{c} and σ_c are respectively the mean and the standard deviation of the intensity inside c , \bar{i}_{jk} and $\sigma_{i_{jk}}$ are the mean and the standard image of the subset of the interrogation area shifted by (j, k) . In practice, Equation 6.17 is computed in the Fourier domain (where the calculation is more efficient). The 2D Fourier transform of the cells/interrogation areas is performed with Fast Fourier Transform (FFT) [121].

The result is a grid of 2D displacements vectors corresponding to the estimated movements for each cell. For all the PIV processing tasks described in the following sections, we use an open-source Matlab application, called PIVlab, by Thielicke & Stamhuis [126]. This application

includes the possibility of filtering the results by deleting the vectors which norms are higher by a threshold proportional to their standard deviation. Vectors can also be manually deleted, or estimated by interpolation of neighbouring vectors when the algorithm failed to find one, or when the vector was filtered.

Application: Elastic Deformation

We use PIV to compute local distortions from the current mosaic to the reference orthophoto. PIV only estimates local translations, and does not deal with rotations or rescaling transformations; however, at this stage, the mosaic and the orthophoto should match well enough so that the differences between the two images can be approximated by a set of local shifts.

At this stage, we have noticed that residual radiometric discrepancies between the two sensors impact the co-registration significantly. To mitigate these effects, we have studied the possibility of using gradient images. Let us call Gr_x and Gr_y the gradients of an image of interest along its x and y axis: we use the gradient magnitude, $Gr = \sqrt{Gr_x^2 + Gr_y^2}$; we have let an algorithm select 50 random patterns of fixed size (30×30 pixels) from the mosaic computed in the previous steps and shown on Figure 6.7c. The 2D unbiased, normalised cross-correlation (which is the criterion maximised by the PIV algorithm) of each pattern with a 90×90 pixels pattern from the reference orthophoto was computed both for the original patterns, and for their gradients. We have plotted on Figure 6.5 the average cross-correlations along the vertical axis (the results along the horizontal axis were similar) for the images and the gradients.

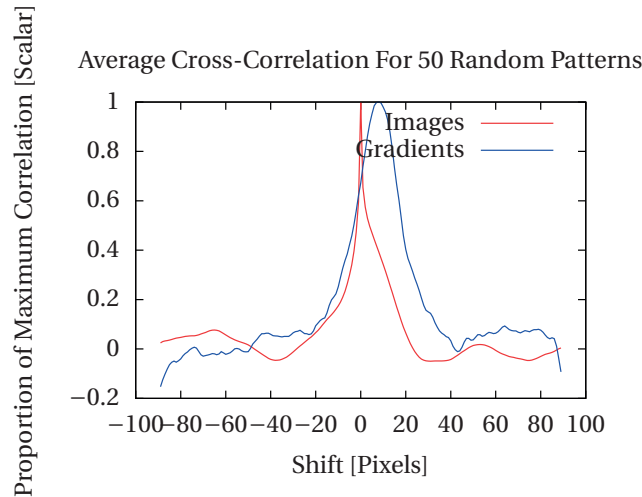


Figure 6.5 Averages of the cross-correlations of corresponding patterns between a reference orthophoto and a co-registered mosaic, for the patterns and their gradients.

Some examples of comparison between images co-registration and gradients co-registration are shown on Figure 6.6.

As can be seen on Figure 6.5, the use of PIV on original images suggests that they are well co-registered with no further shift, while PIV applied to gradients images indicates that the best match is for an average shift of 8 pixels up. Consequently, we proceed with gradient

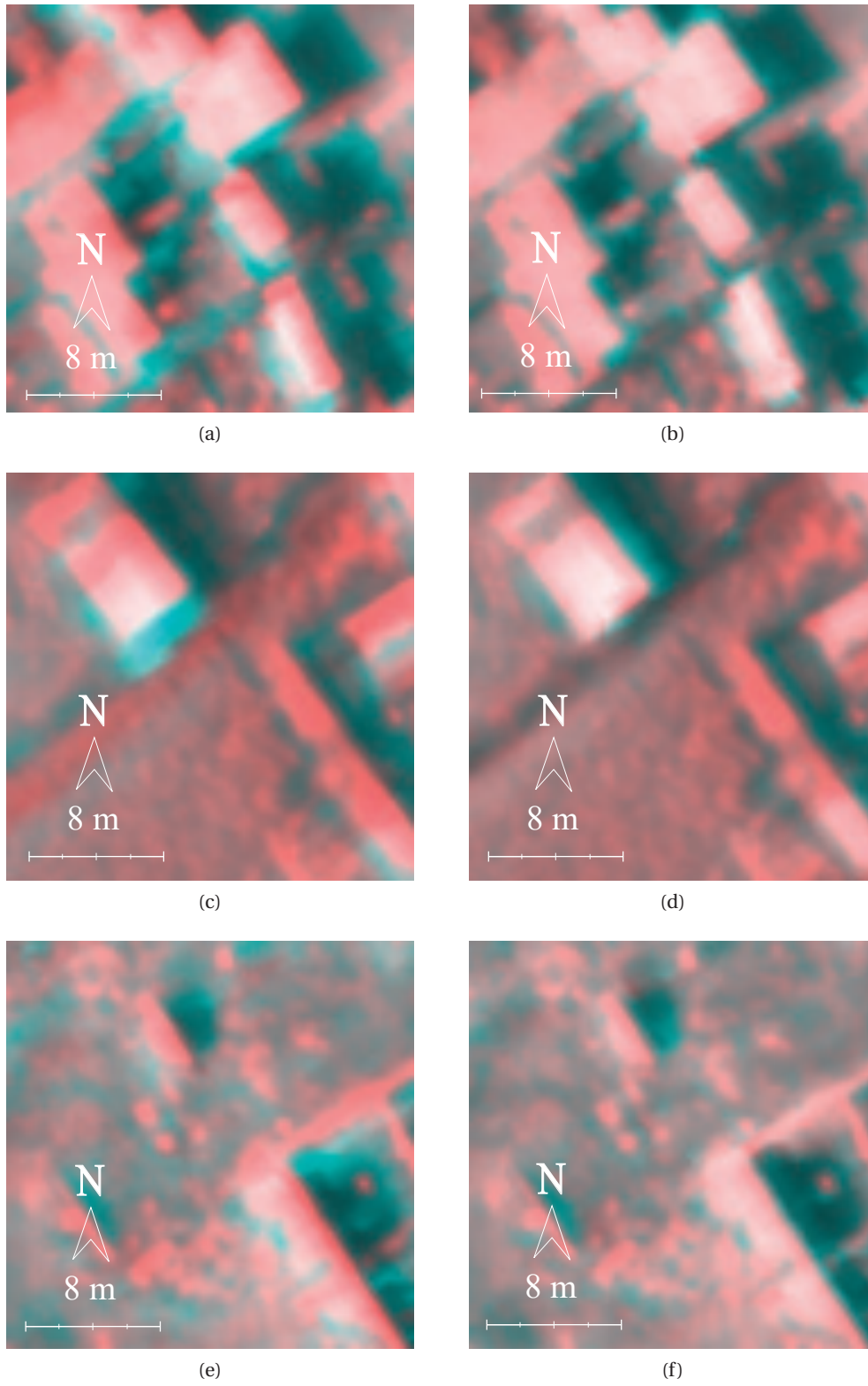


Figure 6.6 Examples of co-registered patterns using PIV on original images ((a),(c),(e)) and on gradient images ((b),(d),(f))

images; PIV is computed with the following parameters: the cell size is 128×128 pixels, the interrogation area size is 256×256 pixels, and the output vector field is filtered to contain only vectors which norms are within the range $[\mu - 0.5\sigma, \mu + 0.5\sigma]$ where μ and σ are respectively the mean and the standard deviation of the norm of vectors output by the PIV algorithm. The resulting vector field is sparse compared with the resolution of the mosaic, hence we interpolate the vector field so that a shift is assigned to every pixel of the mosaic. By translating every pixel following its assigned shift, a new mosaic is created (see Figure 6.7e).

6.1.6 Estimation of the Orientation Parameters

PIV results are considered as tie points: for each pixel projected on a ground point, corresponds a corrected projection indicated by PIV. Using this information, we can perform a bundle adjustment to retrieve the corrected exterior orientation parameters for each scan line. Considering N_L and N_P to be respectively the number of scan lines and the number of pixels per line, $(X_{oC_i}, Y_{oC_i}, Z_{oC_i})$ and (r_i, p_i, y_i) the EOP for line i , $(X_{G_{i,j}}, Y_{G_{i,j}}, Z_{G_{i,j}})$ the real ground point for pixel j of line i and $\mu_{i,j}$ the collinearity coefficient for pixel j of line i , we wish to minimise the squares of the set of Equations 6.18.

$$\begin{aligned} \mu_{i,j} R(r_i, p_i, y_i) \begin{bmatrix} 0 - u_{pp} + \delta u \\ v - v_{pp} + \delta v \\ f \end{bmatrix} - \begin{bmatrix} X_{oC_i} - X_{G_{i,j}} \\ Y_{oC_i} - Y_{G_{i,j}} \\ Z_{oC_i} - Z_{G_{i,j}} \end{bmatrix} &= 0 \\ X_{oC_i} - X_{oC_i}^\circ &= 0 \\ Y_{oC_i} - Y_{oC_i}^\circ &= 0 \\ Z_{oC_i} - Z_{oC_i}^\circ &= 0 \\ r_i - r_i^\circ &= 0 \\ p_i - p_i^\circ &= 0 \\ r_i - \hat{r}_i &= 0 \\ u_{pp} - u_{pp}^\circ &= 0 \\ v_{pp} - v_{pp}^\circ &= 0 \\ f - \hat{f}_{SURF} &= 0 \\ K_1 - \hat{K}_{1SURF} &= 0 \\ K_2 - \hat{K}_{2SURF} &= 0 \\ P_1 - \hat{P}_{1SURF} &= 0 \\ P_2 - \hat{P}_{2SURF} &= 0 \end{aligned} \tag{6.18}$$

The first line in the set of Equations 6.18 corresponds to the collinearity equation (Equation 6.10), and provides 2 constraints (3, one of which is used to determine $\mu_{i,j}$) per pixel. Therefore, collinearity equations provide $2 \times N_L \times N_P$ constraints. The rest of the constraints ensure that the final estimated parameters stay close to their initial estimates (noted with a circle) obtained either in Section 6.1.2 or Section 6.1.4 (some IOP were estimated using SURF matching and

were noted with a "SURF" subscript). There are 6 EOP per line and 7 IOP; in total, the least-square algorithm estimates $6 \times N_L + 7$ parameters from $2 \times N_L \times N_P + 6 \times N_L + 7$ constraints. Calling A_{PIV} the Jacobian matrix of the system of Equations 6.18 and \hat{v}_{PIV} the opposite of its residuals, the least squares adjustment theory increments the parameters at each iteration by $(A_{PIV}^T W A_{PIV})^{-1} A_{PIV}^T \hat{v}_{PIV}$. Unlike the adjustment performed using SURF points, a weight matrix W must be used in this second adjustment, as there are different types of observations. W is a diagonal matrix; its first $2 \times N_L \times N_P$ elements are related to the expected error of the matching operated by PIV. We consider the ground points output by the PIV to have a standard deviation of $0.5m$, resulting in a weight $4m^{-2}$ for the first $2 \times N_L \times N_P$ constraints (Equation 6.19).

$$W_{1,1} = \dots = W_{2N_L N_P, 2N_L N_P} = 4m^{-2} \quad (6.19)$$

The uncertainties of the position and attitude parameters for each line are given by the manufacturer of the GPS+IMU system: 2 cm for position measurements, 0.02° for roll and pitch angles, and 0.05° for yaw angles (Equation 6.20).

$$\begin{aligned} \forall l \in [0, N_L - 1], \\ W_{2N_L N_P + 6l + 1, 2N_L N_P + 6l + 1} &= 2500 \text{ m}^{-2} \\ W_{2N_L N_P + 6l + 2, 2N_L N_P + 6l + 2} &= 2500 \text{ m}^{-2} \\ W_{2N_L N_P + 6l + 3, 2N_L N_P + 6l + 3} &= 2500 \text{ m}^{-2} \\ W_{2N_L N_P + 6l + 4, 2N_L N_P + 6l + 4} &= 8.2 \times 10^6 \text{ rad}^{-2} \\ W_{2N_L N_P + 6l + 5, 2N_L N_P + 6l + 5} &= 8.2 \times 10^6 \text{ rad}^{-2} \\ W_{2N_L N_P + 6l + 6, 2N_L N_P + 6l + 6} &= 1.3 \times 10^6 \text{ rad}^{-2} \end{aligned} \quad (6.20)$$

The standard deviations for the remaining parameters (IOP) are output by the least squares adjustment following the SURF (Table 6.2), except for the principal point coordinates. From our experience with digital cameras, we have set the initial standard deviation on the principal point coordinates to be 20 pixels of the camera, which corresponds to 1.5×10^{-4} m. From the output orientation parameters, we produce a new orthorectified image of the scan lines by using the same projection technique as described in Section 6.1.3. The result is shown on Figure 6.7f.

6.2 Results

Five test sites were chosen to illustrate the performance of our method. The five acquisitions differed by the stability of the attitude, the homogeneity of the surfaces imaged, the altitude of

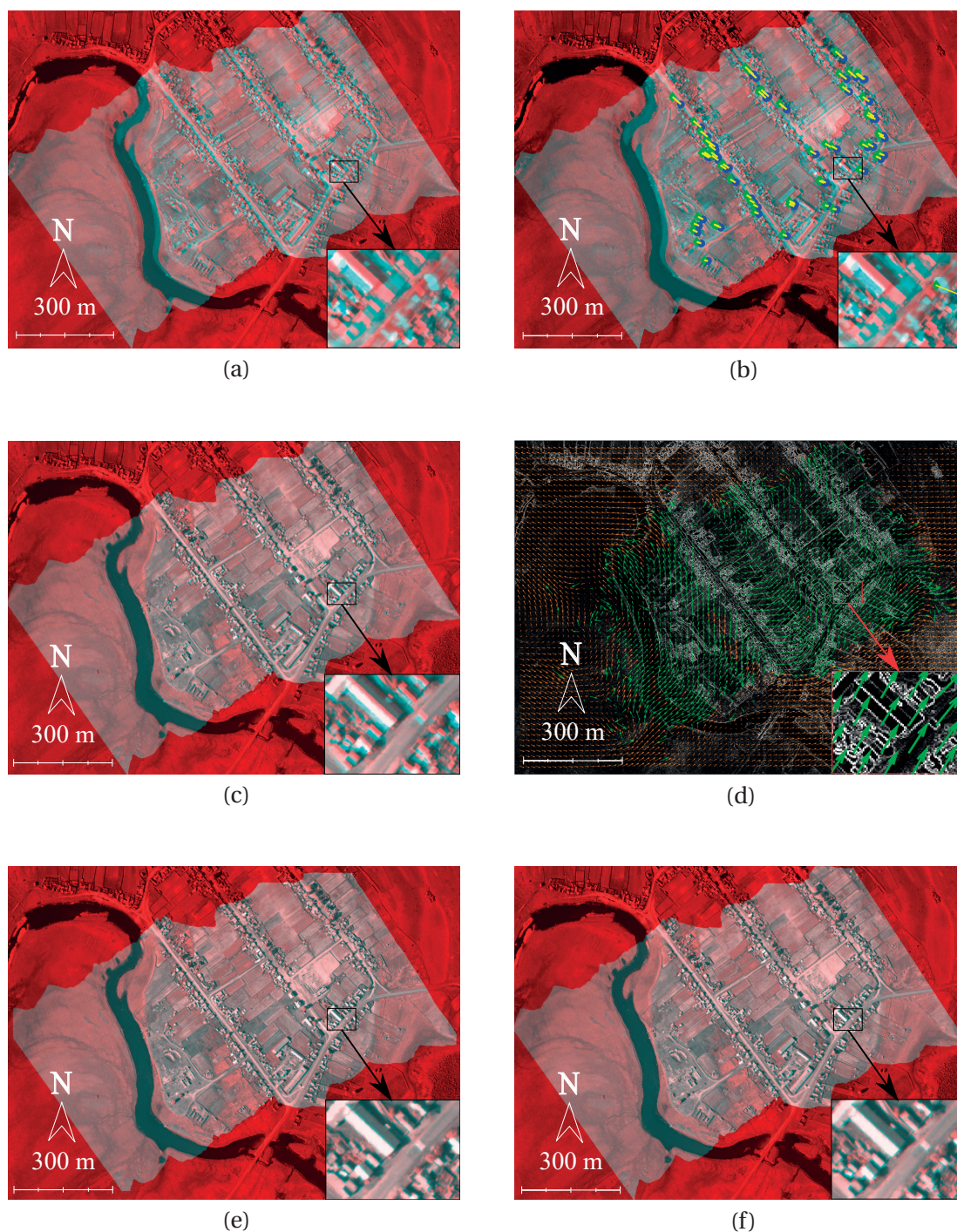


Figure 6.7 Illustrations of the various steps of our algorithm for a test flight over a village of the Selenga Delta (Russia, 17 August 2014). All images show the superimposed scan lines (in cyan) on top of the reference orthophoto (in red). **(a)** Initial projection with uncalibrated IOP; **(b)** Feature matching using SURF; **(c)** Projection with calibrated IOP and boresight; **(d)** PIV performed on the gradient images; **(e)** Deformation of the scan lines, following the PIV; **(f)** Projection after correction of the EOP.

	Selenga Village 1	Selenga Village 2	Selenga Rivers	Gremyachinsk	Lake Geneva Shore
Flight Altitude (m)	1000	1000	1000	1000	500
Flight Attitude	Stable	U-turn	Stable	Stable	Wavy
Surface Homogeneity	Heterogeneous	Heterogeneous	Heterogeneous	Homogeneous	Heterogeneous
Content	Fields, built structures	Fields, built structures	Rivers, swamps	Water, sand	Built Structures
Frame Camera GSD (m)	0.28	0.28	0.28	0.31	0.14
Pushbroom Across-Track GSD (m)	0.6	0.6	0.6	0.6	0.3
Pushbroom Along-Track GSD (m)	0.6	0.6	0.6	0.6	0.5

Table 6.3 Characteristics of the five test acquisitions.

the aircraft during acquisition and the resulting Ground Sampling Distances (GSD) for the two cameras. The GSD of the frame camera is unambiguously defined as the distance between the centres of two adjacent pixels of the orthophoto. For the pushbroom scanner, two GSDs are given: the across-track GSD, which mainly depends on the geometry of the sensor, the flight altitude and attitude, and the along-track GSD, which depends on the speed of the aircraft, the acquisition frequency and the attitude. Due to the varying altitude and attitude of the aircraft, the GSDs are not constant during the flights; indicative GSDs without roll and pitch, and for the mean altitude and speed of each flight, are provided with one significant figure. These characteristics are summarised in Table 6.3.

Selenga areas and the area on the shore of Lake Geneva all contain many salient points that can be recognised and used by the SURF/PIV algorithms. These four acquisitions differ by the global attitude of the ultralight plane during the acquisition: the aircraft operated a U-turn over the Selenga village 2 and had a wavy motion above the shore of Lake Geneva; this last flight was also performed at a lower altitude (500 m), compared with the other flights. The Gremyachinsk area did not contain many salient points: the image essentially consists in water, sand and forest, making the use of feature-based and area-based matching techniques unreliable. We have decided to include this area among our tests to give an idea of the behaviour of our algorithm in difficult conditions. For each of the 5 test areas, the original mosaic produced with the scan lines (before geocorrection) and the corrected mosaic (after geocorrection) were superimposed on the reference orthophoto. For Selenga village 1, the results are already visible on Figures 6.7a and 6.7f; for the other areas, the results are shown on Figures 6.8 and 6.9.

To provide quantitative results, we have determined the planar Root Mean Square Error (RMSE) on samples of 50 points for every test area. To provide the most objective statistics

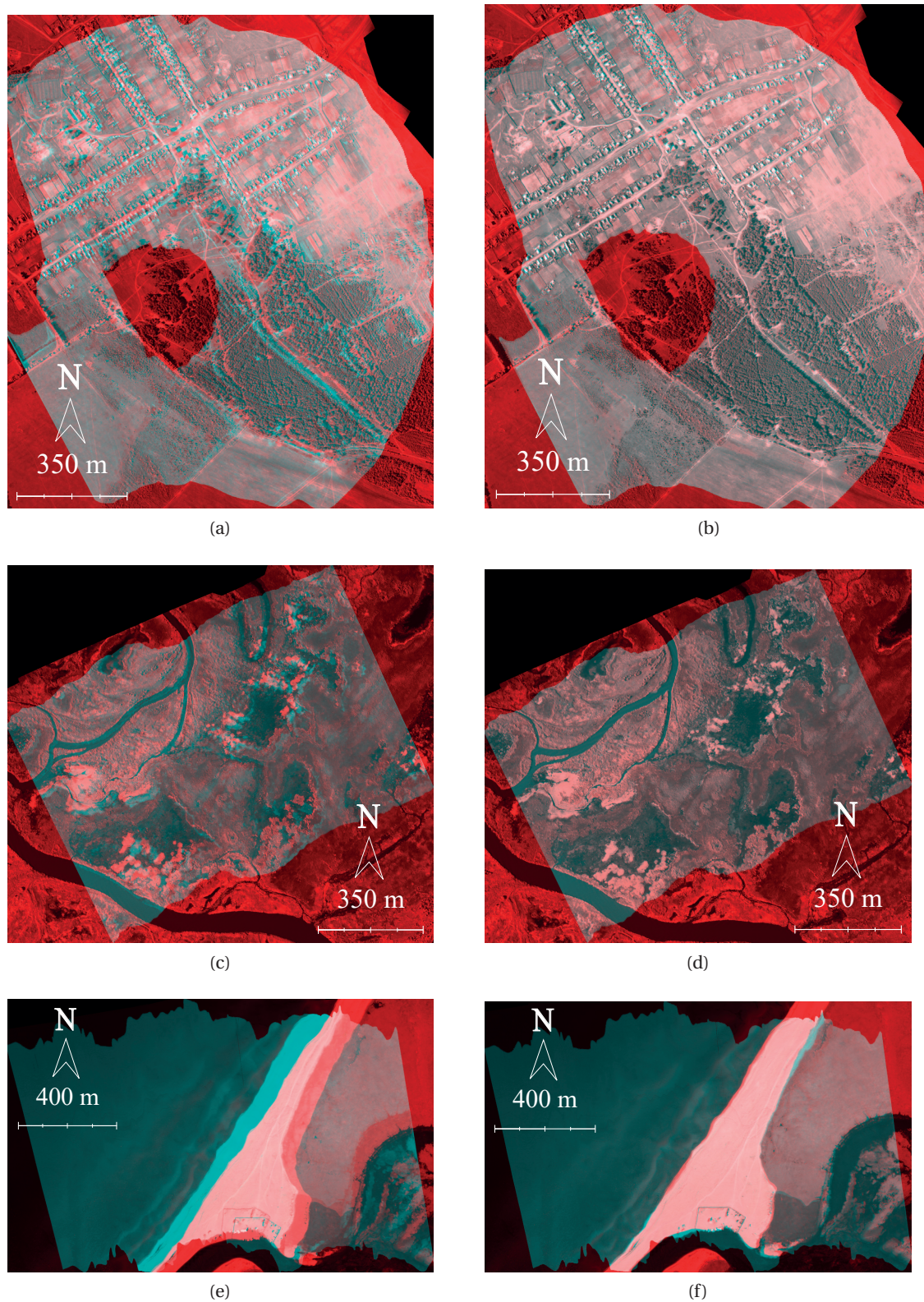
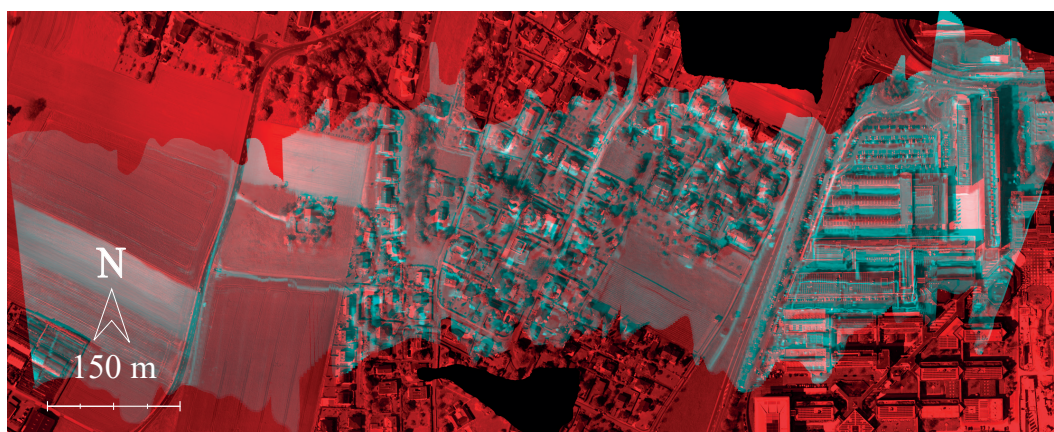
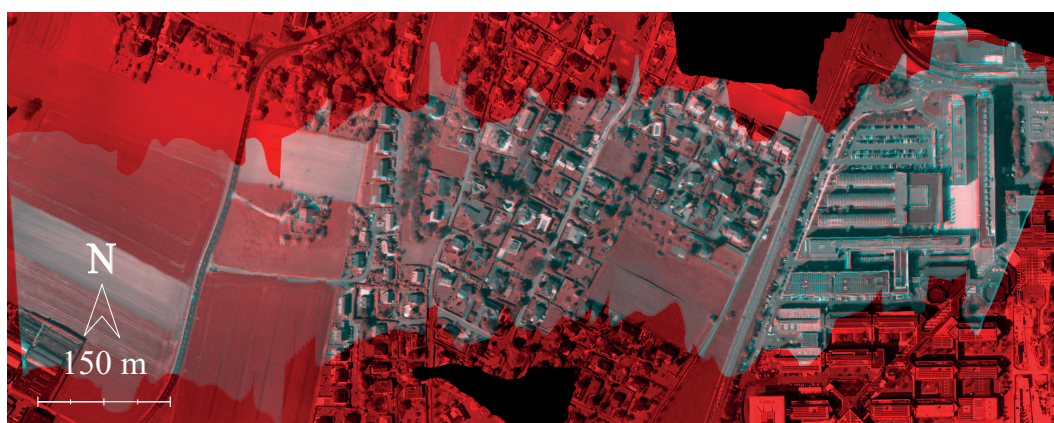


Figure 6.8 Superposition of the reference orthophotos and the mosaic produced with the scan lines: (a), (c), (e) before geocorrection and (b), (d), (f) after geocorrection. (a), (b): Selenga Village 2; (c), (d): Selenga Rivers; (e), (f): Gremyachinsk.



(a)



(b)

Figure 6.9 Superposition of the reference orthophoto and the mosaic produced with the scan lines **(a)** before geocorrection and **(b)** after geocorrection, for our test region on the shore of Lake Geneva.

Chapter 6. Pushbroom Images Georeferencing

Planar RMSE	Selenga Village 1	Selenga Village 2	Selenga Rivers	Greymachinsk	Lake Geneva Shore
Initial Projection	24.5 m / 40.8 px	24.6 m / 41 px	24.5 m / 40.8 px	45.5 m / 75.8 px	10.8 m / 27 px
After IOP and Boresight Correction	2.4 m / 4 px (-90%)	13.6 m / 22.7 px (-45%)	1.3 m / 2.2 px (-95%)	8.2 m / 13.7 px (-82%)	3.7 m / 9.2 px (-66%)
After PIV Deformation	0.9 m / 1.5 px (-67%)	1.6 m / 2.7 px (-88%)	0.6 m / 1 px (-54%)	6.1 m / 10.2 px (-26%)	1.8 m / 4.5 px (-51%)
With Corrected Orientation Parameters	1.1 m / 1.8 px (+22%)	1.8 m / 3 px (+13%)	0.8 m / 1.3 px (+33%)	6.5 m / 10.8 px (+6%)	1.6 m / 4 px (-11%)

Table 6.4 Planar RMSE for each test area, and percentage evolution from previous step, at each step of the geocorrection.

possible, these points were selected as follows: a series of random patterns of given size, extracted for the image of interest, was generated; inside each pattern, a point was chosen in the orthophoto and the four images corresponding to each step of our algorithm (first projection, after boresight/IOP calibration, after PIV and after estimation of the EOP). The results are given in Table 6.4.

For the first three areas, the RMSE decreased from about 25 metres (before correction) to about one metre (after correction). While many tie points were found by SURF for Selenga Village 1 and Selenga Rivers, few were found for Selenga Village 2. The reason is the U-turn motion of the aircraft implied important gaps between the scan lines; to create the mosaic, data was interpolated between these scan lines, and no salient point recognisable by SURF can be detected in this synthetic data. However, in spite of the lesser decrease of the RMSE at the SURF stage (13.6 metres, against 2.4 metres and 1.3 metres for Village 1 and Rivers, respectively), PIV performs very well and the final RMSE is approximately the same for the three areas. This result suggests that local normalised cross-correlation can deal with significant rotations like the ones that affected the Village 2 image. The final RMSE in the Greymachinsk area (6.5 metres), although seemingly worse than the others, is encouraging as the initial RMSE was significantly higher (45.5 metres) and the image does not exhibit a significant heterogeneity; only 11 points were matched by SURF, all gathered on the few built structures at the bottom centre of the image. The application of PIV then allowed to decrease the RMSE by an additional 26 %. On the shore of Lake Geneva, significant discrepancies were observed in the first projection, where adjacent scan lines appeared to be taken with different attitudes; as a consequence, the correction operated by PIV, although satisfying, did not respect the inherent geometrical properties of the pushbroom scanner: the shifts estimated by PIV showed very different values and directions within each single scan line. As a consequence, and for this test area only, the mosaic produced after correction of the EOP was better (RMSE = 1.6 m) than the one produced by PIV (RMSE = 1.8 m). It should be noted that the opposite is expected, and observed for the four other test areas, as the final mosaic is produced by an orthorectification algorithm, while PIV produces a mosaic regardless of the geometrical nature of the problem. Overall,

the geocorrection algorithm performs well on areas with enough salient points, whether the motion of the aircraft is smooth (Selenga Village 1, Selenga Rivers) or irregular (Selenga Village 2, Lake Geneva Shore).

Software Management of

Hyperspectral Data

Part III

7 Orthorectification and Viewing of Hyperspectral Data

The Léman-Baïkal project involved the development of a hardware system, including navigation sensors, a frame and a pushbroom camera, a processor, and the architecture allowing the communication between all these devices. This was the work of a former Ph.D student of the Geodetic Engineering Laboratory, Dragos Constantin. The data produced by this system were the hypercubes (as .bil files) and the navigation and time data, in the shape of formatted text (.hdr files). However, at this stage, no open source scientific solution was available to handle this data practically, that is, orthorectify it on a given DEM, allow to view it on a digital world map and reprocess or export this data as mosaics. Consequently, a large part of our work was the design of a software solution to these problems.

7.1 Software Architecture

We have designed a software called HYPerspectral Orthorectification Software (HypOS) to assume the specific tasks related to the processing of airborne hyperspectral image and their corresponding navigation data. HypOS includes an orthorectification tool and allows to view and export hyperspectral mosaics as .bil files. The software is built using a Java Software Development Kit (SDK) called WorldWind, developed by NASA. This SDK contains a digital model of the Earth, and various tools to represent georeferenced features (points, lines, areas, images), work with geographic or projected coordinate systems, and export files in .kml, .kmz or geotiff.

Figure 7.1 shows the opening screen of HypOS, and highlights the 3D world view (included in the SDK) and the panels on the side, which contain the tools we developed.

The software reads a series of .bil files (together with their corresponding .hdr). In the .hdr, the navigation data is written; the software orthorectifies the hyperspectral data using the process described in the following section. The object-oriented programming allows to build HypOS in modules: the processing is linear and, in case of development of new processing algorithms, this processing can be added to the processing chain of HypOS in a new tab on the right of the

Chapter 7. Orthorectification and Viewing of Hyperspectral Data

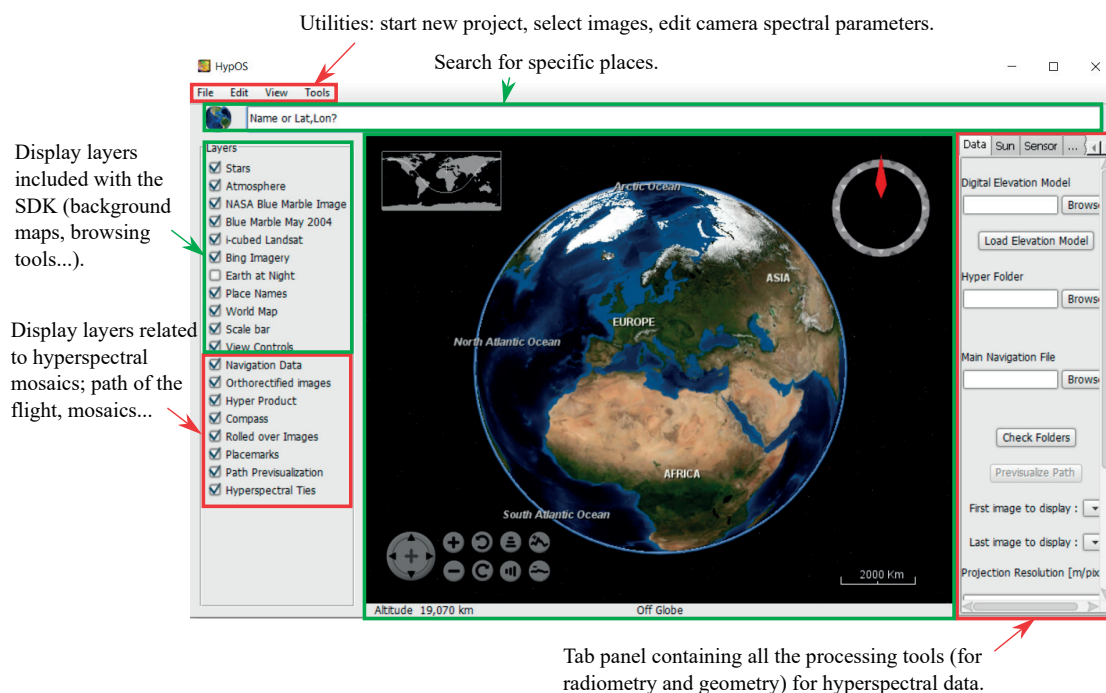


Figure 7.1 Opening screen of HypOS. The green features were included with the SDK. The red features are hyperspectral-specific features that we developed and incorporated in the user interface.

screen. Currently, the processing chain included in HypOS is the following:

- loading of the data, with viewing of the path of the aircraft.
- orthorectification of the data, at a given resolution.
- possible radiometric calibration from dark and Spectralon measurements (if available).
- correction of the variations of illumination during the flight.
- geometric correction: new estimations of interior orientation parameters from tie points manually input by the user.
- export of an area of interest to ENVI .bil + .hdr files.

7.2 Orthorectification Process

The projection algorithm is similar to the one described in Section 6.1.3. Only two aspects differ. First, the DEM is either the default one (provided by the WorldWind SDK) or a DEM imported from an external file, given by the user. Second, a ray casting algorithm is included with the WorldWind SDK. Although it is similar to the one described in Section 6.1.3, its

essential difference is the recursive process it uses: from the optical centre $\begin{bmatrix} X_{oC} \\ Y_{oC} \\ Z_{oC} \end{bmatrix}$, terrain is

searched in the direction of the ray $R_{pb}^{enu} \begin{bmatrix} 0 - u_{pp} + \delta u \\ v - v_{pp} + \delta v \\ f \end{bmatrix}$. The ray is initially multiplied by a

large factor (30) to find the intersection with the terrain quickly. A precision on the intersection point (for instance, 1 m) is input by the user. When the current point is below the terrain, the search goes back from the previous point, and the factor is divided by 10, so that once the intersection is reached again, it is known with better precision. The recursion ends when the precision is smaller than the precision required by the user. Figure 7.2a and 7.2b show an example of DEM seen in HypOS for a flight passing above EPFL, before and after projection of the hyperspectral data.

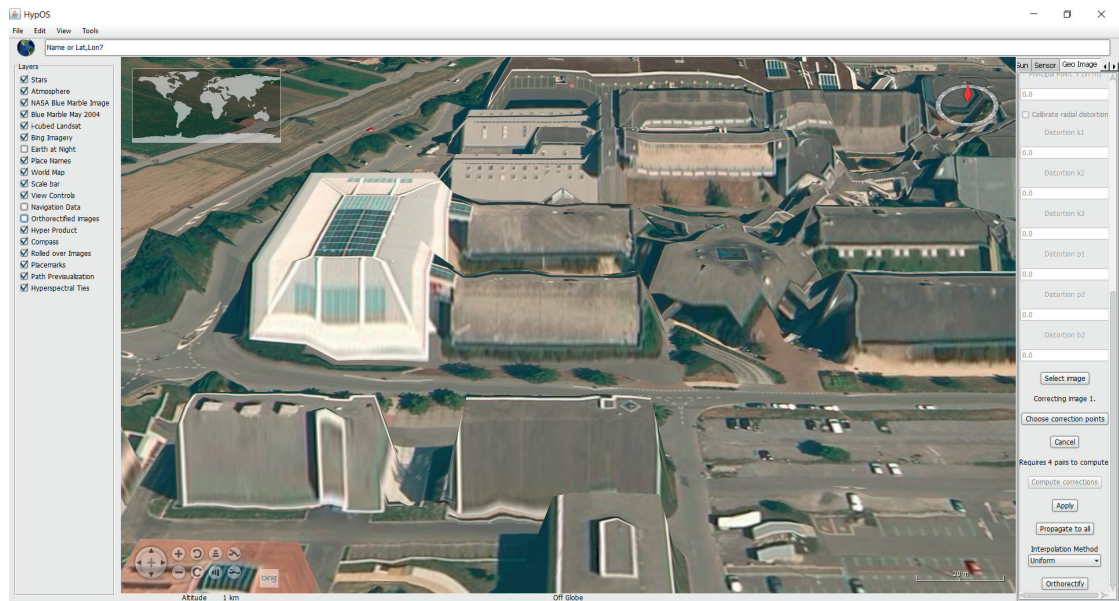
If a higher resolution than the one inherent to the acquisition is required, HypOS includes the possibility to interpolate the data with a bilinear method.

7.3 Correction for the Variation of Sky Downwelling Irradiance

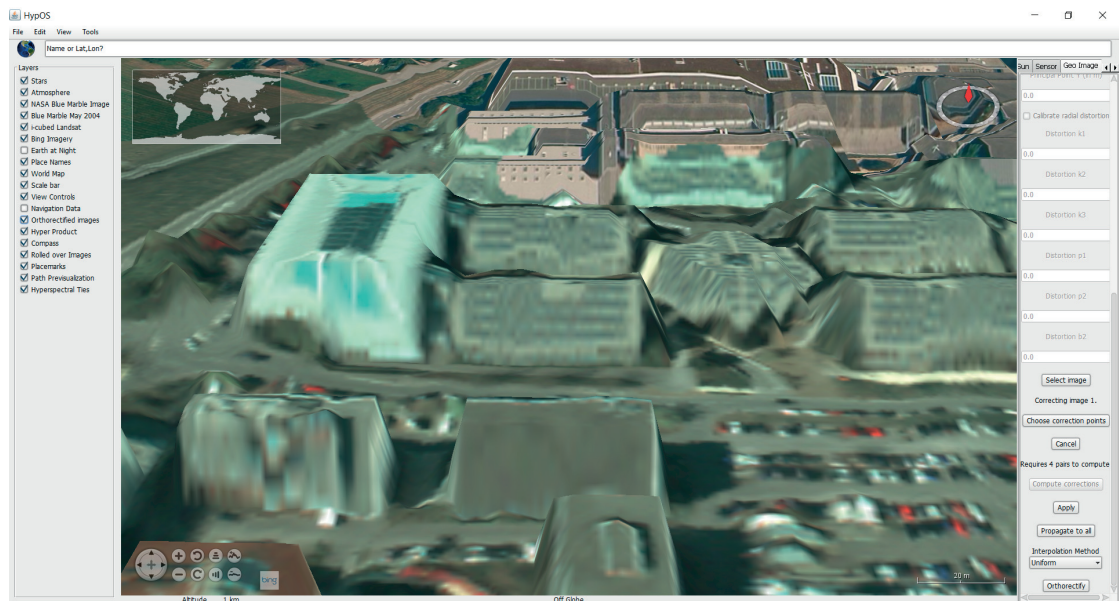
In chapter 5, we presented our radiometric calibration algorithm, with some parts (glint correction, BRDF correction) specifically dedicated to calibrating water spectra. These tools are not included as such in HypOS. However, HypOS gives the possibility to correct data radiometrically when Spectralon measurements, collected just before/just after the flight are available. The Spectralon data gives an estimate of the downwelling irradiance E_d ; if measurements are available before and after the flight, they can be interpolated to produce a time-dependent estimate of E_d . The problem is that some data from the 2014 campaign in Baikal were collected without proper Spectralon acquisitions, prior to the start of our contribution to the project. The resulting mosaics, when they were first projected in HypOS, showed visible brightness differences between overlapping data from adjacent flight lines (see Figure 7.3).

In order to deliver more uniform mosaics, we have programed an algorithm that estimates the brightness difference due to the variation of the sun elevation angle, so as to adjust the brightness of each scan line. We model the phenomena by assigning each scan line of index i an illumination coefficient, η_i . η_i is not observed directly; the only observations are the difference of illumination between overlapping points from different scan lines. Pair of overlapping points are filtered: if the SAM (see Equation 5.10) between the two spectrums involved is higher than a given threshold, then the pair is discarded. For the remaining pairs, only the ratio between the illumination coefficients is observed, as $\frac{\eta_i}{\eta_j} = \frac{\bar{\rho}_i}{\bar{\rho}_j}$, where $\bar{\rho}_i$ is the the reflectance, averaged along the spectral dimension. The model for the illumination is

Chapter 7. Orthorectification and Viewing of Hyperspectral Data



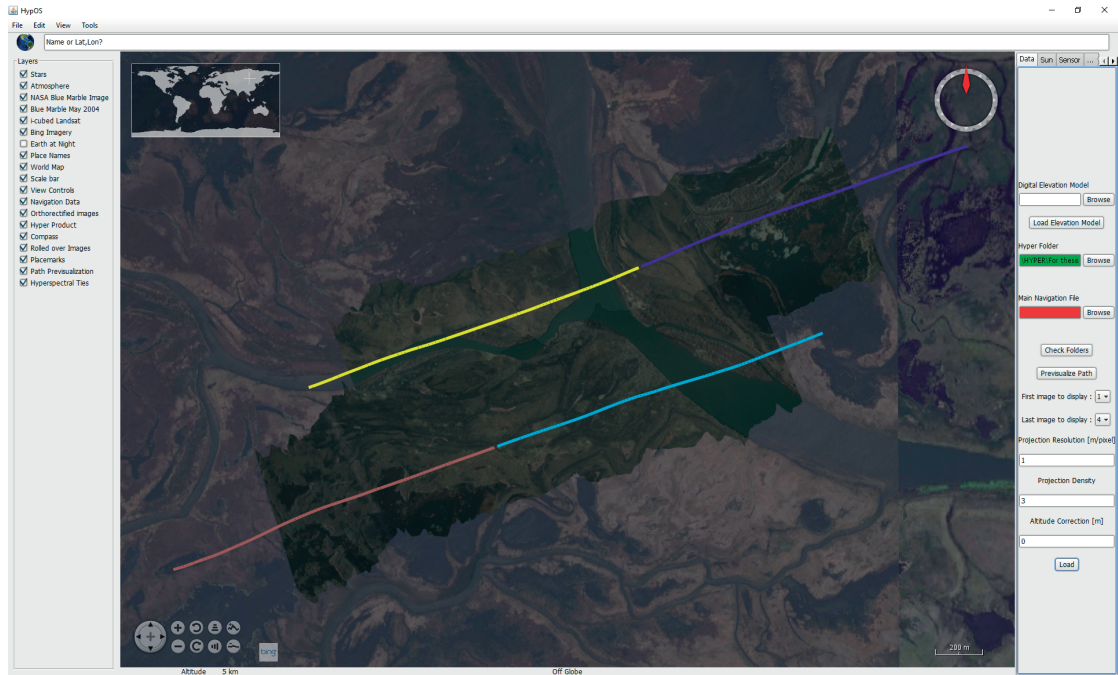
(a)



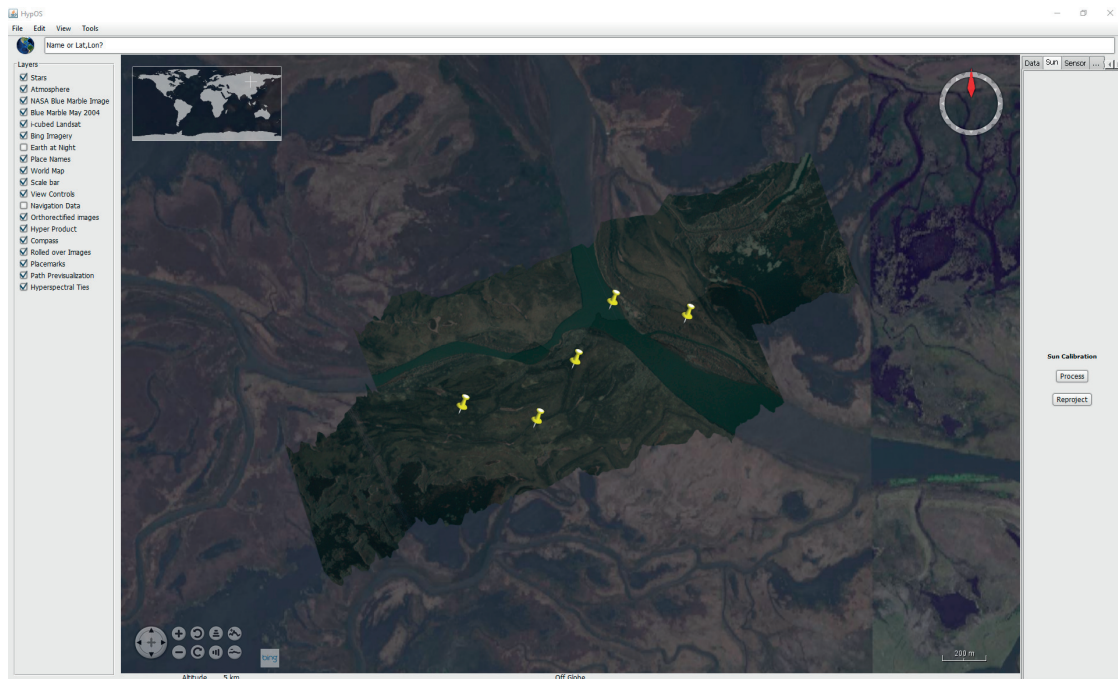
(b)

Figure 7.2 DEM of a part of EPFL, (a) without and (b) with corresponding hyperspectral data superimposed, visualised in HypOS.

7.3. Correction for the Variation of Sky Downwelling Irradiance



(a)



(b)

Figure 7.3 Visualisation of a flight from August 2014 over the Selenga Delta. **(a):** projection, with the flight lines seen as coloured lines; **(b):** selected points for computation of the difference of illumination.

quadratic (see Equation 7.1).

$$\eta_i = \alpha i^2 + \beta i + 1 \quad (7.1)$$

In Equation 7.1, the index i of the scan line is assimilated as the time. An arbitrary scan line is designated as scan line of index 0 and assigned a reference unitary illumination. For each observation $l_{i,j} = \frac{\eta_i}{\eta_j}$, we can write Equation 7.2.

$$\begin{aligned} l_{i,j} &= \frac{\alpha i^2 + \beta i + 1}{\alpha j^2 + \beta j + 1} \\ \Leftrightarrow \underbrace{\alpha(i^2 - l_{i,j}j^2)}_{U_{i,j}} + \underbrace{\beta(i - l_{i,j}j)}_{V_{i,j}} &= \underbrace{l_{i,j} - 1}_{W_{i,j}} \end{aligned} \quad (7.2)$$

At this point, a least squares optimisation can output the best values for the parameters α and β . However, numerical derivation of the equations also allows to express α and β directly (Equation 7.3).

$$\begin{bmatrix} \alpha \\ \beta \end{bmatrix} = \frac{1}{\sum U_{i,j}^2 \sum V_{i,j}^2 - (\sum U_{i,j} V_{i,j})^2} \begin{bmatrix} \sum V_{i,j}^2 & -\sum U_{i,j} V_{i,j} \\ -\sum U_{i,j} V_{i,j} & \sum U_{i,j}^2 \end{bmatrix} \begin{bmatrix} \sum U_{i,j} W_{i,j} \\ \sum V_{i,j} W_{i,j} \end{bmatrix} \quad (7.3)$$

Once α and β are retrieved, the values in each scan line i are divided by their corresponding η_i . Figure 7.4 shows an example of correction, performed on the same mosaic as shown in Figure 7.3. Figure 7.5 zooms on the border between the two flight lines to illustrate the performance of the correction.

7.4 Boresight Correction from Manual Tie Points

HypOS can be used with either the corrected orientation parameters (obtained using our geocorrection method, described in Chapter 6) or with the navigation data output by the GPS+IMU system. In the second case, the mosaic produced is not coherent with the background image from Bing Maps. However, the user still has the possibility to give tie points manually so that the software can estimate better IOP and boresight and produce a mosaic fitting the background better. From a click on a point of the mosaic, the index of the corresponding scan line l and the corresponding pixel in this line k , as well as the current orientation parameters for this line ($X_{oC_l}, Y_{oC_l}, Z_{oC_l}$) and (r_b, p_b, y_b) , are retrieved. A second click allows to point at the corrected location where the pixel in question should have been

7.4. Boresight Correction from Manual Tie Points

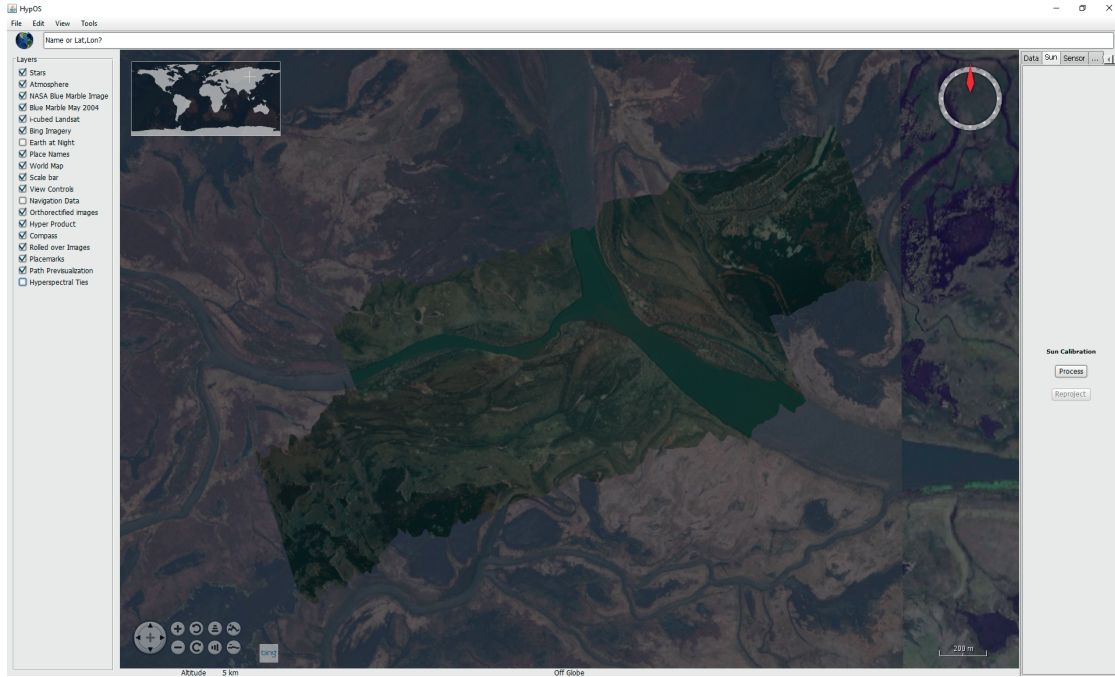


Figure 7.4 Visualisation of a flight from August 2014 over the Selenga Delta, after illumination correction.

projected: $(X_{G_{k,l}}, Y_{G_{k,l}})$ are the UTM coordinates of this point, and $Z_{G_{k,l}}$ is the value of the DEM at coordinates $(X_{G_{k,l}}, Y_{G_{k,l}})$. Then, using the process described in Section 6.1.4, the boresight parameters, the focal length of the camera and the distortion parameters K_1, K_2, P_1 and P_2 can be re-estimated.

To show the performance of this tool, we orthorectified three flights from the Léman-Baïkal campaign. The first flight was performed on the shore of Lake Geneva in April 2015, at an altitude of 500 m. The second and third flights were performed above the Selenga Delta of Lake Baikal on August 2014, at two other altitudes (1000 m and 1500 m). Figures 7.6 and 7.7 show these flights as seen in HypOS, and the effect of the correction on a part of the mosaics.

For the three flights of interest, the RMSE before correction and after correction has been computed, so as to illustrate the quantitative performance of the correction (Table 7.1).

	Mean Elevation [m]	RMSE Before Correction	RMSE After Correction
Flight 1	500	13.8 m / 27.6 px	3.1 m / 6.2 px
Flight 2	1000	49.2 m / 50.2 px	4.0 m / 4.1 px
Flight 3	1500	46.3 m / 32.4 px	5.2 m / 3.6 px

Table 7.1 Comparison of mean residual before and after correction for three flights of different altitudes.

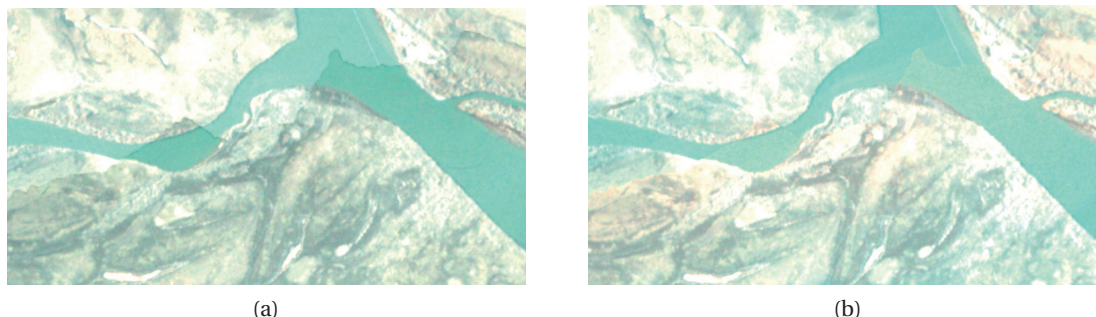


Figure 7.5 Comparison of the mosaics, before and after illumination correction. Brightness was adjusted in both cases to make the differences clear.

It is no surprise that the results are comparable to the ones obtained after SURF (but before PIV) in our prototype geocorrection algorithm (Table 6.4), since the method employed is the same, the only difference being that the tie points are chosen by the user and not by SURE. The purpose of the presence of this tool in HypOS is not only to be able to work with the data directly output by the navigation sensors, but also to allow for systematic error correction if the data has been aligned with another RGB reference, and needs to be modified to be aligned with the Bing Maps reference.

7.5 Mosaic Export

Hyperspectral mosaics produced by HypOS can be exported as georeferenced .bil hypercubes. The geometric resolution, as well as the bands to export can be changed by the user. Figure 7.8 shows an example of such export.

The data is exported as a .bil file with a .hdr file according to the ENVI header standards; inside the ENVI header, the UTM coordinates and the UTM zone of the rectangle zone exported are mentioned, so that the mosaic's georeference is read directly by state-of-the-art remote sensing softwares such as ENVI or ERDAS Imagine.

7.6 HypOS Scientific Value and Use in Research

During the Léman-Baïkal project, HypOS was the key to produce orthorectified hyperspectral mosaics of areas of interest. The possibility of processing data directly output by the hyperspectral system mounted on the ULM allowed to process data quickly for use for further analysis. A list of applications of images output by HypOS can be found in Chapter 8. Outside the Léman-Baïkal project, HypOS has been used by a team of scientists from the Université de Bretagne Occidentale to perform direct georeferencing of airborne pushbroom hyperspectral data acquired from a drone [60].

With further development (mainly, file formats compatibility, for inputs and outputs), HypOS

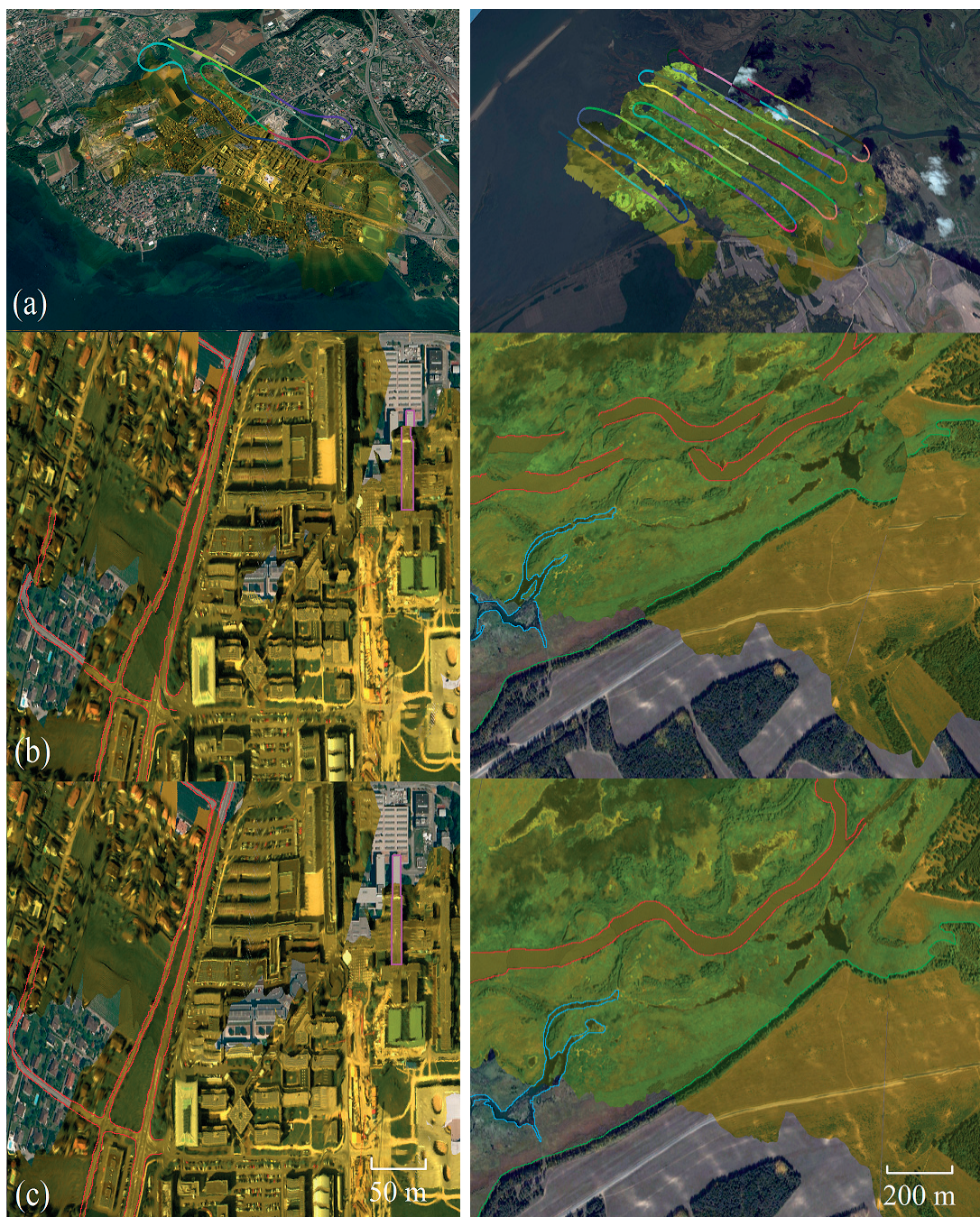


Figure 7.6 Extracts from flights 1 and 2, corrected using manually input tie points: **(a)** overview of the flight from an isometric view in HypOS; **(b)** extract before correction; **(c)** extract after correction. To put in evidence the effect of the correction, features have been highlighted using red, green and blue colours.

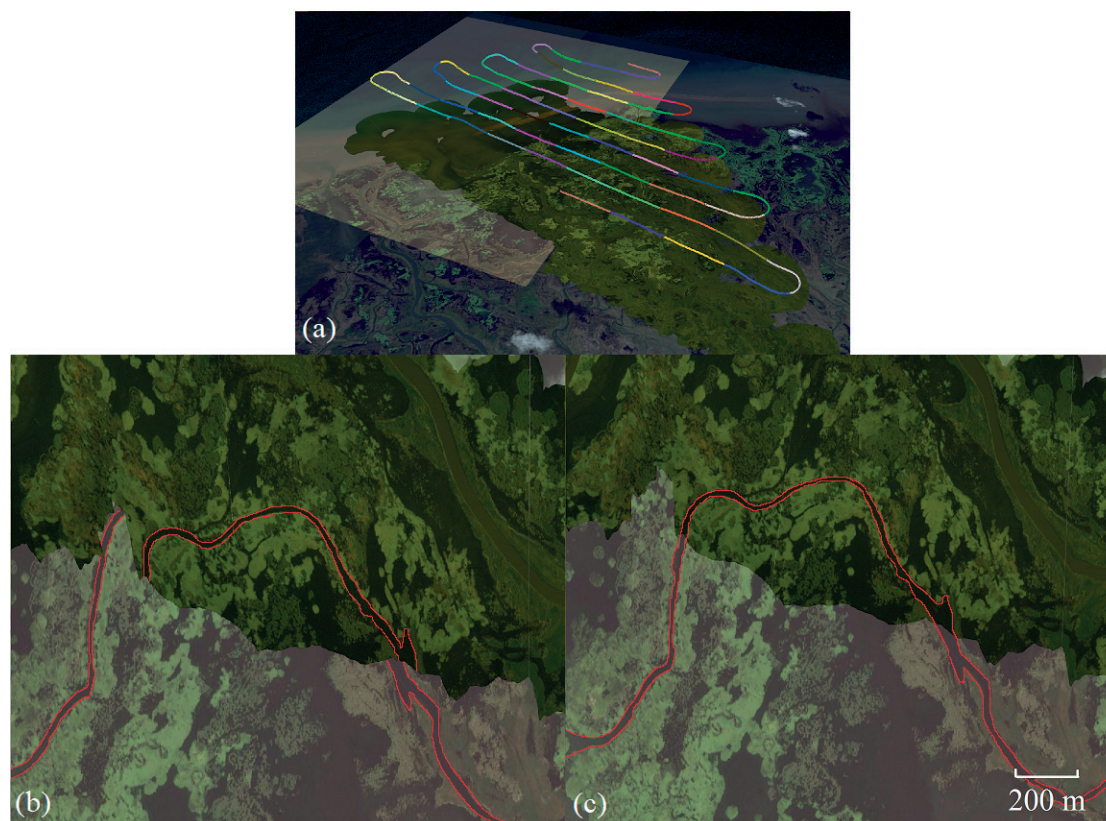
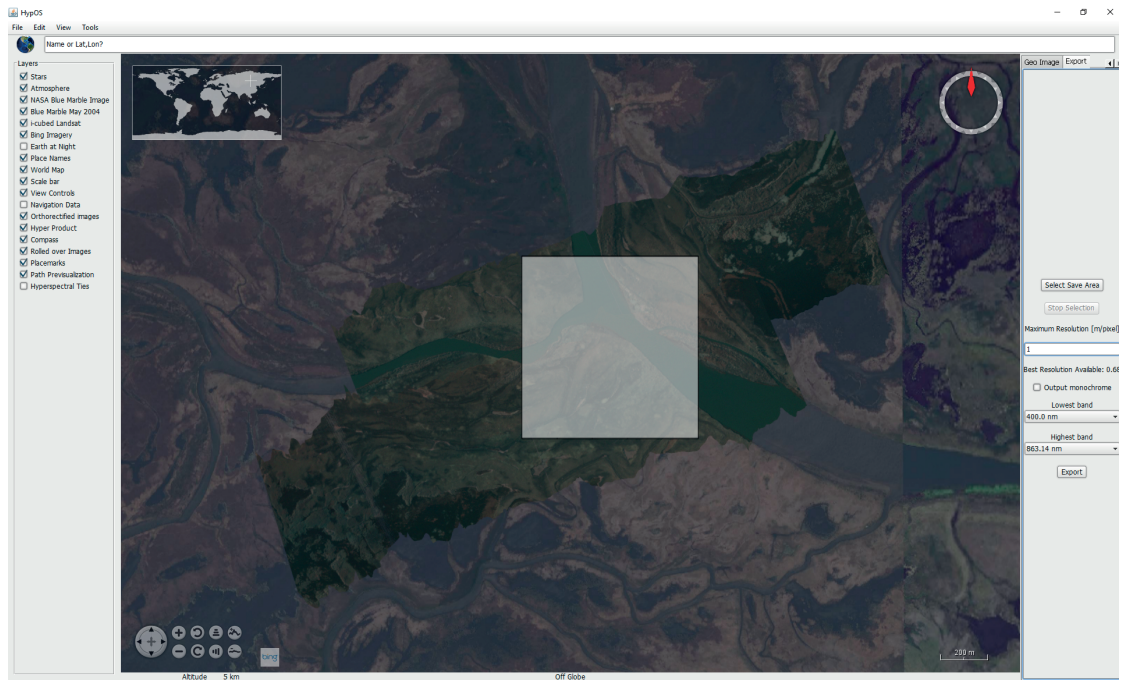


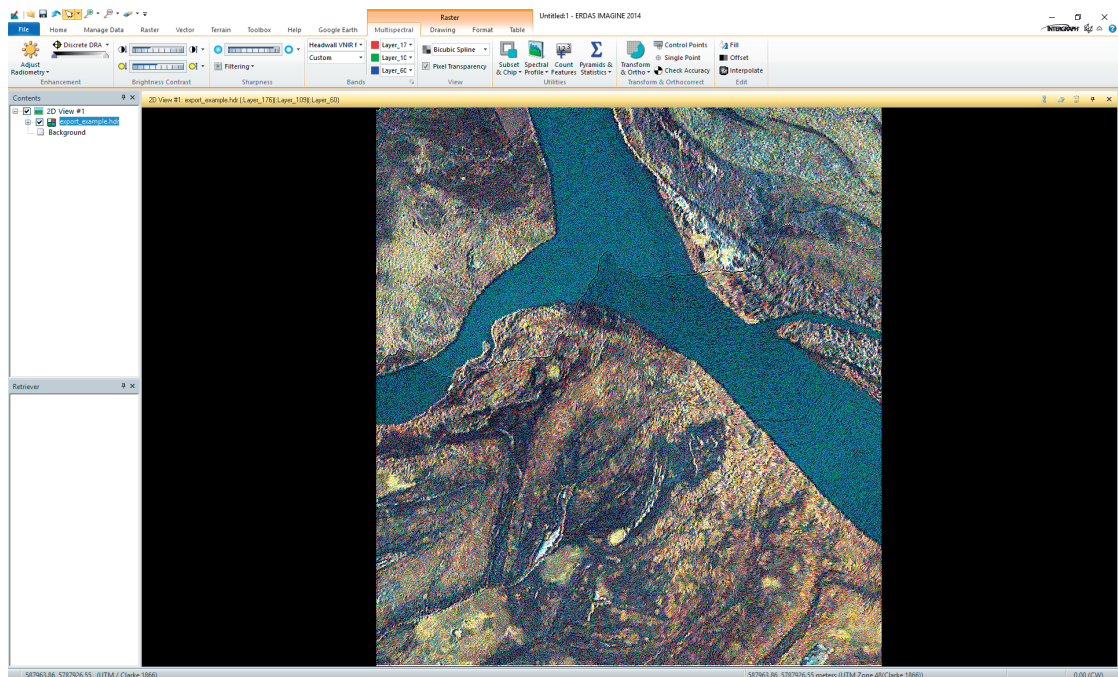
Figure 7.7 Extract from flight 3, corrected using manually input tie points: **(a)** overview of the flight from an isometric view in HypOS; **(b)** extract before correction; **(c)** extract after correction. To put in evidence the effect of the correction, a feature has been highlighted with a red outline.

could grow into an open source software, one of the only open source softwares available to perform orthorectification, calibration and export of pushbroom hyperspectral data.

7.6. HypOS Scientific Value and Use in Research



(a)



(b)

Figure 7.8 Example of (a) export of a mosaic from HypOS and (b) subsequent visualisation in ERDAS Imagine.

Data Analysis Part IV

8 Applications of the Calibrated Léman-Baïkal Data

8.1 Estimation of the Concentration in Chlorophyll- α

8.1.1 Spectral Properties of Chlorophyll- α

The primary uses of hyperspectral data in water quality assessment are the estimations of the levels of chlorophyll- α and turbidity of the water. Chlorophyll- α is known to absorb significantly radiations in the range 660 nm - 690 nm [19]. This property is one of the corner stones of the use of airborne hyperspectral remote sensing to study large lakes. As can be seen in our radiometric calibration results (Section 5.2), in the range 660 nm - 690 nm, some points show a plateau while others exhibit smaller values than in neighbour bands. This phenomenon is closely correlated with the concentration of chlorophyll- α . To take advantage of this property, various formulas related to this concentration have been proposed. Matthews [92] has published a review of all the formulas existing in the literature: most of them consist of a band ratio with a band in the red region of interest and another red further in the near infrared. For instance, Mittenzwey et al. [95] state that the ratio $\frac{\rho_{rs}(705nm)}{\rho_{rs}(670nm)}$ is strongly correlated ($r > 0.98$) to the ground measurements of concentration, and propose a regression model to estimate the concentration as a function of this ratio. Gons et al. [45] have found an empirical correlation between the chlorophyll concentration and the fluorescence line height in oligotrophic lakes. Other formulas all follow the same principle of using a band around 670 nm and another one around 710 nm.

8.1.2 Chlorophyll- α Concentration in the Rhône Delta

Remote sensing was already used to study chlorophyll and phytoplankton at larger scales with spaceborne sensors [17, 72]. The purpose of the use of airborne measurements is to map these quantities with a much better resolution (1 m per pixel).

In Section 5.2, our calibrated water reflectance measurements in the Rhône Delta in April 2015 have been given. The data has been orthorectified using HypOS. The resulting calibrated mosaic is given in Figure 8.1.

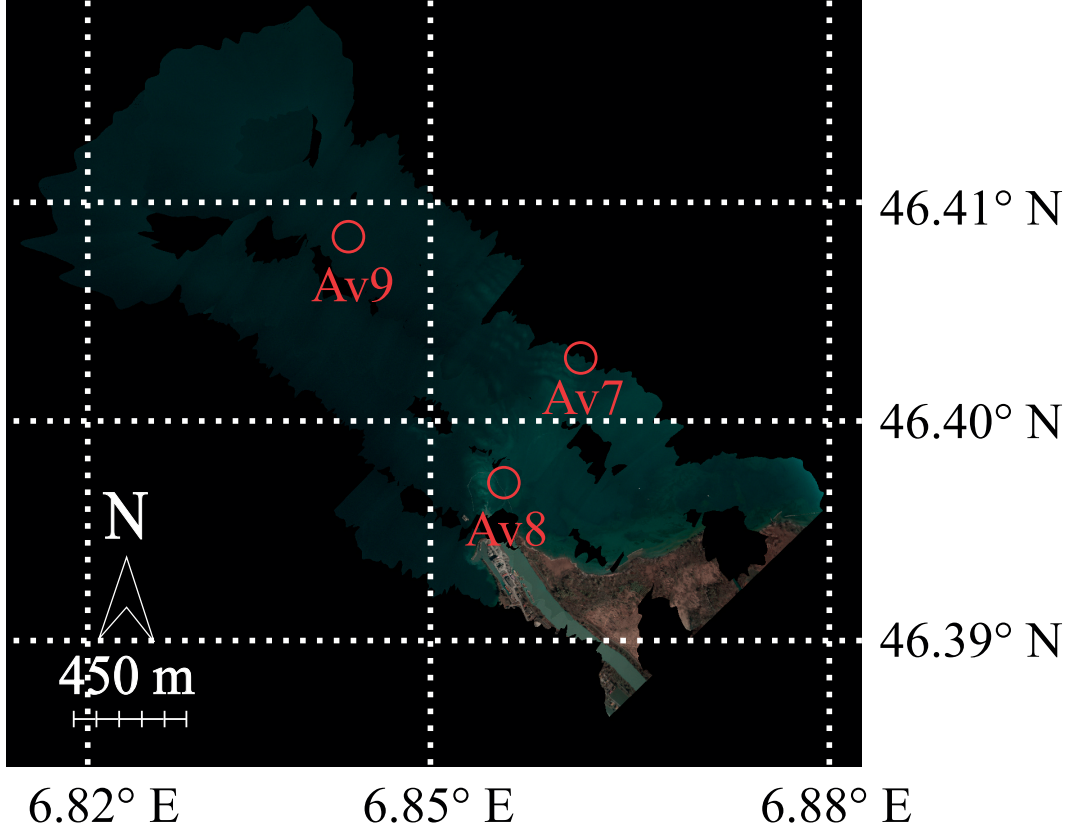


Figure 8.1 Hyperspectral mosaic produced in the Rhône Delta of Lake Geneva, 21 April 2015.

To produce a chlorophyll- α map, we use the formula given by Equation 8.1 (see [44] for reference).

$$chl_{\alpha} \propto \rho_{rs}(750nm) \left(\frac{1}{\rho_{rs}(670nm)} - \frac{1}{\rho_{rs}(710nm)} \right) \quad (8.1)$$

The proportionality coefficient, called β , can be estimated using the ground measurements provided by our colleagues of the Limnology Laboratory of EPFL. In the points Av7, Av8 and Av9 (shown on Figure 8.1), the concentration in chlorophyll- α was measured from water samples. Together with the corresponding image values in the mosaic, they are reported in Table 8.1.

Calling $chl_{\alpha,i}, i \in [1,3]$ the three concentrations measured and $imval_i, i \in [1,3]$ the corresponding image values, the best proportionality coefficient β minimises $\sum_{i=1}^3 (chl_{\alpha,i} - \beta imval_i)^2$,

hence $\beta = \frac{\sum_{i=1}^3 chl_{\alpha,i} imval_i}{\sum_{i=1}^3 imval_i^2} \simeq 4.13 \mu g/l$. The map produced is shown on Figure 8.2.

	Concentration [$\mu\text{g/l}$]	Image Value [Scalar]
Av7	3.1	0.74
Av8	2.6	0.67
Av9	3.2	0.75

Table 8.1 Concentration in chlorophyll- α and image values in the mosaic, for the three points of interest during our experiments in the Rhône Delta of Lake Geneva, 21 April 2015.

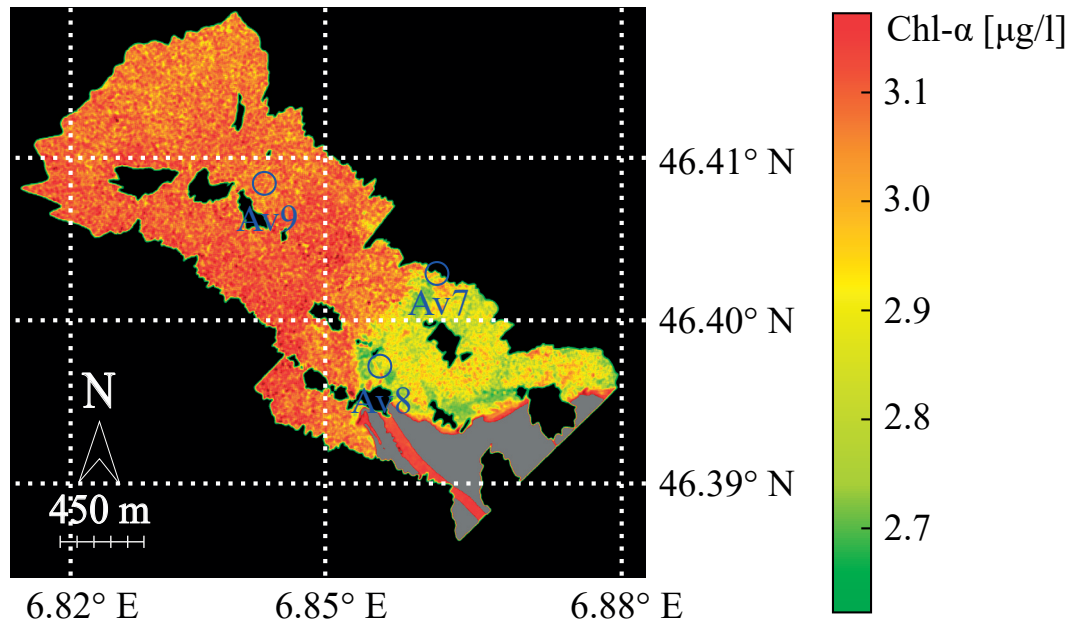


Figure 8.2 Chlorophyll- α concentration map in the Rhône Delta of Lake Geneva, 21 April 2015. Grey areas are land, excluded from the processing.

The map created shows clear patterns of distribution of chlorophyll- α close to the coast. In particular, the concentration is high until 50 m away from the shore, and then decreases in the East part of the delta, while there is a significant increase when going towards the inner part of the lake at the West. Interpretation of this map is beyond the scope of this thesis, and is the responsibility of the Limnology Laboratory of EPFL.

8.2 Study of Baikal Data

The work presented in this Section is only partially ours. The aim is to show which use of the calibrated and orthorectified data was made by our partners in the Léman-Baikal project.

8.2.1 Filtering of Total Suspended Matter in the Delta

The Selenga Delta of Lake Baikal is of high interest in the scientific study of the health of the lake. This is where the Selenga river falls in the lake. Large quantities of sediments are

transported by the river towards the lake; the morphology of wetlands and channels in this area determines how the waters are filtered (from metals, in particular) before arriving in Baikal Lake. For this reason, our airborne acquisitions in Russia have been primarily focused on the delta, with nearly the whole delta (approximately 1000 km²) covered by ultralight plane flights during the two campaigns, in summer 2014 and summer 2015. This data has been calibrated and orthorectified using HypOS. The resulting mosaics were used by Mikhail Tarasov, from Moscow State University, to map small yellow pond lily, reed and pondweeds with watermilfoil [124]. Chalov et al. [24], our colleagues in the project as well, derived the Total Suspended Matter (TSM) from our hyperspectral images (Figure 8.3).

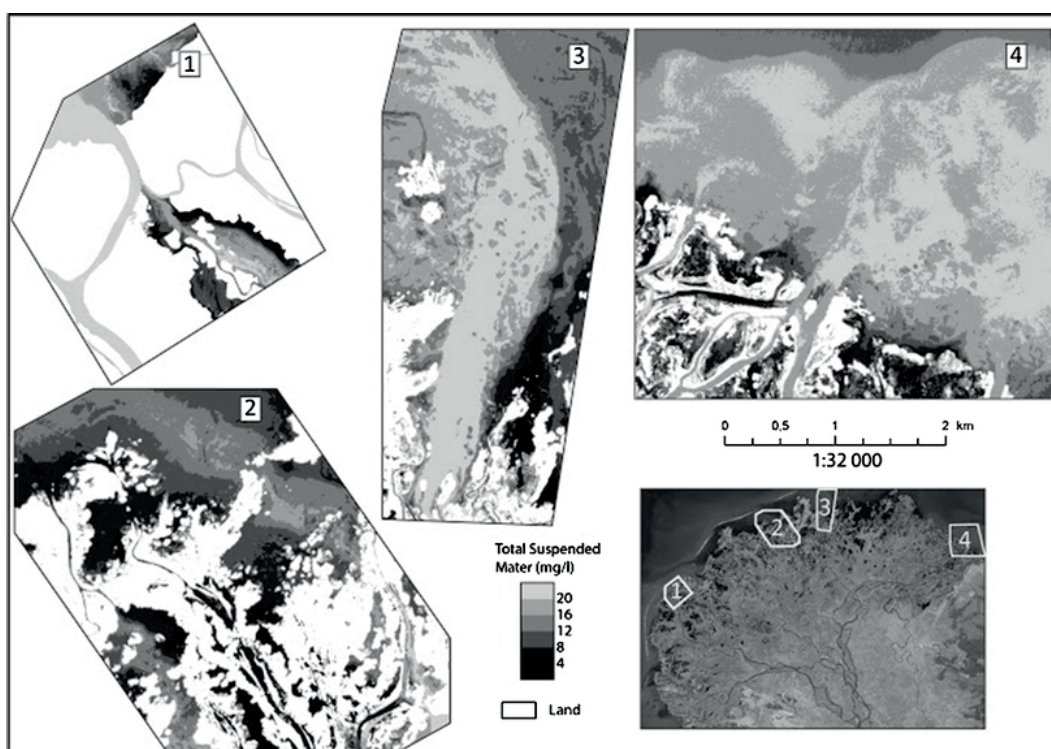


Figure 8.3 (Copyright © Springer 2017) Total suspended matter maps in four areas of the Selenga Delta. The maps were processed from our calibrated hyperspectral data.

The main conclusions of these studies are that the rise of the waters in the delta (0.7 m) is due to the retention of matter by the wetlands and the streams; the changes in morphology of wetlands and streams greatly affect the effectiveness of the retention, which is crucial since a large part of heavy metals (Al, Cd, Cu, Pb, and Zn) flowing down the Selenga are filtered by the delta before reaching the lake.

8.2.2 Other Related Works

Using airborne and ground data acquired in Baikal, colleagues of the Geodetic Engineering Laboratory developed a new atmospheric correction algorithm entirely image-based [31],

like QUAC. This algorithm used a simplified version of the radiative transfer equation, and estimates the atmospheric effects considering they are essentially high frequency effects in the spectra. This algorithm is proved more reliable than QUAC for two points of interest which spectrums were acquired on the ground in the region of Baikal.

As already mentioned in Chapter 7, a similar hyperspectral system as ours has been used on a drone designed by colleagues from the University of Brest [60]. They have used HypOS extensively to orthorectify data acquired over coastal areas or fields in the surroundings of Brest, France.

9 Large Scale Ice Coverage Monitoring with Satellite Imagery

Note: parts of this section were extracted from our article Icy Lakes Extraction and Water-Ice Classification using Landsat 8 OLI Multispectral Data [5], in the International Journal of Remote Sensing. They are copied in accordance with the Creative Commons Attribution-Non-Commercial License.

The ice coverage of large lakes is a very impactful phenomenon for their local ecosystems. The formation and the melt of the ice strongly influence the organic life of the lakes, like the carbon cycle [11] or the phytoplankton dynamics [39, 117], but also act as indicators of climate change [57, 81]. Consequently, it is of interest to study the evolution of the ice coverage of large lakes, in terms of spatial distribution, ice characteristics (structure, temperature, radiative properties, optical properties) and temporal evolution.

The ice coverage of large lakes is usually monitored using remote sensing, and in particular satellite images, since they cover very large areas. Satellite data is essentially divided in two categories: visible and/or infrared (near, shortwave or thermal) spectral data, and Radar data. In the lake ice remote sensing literature, the latter is heavily favoured: indeed, microwave Synthetic Aperture Radar (SAR) can penetrate clouds [42], whereas visible and near infrared data are affected by clouds. SAR imagery can even be used not only to discriminate ice from open water, but also to classify ice according to its structure [102, 87]. However, in order to monitor the ice coverage over short periods of time, one cannot rely on only one satellite data source. The satellites equipped with a SAR sensor most commonly used in the literature have an important repeat cycle: 12 days for Sentinel-1, 24 days for RADARSAT-2, and 35 days for ENVISAT. Overlapping images sensed from different orbits can enhance the temporal resolution of the images. Another way to increase temporal resolution is to merge data from different sources, not only from SAR sensors but also multispectral sensors. In particular, Landsat multispectral data can complement the SAR data nicely for studies related to water and ice [104, 42, 58]. In this regard, we are interested in designing a water-ice discrimination procedure for Landsat 8 Operational Land Imager (OLI) images, with the further perspective of merging the resulting classifications with similar classifications using SAR data to obtain a high temporal resolution monitoring of the ice coverage of glacial lakes.

We present here a procedure to extract the bodies of icy lakes and perform water-ice classification in these bodies, using new radiometric indexes and supervised classification methods on images sensed by the Landsat 8 OLI. This chapter is structured as follows: after detailing the pre-processing of the data in Section 9.1, we explain our methodology to extract the borders of the lakes in the Landsat images, relying on a new index called Icy lakes Index (ILI) to segment the lake area (whether it is fully or partly frozen, or solely open water) in Section 9.3. The performance of the ILI is tested and compared with state-of-the-art indexes, in terms of Kappa coefficient, commission and omission errors. In Section 9.4, we present our water-ice classification algorithm, using a decision tree relying on radiometric and texture features of the Landsat 8 OLI multispectral images. In Section 9.5, the results of this classification algorithm are finally assessed by comparing the output classifications to manually digitised reference data, but also to concurrent data from Sentinel-1 SAR images.

9.1 Landsat 8 Pre-Processing

The Landsat 8 images are provided with band-wise gains and offsets, as well as the scene sun elevation angle, to perform calibration to Top-Of-Atmosphere (TOA) reflectance. In our study, we will work with the TOA reflectance; the reason we wish to design a classification algorithm independent of any atmospheric correction is that we work on a large variety of lakes, located at very different places of the globe, and at different altitudes. The need to know the water vapour and aerosols properties, or the necessity of using a third-party software to perform atmospheric correction, can be an important constraint for the end user of the algorithm. Furthermore, this paper proves the classification procedure to be efficient even in the absence of atmospheric correction.

9.2 State of the Art

Our problem is the discrimination between ice and open water using satellite images. In the following, we list existing contributions in the domain of water-ice classification using satellite Radar and multispectral remote sensing. Most known contributions in the domain of water-ice classification use SAR images, so the first part of the state of the art is dedicated to the SAR processing. In the second part, we refer to various studies of water and ice bodies extraction, as well as classification, using multispectral data, with a special emphasis on the radiometric indexes and the machine learning methods used.

9.2.1 Ice-Water Discrimination using SAR

Satellite SAR images allow to study the ice dynamics and the ice structure of large lakes very efficiently. Applications include the monitoring of ice formation and decay [104, 85], the characterisation of the ice structure [102, 87, 86], but also water-ice discrimination. Many of these classification methods use local texture properties: [68] first segment SAR images,

and then classify them according to a local autocorrelation criterion. [27] have developed an interface for the MAGIC algorithm, which itself is based on the work of [141]: the images are first oversegmented using a watershed algorithm; the segmented regions, represented by a region adjacency graph, are iteratively merged/discriminated according to various criteria such as average region value, texture and shape. This process, known as Iterative Region Growing by Semantics (IRGS), is reused by [84], together with a Support Vector Machine (SVM) algorithm based on the texture features of the HH SAR images. [143] also use texture properties, namely the grey-level co-occurrence matrix and its derived properties [55] and classify the RADARSAT-2 images using these features and training the classification with a SVM algorithm.

Other works, where the classification procedure does not use texture properties, include [113, 114], who discriminate classes using a Bayesian minimum distance classifier with features based on the backscatter of HH, HV and VV bands, but also properties from their coherency matrix. [43] determined a decision tree based on the value of the co-polarised ratio of the VV and HH backscatter coefficients of the ENVISAT ASAR.

9.2.2 Ice and Water Studies using Multispectral Images

The literature largely discusses the problem of extracting open water bodies from Landsat imaging. Some of the first attempts relied on thresholding single band values [12, 91], relying on the low reflectance of water for the longer wavelengths ($> 600nm$). These methods were rapidly proved to be image and application-dependent [38, 131], as others common materials, but also shadowed areas, exhibit very low spectral responses in these wavelengths. Therefore, multi-band processing must be performed to solve segment water bodies efficiently. The most common solution is the use of indexes, based on algebraic operations (like band ratios) on the bands of the Landsat images. The Normalised Difference Water Index (NDWI) was the first index designed to enhance the differences between water and other materials [93]. It was later refined into the Modified Normalised Difference Water Index (MNDWI) by [138] which better achieved the initial purpose of NDWI. To tackle the problem of ice/snow being retrieved by the MNDWI, [119] proposed a method combining machine learning with the Water Ratio Index (WRI). Finally, to further mitigate the effects of clouds and shadows, [37] proposed a new index called Automated Water Extraction Index (AWEI), that uses the low reflectance of water in both the near infrared (NIR) and the shortwave infrared (SWIR) to achieve a better classification. [75] train decision trees using the OLI TOA reflectances, the NDWI and the MNDWI as features, to extract lake and river bodies from Landsat 8 images.

Retrieval of mixed water/ice bodies is also discussed in the literature. The MNDWI itself, combined with non local active contour (NLAC) techniques, was used by [25] to extract the contours of glacial lakes in Tibet Plateau in Landsat 8 OLI images. A similar study by [77] also used the MNDWI as well as the AWEI. Other modified versions of the NDWI were tested for either the extraction of water bodies in Antarctica [61] or lake bodies in the same context [63]. [62] reference all the methodologies known to extract cryospheric lake bodies. They separate them into three categories: feature extraction using pixel-based and object-based

classification, and spectral index ratios, some of which are tested in Section 9.3.1. [107] map water and ice in supraglacial lakes of the Everest using a decision tree involving multiple radiometric indexes for ASTER images. [139] delineate water streams in WorldView 2 images by multithresholding images processed with another modified version of NDWI, coined $NDWI_{ice}$. Landsat data is also used for icy lakes extraction [21, 66] in Greenland, just like MODIS [122, 116]. However, to the best of our knowledge, no classification technique for Landsat images was proved to work for a variety of large icy lakes.

9.3 Extraction of the Lake Body

For each lake image on which we wish to perform water-ice classification, we first need to demarcate the lake area. We refer to the binary image where the lake pixels are white, and the rest black, as the "mask" of the lake for the given image. Landsat 8 OLI images are typically 8000×8000 pixels large, outright excluding the possibility of drawing the mask manually. Hence, we need to design an automated algorithm extracting mixed ice/water bodies from Landsat 8 images.

9.3.1 Performance of Existing Indexes

To show the necessity of designing a new radiometric index for discriminating lands from (partially) frozen lakes on Landsat 8 images, we have tested the performance of three of the available indexes in the literature: the MNDWI, the WRI and another version of NDWI from [54] that we call $NDWI_H$. Their formulas are given in Equations 9.1 to 9.3.

$$MNDWI = \frac{(Green) - (SWIR1)}{(Green) + (SWIR1)} \quad (9.1)$$

$$WRI = \frac{(Green) + (Red)}{(NIR) + (SWIR1)} \quad (9.2)$$

$$NDWI_H = \frac{(NIR) - (Blue)}{(NIR) + (Blue)} \quad (9.3)$$

All designations are clarified in table 9.1.

It is to be noted that, while the $NDWI_H$ was designed for applications related to cryospheric lakes, this is not the case for the MNDWI and the WRI, which were originally created to highlight water areas, and not mixed ice/water areas. However, [25], for instance, used the

Band Number	Name	Designation	Wavelengths (μm)
1	Ultra Blue	Ultra_Blue	0.43 - 0.45
2	Blue	Blue	0.45 - 0.51
3	Green	Green	0.53 - 0.59
4	Red	Red	0.64 - 0.67
5	Near Infrared	NIR	0.85 - 0.88
6	Shortwave Infrared 1	SWIR1	1.57 - 1.65
7	Shortwave Infrared 2	SWIR2	2.11 - 2.29

Table 9.1 Landsat 8 bands specification.

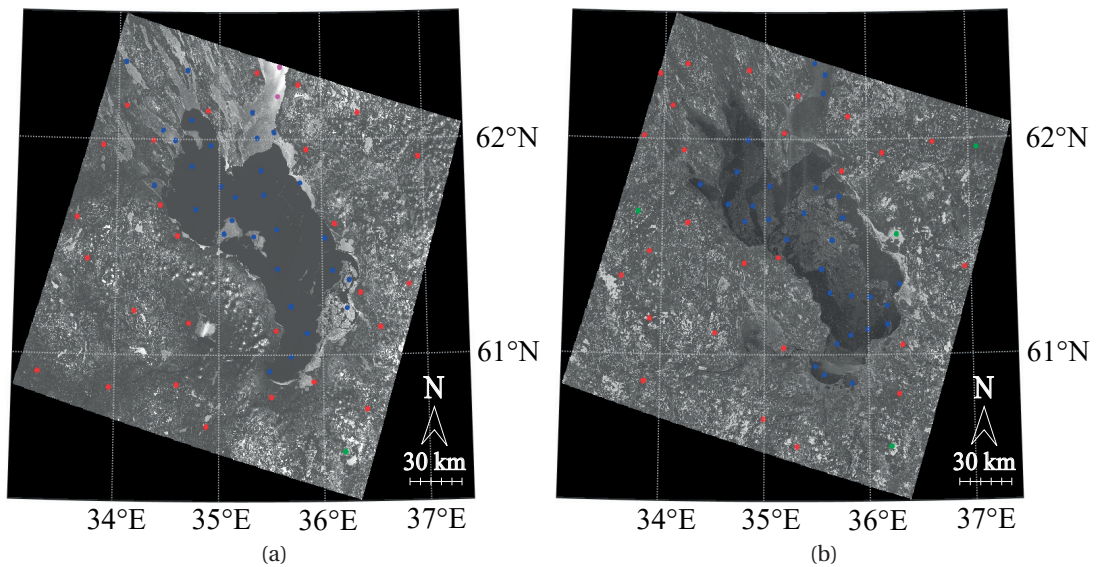


Figure 9.1 Sample points from Lake Onega: **(a)** April 10th, 2014; **(b)** March 12th, 2015. Blue points are open water/ice cover, green points are snow, red points are land, and the two magenta points at the top of **(a)** are ice with crusted snow/with snow cover.

MNDWI with great success to extract glacial lakes, thus making the comparison pertinent; the WRI is proved in the following to also be suitable for this task, to some extent.

The purpose of the formulas given in Equations 9.1 to 9.3 is to benefit from the high reflectance of water in the blue and the green and its low reflectance in the near and shortwave infrared, while the vast majority of ground materials (vegetation, soil and built structures) have higher reflectance in the near and shortwave infrared. Such logic does not apply similarly to ice, which can have a significant NIR reflectance. We highlight this problem by computing the performance of the three indexes on two Landsat images of Lake Onega (Republic of Karelia, Russia) on April 10th, 2014 and March 12th, 2015. For each image, 60 sample points, including open water, very clear ice, opaque ice, ice with crusted snow, snow and land materials, had their scores computed for each index. These points were chosen arbitrarily, to represent a wide variety of materials and geographical locations. They are represented on Figure 9.1.

The scores have been plotted horizontally against their classes (land, snow, or lake). The snow

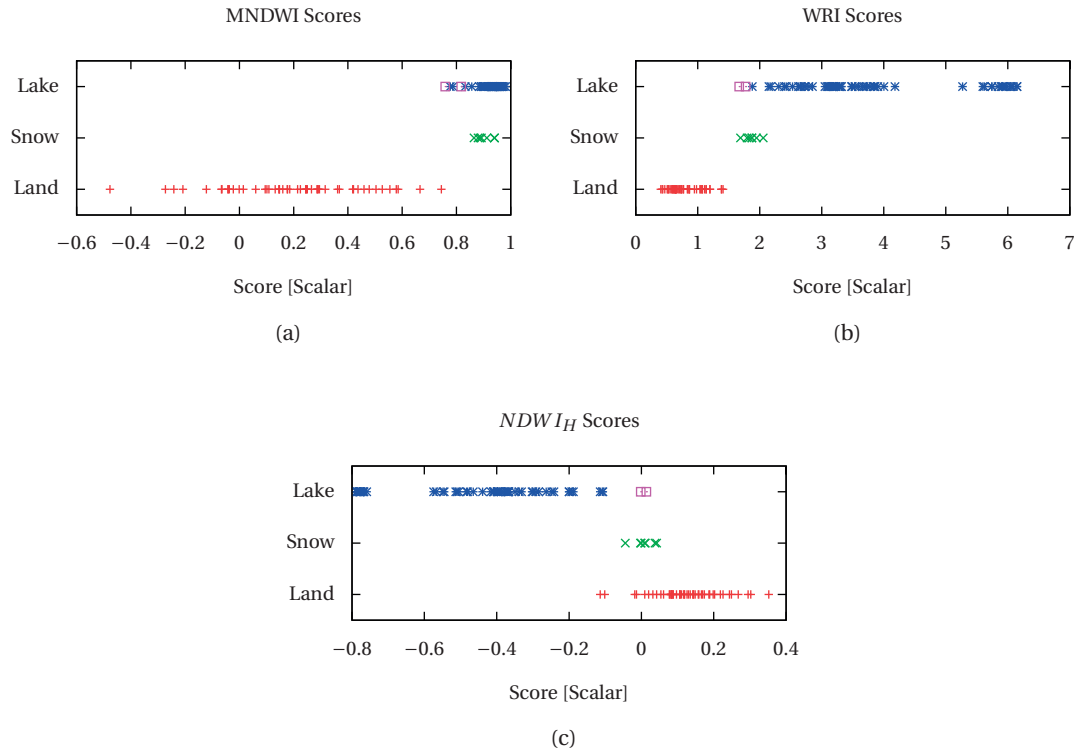


Figure 9.2 Scores of the three tested indexes for the 120 sample points.

class includes all snow pixels on the ground; the lake class includes open water features, ice cover features, and mixed snow/ice features. We are looking for the best possible index to separate ice/water features (blue) from land features, including snow (land in red, snow in green). The plots are shown on Figure 9.2. We can make a few remarks about the indexes performances.

- With a threshold of approximately 0.75, the MNDWI would segment ice and water pixels from land pixels rather efficiently. However, the gap between the highest land score and lowest lake score is very small. The reliability of the MNDWI outside our sample points is uncertain.
- The WRI is the index closest to fit our requirements: it separates properly water and ice features from land, with a very clear gap between their scores.
- The $NDWI_H$ relies heavily on the NIR. For this reason, very opaque ice/ice with crusted snow tend to have similar values as land pixels, thus mitigating its efficiency for retrieving frozen lakes bodies.

9.3.2 Icy Lakes Index

Snow having the same spectral response whether it covers land or a frozen lake, it is difficult to classify the scene properly when the snow cover is significant. The case of lakes covered with snow is discussed in Section 9.3.4. In the present section, we explain our methodology to extract lakes when the snow cover is negligible (which was the case for all the images studied in this chapter, except one).

Taking inspiration from the Water Ratio Index (WRI), we have designed another index that relies on the high reflectance of most land features in the near and shortwave infrared. The purpose of the WRI is to take advantage of the high response of water in the green, and its low response in the infrared (both near and shortwave). In our problem, where ice also has to be retrieved, all classes can present similar reflectances in the visible bands (especially the blue and green bands), while infrared bands discriminate land and water/ice much better. Hence, we use the following index, called Icy Lakes Index (ILI), to segment icy lakes from the rest of the scene in Landsat 8 images (Equation 9.4).

$$ILI = \frac{(Red) + (SWIR2)}{(NIR) + (SWIR1)} \quad (9.4)$$

The rationale of the ILI is the following: common ground materials have a decreasing reflectance from NIR to SWIR1 and from SWIR1 to SWIR2. It is the case of vegetation [130, 49], but also materials used for built-in structure like concrete and asphalt [3]. In addition, this decrease is also observed for optically thick clouds [35]. For all these materials, the ILI is quite low. On the other hand, both ice and water have stable reflectance from SWIR1 to SWIR2, and higher visible (red) reflectance than NIR, SWIR and SWIR2 reflectances [3, 135], making their ILI scores high. The performance of this index has been tested on the same 120 sample points presented in Section 9.3.1. The scores are plotted on Figure 9.3.

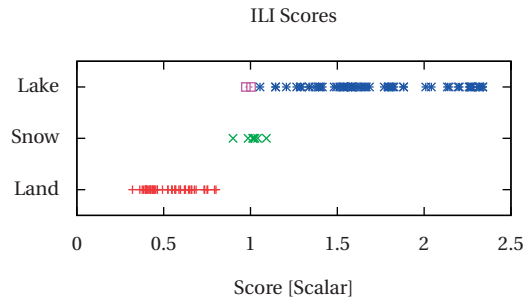


Figure 9.3 *ILI* scores for the 120 sample points.

The ILI clearly separates water/ice features from land features. While the distribution of its scores looks similar to the one of the WRI (Figure 9.2b), the relative gap between the land class and the lake class is higher: the maximum land score is 0.79 for the ILI (1.41 for the WRI) and

Chapter 9. Large Scale Ice Coverage Monitoring with Satellite Imagery

the minimum lake score is 0.97 (1.66 for the WRI), which represents a 18 % relative difference (15 % for the WRI). Therefore, on our sample, a range of threshold (from 0.79 to 0.97) would allow to classify properly lake and non-lake features in a snow-free image. In the next section, we further prove the usefulness of the ILI against state-of-the-art indexes.

9.3.3 Results

The ILI performance at extracting lake bodies has been tested against the MNDWI, the WRI and the $NDWI_H$, on five images, each one representing a different lake. These images are marked as "used for mask extraction" in Table 9.2.

Lake	Central Point	Country	Mean Elevation (m)	Date	Used for Mask Extraction	Water/Ice Extraction Sampling	Water-Ice Discrimination Sampling
Great Bear Lake	66.08°N, -120.83°E	Canada	160	2013-06-27	X		X
Great Slave Lake	61.58°N, -114.23°E	Canada	160	2015-05-22	X		
Lake Amadjuak	64.88°N, -71.15°E	Canada	110	2016-08-08 2016-08-24	X		
Lake Ladoga	60.81°N, 31.51°E	Russia	5	2015-04-11			
Lake Onega	61.62°N, 35.56°E	Russia	30	2014-04-10 2015-03-12	X	X X	X X
Lake Uvs	50.30°N, 92.72°E	Mongolia	760	2015-05-16 2014-12-23	X		

Table 9.2 List of Landsat 8 images used in our study.

For each image, the binary classification of each index has been computed. The thresholds were chosen according to Figures 9.2a, 9.2b, 9.2c and 9.3: pixels were classified as water/ice or neither according to the criteria > 0.75 for MNDWI, > 1.5 for WRI, < -0.1 for $NDWI_H$ and > 0.95 for ILI. Only the biggest blob of each binary image is retrieved. The overall extraction for all five lakes, as well as the zones used for the quantitative results, are shown in Figure 9.4.

It is very difficult and time-consuming to manually label the pixels of Landsat 8 images due to their sizes. Hence, we have focused on quantifying the results in specific areas of the lakes for which we have manually labelled the pixels as either "water/ice" or "other". We have selected eight zones, represented in Figure 9.4, to compute quantitative results. These zones were chosen according to two criteria: they represent various surfaces (water, ice, vegetation, built

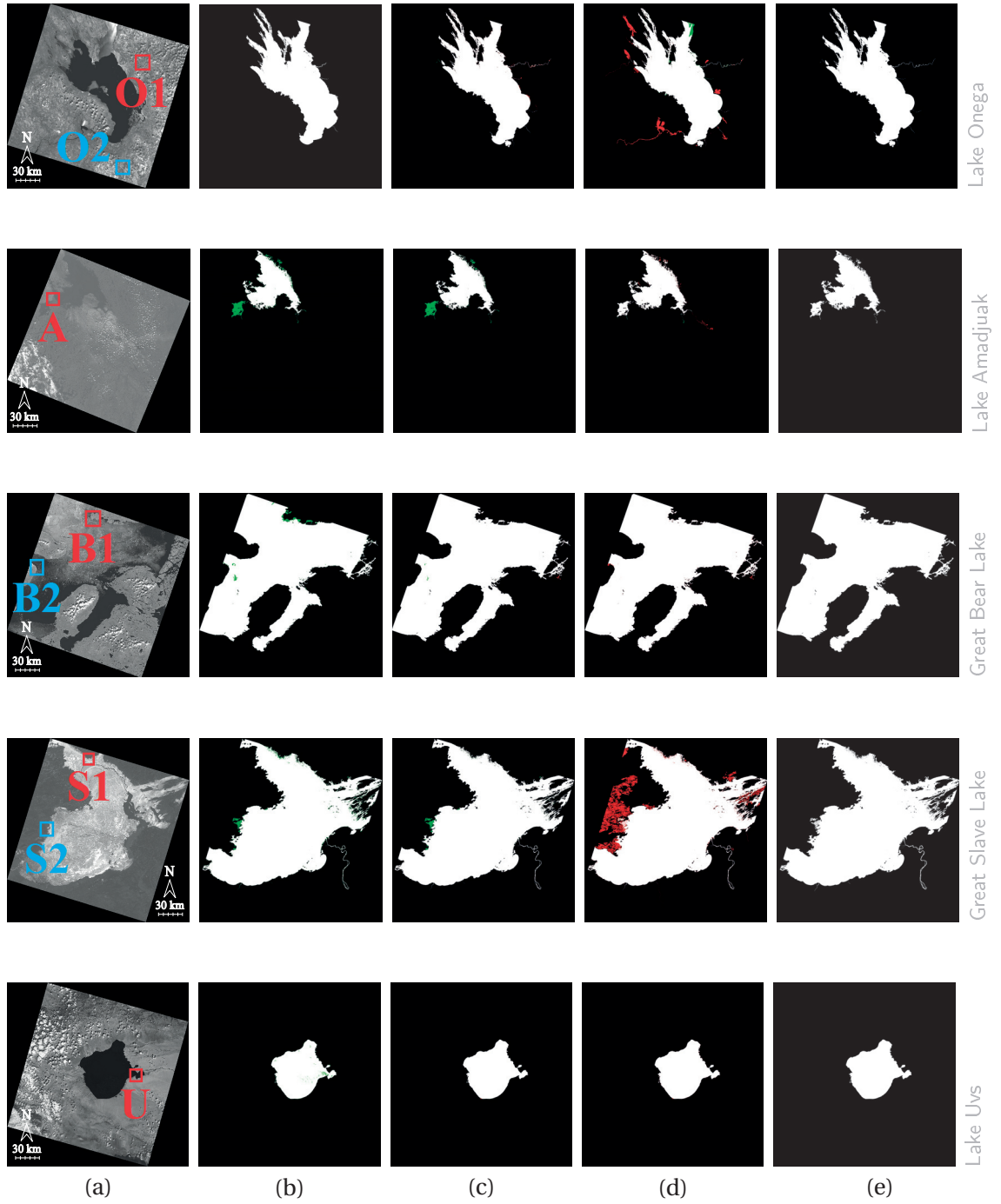


Figure 9.4 Comparison of the performances of the indexes for lake extraction on the 5 lakes. (a) is the original NIR image with enhanced brightness; (b) is the MNDWI binary classification, (c) is the WRI, (d) is the $NDWI_H$ and (e) is the ILI. The red features are pixels retrieved by the corresponding index and not by the ILI; the green features are negative for the corresponding index and positive for the ILI. The zones used for quantitative results are tagged in the original images.

structures, clouds) all of which have different spectral signatures; these zones also appeared to discriminate the indexes the most in the overall classifications (Figure 9.4). Results were characterised by the resulting Kappa coefficients and errors, and by the stability of the optimal threshold for each index.

Accuracies and Errors

The Kappa coefficient, the commission and the omission errors have been computed for the four indexes, binarised with three different fixed thresholds each. As pointed out by [65] and [37], high variability of the optimal threshold for a given index makes its use harder in classifications tasks, so we start by computing the results in fixed, narrow ranges of thresholds suggested by Figures 9.2a, 9.2b, 9.2c and 9.3; for optimal thresholds (given later on Figure 9.8) potentially outside of these ranges, Kappa, commission and omission errors were also computed, and are obtainable by contacting the corresponding author of the present article. Results are given in Tables 9.3, 9.4 and 9.5. The corresponding images for all indexes (using the best of the three thresholds in terms of Kappa coefficient achieved) are shown in Figures 9.5, 9.6 and 9.7.

The zones O1, O2 and B2 contain a significant proportion of clouds. The WRI and the $NDWI_H$ classifications are heavily impacted by the clouds, whereas the ILI and the MNDWI perform much better in cloudy conditions. The MNDWI, however, does not perform well on ice-covered parts, as shown by the results in zones B1 and U. The only zone where the ILI was significantly outperformed was zone S2: this is a marshy area for which we did not label the swamps as positive in our reference image. Swamps contain vegetation and water; the high reflectance of the vegetation in the infrared bands (NIR, SWIR and SWIR2) makes the MDWNI and the WRI classify swamps as not water/ice, and pushes the $NDWI_H$ to classify the corresponding pixels as water/ice. The ILI is balanced between these two directions and achieves a Kappa of 0.939, while the WRI reaches a Kappa of 0.994 (Table 9.5). In zones O1, B2 and S1, the ILI performs better than the three other indexes tested, with Kappa coefficients of 0.889 in O1 (second best is the MNDWI with 0.685), 0.991 in B2 (second best is the WRI with 0.983) and 0.989 in S1 (second best is the WRI with 0.976). The ILI is marginally better in zone U, with a Kappa coefficient of 1 (at the three significant digits precision) against 0.998 for the WRI, and marginally outperformed by the MNDWI ($\kappa = 0.731$, against 0.712 for ILI) in zone O2, and by the $NDWI_H$ in zones A and B1 ($\kappa = 0.989$ and 0.991 respectively, against 0.978 and 0.989 for ILI). Across the 8 zones studied, the ILI is the only of the four indexes that performs good classifications consistently, whereas other indexes show their limitations for clouds (WRI, $NDWI_H$), ice (MNDWI) and shores (MNDWI, $NDWI_H$).

Threshold Variability

The optimal threshold for each index and each zone has been computed, as the threshold that maximises the Kappa coefficient between the classification and the reference data. Results are

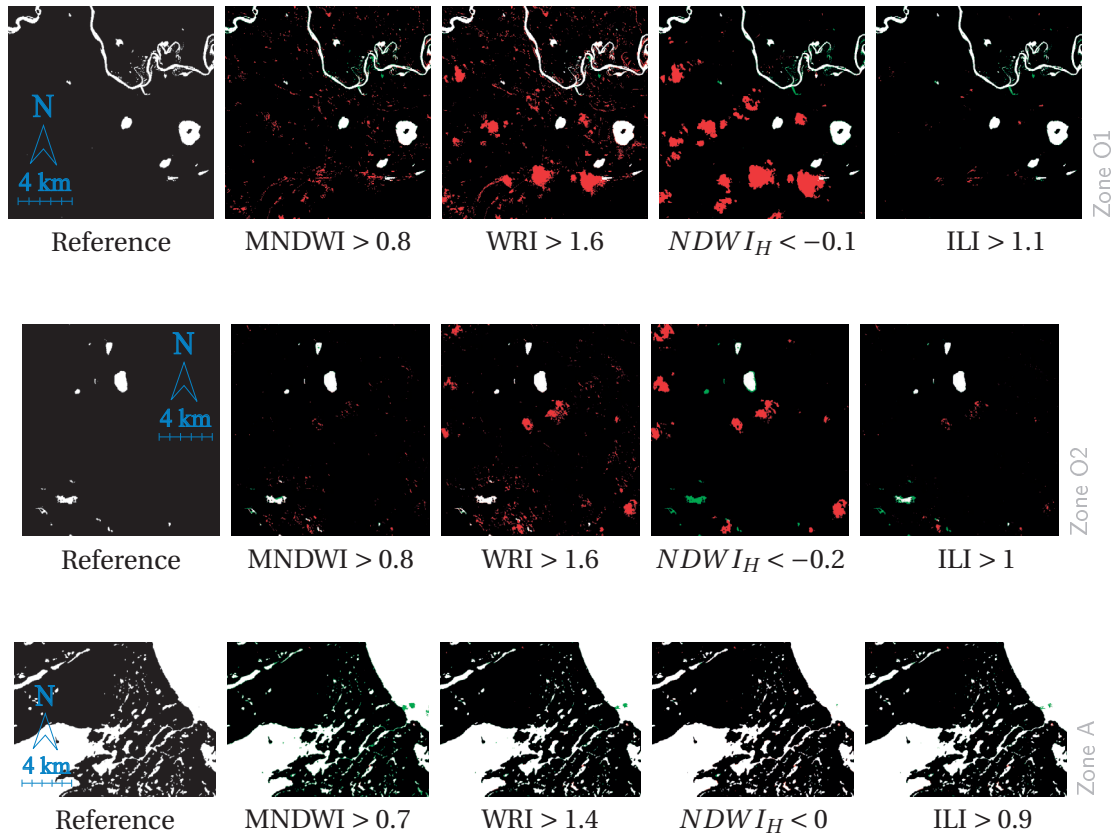


Figure 9.5 Comparison of the performances of the indexes in zones O1, O2 and A. The red features are false positives; the green features are false negatives.

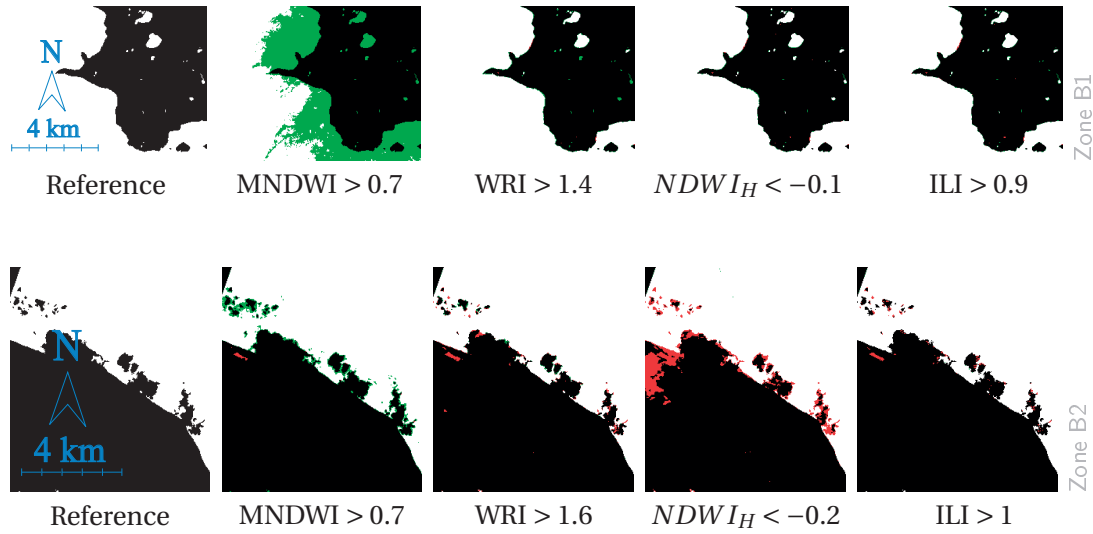


Figure 9.6 Comparison of the performances of the indexes in zones B1 and B2. The red features are false positives; the green features are false negatives.

reported on Figure 9.8.

The standard deviation of the optimal threshold was 0.33 for the MNDWI, 0.57 for the WRI, 0.10 for the $NDWI_H$ and 0.11 for the ILI. Unlike the MNDWI and the WRI, the ILI performs very consistently across all the test zones with a fixed threshold of 1 (see Tables 9.3, 9.4 and 9.5); its optimal threshold oscillates between 0.8 and 1.1, that is, with a much lower amplitude than the MNDWI and the WRI. Only the $NDWI_H$ shows a similar stability. However, the $NDWI_H$ also showed poor classification results in several zones (see Section 9.3.3). As a synthesis of this section, the ILI outperforms other indexes in four test zones, and showed its limitation only in Zone S2 (containing marshy areas); the ILI is also very stable threshold-wise, unlike two of the three other indexes tested, making it very appropriate for use with classification trees [65].

9.3.4 Extraction of Lakes Covered by Snow

Continuous snow cover at the borders of the lakes makes the identification of these borders very difficult: it is the case for Lake Uvs in the Landsat 8 OLI image sensed on December 23rd, 2014 (Figure 9.9a). To overcome this issue, the mask of the lake can be extracted from an OLI image of another date, and translated in the reference frame of the image of interest using UTM coordinates. The result is shown on Figure 9.9b.

While the mask transferred using UTM coordinates is a good starting point, it cannot be considered as a perfect reference because:

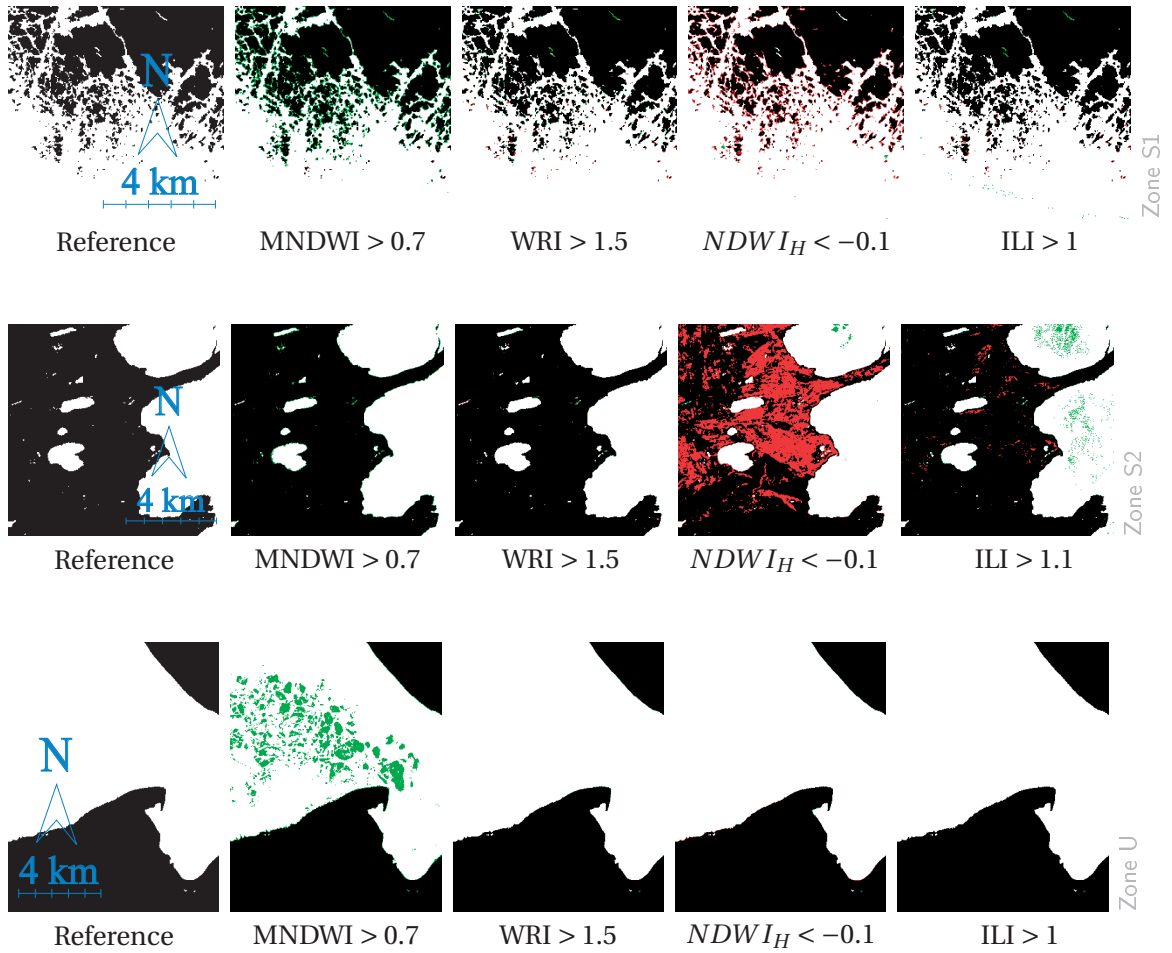


Figure 9.7 Comparison of the performances of the indexes in zones S1, S2 and U. The red features are false positives; the green features are false negatives.

Chapter 9. Large Scale Ice Coverage Monitoring with Satellite Imagery

	MNDWI			WRI			$NDWI_H$			ILI		
Threshold	0.70	0.75	0.80	1.4	1.5	1.6	0	-0.10	-0.20	0.9	1	1.1
Zone O1												
κ	0.431	0.539	0.685	0.331	0.413	0.509	0.468	0.481	0.474	0.53	0.83	0.889
Water/Ice Comm. Error (%)	68.43	58.08	39.39	76.56	70.60	62.59	66.27	62.75	60.31	61.16	25.17	5.62
Water/Ice Omi. Error (%)	9.54	12.80	16.81	1.46	2.12	3.30	1.11	18.25	31.37	0.24	4.75	15.07
Other Comm. Error (%)	0.48	0.61	0.78	0.08	0.11	0.16	0.06	0.88	1.48	0.01	0.22	0.69
Other Omi. Error (%)	8.96	5.52	2.47	14.71	10.74	7.39	8.88	6.29	4.76	7.18	1.46	0.23
Zone O2												
κ	0.358	0.517	0.731	0.214	0.291	0.407	0.194	0.222	0.235	0.409	0.712	0.699
Water/Ice Comm. Error (%)	77.22	63.96	37.62	87.05	82.08	73.54	87.48	85.08	83.18	73.39	30.61	11.91
Water/Ice Omi. Error (%)	1.71	3.27	10.78	0.30	0.71	1.60	36.57	44.63	53.40	0.97	26.27	41.73
Other Comm. Error (%)	0.02	0.04	0.12	0.00	0.01	0.02	0.42	0.51	0.60	0.01	0.29	0.46
Other Omi. Error (%)	3.68	1.90	0.59	7.41	5.02	3.02	4.90	3.49	2.55	3.02	0.36	0.09
Zone A												
κ	0.932	0.924	0.909	0.972	0.969	0.966	0.989	0.984	0.975	0.978	0.969	0.963
Water/Ice Comm. Error (%)	0.10	0.08	0.07	0.29	0.28	0.26	0.95	0.41	0.26	0.35	0.29	0.23
Water/Ice Omi. Error (%)	8.62	9.69	11.64	3.39	3.77	4.13	0.55	1.65	3.02	2.56	3.70	4.57
Other Comm. Error (%)	4.29	4.80	5.71	1.74	1.93	2.11	0.29	0.85	1.55	1.32	1.89	2.33
Other Omi. Error (%)	0.05	0.04	0.03	0.15	0.14	0.13	0.50	0.21	0.13	0.18	0.14	0.12

Table 9.3 Errors and κ for the four indexes, in Zones O1, O2 and A.

- the georegistration of Landsat 8 OLI images is not perfect; significant shifts can appear when co-registering one image onto another.
- lake borders are dynamic, they are subject to changes over long periods of time.

9.3. Extraction of the Lake Body

	MNDWI			WRI			$NDWI_{IH}$			ILI		
Threshold	0.70	0.75	0.80	1.4	1.5	1.6	0	-0.10	-0.20	0.9	1	1.1
Zone B1												
κ	0.552	0.409	0.295	0.984	0.981	0.971	0.99	0.991	0.593	0.989	0.955	0.6
Water/Ice Comm. Error (%)	0.00	0.00	0.00	0.08	0.06	0.05	0.75	0.11	0.07	0.13	0.07	0.07
Water/Ice Omi. Error (%)	40.91	55.21	67.03	1.30	1.57	2.44	0.08	0.66	36.81	0.78	3.79	36.21
Other Comm. Error (%)	35.55	42.67	47.47	1.72	2.07	3.19	0.10	0.88	33.18	1.04	4.86	32.82
Other Omi. Error (%)	0.00	0.00	0.00	0.11	0.08	0.06	1.02	0.15	0.06	0.17	0.09	0.06
Zone B2												
κ	0.954	0.931	0.656	0.96	0.976	0.983	0.814	0.878	0.919	0.95	0.991	0.98
Water/Ice Comm. Error (%)	0.20	0.16	0.10	4.03	2.24	1.35	16.87	11.71	8.04	5.12	0.96	0.35
Water/Ice Omi. Error (%)	4.74	7.24	36.00	0.13	0.27	0.44	0.00	0.00	0.02	0.00	0.01	1.79
Other Comm. Error (%)	3.92	5.88	23.67	0.11	0.24	0.38	0.00	0.00	0.02	0.00	0.01	1.52
Other Omi. Error (%)	0.16	0.13	0.05	3.61	1.96	1.18	17.47	11.42	7.53	4.64	0.83	0.29

Table 9.4 Errors and κ for the four indexes, in Zones B1 and B2.

For the image of Lake Uvs (December 23rd, 2014), which was the only image where snow prevented the ILI from working properly, the quality of the mask translated from the image of May 16th, 2015 was tested by comparing the manually drawn reference border to the computed border in Zone U. The result is shown on Figure 9.9c. Comparison between the resulting classification lake/non-lake gave a Kappa coefficient of 0.987; the local divergence between the two borders ranged from 0 to 4 pixels (120 m). An active contour algorithm [69] was tested on the Normalised Difference Snow and Ice Index [137] to refine the delineation, but achieved no significant improvement: the snow cover blurs the borders of the lake, making it difficult to delineate them properly, even manually. The mask translated via UTM coordinates is acceptable for this image of Lake Uvs (December 23rd, 2014) for large-scale ice cover monitoring, but the residual error can become significant for applications at smaller scales (a few kilometres).

9.4 Water-Ice Classification

9.4.1 Problem Formulation

In our study, we use the ILI to demarcate the lakes' borders. In the segmented areas, we now wish to discriminate water and ice pixels. The aim is to design an automated water-ice

	MNDWI			WRI			$NDWI_{IH}$			ILI		
Threshold	0.70	0.75	0.80	1.4	1.5	1.6	0	-0.10	-0.20	0.9	1	1.1
Zone S1												
κ	0.856	0.833	0.795	0.976	0.976	0.97	0.816	0.873	0.297	0.947	0.989	0.86
Water/Ice Comm. Error (%)	0.07	0.05	0.03	1.20	0.70	0.44	11.55	8.27	10.55	3.61	0.45	0.23
Water/Ice Omi. Error (%)	11.07	12.93	16.04	0.61	1.11	1.82	0.02	0.12	56.38	0.17	0.35	10.61
Other Comm. Error (%)	15.78	17.94	21.32	1.04	1.86	3.00	0.05	0.23	51.06	0.30	0.60	15.24
Other Omi. Error (%)	0.10	0.07	0.04	2.04	1.18	0.73	22.07	15.22	8.69	6.32	0.76	0.34
Zone S2												
κ	0.974	0.97	0.964	0.994	0.994	0.993	0.343	0.57	0.46	0.629	0.805	0.939
Water/Ice Comm. Error (%)	0.03	0.01	0.00	0.31	0.16	0.09	52.58	39.72	30.58	35.86	21.63	2.84
Water/Ice Omi. Error (%)	3.38	3.91	4.69	0.44	0.62	0.89	0.02	0.60	43.39	0.03	0.07	5.25
Other Comm. Error (%)	1.69	1.95	2.33	0.22	0.32	0.45	0.02	0.46	20.17	0.02	0.04	2.64
Other Omi. Error (%)	0.01	0.00	0.00	0.16	0.08	0.04	56.37	33.31	12.68	28.42	14.02	1.41
Zone U												
κ	0.833	0.657	0.456	0.998	0.998	0.998	0.992	0.997	0.997	0.762	1	0.997
Water/Ice Comm. Error (%)	0.00	0.00	0.00	0.07	0.02	0.00	0.51	0.13	0.00	13.86	0.00	0.00
Water/Ice Omi. Error (%)	12.64	27.29	46.26	0.10	0.13	0.16	0.03	0.09	0.24	0.01	0.01	0.20
Other Comm. Error (%)	18.33	32.65	45.10	0.17	0.22	0.27	0.05	0.15	0.42	0.01	0.01	0.35
Other Omi. Error (%)	0.00	0.00	0.00	0.12	0.04	0.01	0.92	0.24	0.00	28.57	0.00	0.00

Table 9.5 Errors and κ for the four indexes, in Zones S1, S2 and U.

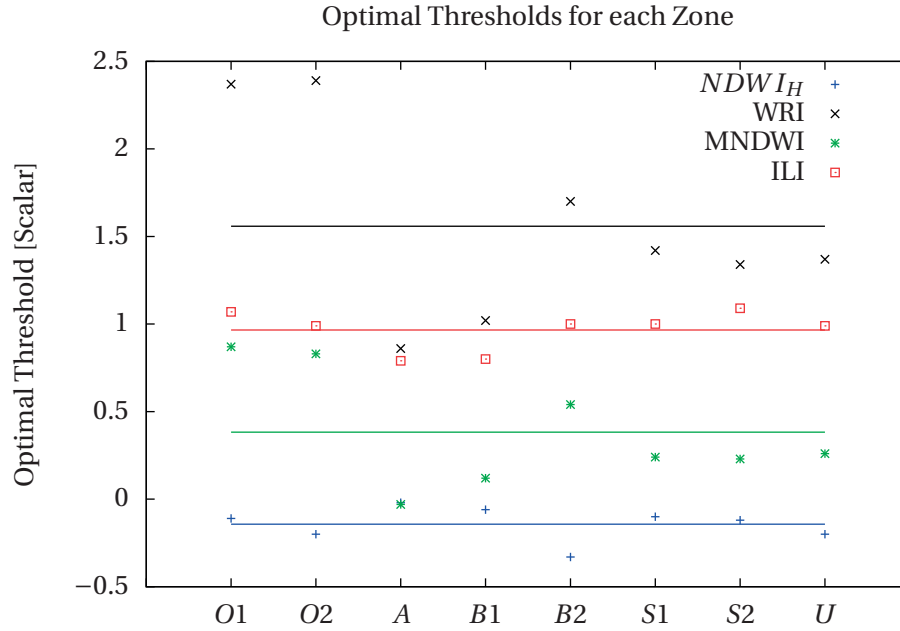


Figure 9.8 Optimal threshold for each zone and each index; straight lines indicate the average optimal threshold for each index.

classifier based on radiometric properties of the images. The classification procedure shall work on the TOA reflectance Landsat 8 images, for the reasons explained in Section 9.1.

In a lake area, various materials can be found; according to their spectral features, we have split them in four categories (Figure 9.10):

- open (deep) water. The reflectance of deep water is usually the lowest of the four elements.
- shallow water. At locations where the lake of interest is not deep enough, the reflectance is impacted by the material lying below the surface of the water. The main difference with deep water reflectance is it is visibly brighter (higher reflectance in blue, green and/or red). Although the "shallow water" category gathers a lot of different pixels (depending on the material below the water), they share the common property of stable ultra blue values and very low shortwave infrared values.
- (opaque) ice. Ice often has a much higher reflectance in the visible bands and the near infrared.
- clear ice. The ice cover can be very transparent and thus exhibit a reflectance that is very similar to the water below it. Although red and near infrared values of clear ice are sometimes enough to distinguish them from open water, in other cases only the contextual information (the geometrical structures and the texture of the surrounding pixels) allows the human interpretation to correctly classify clear ice.

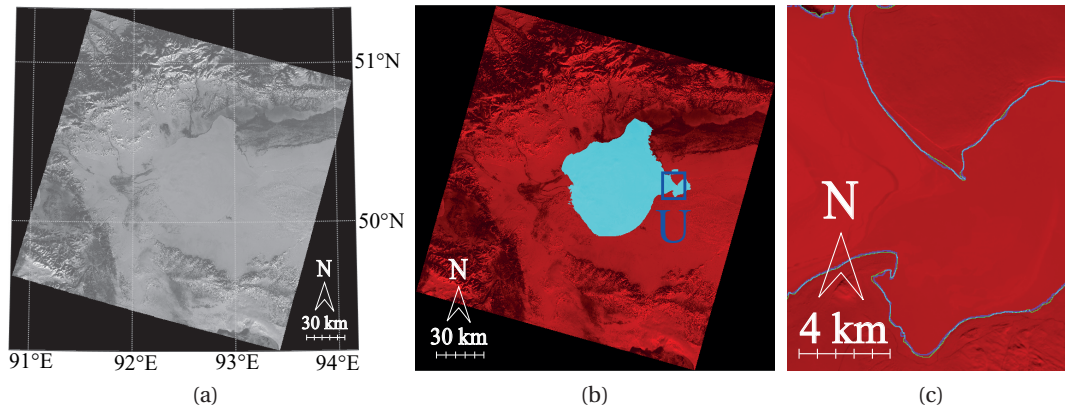


Figure 9.9 Illustration of the difficulty to delineate lake borders in case of important snow cover. **(a)** is the original Landsat 8 image of Lake Uvs (December 23rd, 2014). It is completely snow-covered and the lake is barely recognisable. **(b)** is an overlay of the UTM-transferred mask extracted from the image of May 16th, 2015, on top of the red background being the original image. **(c)** is the comparison of the extracted shoreline in Zone U (blue) with the reference shoreline, drawn manually (green).

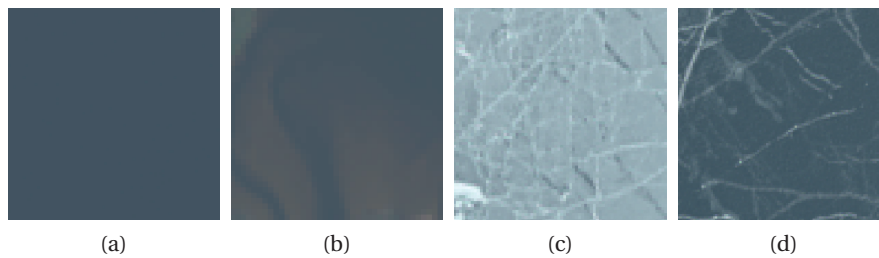


Figure 9.10 The four categories of materials found in lakes: **(a)** deep water, **(b)** shallow water/-mixed water - land pixels, **(c)** opaque ice, **(d)** clear ice.

These four categories are not clearly separable: there is a continuity between clear ice and ice properties, just like there is one between shallow water and deep water. However, we still use this split in our study as it helps to understand the reasoning that led to our final algorithm. We aim at discriminating the water and shallow water pixels from the ice and clear ice pixels in our images. This classification is difficult because no clear pixel-wise radiometric feature allows to discriminate these categories efficiently. We illustrate the similarities of spectral properties in Figure 9.11: we have gathered the spectral signatures of 119 sample points from Lake Onega and the Great Bear Lake, and displayed their box plots in each category. These sample points have been chosen to represent a wide variety of pixel types: deep water, coastal water (sometimes mixed with land), uniform ice, very transparent ice and very heterogeneous ice.

As can be seen on Figure 9.11, water and opaque ice could be easily separable, but clear ice and shallow waters exhibit very similar values in most of the bands. Shallow water areas usually

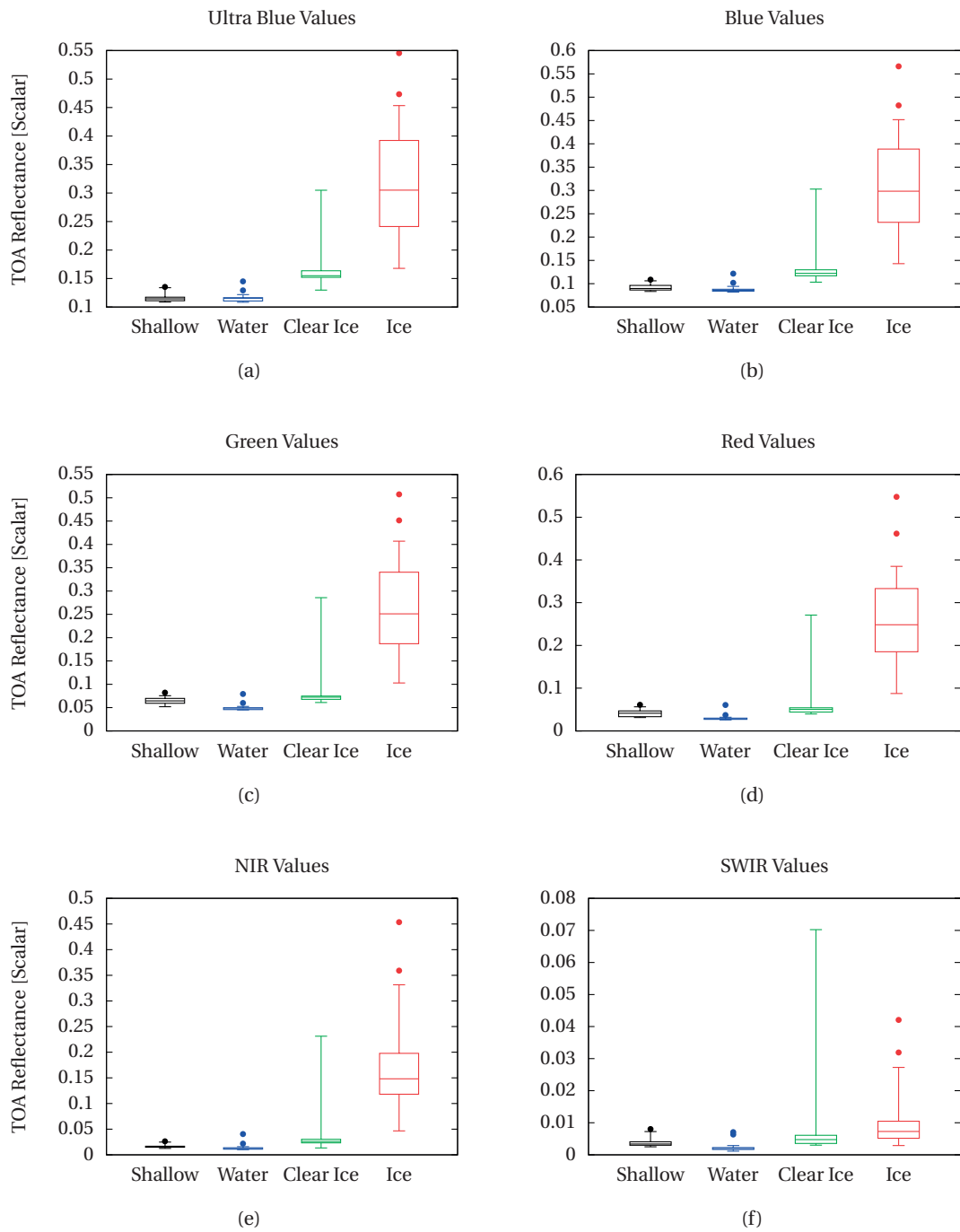


Figure 9.11 Box plots of the Landsat 8 TOA reflectances for its first six bands, for the 119 sample points. The horizontal segments represent the 5th, 25th, 50th, 75th, and 95th percentiles; the circles are sample values lying out of the 90% represented by the extreme segments.

have lower values in the blue and ultra blue bands, but not always, thus not allowing to reliably discriminate shallow water from clear ice. Pixel-by-pixel processing indeed ignores the texture of materials, which is an essential aspect for the human eye to identify ice: unlike water and shallow water which are usually very smooth (when seen as 2D signals), ice shows a high local variability of its pixels values. We take advantage of this property in our algorithm.

9.4.2 Local Texture and Water-Ice Classification Index

To achieve a better discrimination, we wish to use information about the local texture of the material, like similar algorithms for SAR data [141, 84]. We bring in this study the information of texture in two forms. The first one is the local average gradient of the pixel values in each band. The local average gradient of a pixel is defined as the mean of the gradient image in the $n \times n$ neighbourhood of the pixel, where n is an odd positive integer. The gradient represents the variation of the pixel value; the local average gradient is high when neighbouring pixels have very different values and low if they have similar values. The second information about texture is the local standard deviation of the pixel value in each band. The local standard deviation of a pixel is defined as the standard deviation in its $n \times n$ neighbourhood. The local standard deviation differs from the local average gradient, as it characterises changes in the pixel values of the neighbourhood even when they are smooth; the local average gradient is high only if the difference between values is high for adjacent pixels. For instance, the ice represented on Figure 9.10c would have high local average gradients and standard deviations, but the shallow water represented on Figure 9.10b would have high local standard deviations (different values in the image) but low local average gradients, as the changes in intensity are very smooth.

The choice of n is a balance between two properties: a large neighbourhood represents the texture better, but creates artefacts at the border between ice and water regions, because neighbour ice and water pixels mutually affect their local standard deviation; a small neighbourhood introduces less artefacts, but is more sensitive to the local noise of the data. In our study, we have chosen to work with 5×5 neighbourhoods. We define as $\bar{g}_{BandName}$ the local average gradient in the band named "Band Name" in the Landsat 8 data, and as $\sigma_{BandName}$ the local standard deviation in the band named "Band Name".

In our first tests, we have determined a decision tree based on two features: the NIR TOA reflectance, and the local average gradient of the ultra blue TOA reflectance, \bar{g}_{Ultra_Blue} . The NIR reflectance was chosen because water usually absorbs most of the near infrared radiations, while ice partially reflects them (Figure 9.11e); the NIR alone does not allow for a good classification as shallow water pixels can have significant NIR reflectance coming from the bottom of the lakes. The second feature, \bar{g}_{Ultra_Blue} , was chosen because it is the band in which ice and clear ice show the highest variability in our sample (Figure 9.11a). We have extended our sample to 1000 geographic points (still from Lake Onega and the Great Bear Lake) and plotted them as 2D points which coordinates are the NIR and \bar{g}_{Ultra_Blue} . The plot is shown in Figure 9.12a. From the nature of the separation, it is clear that a decision tree was suitable for classification. We have learnt this tree on this sample, using the standard

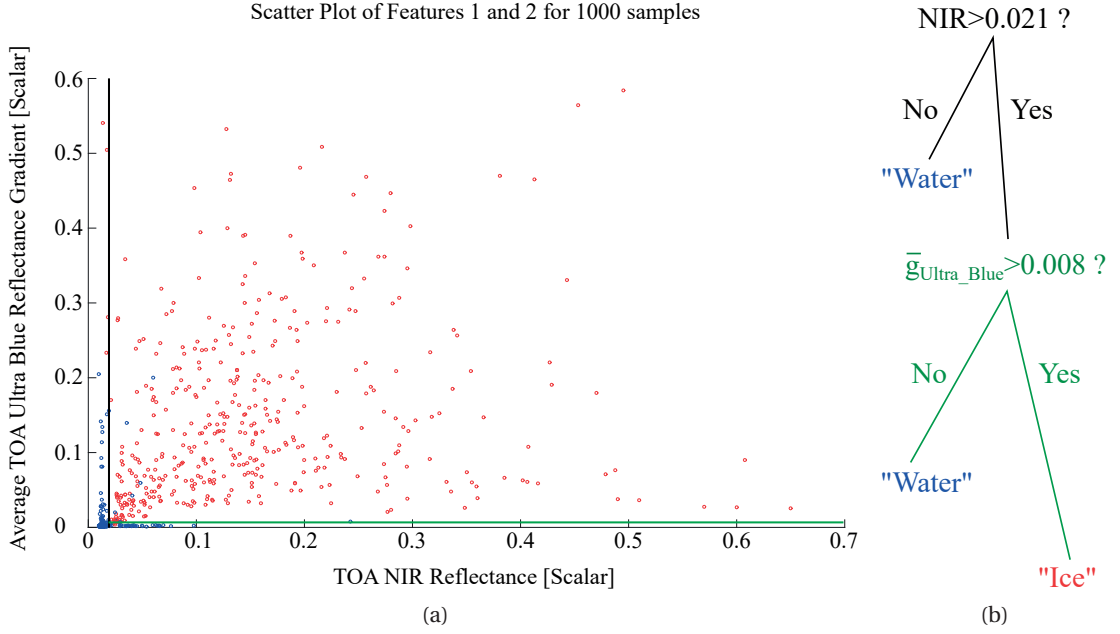


Figure 9.12 (a) 2D plot of the 1000 training samples for training the water-ice discrimination algorithm. The x coordinate is the NIR reflectance, the y coordinate is the average gradient in a 5×5 pixels neighbourhood of the sample point in the ultra blue reflectance. Red points correspond to ice or clear ice, blue points correspond to water or shallow water. The decision tree learnt on this sample is illustrated by the black line ($NIR = 0.021$) and the green line (Average Gradient = 0.008), and shown in (b).

implementation of the decision tree learning in Matlab, which uses the Classification And Regression Trees (CART) algorithm [18] to build the tree. The resulting tree is shown in Figure 9.12b and displayed as two separating lines in Figure 9.12a.

After a few tests, it appeared that this classification was good in most cases, but still failed to discriminate some shallow water pixels from ice. For this reason, we have decided to use a third feature in the classification. We have designed an index, called Water-Ice Classification Index (WICI), which aims at removing the shallow water pixels: it relies on the uniformity of the reflectance of water in the near and shortwave infrared, while ice exhibits significant differences between near infrared and shortwave infrared. Its formula is given in Equation 9.5.

$$WICI = \frac{\sigma_{SWIR} + \sigma_{SWIR2}}{2\sigma_{NIR}} \quad (9.5)$$

The scores of the WICI are plotted on Figure 9.13.

As can be seen on Figure 9.13, the WICI separates shallow water but also deep water pixels from ice and clear ice very well. The ability to separate shallow water, in particular, makes the WICI

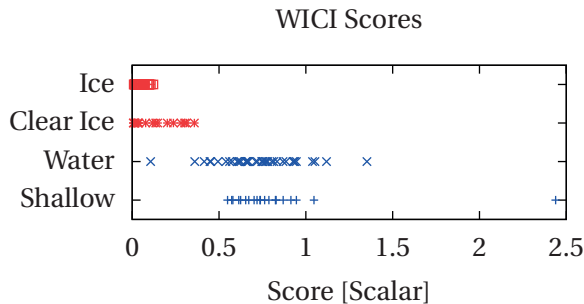


Figure 9.13 WICI scores for the sample points.

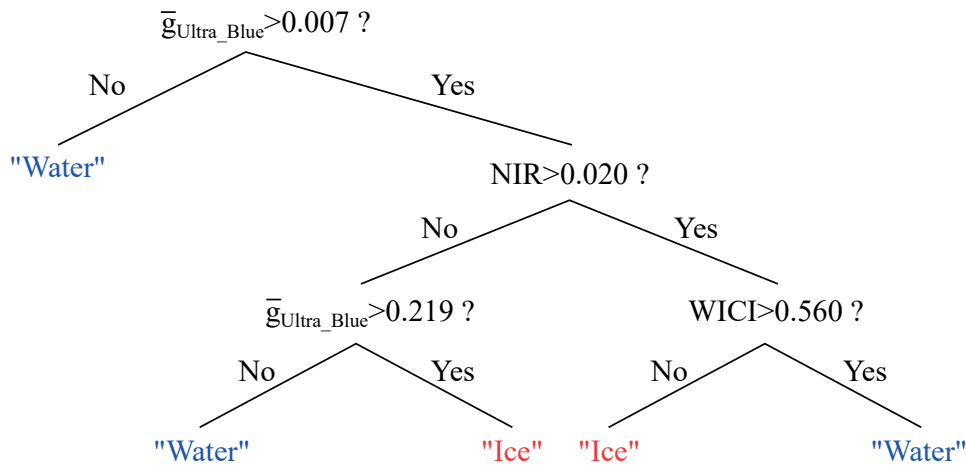


Figure 9.14 Decision tree used for our water-ice classification algorithm.

very complementary to our first two features. Our final decision tree, used for classification, is learnt again using the CART algorithm. It is displayed on Figure 9.14.

Although the decision tree we use (Figure 9.14) was determined algorithmically, we can comment on its physical interpretation: the top node means that homogeneous surfaces are water; if the surface is not homogeneous, its NIR reflectance is tested. If it is low, there is still a possibility that the pixel is ice, in which case the local heterogeneity has to be very high. If the NIR reflectance is high, there is still a possibility that the pixel is shallow water, and this is assessed by the WICI. The results of this classification algorithm are given in the following section.

9.5 Results

This section is split in two parts. In the first part, we give the quantitative results of the classification for five specific zones from five different lakes (Lake Onega, Lake Amadjuak, Great Bear Lake, Great Slave Lake and Lake Uvs). In the second part, we compare our classification on

Lake Ladoga to a concurrent classification using the Sentinel-1 SAR data.

9.5.1 Comparison to Reference Data

We have run our classification algorithm on six images Landsat 8 images: Lake Onega, April 10th, 2014; Lake Amadjuak, August 8th, 2016; Great Bear Lake, June 27th, 2013; Great Slave Lake, May 22th, 2015; Lake Uvs, May 16th, 2015; Lake Onega, March 12th, 2015. The results are shown on Figures 9.15 and 9.16.

To compute quantitative results, we have manually labelled the pixels as ice or not ice in five zones marked on Figures 9.15 and 9.16. These zones were chosen to illustrate the performance of the algorithm on a variety of edge cases: zones C_O14 (Figure 9.15a) and C_A (Figure 9.15b) present a mix of water and ice and allow to see the behaviour of the algorithm at the borders between the two; zones C_B (Figure 9.15c) and C_U (Figure 9.16b) contain ice with varying transparency and heterogeneity; zone C_S (Figure 9.16a) includes a large shallow water part where the reflectance is much higher than the one of deep water. The comparison between the manually digitised reference and the output of our algorithm is quantified in terms of Kappa coefficient, and commission and omission errors for the ice and the water. Pixels that are neither ice nor water do not alter the results, which are only computed in the area delineated by the ILI. The original images, reference classifications and computed classifications are shown on Figures 9.17 and 9.18. The quantitative results are given in Table 9.6.

	Zone C_O14	Zone C_A	Zone C_B	Zone C_S	Zone C_U
κ	0.935	0.953	0.966	0.844	0.973
Ice Comm. Error (%)	4.37	3.13	0.28	9.30	2.56
Ice Omi. Error (%)	0.04	0.01	3.96	0.07	0.81
Water Comm. Error (%)	0.04	0.02	7.84	0.16	0.50
Water Omi. Error (%)	4.70	3.46	0.58	19.31	1.58

Table 9.6 Kappa coefficients, commission and omission errors of our water-ice classification in the zones of interest.

Our classification algorithm performs very well across the five test zones. The main source of error, particularly visible in zone C_S, comes from the classification of the pixels at the borders between water and ice. Pixels representing surfaces of $30m \times 30m$, they can be composed of both ice and water, which makes their classification difficult, even during the manual labelling phase. This reason alone explains the residual ice commission error for zones C_O14 and C_A, but not for zone C_S: the water in this zone is not very deep and has a non-negligible NIR

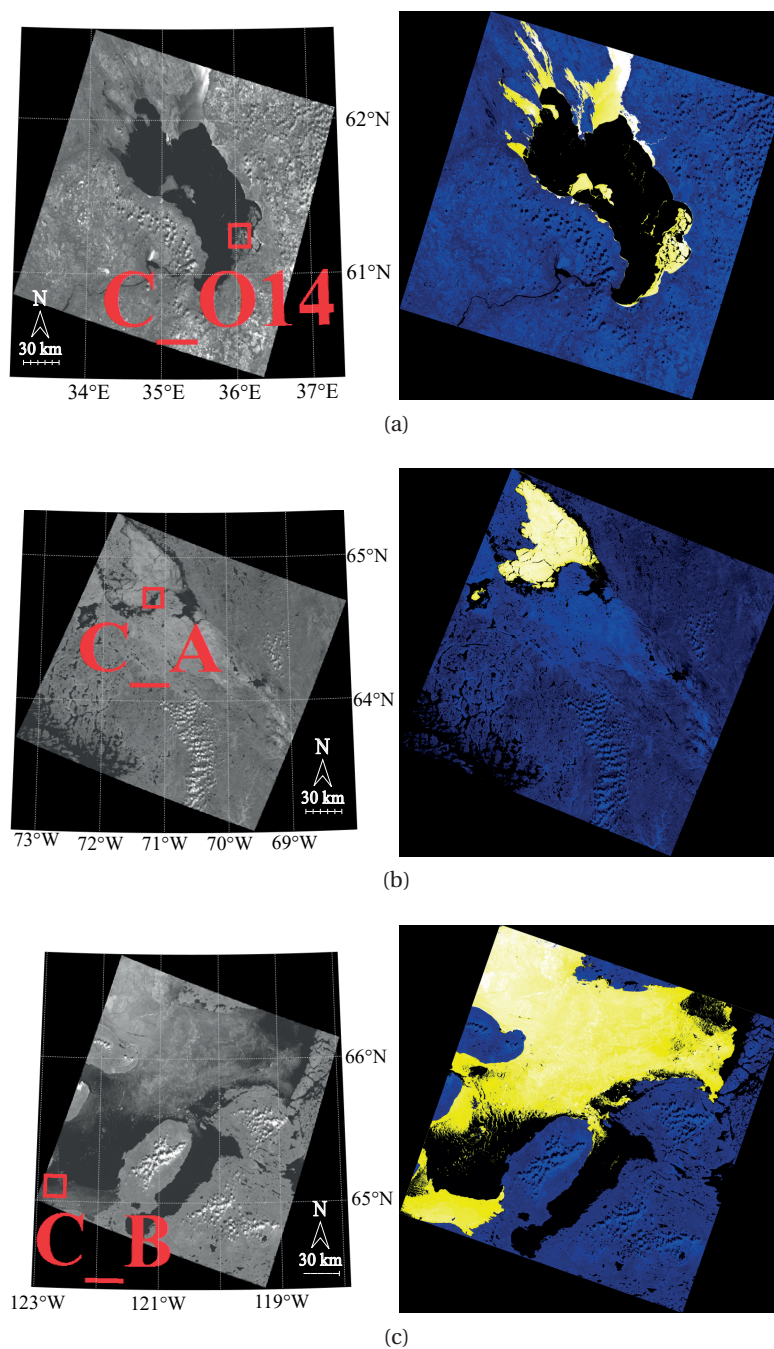


Figure 9.15 Water-ice classification results, part 1: **(a)** Lake Onega, April 10th, 2014; **(b)** Lake Amadjuak, August 8th, 2016; **(c)** Great Bear Lake, June 27th, 2013. Images on the left are the unprocessed Landsat 8 OLI images (NIR band with enhanced brightness), and images on the right are the classifications, with ice in yellow on top on the original image in blue. Zones used to quantify the results are indicated in red.

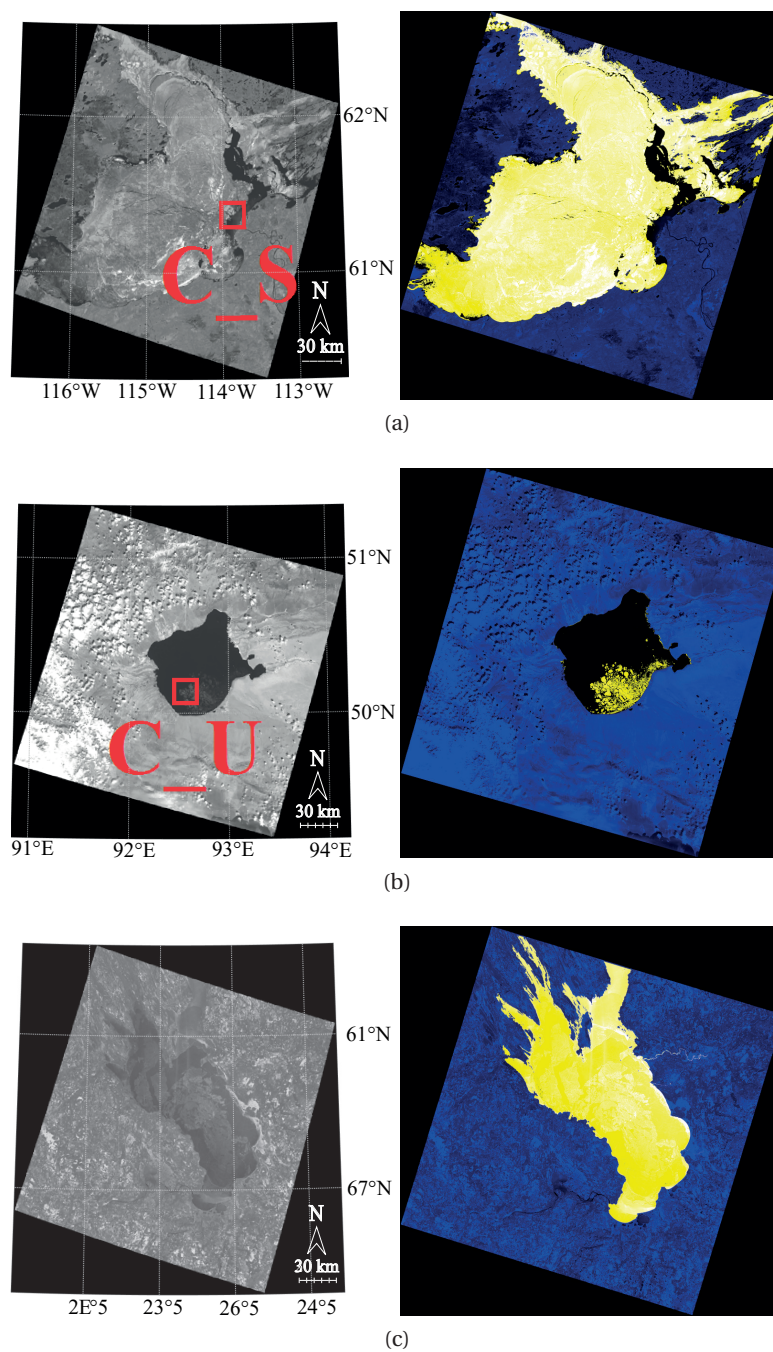


Figure 9.16 Water-ice classification results, part 2: **(a)** Great Slave Lake, May 22th, 2015; **(b)** Lake Uvs, May 16th, 2015; **(c)** Lake Onega, March 12th, 2015. Images on the left are the unprocessed Landsat 8 OLI images (NIR band with enhanced brightness), and images on the right are the classifications, with ice in yellow on top on the original image in blue. Zones used to quantify the results are indicated in red.

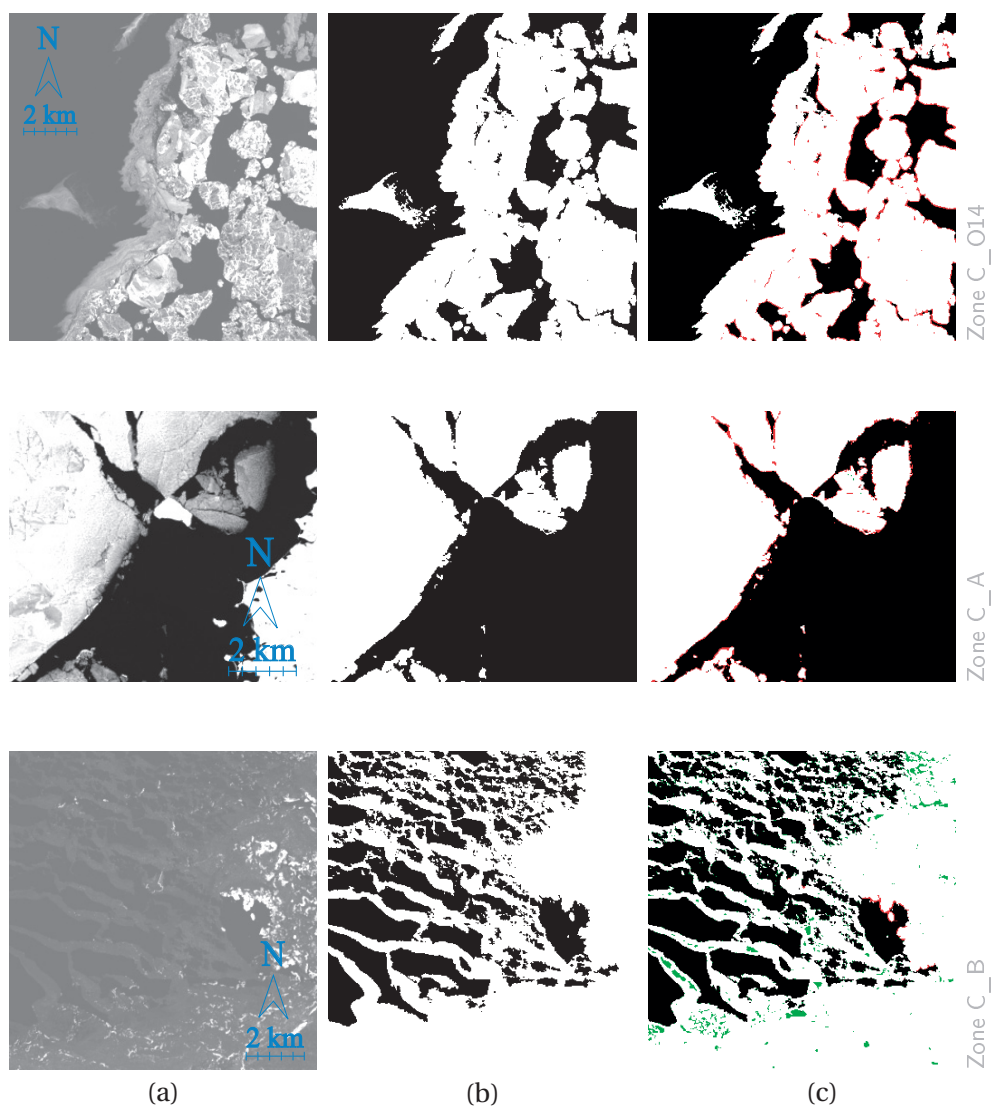


Figure 9.17 Classification results for zones C_O14, C_A and C_B. (a) is the original Landsat 8 NIR image with enhanced brightness; (b) is the manually digitised reference data; (c) is our classification, with false positives coloured in red, and false negatives coloured in green.

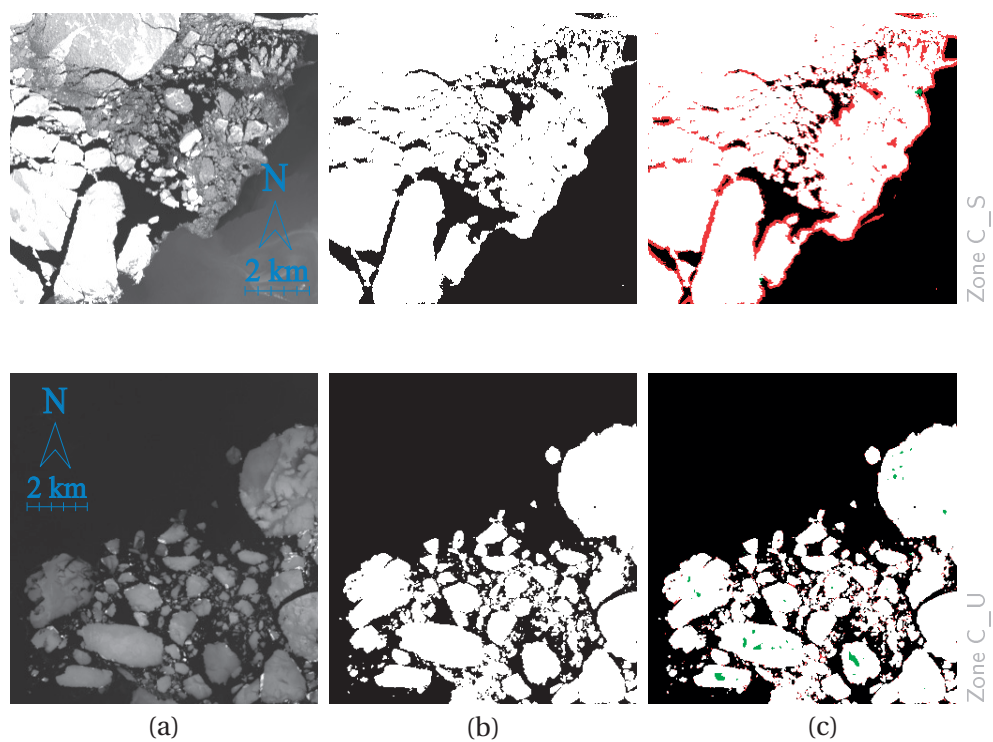


Figure 9.18 Classification results for zones C_S and C_U. (a) is the original Landsat 8 NIR image with enhanced brightness; (b) is the manually digitised reference data; (c) is our classification, with false positives coloured in red, and false negatives coloured in green.

reflectance. The two other features used in our supervised classification being neighbourhood properties, they are altered at the borders between water and ice, resulting in this significant ice commission error. The ice omission error is low for all our images; there is a noticeable ice omission error only in zone C_B, where some locally very homogeneous and low reflectance ice was misclassified. Otherwise, the global quantitative results are satisfying, with Kappa coefficients ranging from 0.93 to 0.97, except zone C_S (Kappa = 0.84).

9.5.2 Comparison to Sentinel-1 SAR Data

In addition to the results presented in Section 9.5.1, we wish to compare our classification results to similar classifications performed using different sensors, so as to assess the performance of our algorithm at a much larger scale. Due to the recognised efficiency of the SAR data for water-ice discrimination (see Section 9.2.1), we have chosen to process such classification on Sentinel-1 SAR data and compare it to our classification using the Landsat 8 OLI data. To provide meaningful quantitative assessment to the reader, the choice of the images is constrained by two factors: the images must have a significant proportion of ice and water, and both Sentinel-1 SAR data and Landsat 8 OLI data must be available at the same date. Therefore, quantitative assessment has been done for the image of Lake Ladoga on April 11th, 2015, which respects both requirements.

Processing of the SAR Data

Pre-Processing For the initial processing of the SAR image, we have used the Sentinel-1 Toolbox (S1TBX). The S1TBX is an open source toolbox consisting of a collection of processing tools for data from European Space Agency (ESA) SAR missions like the Sentinel-1 mission. The pre-processing is divided into several steps: calibration to backscatter, speckle noise removal, and terrain correction. The calibration to backscatter transforms the pixel values from the band of interest (HH, HV, VH or VV) to backscatter values (σ_0); the speckle noise removal reduces the noise in the image using averaging filters; terrain correction geocodes the image by correcting SAR geometric distortions using a Digital Elevation Model (DEM) and producing a map projected product to correct for inherent SAR geometry effects such as foreshortening, layover and shadow. All these tasks were performed using the toolbox. Figure 9.19 shows an example of such pre-processed SAR image.

Co-Registration to Reference Landsat Data The SAR data is translated onto the corresponding Landsat image using UTM coordinates. We compute the UTM coordinates of every pixel in the appropriate zone (36N for Lake Ladoga), and convert them to pixel coordinates in the reference Landsat image. The resolution of the Sentinel-1 SAR data ($50m \times 50m$) is inferior to the resolution of the Landsat data ($30m \times 30m$), resulting in a sparse image. To solve this issue, we perform a bilinear interpolation, to fill the gaps between the translated pixels. The quality of the co-registration is controlled by computing the position error of 30 tie points (manually

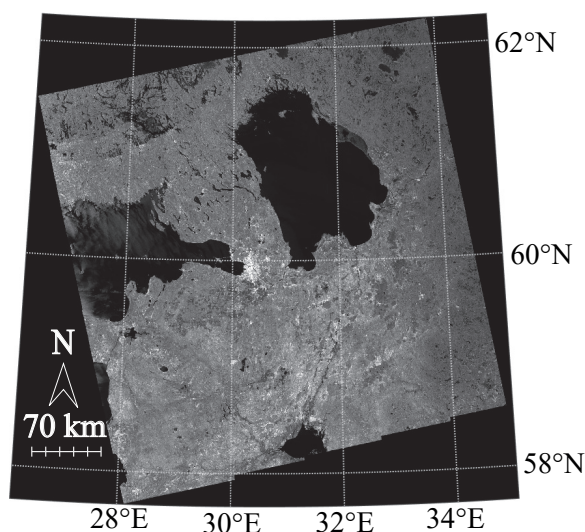


Figure 9.19 SAR HH image of Lake Ladoga (April 11th, 2015), pre-processed with the Sentinel-1 Toolbox.

identified in both images) and the resulting Root Mean Square Error (RMSE). The composite image, as well as the tie points and their errors, are shown on Figure 9.20.

The RMSE over the 30 tie points is 3.3 pixels (100 m). This result is the consequence of a systematic deformation illustrated in Figure 9.20b. The deformation observed can be caused by the inaccurate georeferencing of either image but also the difference of spatial resolution between the two sensors. We have considered correcting the SAR image geometrically, by computing the best parameters for a Helmert transformation turning the tie points' coordinates in the Sentinel-1 image into their equivalent coordinates in the Landsat image. This optimisation was achieved through a least square method, and led to a new RMSE of 1.99 pixels. However, the correction was beneficial mostly to the inland pixels, while the pixels on the shores of the lake actually showed an increased error in the co-registration. Therefore, we decided to proceed with the co-registered image obtained before the Helmert transformation, as none of the pixels around the lake had a co-registration error of more than 3 pixels.

Binary Classification To process water-ice classification on SAR data, the algorithms described in the literature use different polarization modes. A pragmatic approach consisting in thresholding the co-polarised ratio [43] was first considered; however, the VV and HH acquisitions over Lake Ladoga on April 11th, 2015 occurred at very different times of the day (04:16 UTC for the VV, 15:31 UTC for the HH). As we show later in Section 9.5.2, there were significant drifts of the ice in the meantime, making the effective use of the co-polarised ratio impossible. Therefore, we have adopted another approach consisting in a supervised classification based on the grey level co-occurrence matrix (GLCM) texture features. The GLCM features [55] are specific features designed to characterise the textures in greyscale images. They are computed as follows: the original image intensity values are binned into K quantization levels; pairs of

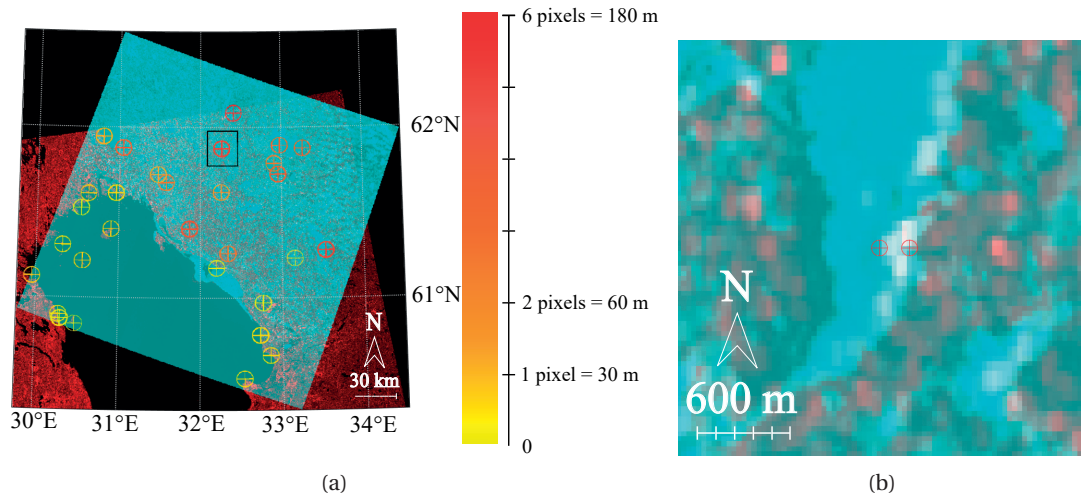


Figure 9.20 (a) is the composite of the Landsat blue band image (cyan) and the co-registered Sentinel-1 HH image (red). 30 tie points used for assessing the quality of the co-registration are displayed in yellow to red colours, according to the distance between their locations in the Sentinel-1 image and the Landsat image. An area, highlighted by a rectangular black border, is zoomed on and shown in (b).

pixels are created according to a distance d and a direction $\theta = 0^\circ, 45^\circ, 90^\circ$ or 135° (for instance, if $d = 2$ and $\theta = 45^\circ$, pixel (k, l) is paired with pixel $(k-2, l+2)$, considering the top-left corner as the origin of the image); in each window of size s (defined by the user) of the image, the co-occurrence of value i and j inside pixel pairs is counted, and placed in the co-occurrence matrix at coordinates (i, j) . From this matrix, multiple texture properties can be derived.

GLCM features have been used successfully in water-ice classification of SAR data [143, 84]. We proceed similarly as [143] by extracting GLCM features in an image split in 16 intensity bins, in subwindows of size $s = 16$, with a distance $d = 2$, averaged in the four possible directions. We have found the contrast, the energy and the homogeneity features (see [55] for their formulas) to be very good at discriminating water and ice in our image (see Figure 9.21). Alongside with the HH backscatter, these are four features we use for our supervised classification.

The classification process was learnt on a sample of 400 points (200 water points, 200 ice points) using a Support Vector Machine (SVM) algorithm with a linear kernel. All the image pixels in the region of the lake mask determined by the ILI were then classified.

Comparison from Landsat to Sentinel-1

The Sentinel-1 SAR data has been processed as described in Section 9.5.2. Figure 9.22 shows the Landsat classification, processed with the WICI, and the concurrent classification from the SAR. In the lake part of the image shown on Figure 9.22, the agreement between the two classifications is 98 %, and the Kappa coefficient is 0.85. To analyse the results in more details, we have zoomed on four particular areas, shown in Figure 9.23.

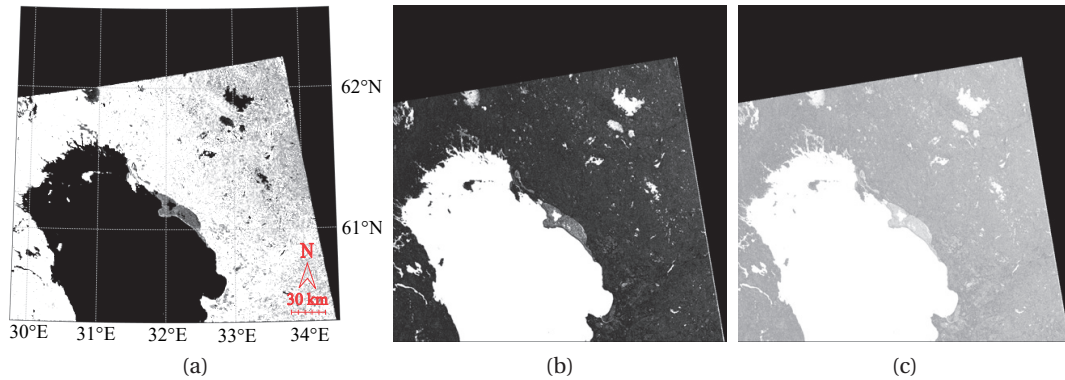


Figure 9.21 Features used for the SVM classification of the Sentinel-1 SAR image of Lake Ladoga (April 11th, 2015). **(a)**: Contrast; **(b)**: Energy; **(c)**: Homogeneity.

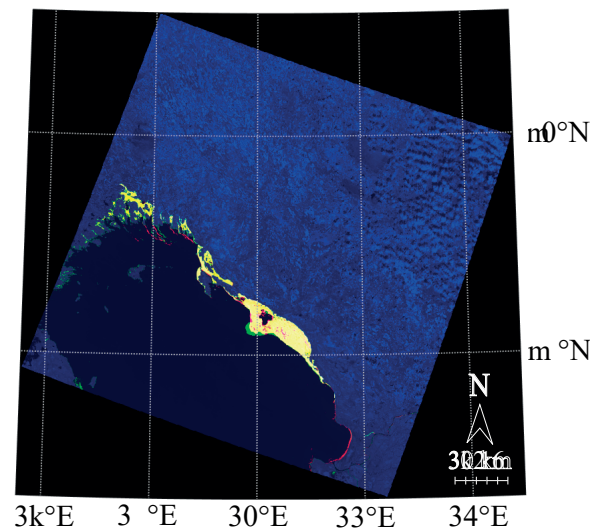


Figure 9.22 Composite image showing the Landsat 8 OLI and the Sentinel-1 SAR binary classification in the northern part of Lake Ladoga, April 11th, 2015. The yellow pixels are the locations classified as ice by both methods; the green pixels are positive for the SAR and not for the OLI; red pixels are positive for the OLI and not for the SAR.

We have observed shifts in Figure 9.23a and Figure 9.23c due to the displacements of the icebergs during the day. Indeed, the Landsat image was acquired at 09:03 (UTC) and the Sentinel-1 image was recorded at 15:31 (UTC). On these two Figures, we can observe drifts of the ice of about 1 km. These differences, due to the difference in time of acquisition, contribute to lowering the Kappa coefficient between the two classifications. In the zone represented by Figure 9.23b, no significant shift is observed, and the Kappa coefficient is 0.92. In the last zone (Figure 9.23d), both classifications show their limitations: while the Landsat retrieves a significant coastal ice zone that the Sentinel-1 failed to detect, it also show a few false positives in the form of "grains" of water, where the local standard deviations were affected by local noise. Our algorithm, however, mostly classifies properly the river pixels that are all water

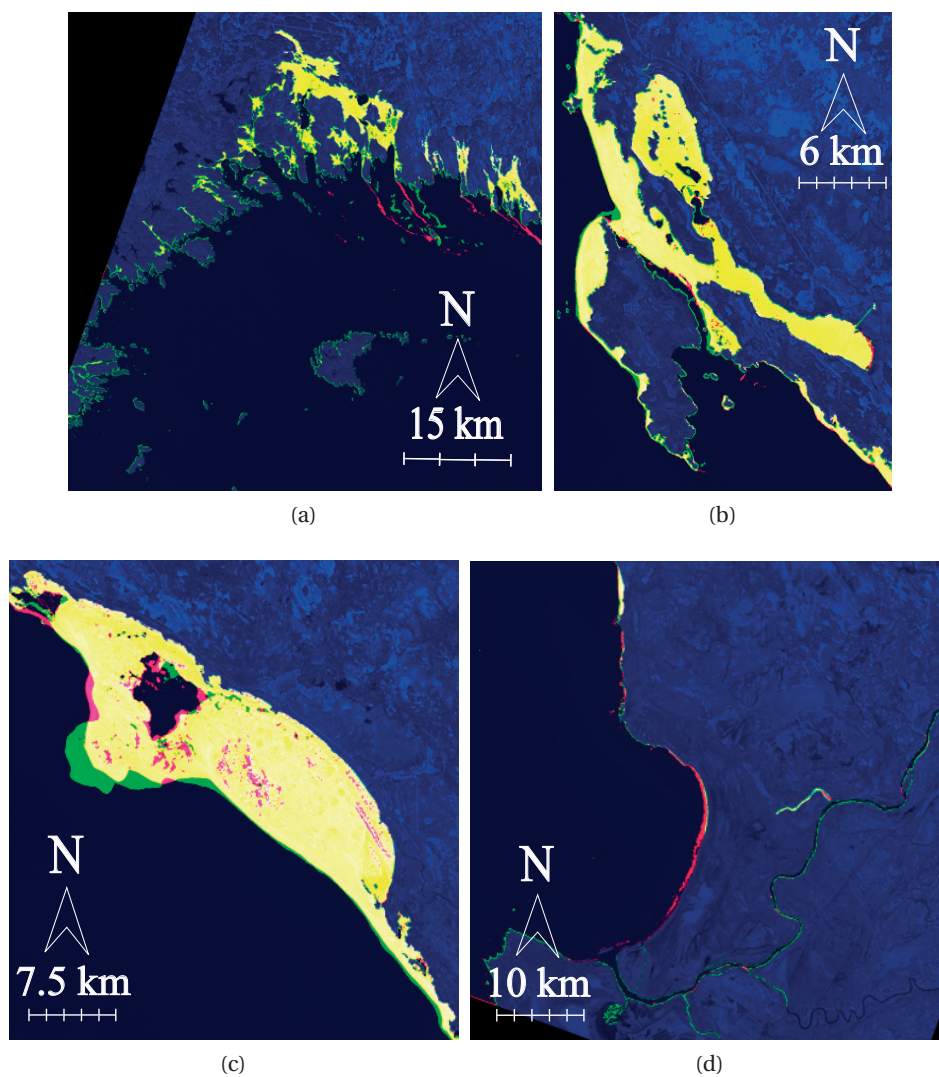


Figure 9.23 Zoom on four parts of Figure 9.22, from West (a) to East (d).

(unlike our processing of the SAR). Overall, considering that there are significant shifts of the icebergs from the Landsat acquisition to the Sentinel-1 acquisition, the two classifications are quite coherent.

Conclusion

The work presented here represents a full algorithmic and software solution for producing hyperspectral reflectance maps in coastal areas, from the acquisition of raw data to the delivery of a radiometrically calibrated, orthorectified product, or even a thematic product such as a chlorophyll- α concentration map.

In the context of the Léman-Baïkal project, the work presented in this thesis dealt with every aspect of the processing of the hyperspectral data collected with a pushbroom sensor. Firstly, the data was radiometrically calibrated: in particular, we proposed a novel approach to perform spectral calibration, which uses Dynamic Time Warping to match high frequency features from the spectrums acquired to a reference acquisition, relying on the presence of atmospheric absorption peaks in our data. After removal of noise, glints and BRDF effect, the calibrated data was proved to correspond well to the ground measurements obtained with spectrometers. Then, we develop a new method to georeference data from pushbroom sensors, which uses SURF and Particle Image Velocimetry to match the pushbroom scan lines to an RGB reference computed in parallel from frame images. This process allows to correct the orientation parameters for each scan line individually and estimate the interior orientation parameters of the pushbroom camera as well. When comparing the mosaics with the references, the RMSE do not exceed four times the GSD of the acquisition. To offer practical usability of the data to our partners in the project, a software called HypOS was developed, including orthorectification and calibration tools. Together with new data compression techniques for both the images and their calibration, this software solution was an efficient tool for processing the data from the pushbroom sensor and navigation sensors, either from the ULM or drone acquisitions. The resulting orthorectified and calibrated data was used for various studies: the chlorophyll- α concentration map in the Rhône Delta of Lake Geneva, the total suspended matter and its retention in the Selenga Delta of Lake Baikal, but also for other applications, like mapping fields and ponds in Brittany, France. At larger scales, we also developed tools to monitor the ice coverage of great glacial lakes using both Landsat 8 multispectral data and Sentinel-1 SAR data. By fusing the two sources of data, we managed to monitor ice coverage in the North of Lake Ladoga on a single day, in an interval of a few hours. To the best of our knowledge, no such high-frequency monitoring exists in the literature. The primary possible extension for this work is researching an image-based atmospheric correction algorithm for water, for high altitude flights. At the time when this thesis is written, the QUAC and the STEAC (developed by colleagues of the Geodetic Engineering Laboratory)

Conclusion

do not perform well on water since they rely on the assumption that water has a very low reflectance for correction. Finding an atmospheric correction solution for high altitude flights would allow the coverage of larger areas. At the time being, only low altitude flights deliver proper data since the atmospheric scattering is negligible. Other perspectives include the mapping of water quality properties in the other parts of Lake Geneva and Lake Baikal. In particular, it would be crucial to study geochemical properties like the retention of suspended matter observed in Baikal.

A Data Compression

A.1 Radiometric Calibration Storage: UXM Files

The radiometric calibration process described in Section 5.1 implies the use of Dynamic Time Warping (DTW) to match the high frequencies from the reference signal (from the Spectralon) and the signal we wish to calibrate. Once the data is calibrated, the storage of the result can be operated in two ways: either the calibrated signal is stored as such, or the DTW matching is coded and stored into memory. The typical files produced during acquisition contain 1000 scan lines of 1000 pixels in 250 bands; each value being coded on 16 bits (2 bytes), such file weights roughly 488 Megabytes (Mb). In this section, we propose a coding scheme to store the DTW results with a much lower need of memory.

A.1.1 Coding Scheme

To begin with, it is important to understand the matching operated by DTW. To each timestamp of a signal (called signal 1) is associated a timestamp of another signal (called signal 2) according to a distance criterion. The first timestamp is always matched with itself, so is the last; in between, if a timestamp t_1 in signal 1 has been associated with timestamps t_2 in signal 2, the next match can be either $t_1 + \Delta t$ with t_2 , t_1 with $t_2 + \Delta t$ or $t_1 + \Delta t$ with $t_2 + \Delta t$. The first one corresponds to a right move in the DTW matrix, the second corresponds to a down move, and the third corresponds to a diagonal move (Figure A.1).

In order to save this matching, we have designed a file format called Universal Cross Mapping (UXM). This format encodes the path taken through the DTW matrix as a series of bits. A single assumption is made: if a right move follows a down move (or the opposite), one match is useless and the two moves can be simplified to a diagonal move. Then, our encoding process is summarised by the finite state machine represented on Figure A.2.

Algorithm 2 summarises this encoding process. It takes as input the series of moves found using Dynamic Time Warping. The output is a series of bits, put together as bytes in Java.

Data: The DTW paths for all pixels, as arrays $paths[p][m]$ ([pixel][index of the move].)

Result: Series of pixels, following UXM format.

currentState = diagonal;

for p from 1 to # pixels **do**

for m from 1 to # moves **do**

if currentState == diagonal **then**

if $path[p][m] == diagonal$ **then**

 write 1;

else

if $path[p][m] == horizontal$ **then**

 write 00;

 currentState = horizontal;

else

 write 01;

 currentState = vertical;

end

end

else

if $path[p][m] == diagonal$ **then**

 write 1;

 currentState = diagonal;

else

if $path[p][m] == currentState$ **then**

 write 0;

else

 /* Down and Right (or vice-versa), simplify with a
 diagonal move. */;

 delete bits written at previous steps;

 write 1;

 currentState = diagonal;

end

end

end

end

end

Algorithm 2: Encoding algorithm for calibration through DTW.

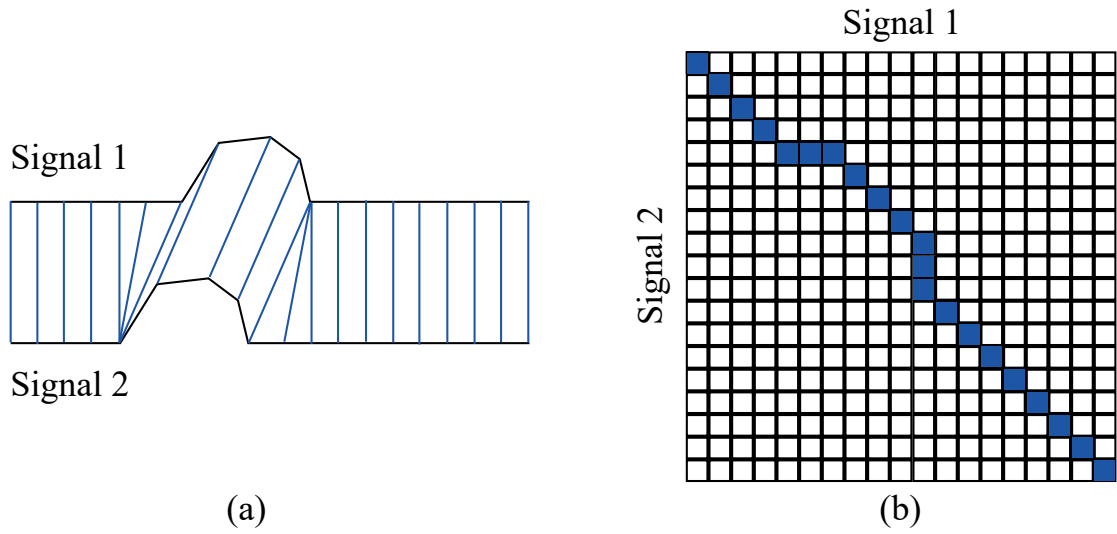


Figure A.1 Example illustrating (a) the matching operated by DTW, and (b) the corresponding path in the DTW matrix.

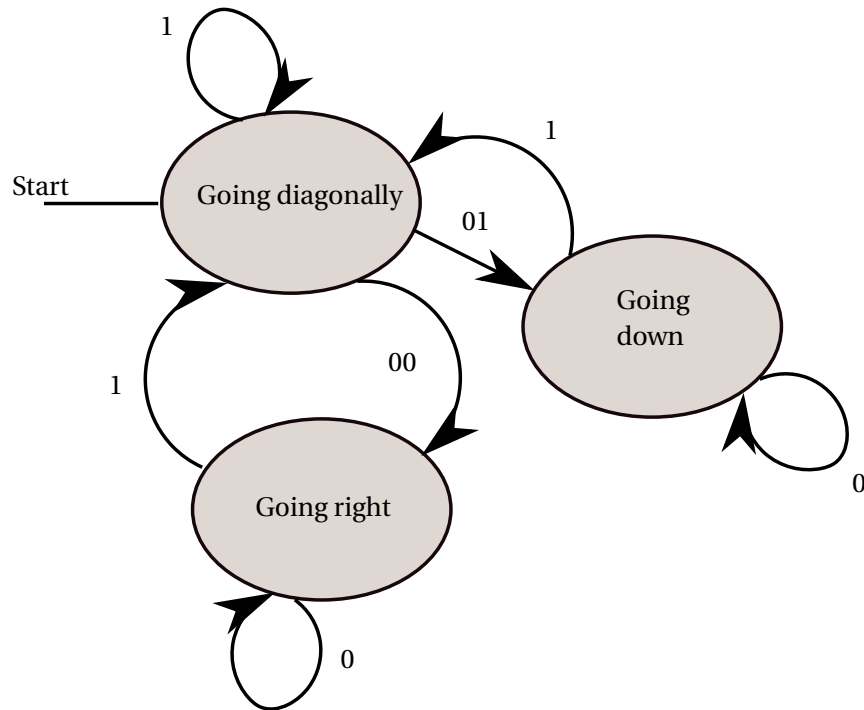


Figure A.2 Finite state machine representing the coding of the DTW path.

A.1.2 UXM Memory Consumption

The size of the resulting code is bounded according to Property 1.

Property 1. *The UXM code representing the DTW matching between two signals of size N is at*

Appendix A. Data Compression

most $2(N-1)$ bits ($\frac{N-1}{4}$ bytes).

We demonstrate Property 1 with the following reasoning: for two signals of size N , the DTW path must operate $N-1$ right moves, and $N-1$ down moves, that is, $2(N-1)$ moves in total. According to the finite state machine (Figure A.2), any 2D-move operated after a 2D-move of the same nature costs at most one bit per move (less if it is a diagonal move). Only going right or down after a diagonal moves costs two bits: in this case the total number of moves operated is 3 (2 by the diagonal, 1 by the next move) and the total cost in bits is 3 (a diagonal move is two one-dimensional move, plus the next move operated), which also results in a cost of one bit per move. As a result, the code requires at most one bit per 1D-move, that is, $2(N-1)$ bits.

As already mentioned, recording the calibrated hyperspectral image of size 1000 by 1000 with 250 bands would require 488 Mb. Comparatively, the UXM file requires at most $1000 \times 1000 \times \frac{(250-1)}{4} = 62\,250\,000$ bytes ≈ 59.4 Mb. Conversely, we can prove that the minimal memory required is approximately 29.7 Mb (obtained when all the moves are diagonal). Coding the calibration with the UXM scheme effectively results in a division of a factor between 8.2 and 16.4 of the memory weight.

In the decoding phase, the algorithm counts how many horizontal and vertical moves have been made so far; when both counts reach the number of bands, we know that one whole signal (corresponding to a pixel) has been decoded. We can therefore concatenate all the codes for all pixels within one single file and still have it decoded properly.

A.2 Hyperspectral Files Lossless Compression

To further optimise the memory consumption of hyperspectral files, we have implemented a lossless compression scheme inspired of those found in the literature. Because of their very fine spectral resolution, the adjacent bands of hyperspectral cubes are very strongly correlated. This property is the foundation of all compression techniques used today for hyperspectral data compression: data in band $n-1$ serves to predict the data found in band n ; instead of coding the full values contained in band n , we can restrict the coding to the residual between the predicted value and the actual value. The standard system design for compression of hyperspectral cubes is given by [20] and summarised on Figure A.3.

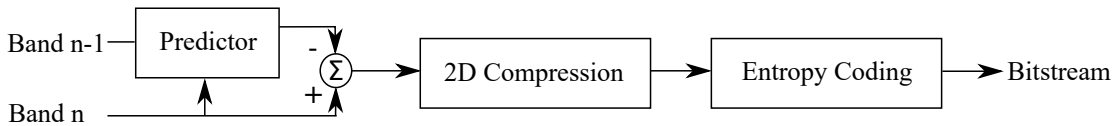


Figure A.3 Standard system design for compression of hyperspectral images.

The purpose of the compression we implemented was not to compete with state-of-the-art algorithms, but rather provide the users of HypOS with a low-complexity algorithm allowing to save significant memory.

A.2.1 Prediction Phase

Two possibilities were explored for the prediction:

- a simple prediction: in band n , the predicted value $\hat{x}_{i,j,n}$ of the pixel at coordinates (i, j) is simply the value in the previous band, $x_{i,j,n-1}$.
- a more complex prediction, where the pixels are first clustered by a K-means algorithm. The predicted value for each pixel is the value of the mean spectrum of the cluster in which this pixel has been put.

The second method was inspired from Mielikainen et al. [94]. This method has been tried on hyperspectral cubes of size $200 \times 200 \times 10$ but did not show significant compression rates (60 % on average, against almost 70 % for the other method tested - see following section). Additionally, no implementation of the K-means algorithm allowed to obtain a reasonable computation time (less than a day) for our standard hyperspectral images, which size is $1000 \times 1000 \times 250$. Computation time being an essential criterion for choosing a compression method, we have opted for the first prediction method. The rest of the compression algorithm is described in the following section.

A.2.2 Entropy Coding

From the prediction phase, we produce a hypercube called residuals hypercube, which is the hypercube to compress, minus its prediction hypercube. Given the nature of the prediction, the residuals hypercube is composed with very small values (except in band 1). More importantly, these values are gathered in fewer bins. For example, the histograms of one of our hyperspectral images of Lake Geneva, coded on 12 bits (which means the values are integers between 0 and 4095), for both the original hypercube and the residuals hypercube, are shown on Figure A.4.

The data being gathered in limited number of values, its entropy is now very low and can be coded using an entropy coder. For the entropy coder, we use Huffman coding. Huffman coding is a universally used entropy coder. The purpose of this section is not to explain the principle of Huffman coding, which is very standard in the domain of information theory. However, we wish to explain in this section why our implementation is computationally efficient.

For decoding purposes, both the Huffman tree and the dictionary must be saved: then, at the decoding stage, bits can be read linearly. At each bit read, we either go down the tree according to the value read, or go back up to the top if a leaf (node with no node of interior level) has been reached, in which case the code is searched in the dictionary and converted to its corresponding character. To allow for the creation of the dictionary and the tree in the same loop, we use an extra array called "leaves", which tracks, at each iteration, what are the leafs reachable by going down from the current node. This allows to keep track of which characters should have their codes updated when creating a new node in the Huffman tree.

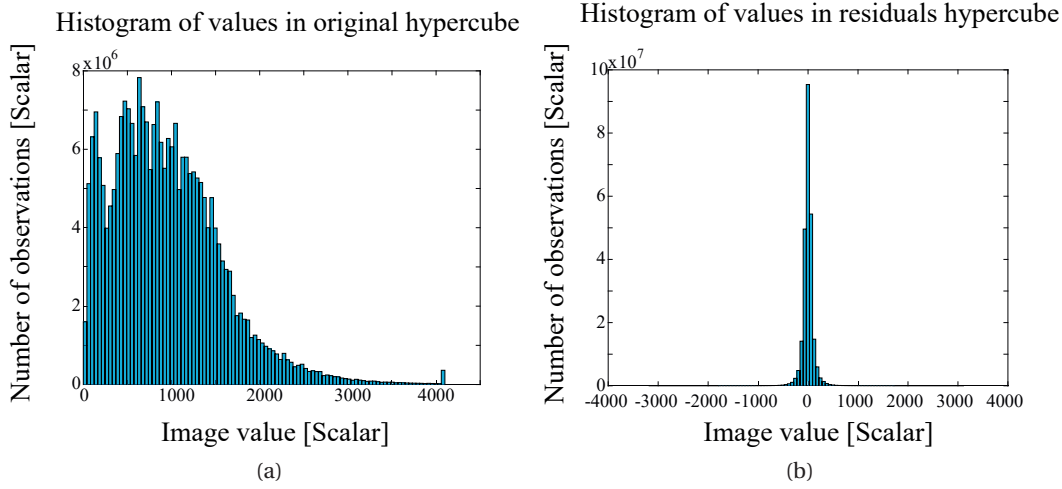


Figure A.4 Histogram of values for **(a)** the original hypercube and **(b)** the residuals hypercubes.

Instead of proposing the pseudo-code of this algorithm, we illustrate it on a simple example where $chars = [a, b, c, d]$ and $pr = [0.4, 0.3, 0.2, 0.1]$ (Figures A.5 and A.6).

Initially (Figure A.5a), each node leads to its associated character and the leaves of this node are simply the nodes themselves. Huffman entropy coding theory gathers the two characters with the lowest probabilities, that is, "c" and "d". Hence we know the last bit of the code of "c" (respectively "d") is 0 (respectively 1). The new node created, indexed 5, has two children, 3 and 4, and the leaves of this node are also 3 and 4 (Figure A.5b). At the following iteration (Figure A.6a), both nodes 2 and 5 have the lowest probability (0.3) so they are branched by the Huffman tree. Node 6 is created, and has 2 and 5 as children. Algorithmically, its leaves are determined as the concatenation of all the leaves of its two children, which effectively gives 2, 3 and 4. The advantage of updating the leaves array, is that now the update of the codes in the dictionary is straightforward: the dictionary should add a 0 at the beginning of the codes of the leaves of node 2, and add a 1 at the beginning of the codes of the leaves of node 5. The principle is the same for all the subsequent iteration, which is one single iteration in our example (Figure A.6b).

The encoding stage turns the hypercube is a one dimensional array, and converts a each character into its code in the dictionary. Since the dictionary keys are the residuals of the hypercube, they do not follow any specific indexing order. This means that, at each read of a character, we would have to browse through the dictionary to find this specific character. However, in our case, the characters are the residuals; the hypercubes of the Léman-Baïkal project are integers between 0 and 4095, which means the characters to code are integers in the range $[-4095, 4095]$. To index the elements of the dictionary, we create a lookup table (LUT) of size 8191; for each element of the dictionary, the associated binary code is placed at index $4095 + res$, where res is the value of the residual to code. Doing so, whenever a character res is read, its corresponding binary code is directly read at index $4095 + res$ of the LUT, saving a lot of computational time.

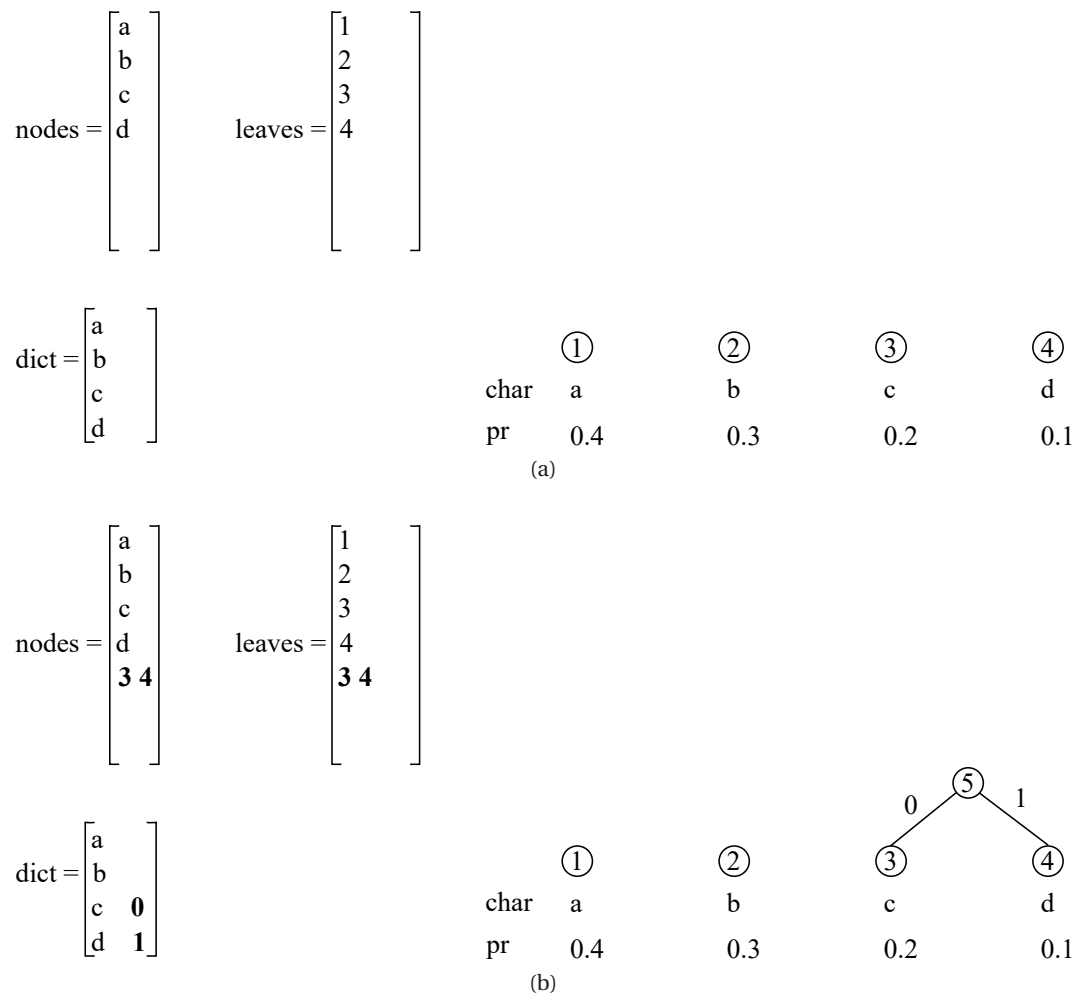
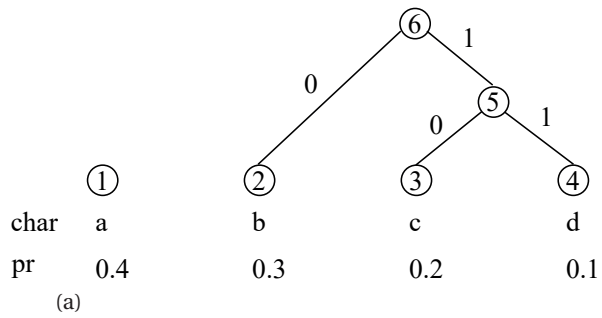


Figure A.5 First two iterations of our Huffman tree and dictionary function.

$$\text{nodes} = \begin{bmatrix} a \\ b \\ c \\ d \\ 3\ 4 \\ \mathbf{2\ 5} \end{bmatrix} \quad \text{leaves} = \begin{bmatrix} 1 \\ 2 \\ 3 \\ 4 \\ 3\ 4 \\ \mathbf{2\ 3\ 4} \end{bmatrix}$$

$$\text{dict} = \begin{bmatrix} a \\ b \\ c \\ d \end{bmatrix} \begin{bmatrix} \mathbf{0} \\ 0 \\ 10 \\ 11 \end{bmatrix}$$



$$\text{nodes} = \begin{bmatrix} a \\ b \\ c \\ d \\ 3\ 4 \\ 2\ 5 \\ \mathbf{1\ 6} \end{bmatrix} \quad \text{leaves} = \begin{bmatrix} 1 \\ 2 \\ 3 \\ 4 \\ 3\ 4 \\ 2\ 3\ 4 \\ \mathbf{1\ 2\ 3\ 4} \end{bmatrix}$$

$$\text{dict} = \begin{bmatrix} a \\ b \\ c \\ d \end{bmatrix} \begin{bmatrix} \mathbf{0} \\ 10 \\ 110 \\ 111 \end{bmatrix}$$

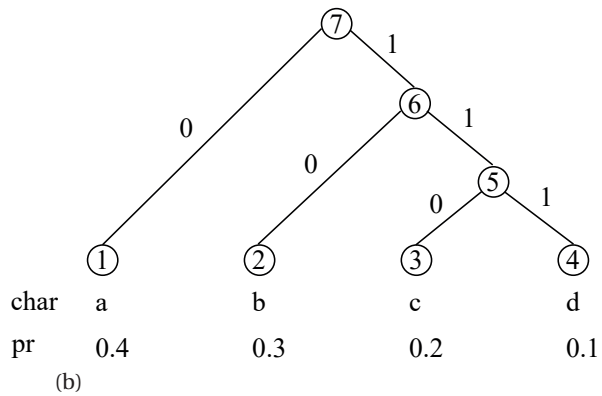


Figure A.6 Last two iterations of our Huffman tree and dictionary function.

A.2.3 Computational Time and Compression Rate

We compressed 10 hypercubes using the process described in the previous sections. The computation was performed on a computer equipped with an Intel Core i7-4800 MQ 2.7 Ghz QuadCore. The average computational time was 615.58 seconds, and the average compression ratio (ratio of the compressed size, divided by the original size) was 0.328, with a standard deviation of 0.006. Comparatively, zip compression is performed in 32.8 seconds on average, but achieves an average of 0.561 (standard deviation 0.090). These results were obtained for images of different surfaces (water, vegetation, built structures). In spite of a rapid increase of reflectance in the near infrared, vegetation pixels, for instance, did not alter the performance of the band-to-band prediction. This compression scheme is reliable and achieves a compression rate that is comparable to more complex, state-of-the-art techniques, but takes time to compress large folders of data.

Bibliography

- [1] S. Adler-Golden, A. Berk, L. Bernstein, S. Richtsmeier, P. Acharya, M. Matthew, G. Anderson, C. Allred, L. Jeong, and J. Chetwynd. FLAASH, a MODTRAN4 atmospheric correction package for hyperspectral data retrievals and simulations. In *7th Annual JPL Airborne Earth Science Workshop*, pages 9–14, Pasadena, California, USA, 1998.
- [2] R. J. Adrian and J. Westerweel. *Particle image velocimetry*. Cambridge University Press, Cambridge, UK, 2011.
- [3] A. Baldridge, S. Hook, C. Grove, and G. Rivera. The ASTER spectral library version 2.0. *Remote Sensing of Environment*, 113(4):711–715, 2009.
- [4] K. Barbieux. Pushbroom hyperspectral data orientation by combining feature-based and area-based co-registration techniques. *Accepted for publication in Remote Sensing, and online in Preprints*, 2018030226, 2018.
- [5] K. Barbieux, A. Charitsi, and B. Merminod. Icy lakes extraction and water-ice classification using landsat 8 oli multispectral data. *International Journal of Remote Sensing*, 39(11):3646–3678, 2018.
- [6] K. Barbieux, D. Constantin, and B. Merminod. Correction of airborne pushbroom images orientation using bundle adjustment of frame images. In *International Archives of the Photogrammetry, Remote Sensing & Spatial Information Sciences*, page 813, Praha, Czech Republic, 2016.
- [7] K. Barbieux, V. Nouchi, and B. Merminod. Airborne hyperspectral sensor radiometric self-calibration using near-infrared properties of deep water and vegetation. In *SPIE Remote Sensing*, page 99990M, Edinburgh, UK, 2016.
- [8] A. Baumgartner, P. Gege, C. Köhler, K. Lenhard, and T. Schwarzmaier. Characterisation methods for the hyperspectral sensor HySpex at DLR’s calibration home base. In *Sensors, Systems, and Next-Generation Satellites XVI*, page 85331H, Edinburgh, UK, 2012.
- [9] H. Bay, A. Ess, T. Tuytelaars, and L. Van Gool. Speeded-up robust features (surf). *Computer vision and image understanding*, 110(3):346–359, 2008.

Bibliography

- [10] H. Bay, T. Tuytelaars, and L. Van Gool. SURF: Speeded Up Robust Features. In *European conference on computer vision*, pages 404–417, Graz, Austria, 2006.
- [11] C. Belzile, J. A. Gibson, and W. F. Vincent. Colored dissolved organic matter and dissolved organic carbon exclusion from lake ice: Implications for irradiance transmission and carbon cycling. *Limnology and Oceanography*, 47(5):1283–1293, 2002.
- [12] M. W. A. Bennett. Rapid monitoring of wetland water status using density slicing. In *Fourth Australasian Remote Sensing Conference*, pages 682–691, Adelaide, Australia, 1987.
- [13] E. Bergamini, G. Ligorio, A. Summa, G. Vannozzi, A. Cappozzo, and A. M. Sabatini. Estimating orientation using magnetic and inertial sensors and different sensor fusion approaches: accuracy assessment in manual and locomotion tasks. *Sensors*, 14(10):18625–18649, 2014.
- [14] A. Berk, G. P. Anderson, L. S. Bernstein, P. K. Acharya, H. Dothe, M. W. Matthew, S. M. Adler-Golden, J. H. Chetwynd Jr, S. C. Richtsmeier, B. Pukall, et al. MODTRAN 4 radiative transfer modeling for atmospheric correction. In *SPIE's International Symposium on Optical Science, Engineering, and Instrumentation*, pages 348–353, Denver, Colorado, USA, 1999.
- [15] L. S. Bernstein, S. M. Adler-Golden, R. L. Sundberg, R. Y. Levine, T. C. Perkins, A. Berk, A. J. Ratkowski, G. Felde, and M. L. Hoke. A new method for atmospheric correction and aerosol optical property retrieval for VIS-SWIR multi-and hyperspectral imaging sensors: QUAC (QUick Atmospheric Correction). Technical report, SPECTRAL SCIENCES INC BURLINGTON MA, 2005.
- [16] A. Börner, L. Wiest, P. Keller, R. Reulke, R. Richter, M. Schaepman, and D. Schlöpfer. Sensor: a tool for the simulation of hyperspectral remote sensing systems. *ISPRS Journal of Photogrammetry and Remote Sensing*, 55(5):299–312, 2001.
- [17] D. Bouffard, I. Kiefer, A. Wüest, S. Wunderle, and D. Odermatt. Are surface temperature and chlorophyll in a large deep lake related? an analysis based on satellite observations in synergy with hydrodynamic modelling and in-situ data. *Remote Sensing of Environment*, 209:510–523, 2018.
- [18] L. Breiman, J. Friedman, C. J. Stone, and R. A. Olshen. *Classification and regression trees*. CRC press, Boca Raton, Florida, USA, 1984.
- [19] A. Bricaud, M. Babin, A. Morel, and H. Claustre. Variability in the chlorophyll-specific absorption coefficients of natural phytoplankton: Analysis and parameterization. *Journal of Geophysical Research: Oceans*, 100(C7):13321–13332, 1995.
- [20] B. V. Brower, A. Lan, and J. M. McCabe. Hyperspectral lossless compression. In *SPIE's International Symposium on Optical Science, Engineering, and Instrumentation*, pages 247–257, Denver, Colorado, USA, 1999.

-
- [21] L. Brown and K. L. Young. Assessment of three mapping techniques to delineate lakes and ponds in a Canadian High Arctic wetland complex. *Arctic*, 59(3):283–293, 2006.
- [22] C. Cariou and K. Chehdi. Automatic georeferencing of airborne pushbroom scanner images with missing ancillary data using mutual information. *IEEE Transactions on Geoscience and Remote Sensing*, 46(5):1290–1300, 2008.
- [23] X. Ceamanos and S. Douté. Spectral smile correction of CRISM/MRO hyperspectral images. *IEEE Transactions on Geoscience and Remote Sensing*, 48(11):3951–3959, 2010.
- [24] S. Chalov, J. Thorslund, N. Kasimov, D. Aybullaev, E. Ilyicheva, D. Karthe, A. Kositsky, M. Lychagin, J. Nittrover, M. Pavlov, et al. The Selenga river delta: a geochemical barrier protecting Lake Baikal waters. *Regional Environmental Change*, 17(7):2039–2053, 2017.
- [25] F. Chen, M. Zhang, B. Tian, and Z. Li. Extraction of glacial lake outlines in Tibet Plateau using Landsat 8 imagery and Google Earth engine. *IEEE Journal of Selected Topics in Applied Earth Observations and Remote Sensing*, 10(9):4002–4009, 2017.
- [26] H.-M. Chen, P. K. Varshney, and M. K. Arora. Performance of mutual information similarity measure for registration of multitemporal remote sensing images. *IEEE Transactions on Geoscience and Remote Sensing*, 41(11):2445–2454, 2003.
- [27] D. Clausi, A. Qin, M. Chowdhury, P. Yu, and P. Maillard. MAGIC: MAP-Guided Ice Classification system. *Canadian Journal of Remote Sensing*, 36(S1):S13–S25, 2010.
- [28] T. Cocks, R. Jenssen, A. Stewart, I. Wilson, and T. Shields. The HyMapTM airborne hyperspectral sensor: the system, calibration and performance. In *Proceedings of the 1st EARSeL workshop on Imaging Spectroscopy*, pages 37–42, Zurich, Switzerland, 1998.
- [29] S. Collings, P. Caccetta, N. Campbell, and X. Wu. Techniques for BRDF correction of hyperspectral mosaics. *IEEE Transactions on Geoscience and Remote Sensing*, 48(10):3733–3746, 2010.
- [30] D. Constantin. *Miniature hyperspectral systems*. PhD thesis, Ecole Polytechnique Fédérale de Lausanne, Lausanne, Switzerland, 2017.
- [31] M. S. P. Cubero-Castan, D. Constantin, K. S. Barbieux, V. M. Nouchi, Y. Akhtman, and B. Merminod. A new smoothness based strategy for semi-supervised atmospheric correction: application to the Léman-Baïkal campaign. In *7th Workshop on Hyperspectral Image and Signal Processing: Evolution in Remote Sensing*, pages 1–4, Tokyo, Japan, 2015.
- [32] A. Dadon, E. Ben-Dor, and A. Karnieli. Use of derivative calculations and minimum noise fraction transform for detecting and correcting the spectral curvature effect (smile) in Hyperion images. *IEEE Transactions on Geoscience and Remote Sensing*, 48(6):2603–2612, 2010.

Bibliography

- [33] J. P. De Villiers, F. W. Leuschner, and R. Geldenhuys. Centi-pixel accurate real-time inverse distortion correction. In *International Symposium on Optomechatronic Technologies*, page 726611, San Diego, California, USA, 2008.
- [34] D. Doxaran, R. N. Cherukuru, and S. Lavender. Estimation of surface reflection effects on upwelling radiance field measurements in turbid waters. *Journal of Optics A: Pure and Applied Optics*, 6(7):690, 2004.
- [35] J. Dozier. Remote sensing of snow in visible and near-infrared wavelengths. *Theory and applications of optical remote sensing*, pages 527–547, 1989.
- [36] C. B. Duane. Close-range camera calibration. *Photogramm. Eng.*, 37(8):855–866, 1971.
- [37] G. L. Feyisa, H. Meilby, R. Fensholt, and S. R. Proud. Automated Water Extraction Index: A new technique for surface water mapping using Landsat imagery. *Remote Sensing of Environment*, 140:23–35, 2014.
- [38] P. S. Frazier, K. J. Page, et al. Water body detection and delineation with Landsat TM data. *Photogrammetric engineering and remote sensing*, 66(12):1461–1468, 2000.
- [39] C. H. Fritsen and J. C. Priscu. Seasonal change in the optical properties of the permanent ice cover on Lake Bonney, Antarctica: consequences for lake productivity and phytoplankton dynamics. *Limnology and Oceanography*, 44(2):447–454, 1999.
- [40] J. G. Fryer and D. C. Brown. Lens distortion for close-range photogrammetry. *Photogrammetric engineering and remote sensing*, 52(1):51–58, 1986.
- [41] P. Geladi, J. Burger, and T. Lestander. Hyperspectral imaging: calibration problems and solutions. *Chemometrics and intelligent laboratory systems*, 72(2):209–217, 2004.
- [42] T. Geldsetzer, J. v. d. Sanden, and B. Brisco. Monitoring lake ice during spring melt using RADARSAT-2 SAR. *Canadian Journal of Remote Sensing*, 36(S2):S391–S400, 2010.
- [43] T. Geldsetzer and J. Yackel. Sea ice type and open water discrimination using dual co-polarized C-band SAR. *Canadian Journal of Remote Sensing*, 35(1):73–84, 2009.
- [44] A. A. Gitelson, B.-C. Gao, R.-R. Li, S. Berdnikov, and V. Saprygin. Estimation of chlorophyll-a concentration in productive turbid waters using a hyperspectral imager for the coastal ocean—the Azov Sea case study. *Environmental Research Letters*, 6(2):024023, 2011.
- [45] H. J. Gons, M. T. Auer, and S. W. Effler. Meris satellite chlorophyll mapping of oligotrophic and eutrophic waters in the laurentian great lakes. *Remote Sensing of Environment*, 112(11):4098–4106, 2008.
- [46] D. G. Goodenough, A. Dyk, K. O. Niemann, J. S. Pearlman, H. Chen, T. Han, M. Murdoch, and C. West. Processing Hyperion and ALI for forest classification. *IEEE transactions on geoscience and remote sensing*, 41(6):1321–1331, 2003.

-
- [47] J. A. Goodman, Z. Lee, and S. L. Ustin. Influence of atmospheric and sea-surface corrections on retrieval of bottom depth and reflectance using a semi-analytical model: a case study in Kaneohe Bay, Hawaii. *Applied Optics*, 47(28):F1–F11, 2008.
- [48] H. R. Gordon and M. Wang. Influence of oceanic whitecaps on atmospheric correction of ocean-color sensors. *Applied Optics*, 33(33):7754–7763, 1994.
- [49] M. Govender, K. Chetty, and H. Bulcock. A review of hyperspectral remote sensing and its application in vegetation and water resource studies. *Water Sa*, 33(2):145–151, 2007.
- [50] E. Grafarend. The optimal universal transverse Mercator projection. In *Geodetic Theory Today*, pages 51–51, L'Aquila, Italia, 1995.
- [51] A. A. Green, M. Berman, P. Switzer, and M. D. Craig. A transformation for ordering multispectral data in terms of image quality with implications for noise removal. *IEEE Transactions on geoscience and remote sensing*, 26(1):65–74, 1988.
- [52] N. Haala, D. Fritsch, D. Stallmann, and M. Cramer. On the performance of digital airborne pushbroom cameras for photogrammetric data processing-a case study. *International Archives of Photogrammetry and Remote Sensing*, 33(B4/1; PART 4):324–331, 2000.
- [53] A. Habib, W. Xiong, F. He, H. L. Yang, and M. Crawford. Improving orthorectification of UAV-based push-broom scanner imagery using derived orthophotos from frame cameras. *IEEE Journal of Selected Topics in Applied Earth Observations and Remote Sensing*, 10(1):262–276, 2017.
- [54] M. A. Haq, K. Jain, and K. Menon. Monitoring glacial lakes using remote sensing tech. In *14th Annual International Conference and Exhibition on Geospatial Information Technology and Applications, India Geospatial Forum*, pages N/A–N/A, Gurgaon, India, 2012.
- [55] R. M. Haralick, K. Shanmugam, et al. Textural features for image classification. *IEEE Transactions on systems, man, and cybernetics*, SMC-3(6):610–621, 1973.
- [56] J. Hedley, A. Harborne, and P. Mumby. Technical note: Simple and robust removal of sun glint for mapping shallow-water benthos. *International Journal of Remote Sensing*, 26(10):2107–2112, 2005.
- [57] G. A. Hodgkins, I. C. James, and T. G. Huntington. Historical changes in lake ice-out dates as indicators of climate change in New England, 1850–2000. *International Journal of Climatology*, 22(15):1819–1827, 2002.
- [58] S. Hong, H. Jang, N. Kim, and H.-G. Sohn. Water area extraction using radarsat SAR imagery combined with landsat imagery and terrain information. *Sensors*, 15(3):6652–6667, 2015.

Bibliography

- [59] K. I. Itten, F. Dell’Endice, A. Hueni, M. Kneubühler, D. Schläpfer, D. Odermatt, F. Seidel, S. Huber, J. Schopfer, T. Kellenberger, et al. APEX-the hyperspectral ESA airborne prism experiment. *Sensors*, 8(10):6235–6259, 2008.
- [60] M. Jaud, N. Le Dantec, J. Ammann, P. Grandjean, D. Constantin, Y. Akhtman, K. Barbieux, P. Allemand, C. Delacourt, and B. Merminod. Direct georeferencing of a pushbroom, lightweight hyperspectral system for mini-UAV applications. *Remote Sensing*, 10(2):204, 2018.
- [61] S. Jawak and A. Luis. A rapid extraction of water body features from antarctic coastal oasis using very high-resolution satellite remote sensing data. *Aquatic Procedia*, 4:125–132, 2015.
- [62] S. D. Jawak, K. Kulkarni, and A. J. Luis. A review on extraction of lakes from remotely sensed optical satellite data with a special focus on cryospheric lakes. *Advances in Remote Sensing*, 4(03):196, 2015.
- [63] S. D. Jawak and A. J. Luis. A semiautomatic extraction of Antarctic lake features using WorldView-2 imagery. *Photogrammetric Engineering & Remote Sensing*, 80(10):939–952, 2014.
- [64] R. R. Jensen, A. J. Hardin, P. J. Hardin, and J. R. Jensen. A new method to correct push-broom hyperspectral data using linear features and ground control points. *GIScience & Remote Sensing*, 48(3):416–431, 2011.
- [65] L. Ji, L. Zhang, and B. Wylie. Analysis of dynamic thresholds for the normalized difference water index. *Photogrammetric Engineering & Remote Sensing*, 75(11):1307–1317, 2009.
- [66] A. M. Johansson and I. A. Brown. Adaptive classification of supra-glacial lakes on the West Greenland ice sheet. *IEEE Journal of Selected Topics in Applied Earth Observations and Remote Sensing*, 6(4):1998–2007, 2013.
- [67] R. E. Kalman et al. A new approach to linear filtering and prediction problems. *Journal of basic Engineering*, 82(1):35–45, 1960.
- [68] J. Karvonen, M. Simila, and M. Makynen. Open water detection from Baltic Sea ice Radarsat-1 SAR imagery. *IEEE Geoscience and Remote Sensing Letters*, 2(3):275–279, 2005.
- [69] M. Kass, A. Witkin, and D. Terzopoulos. Snakes: Active contour models. *International journal of computer vision*, 1(4):321–331, 1988.
- [70] S. Kay, J. D. Hedley, and S. Lavender. Sun glint correction of high and low spatial resolution images of aquatic scenes: A review of methods for visible and near-infrared wavelengths. *Remote Sensing*, 1(4):697–730, 2009.

-
- [71] J. P. Kern and M. S. Pattichis. Robust multispectral image registration using mutual information models. *IEEE Transactions on Geoscience and Remote Sensing*, 45(5):1494–1505, 2007.
- [72] I. Kiefer, D. Odermatt, O. Anneville, A. Wüest, and D. Bouffard. Application of remote sensing for the optimization of in-situ sampling for monitoring of phytoplankton abundance in a large lake. *Science of the Total Environment*, 527:493–506, 2015.
- [73] M. Kim, J. Y. Park, Y. Kopilevich, G. Tuell, and W. Philpot. Correction for reflected sky radiance in low-altitude coastal hyperspectral images. *Applied optics*, 52(32):7732–7744, 2013.
- [74] G. J. Kirkpatrick, D. F. Millie, M. A. Moline, and O. Schofield. Optical discrimination of a phytoplankton species in natural mixed populations. *Limnology and Oceanography*, 45(2):467–471, 2000.
- [75] B. C. Ko, H. H. Kim, and J. Y. Nam. Classification of potential water bodies using Landsat 8 OLI and a combination of two boosted random forest classifiers. *Sensors*, 15(6):13763–13777, 2015.
- [76] S. Kocaman and H. Ingensand. GPS and INS integration with Kalman filtering for direct georeferencing of airborne imagery. Technical report, 2003.
- [77] K. Korzeniowska and O. Korup. Object-based detection of lakes prone to seasonal ice cover on the Tibetan Plateau. *Remote Sensing*, 9(4):339, 2017.
- [78] M. Köhl, C. Lassen, and B. B. Jørgensen. Light penetration and light intensity in sandy marine sediments measured with irradiance and scalar irradiance fiber-optic microprobes. *Marine Ecology Progress Series*, 105(1/2):139–148, 1994.
- [79] T. Kutser, E. Vahtmäe, B. Paavel, and T. Kauer. Removing glint effects from field radiometry data measured in optically complex coastal and inland waters. *Remote Sensing of Environment*, 133:85–89, 2013.
- [80] D. Labate, M. Ceccherini, A. Cisbani, V. De Cosmo, C. Galeazzi, L. Giunti, M. Melozzi, S. Pieraccini, and M. Stagi. The Prisma payload optomechanical design, a high performance instrument for a new hyperspectral mission. *Acta Astronautica*, 65(9):1429–1436, 2009.
- [81] R. Latifovic and D. Pouliot. Analysis of climate change impacts on lake ice phenology in Canada using the historical satellite data record. *Remote Sensing of Environment*, 106(4):492–507, 2007.
- [82] C. Lee and J. Bethel. Georegistration of airborne hyperspectral image data. *IEEE Transactions on Geoscience and Remote Sensing*, 39(7):1347–1351, 2001.

Bibliography

- [83] C. Lee, H. J. Theiss, J. S. Bethel, and E. M. Mikhail. Rigorous mathematical modeling of airborne pushbroom imaging systems. *Photogrammetric Engineering & Remote Sensing*, 66(4):385–392, 2000.
- [84] S. Leigh, Z. Wang, and D. A. Clausi. Automated ice–water classification using dual polarization SAR satellite imagery. *IEEE Transactions on Geoscience and Remote Sensing*, 52(9):5529–5539, 2014.
- [85] M. Leppäranta. Modelling the formation and decay of lake ice. In *The impact of climate change on European lakes*, pages 63–83. 2010.
- [86] G. Leshkevich and S. V. Nghiem. Great lakes ice classification using satellite C-band SAR multi-polarization data. *Journal of Great Lakes Research*, 39:55–64, 2013.
- [87] G. A. Leshkevich and S. V. Nghiem. Satellite SAR remote sensing of Great Lakes ice cover, part 2. ice classification and mapping. *Journal of Great Lakes Research*, 33(4):736–750, 2007.
- [88] D. G. Lowe. Object recognition from local scale-invariant features. In *7th IEEE international conference on computer vision.*, pages 1150–1157, Kerkyra, Greece, 1999.
- [89] J. Lukas, J. Fridrich, and M. Goljan. Digital camera identification from sensor pattern noise. *IEEE Transactions on Information Forensics and Security*, 1(2):205–214, 2006.
- [90] D. R. Lyzenga, N. P. Malinas, and F. J. Tanis. Multispectral bathymetry using a simple physically based algorithm. *IEEE Transactions on Geoscience and Remote Sensing*, 44(8):2251, 2006.
- [91] P. Manavalan, P. Sathyanath, and G. Rajegowda. Digital image analysis techniques to estimate waterspread for capacity evaluations of reservoirs. *Photogrammetric Engineering and Remote Sensing*, 59(9):1389–1395, 1993.
- [92] M. W. Matthews. A current review of empirical procedures of remote sensing in inland and near-coastal transitional waters. *International Journal of Remote Sensing*, 32(21):6855–6899, 2011.
- [93] S. K. McFeeters. The use of the Normalized Difference Water Index (NDWI) in the delineation of open water features. *International journal of remote sensing*, 17(7):1425–1432, 1996.
- [94] J. Mielikainen and P. Toivanen. Clustered dpcm for the lossless compression of hyper-spectral images. *IEEE Transactions on Geoscience and Remote Sensing*, 41(12):2943–2946, 2003.
- [95] K.-H. Mittenzwey, S. Ullrich, A. Gitelson, and K. Kondratiev. Determination of chlorophyll a of inland waters on the basis of spectral reflectance. *Limnology and Oceanography*, 37(1):147–149, 1992.

-
- [96] C. Mobley, E. Boss, and C. Roesler. Ocean optics web book, 2010. Web site.
- [97] C. D. Mobley. Estimation of the remote-sensing reflectance from above-surface measurements. *Applied Optics*, 38(36):7442–7455, 1999.
- [98] A. Morel, D. Antoine, and B. Gentili. Bidirectional reflectance of oceanic waters: accounting for Raman emission and varying particle scattering phase function. *Applied Optics*, 41(30):6289–6306, 2002.
- [99] M. M. Mostafa and J. Hutton. Direct positioning and orientation systems: How do they work? What is the attainable accuracy? In *The American Society of photogrammetry and remote sensing annual meeting*, pages 23–27, St. Louis, Missouri, USA, 2001.
- [100] P. Mouroulis, R. O. Green, and T. G. Chrien. Design of pushbroom imaging spectrometers for optimum recovery of spectroscopic and spatial information. *Applied Optics*, 39(13):2210–2220, 2000.
- [101] J. L. Mueller, C. Davis, R. Arnone, R. Frouin, K. Carder, Z. Lee, R. Steward, S. Hooker, C. D. Mobley, and S. McLean. Above-water radiance and remote sensing reflectance measurements and analysis protocols. Technical report, 2000.
- [102] S. V. Nghiem and G. A. Leshkevich. Satellite SAR remote sensing of Great Lakes ice cover, part 1. Ice backscatter signatures at C band. *Journal of Great Lakes Research*, 33(4):722–735, 2007.
- [103] J. Nieke, J. W. Kaiser, D. Schlaepfer, J. Brazile, K. I. Itten, P. Strobl, M. E. Schaepman, and G. J. Ulbrich. Calibration methodology for the airborne dispersive pushbroom imaging spectrometer (APEX). In *Remote Sensing*, pages 445–452, Maspalomas, Canary Islands, Spain, 2004.
- [104] M. Nolan, G. Liston, P. Prokein, J. Brigham-Grette, V. L. Sharpton, and R. Huntzinger. Analysis of lake ice dynamics and morphology on Lake El’gygytgyn, NE Siberia, using synthetic aperture radar (SAR) and Landsat. *Journal of Geophysical Research: Atmospheres*, 107(D2):ALT 3–1—ALT 3–12, 2002.
- [105] C. M. O’reilly, S. R. Alin, P.-D. Plisnier, A. S. Cohen, and B. A. McKee. Climate change decreases aquatic ecosystem productivity of Lake Tanganyika, Africa. *Nature*, 424(6950):766, 2003.
- [106] M. A. Palmer, C. A. Reidy Liermann, C. Nilsson, M. Flörke, J. Alcamo, P. S. Lake, and N. Bond. Climate change and the world’s river basins: anticipating management options. *Frontiers in Ecology and the Environment*, 6(2):81–89, 2008.
- [107] P. K. Panday, H. Bulley, U. Haritashya, and B. Ghimire. Supraglacial lake classification in the Everest region of Nepal Himalaya. In *Geospatial Techniques for Managing Environmental Resources*, pages 86–99. 2011.

Bibliography

- [108] T. Perkins, S. Adler-Golden, M. W. Matthew, A. Berk, L. S. Bernstein, J. Lee, and M. Fox. Speed and accuracy improvements in FLAASH atmospheric correction of hyperspectral imagery. *Optical Engineering*, 51(11):111707–1, 2012.
- [109] D. Poli, L. Zhang, and A. Gruen. Orientation of satellite and airborne imagery from multi-line pushbroom sensors with a rigorous sensor model. *International Archives of Photogrammetry and Remote Sensing*, 35(B1):130–135, 2004.
- [110] J.-P. Ramirez-Paredes, D. J. Lary, and N. R. Gans. Low-altitude terrestrial spectroscopy from a pushbroom sensor. *Journal of Field Robotics*, 33(6):837–852, 2016.
- [111] R. Richter, D. Schlapfer, and A. Muller. Operational atmospheric correction for imaging spectrometers accounting for the smile effect. *IEEE Transactions on Geoscience and Remote Sensing*, 49(5):1772–1780, 2011.
- [112] Y. Rzhhanov and S. Pe’eri. Pushbroom-frame imagery co-registration. *Marine Geodesy*, 35(2):141–157, 2012.
- [113] B. Scheuchl, R. Caves, I. Cumming, and G. Staples. Automated sea ice classification using spaceborne polarimetric SAR data. In *Geoscience and Remote Sensing Symposium*, pages 3117–3119, Sydney, Australia, 2001.
- [114] B. Scheuchl, I. Hajnsek, and I. Cumming. Sea ice classification using multi-frequency polarimetric SAR data. In *Geoscience and Remote Sensing Symposium*, pages 1914–1916, Toronto, Ontario, Canada, 2002.
- [115] M. J. Scholze, K. S. Barbieux, A. De Simone, M. Boumasmoud, C. C. Suess, R. Wang, and P. Gonczy. PI (4, 5) P2 forms dynamic cortical structures and directs actin distribution and cell polarity in *C. elegans* embryos. *bioRxiv*, page 215079, 2017.
- [116] N. Selmes, T. Murray, and T. James. Fast draining lakes on the Greenland ice sheet. *Geophysical Research Letters*, 38(15):N/A–N/A, 2011.
- [117] S. V. Semovski, N. Y. Mogilev, and P. P. Sherstyankin. Lake Baikal ice: analysis of AVHRR imagery and simulation of under-ice phytoplankton bloom. *Journal of Marine Systems*, 27(1):117–130, 2000.
- [118] P. Senin. Dynamic time warping algorithm review. Technical report, 2008.
- [119] L. Shen and C. Li. Water body extraction from Landsat ETM+ imagery using adaboost algorithm. In *18th International Conference on Geoinformatics*, pages 1–4, Beijing, China, 2010.
- [120] J. Škaloud. *Optimizing georeferencing of airborne survey systems by INS/DGPS*. PhD thesis, University of Calgary, Calgary, Alberta, Canada, 1999.

-
- [121] J. Soria. An investigation of the near wake of a circular cylinder using a video-based digital cross-correlation particle image velocimetry technique. *Experimental Thermal and Fluid Science*, 12(2):221–233, 1996.
- [122] A. Sundal, A. Shepherd, P. Nienow, E. Hanna, S. Palmer, and P. Huybrechts. Evolution of supra-glacial lakes across the Greenland ice sheet. *Remote Sensing of Environment*, 113(10):2164–2171, 2009.
- [123] J. Suomalainen, N. Anders, S. Iqbal, G. Roerink, J. Franke, P. Wenting, D. Hünninger, H. Bartholomeus, R. Becker, and L. Kooistra. A lightweight hyperspectral mapping system and photogrammetric processing chain for unmanned aerial vehicles. *Remote Sensing*, 6(11):11013–11030, 2014.
- [124] M. Tarasov, G. Shinkareva, O. Tutubalina, M. Lychagin, D. Constantin, M. Rehak, Y. Akhtman, B. Merminod, N. Tofield-Pasche, S. Chalov, et al. Investigation of heavy metals distribution in suspended matter and macrophytes of the selenga river delta using airborne hyperspectral remote sensing. In *9th EARSeL SIG Imaging Spectroscopy workshop*, pages N/A–N/A, Luxembourg, 2015.
- [125] N. Terry Jr. How to read the universal transverse mercator (UTM) grid. *GPS World*, 32, 1996.
- [126] W. Thielicke and E. Stamhuis. PIVlab—towards user-friendly, affordable and accurate digital particle image velocimetry in Matlab. *Journal of Open Research Software*, 2(1):e30, 2014.
- [127] M. Tomlinson, T. Wynne, and R. Stumpf. An evaluation of remote sensing techniques for enhanced detection of the toxic dinoflagellate, *Karenia brevis*. *Remote Sensing of Environment*, 113(3):598–609, 2009.
- [128] B. Triggs, P. F. McLauchlan, R. I. Hartley, and A. W. Fitzgibbon. Bundle adjustment—a modern synthesis. In *International workshop on vision algorithms*, pages 298–372, Corfu, Greece, 1999.
- [129] I. Valiela, J. McClelland, J. Hauxwell, P. J. Behr, D. Hersh, and K. Foreman. Macroalgal blooms in shallow estuaries: controls and ecophysiological and ecosystem consequences. *Limnology and oceanography*, 42(5part2):1105–1118, 1997.
- [130] G. Verhoeven and J. Loenders. Looking through black-tinted glasses—a remotely controlled infrared eye in the sky. In *2nd International Conference on Remote Sensing in Archaeology. Proceedings of the 2nd International Workshop.*, pages 73–79, Rome, Italy, 2006.
- [131] C. Verpoorter, T. Kutser, L. Tranvik, et al. Automated mapping of water bodies using Landsat multispectral data. *Limnol. Oceanogr. Methods*, 10(12):1037–1050, 2012.

Bibliography

- [132] P. Viola and W. M. Wells III. Alignment by maximization of mutual information. *International journal of computer vision*, 24(2):137–154, 1997.
- [133] W. Wanner, X. Li, and A. Strahler. On the derivation of kernels for kernel-driven models of bidirectional reflectance. *Journal of Geophysical Research: Atmospheres*, 100(D10):21077–21089, 1995.
- [134] M. H. White, D. R. Lampe, F. C. Blaha, and I. A. Mack. Characterization of surface channel CCD image arrays at low light levels. *IEEE Journal of Solid-State Circuits*, 9(1):1–12, 1974.
- [135] R. S. Williams Jr and J. G. Ferrigno. *State of the Earth's cryosphere at the beginning of the 21st century: glaciers, global snow cover, floating ice, and permafrost and periglacial environments*. US Geological Survey, Reston, Virginia, USA, 2012.
- [136] O. J. Woodman. An introduction to inertial navigation. Technical report, University of Cambridge, Computer Laboratory, 2007.
- [137] X. Xiao, Z. Shen, and X. Qin. Assessing the potential of vegetation sensor data for mapping snow and ice cover: a Normalized Difference Snow and Ice Index. *International Journal of Remote Sensing*, 22(13):2479–2487, 2001.
- [138] H. Xu. Modification of normalised difference water index (NDWI) to enhance open water features in remotely sensed imagery. *International journal of remote sensing*, 27(14):3025–3033, 2006.
- [139] K. Yang and L. C. Smith. Supraglacial streams on the Greenland ice sheet delineated from combined spectral–shape information in high-resolution satellite imagery. *IEEE Geoscience and Remote Sensing Letters*, 10(4):801–805, 2013.
- [140] C.-K. Yeh and V. J. Tsai. Direct georeferencing of airborne pushbroom images. *Journal of the Chinese Institute of Engineers*, 38(5):653–664, 2015.
- [141] Q. Yu and D. A. Clausi. SAR sea-ice image analysis based on iterative region growing using semantics. *IEEE Transactions on Geoscience and Remote Sensing*, 45(12):3919–3931, 2007.
- [142] J. Zadnik, D. Guerin, R. Moss, A. Orbeta, R. Dixon, C. Simi, S. Dunbar, and A. Hill. Calibration procedures and measurements for the COMPASS hyperspectral imager. *Algorithms and Technologies for Multispectral, Hyperspectral, and Ultraspectral Imagery X*, 1:M2, 2004.
- [143] N. Zakhvatkina, A. Korosov, S. Muckenhuber, S. Sandven, and M. Babiker. Operational algorithm for ice–water classification on dual-polarized RADARSAT-2 images. *The Cryosphere*, 11(1):33–46, 2017.
- [144] Y. Zhang, M. A. van Dijk, M. Liu, G. Zhu, and B. Qin. The contribution of phytoplankton degradation to chromophoric dissolved organic matter (cdom) in eutrophic shallow lakes: field and experimental evidence. *water research*, 43(18):4685–4697, 2009.

Kévin Barbieux
Avenue de France 18C
1004 Lausanne
+41 79 505 11 43
Nationality: French
Marital Status: not
married, no child

Curriculum Vitae



EDUCATION

- | | |
|--------------------------------------|---|
| September 2013 – May 2018 (expected) | EPFL Lausanne (Switzerland), PhD in Computer Sciences, on hyperspectral data processing.
Involved in the Lemman-Baikal project, a three years campaign aiming to study the water quality of Lake Geneva and Lake Baikal using airborne pushbroom scanner measurements. Topics of research : <ul style="list-style-type: none"> • Georeferencing of pushbroom scan lines. • Radiometric calibration: camera noise, atmospheric correction, bidirectional reflectance distribution function. • Data analysis, using image processing and machine learning. |
| September 2010 – September 2013 | Mines Paristech (France), Master in Sciences and Executive Engineering, awarded with excellent distinction (GPA: 3.4/4). Minor in Applied Mathematics: image processing, automatics, robotics. |
| September 2008 – September 2010 | “Classes préparatoires” in Lycée Faidherbe, Lille (France). Two years intensive program in mathematics and physics. |

EXPERIENCE

- | | |
|------------------------|---|
| 2014 – 2017 | Teaching assistant for two courses: calculus (functions, sequences, series, integrals) and estimation methods, for bachelor students of EPFL. |
| March – September 2013 | Internship at PSA Peugeot Citroën on Recognition of Hand gestures . |
| January 2013 | Teaching assistant for functions of a complex variable at Mines Paristech, for master students. |
| June – August 2012 | Internship at Infosys Limited (Bangalore, India) on image processing : detection of linear features in a smartphone screen, and development of a software recording the features detected in an Excel sheet. |

PUBLICATIONS

- K. Barbieux. Expected in 2018. **Pushbroom Hyperspectral Data Orientation by Combining Feature-Based and Area-Based Co-Registration Techniques**. Submitted to *IEEE TGRS*.
- K.Barbieux, A. Charitsi, B. Merminod. Expected in 2018. **Icy Lakes Extraction and Water-Ice Classification Using Landsat 8 OLI Multispectral Data**. Accepted for publication in *International Journal of Remote Sensing*.
- K. Barbieux, V. Nouchi, B. Merminod. 2016. **Airborne Hyperspectral Sensor Radiometric Self-Calibration Using Near-Infrared Properties of Deep Water and Vegetation**. *Remote Sensing of the Ocean, Sea Ice, Coastal Waters, and Large Water Regions*, 9999, p. 99990M.

- K. Barbieux, D. Constantin, B. Merminod. 2016. **Correction of Airborne Pushbroom Images Orientation Using Bundle Adjustment of Frame Images**. *International Archives of the Photogrammetry, Remote Sensing & Spatial Information Sciences*, 41, p. 813.
- M. Scholze, K. Barbieux, A. De Simone, M. Boumasmoud, C. Suess, R. Wang, & P. Gonczy. 2017. PI (4, 5) P2 forms dynamic cortical structures and directs actin distribution and cell polarity in *C. elegans* embryos. *bioRxiv*, 215079.
- M. Cubero-Castan, D. Constantin, K. Barbieux, V. Nouchi, Y. Akhtman, & B. Merminod. 2016, June. A new smoothness based strategy for semi-supervised atmospheric correction: Application to the Leman-Baikal campaign. *IEEE 7th Workshop on Hyperspectral Image and Signal Processing: Evolution in Remote Sensing (WHISPERS)*, pp. 1-4.
- M. Jaud, N. Le Dantec, J. Ammann, P. Grandjean, D. Constantin, Y. Akhtman, K. Barbieux, P. Allemand, C. Delacourt & Merminod, B. 2018. Direct Georeferencing of a Pushbroom, Lightweight Hyperspectral System for Mini-UAV Applications. *Remote Sensing*, 10(2), p. 204.

SCIENTIFIC SKILLS

- Hyperspectral data geometric and radiometric calibration (see publications).
- Image processing: image filtering, enhancement, mathematical morphology.
- Machine Learning: SVM, decision trees, neural networks.
- Data compression: entropy coding, linear prediction.

COMPUTER SKILLS

- **Experienced (+5 years) Java developer.**
- Experienced (+4 years) MATLAB developer.
- Able to work with Python (6 months experience).
- Experienced with ERDAS Imagine, AGISOFT Photoscan, ENVI.
- Experienced with Word, Powerpoint, Excel, LaTeX.

LANGUAGES

- French: native speaker.
- English: bilingual (TOEFL iBT score: 105; TOEIC score: 985).
- Spanish: intermediate.

EXTRACURRICULAR ACTIVITIES

- Volunteering to help young children (between 7 and 14 years old) with their homework, from 2014 to 2017.
- Responsible for the fitness training room of Mines Paristech (2012).
- Administrator in the junior firm of Mines Paristech (2012).
- Free time activities: singing, playing strategy games.

